APPLICATION OF SMART CLASSIFICATION TECHNIQUES TO NON-DESTRUCTIVE TESTING OF COMPOSITES

BY: M.Z. ISKANDARANI

(B.Eng (Hon.), M.Sc, AMIEE (GB), MIEEE (USA))

Submitted for the degree of

DOCTOR OF PHILOSOPHY in Engineering

at

University of Warwick

Advanced Technology Centre

Department of Engineering

Coventry, UK

1995

NUMEROUS ORIGINALS IN COLOUR

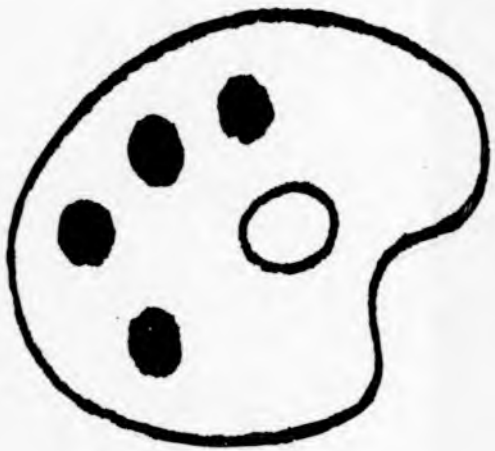

DECLARATION

I declare that all the work appeared in this thesis was carried out by myself unless otherwise acknowledged in the text.

ACKNOWLEDGEMENTS

I would like to express my gratitude and thanks to my excellent supervisor, Dr. Gordon F. Smith for the Total confidence that he placed in me, the full academical and financial support and for his constant encouragement and help.

I would also like to thank Dr. Peter T. Davies (Director of the Advanced Technology Centre) for supporting this project and for valuable comments and disscussions.

My appreciation extends to all the staff of the Advanced technology Centre and warwick Manufacturing Group for their help and contribution, and to the following companies for their co-operation, collaboration and technical support:

(1) SOFRATEST U.K (SPEEDTRONIC DIVISION).

(2) AGEMA INFRARED SYSTEMS.

(3) NCS (NEURAL COMPUTER SCIENCES).

(4) ROVER GROUP.

(5) OMETRON.

(6) COMFORD DESIGN LIMITED.

My personal appreciation goes to Dr.Mike Arrington (SOFRATEST U.K) and Alan Grant (AGEMA INFRARED SYSTEMS) for their personal contribution to this work.

However, my everlasting gratitude and thanks to Ian Pearson of the Advanced Technology Centre for many hours that he spent with me correcting and editing this document and for his support and advice.

SUMMARY

Composites manufactured for applications in the automotive industry were non-destructively tested to determine damage using the following techniques:

(1) Low frequency tapping.

(2) High frequency (C-Scan).

(3) Visual imaging.

(4) Low and high temperature pulse video thermography.

Various levels of impact energy were applied to the following types of composites

(I) RIM: Reaction injection moulded.

(II) Woven Glass.

(III) GMT: Glass mat thermoplastic.

Some interesting results were obtained which could be explained through analytical and numerical modelling. These results were analyzed through developments of the following algorithms:

(a) A novel approach to damage detection using wavelength variation and sequence grouping software.

(b) Correlation of the various NDT techniques through one mathematical equation and software.

(c) The introduction of the uniformity factor concept and software to account for variations among samples quality in relation to experimental results.

(d) The development of smart classification system together with standard neural network algorithms for prediction and classification.

The objectives of this research were all achieved.

CONTENTS

LIST OF FIGURES

LIST OF TABLES

NOMENCLATURE

E_I	:	Applied impact energy.
E_{di}	:	Defect energy, i= 1....n.
ε	:	Balancing energy factors accounts for frictional forces.
δ_t	:	Impulse functions.
E_{th}	:	Threshold Energy.
E_r	:	Response energy.
Z, ζ	:	Complex geometrical plans.
R, θ	:	Polar coordinates.
W	:	Complex potential plan.
η, t	:	Complex potential variables.
g	:	Distance between energy states.
d_t	:	Length of an energy state.
$\underline{f}$	:	Field function.
K_{eff}	:	Effective contact stiffness.
K_c	:	Stiffness over good area.
K_d	:	Stiffness over defective area.
d	:	Defect diameter.
υ,p,q	:	Constants depend on effective boundary conditions.
E	:	Flexural modulus of a material and modulus of elasticity.
h	:	Depth of a defect.
ρ	:	Material density.

X	:	Input signal-low frequency model.
y_1, y_2	:	Output signals-low frequency model.
α, β	:	Gain functions.
$K_{General}$	:	General normalized response factor-low frequency model.
K_{ref}	:	Normalized time response of low frequency tapping model.
K_{avg}	:	Normalized average time response of low frequency tapping.
Ω	:	Multiplication function-low frequency model.
t_{ref}, t_{avg}, t_d	:	Reference, average and defect time responses-low frequency.
κ, χ	:	Differential parameters of tolerance-low frequency model.
C	:	Acoustic velocity.
μ	:	Poissons ratio.
$P(x)$	:	Pressure amplitude.
ξ_a	:	Absorption coefficient.
ξ_s	:	Scattering coefficient.
ξ	:	Attenuation coefficient.
z	:	Acoustic impedance.
r	:	Reflection coefficient
T	:	Transmission coefficient.
I	:	Acoustic energy.
V	:	Analogue voltage.
τ	:	Decay time.
N	:	Number of ring counts.
f	:	Transducer resonant frequency.
E_A	:	Acoustic emission energy.

ϖ	:	proportionality constant.
b	:	Distribution characteristic constant.
TD	:	Thermal diffusivity.
TE	:	Thermal effusivity.
L	:	Material thickness.
Q	:	Heat flux.
L'	:	Radiant emittance.
τ_o	:	Atmosphere transmission coefficient.
ε_o	:	Object emissivity.
L_aT_m	:	Atmosphere radiant emittance.
L_o	:	Object radiant emittance.
ε_a	:	Absorbed radiation.
ρ_r	:	Reflected radiation.
τ_t	:	Transmitted radiation.
ν	:	Frequency of radiation.
h_p	:	Plank's constant.
K	:	Boltzmans constant.
$I(\nu)$	:	Intensity of radiation.
g(X)	:	decision discriminating function-LC.
X_j	:	Input vector.
W_j	:	Weight vector.
Π	:	Bias value.
h(X)	:	Classification function-NNC.
T_c	:	Classification matrix.

S_i : Grouped classification sequences.

r_{ij} : Amplitude factor.

Ξ : Normalizing factor.

T_h : Hybrid column matrix.

q_j : Quantizing vector.

S : Data source.

W_{ssi} : Weight or response factor.

C_{ij} : Grouped subsequences.

f_T : Uniformity factor-column.

h_T : Uniformity factor-row.

$g(x)$: Activation classification function.

h_l : Hidden layer(s).

e_i : Vector of errors.

o : Output layer vector(s).

t_r : Target activation of output layer.

Γ : Learning rate.

Θ : Momentum factor.

th_i : Threshold function.

S_{th} : Threshold level sequence.

L_i : Optical source.

A_p : Appearance function.

N_l : Number of defective layers-low temperature.

N_h : Number of defective layers-high temperature.

D_l : Low temperature defect diameter function.

D_h : High temperature defect diameter function.

CHAPTER 1

INTRODUCTION.

Composites are increasingly being used as structural materials. One of the major advantages of composite materials is their ability to be tailored to meet certain applications. Thus, a particular type of fibre and matrix can be used to produce components acquiring different lay-ups, thicknesses and volume fractions. This implies that a defect which is considered to be critical in one component might be totally acceptable in another. Hence, setting quality control and inspection standards is a very complex task, and is not made any simpler or economical due to the different NDT techniques, each of which is capable of detecting certain defects. Together with employing standard but variable interpretation methods, efforts have been directed toward balancing the cost and complexity of an inspection technique against the quality of information obtained and the flexibility of the technique in detecting various types of defects.

In the automotive industry there is a need to manufacture with larger production rate but tighter quality control which requires inspection techniques with higher speed and better resolution with more intelligence and accuracy compared to the current conventional ones. This work will be looking at past, present and future approaches to NDT.

CHAPTER 2

OBJECTIVES.

As a solution to the problems associated with NDT and its application in the automotive industry, there is a need to establish an intelligent analysis system coupled to a portable detection environment that unifies all different types of inputs and automatically considers various fibre/matrix combinations which leads to elimination of any ambiguity regarding defect severity and its effect on the component under consideration. This suggests the use of an imaging system.

We propose that conversion of various data structures and images in conjunction with **smart classification** (a specially devised finger printing algorithm based on pattern recognition techniques) and **neural networks** (parallel, highly interconnected systems made of many indivisible processing units interacting with each other via adaptive weights) together with **wavelength variations** (incorporation of different energy sources to uncover the presence of damage) to be a promising system for non-destructive testing. Figure 1.1 shows such a system. This automated image capturing system possess the following main characteristics:

(1) The ability to extract important information from a background of irrelevant details.

(2) The capacity to learn from past experience and apply its knowledge to new different situations.

(3) Capable of correlating from distorted and lost data files.

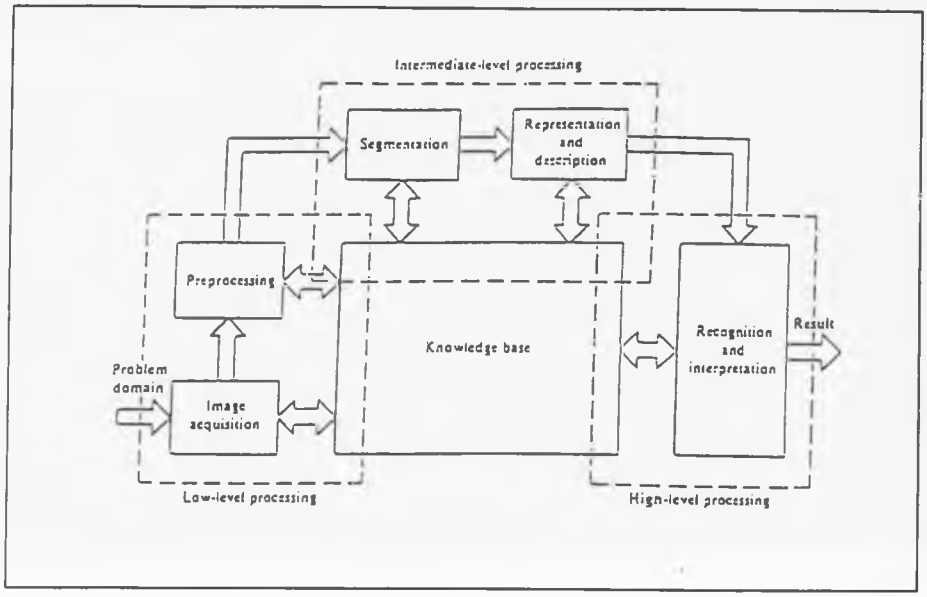

Figure 2.1: An intelligent image capturing, processing and recognition system [214].

CHAPTER 3

COMPOSITES

Composite materials have developed rapidly over the last few years and it is assumed now that they are used in almost every industrial sector. The science and technology of composite materials are based on a design concept which is principally different from that of conventional materials [1],[2],[3]. In the process of designing such materials, we need to establish performance objectives for materials selection, structural configuration and fabrication route.

With fibre composites, the relationship between micro-structure and macroscopic arrangement and their dependence on processing techniques are much stronger than conventional materials. Thus, composites technology offers the potential to design materials for particular uses at different scale levels.

Firstly, at the microscopic level, the internal structure of a component can be controlled through processing. Some examples are:-

(1) Moulding of short-fibre composites, where fibre orientation, length and distribution may be controlled to yield the desired local properties.

(2) Filament winding of continuous fibres.

(3) Hybridization of fibres and textile structural patterns based on weaving, braiding, knitting etc. (Figure 3.1).

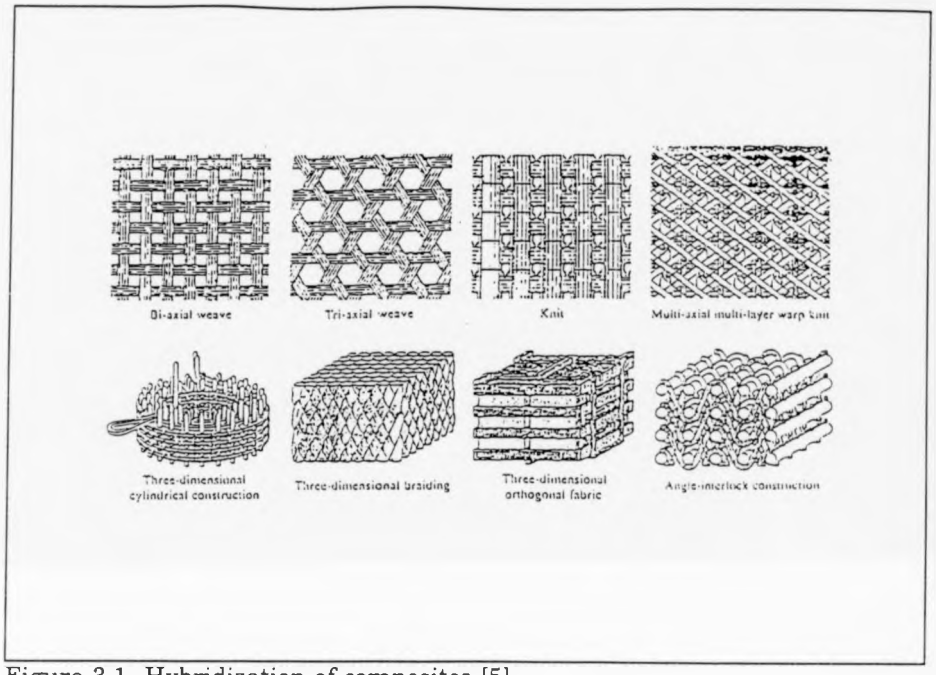

Figure 3.1 Hybridization of composites [5].

In all the above cases, the required local stiffness, strength, toughness and other pre-specified properties can be obtained by controlling the fibre type, orientation and volume fraction throughout the structural component.

Secondly, the external geometrical shape of a structural component can also be designed, for example:-

(1) Advances in the technology of filament winding enable the automated production of components with complex contours.

(2) The ability to fabricate three-dimensional fibre using advanced textile technology.

(3) The capability of producing longer and more integrated structural

components of net shape is enhanced even more.

The integrated and system approach, ranging from microstructure to component net, offers almost unlimited opportunity in composites processing and manufacturing as discussed by various researchers [4-8].

As a result, the concept of tailoring materials at a fundamental level to meet specific design criterion has been a topic of interest to many Engineers and only recently it has been fully incorporated in the overall design (Figure 3.2).

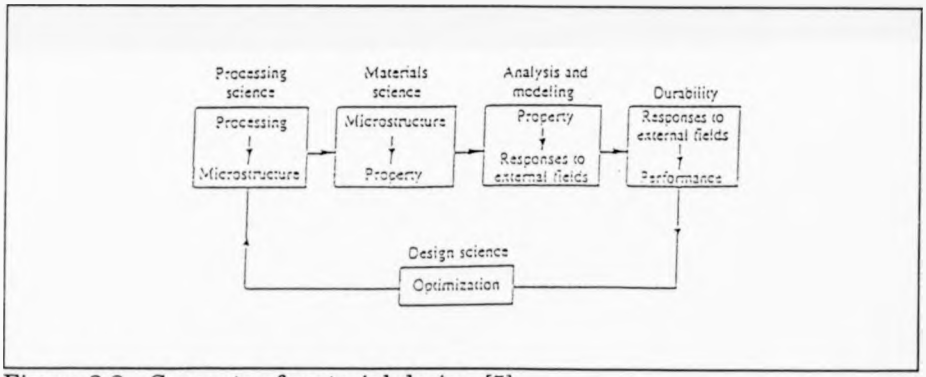

Figure 3.2: Concepts of material design [5].

Fibre reinforced composites provide alternatives often only limited by the designers imagination. They represent excellent examples of the principles of material design where the performance of the whole is greater than the sum of its parts [9] & [10]. Fibres, light-weight, very strong and stiff but easily damaged with limited engineering application, and the matrix, comparatively weak and often brittle and usually not attractive for structural load-bearing applications.

Together, however, they provide a wide range of materials and chance for optimization which is not mechanical properties exclusive but extends to thermal, acoustic, electromagnetic, creep and fatigue characteristics.

From the above, it is expected that the number of material configurations will constantly increase through the use of hybrids and other innovative material constructive forms [11]. Hence, we must choose the path of understanding the properties of the basic material which will require new test and inspection procedures (Figure 3.3).

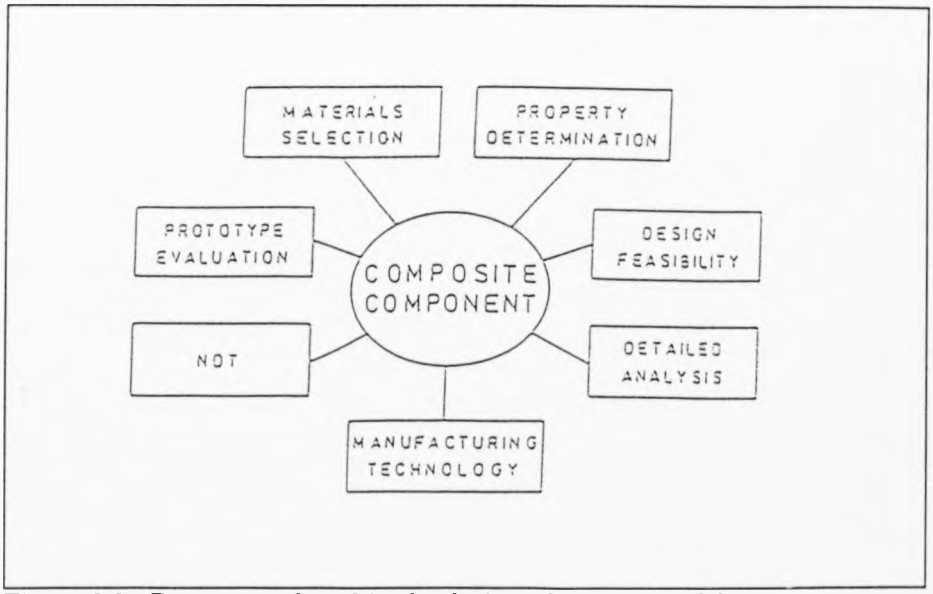

Figure 3.3: Process employed in the design of composites [6].

CHAPTER 4

DAMAGE IN COMPOSITES

4.1 Introduction.

When evaluating the contribution of defects to the failure process it is important to distinguish between two classes of defects:

(a) Defects that act on a microscopic level,

(b) Critical defects in a practical or multi-dimensional component.

For (a) their role can be regarded as substantial from the point of view of quality control based on experiments but with little or no relevance to the standards set for practical components. These aim to combine the fibre and resin into a well consolidated product. The fibre and resin may separate before manufacture or, more usually, they may already be combined in the form of a pre-preg material.

The types of defects introduced can be classified as follows:

(1) Manufacturing Defects.

Composite materials can be manufactured by a number of techniques as mentioned in the previous chapter. The manufacturing technique selected depends partly upon the size and quality of the required composite. During these manufacturing processes, defects can be introduced into the material, although the size and frequency of

occurrences of each type depends upon the particular process cycle. A number of defect types have been identified including:-

(a) Incompletely cured matrix due to incorrect curing cycle or faulty material.

(b) Incorrect fibre volume fraction due to excess or insufficient resin.

(c) Voids due to volatile resin components or improper control of air during cure.

(d) Existence of foreign bodies.

(e) Fibre misalignment. This causes local changes in volume fraction by preventing ideal packing of fibres.

(f) Ply misalignment. This is produced as a consequence of mistakes made in lay-up of the component plies.

(g) Wavy fibres. These are produced by in-plane kinking of the fibres in a ply and can seriously affect laminate strength.

(h) Ply cracking. Thermally induced cracks occur with certain ply lay-ups due to differential contraction of the plies after cure.

(i) Delaminations. These are planar defects usually at ply boundaries and fairly rare during the manufacture of the basic material but may be produced by contamination during lay-up or by machining.

(j) Fibre defects. The presence of defects in the fibres themselves is one of the ultimate limiting factors in determining strength, where sometimes faulty fibres can be identified as the sites from which damage growth has been initiated. These defects are present in

fibres supplied, are always likely to be considered as one of the basic material properties.

(k) Bonding defects. During manufacture components may be bonded together and it is possible for defects to occur in the bondline due to incorrect cure conditions for the adhesive or contamination of the surfaces to be bonded.

(2) In-Service Defects.

Composites can be degraded in service by a number of mechanisms and those of prime importance will depend upon the environment experienced and the sensitivity of the particular materials used. The mechanisms and degradation include static overload, impact, fatigue, hygrothermal effects, overheating, lightning strike and creep. However, although the mechanisms by which defects are initiated and grow are varied, only the following types of defects result:

(a) Fracture or buckling of fibres.

(b) Failure of the interface between the fibres and matrix.

(c) Cracks.

(d) Delaminations.

(e) Bond failures.

(f) Ingress of moisture.

It is obvious that composites can differ from the ideal either during manufacture or in service. The extent to which any of these deviations from

ideal should be considered as defect is a function of the intended use of the material and the significance of the deviation on the required performance. All defect types are known to adversely affect performance in some way.

From previous studies [15-20], the following defects are thought to be of prime importance in current materials.

(a) **Manufacturing Defects.**

(i) Voids

(ii) Foreign bodies

(iii) Incorrect fibre volume fraction

(iv) Bonding defects

In practice the most important manufacturing defect and likely to occur is the presence of voids. Some of the other defects occur very rarely or not at all in isolation. Thus the incorrect fibre volume due to insufficient resin will usually be accompanied by voids as well as incorrectly cured resin.

(b) **In-Service Defects.**

(i) Delamination

(ii) Bonding defects

(iii) Cracks

(iv) Moisture ingress

The major in-service defect to be found is the presence of delaminations. These may be produced by fatigue, bearing damage, impact etc.

Debonding can also be found but as yet no method is available to measure adhesive strength. It is not generally expected that cracks will need to be formed since they will lead to delamination growth before a critical stage is reached.

4.2 Impact Damage.

Structural damage of composites as a result of impact is regarded as one of the most critical aspects of functioning that restricts wider applications. In composites, the possibility of plastic deformation is limited which can lead to a substantial amount of damage upon impact, the influence of which on residual properties is hard to predict.

During an impact certain factors affect the outcome of such an operation, namely,

(1) Material Properties
(2) Boundary Conditions
(3) Failure Mechanism
(4) Environmental Factors
(5) Imposed Constraints
(6) Impact Mechanism

When a material is impacted, a stress field is realized on contact. A series of stress waves is then propagated through the material which may or may not cause damage.

During the impact a large number of damage mechanisms may occur affecting the composite material in different ways through each damage specific

characteristics. Damages include, splitting, debonding, matrix cracking, fibre pull-out, fibre-breakage and delamination [21] & [22].

The extent to which a specific failure mechanism occurs depends on the properties of the fibre, matrix and interphase as well as the geometric form and arrangement of the fibres, hence, efficiency. This efficiency in load transfer between a fibre and its surrounding matrix depends on the length of the fibre relative to its critical length. If the length of the fibre is shorter than the critical length, then fibre pull-out and matrix fracture are the dominating mechanisms of energy absorption after an impact. On the other hand, when the fibre length is longer than the critical one, the fibres will, in some cases, break and in others be pulled out. Both fibre failure mechanisms are influenced by the fibre location and orientation with respect to the crack.

It has been shown [23] that for a fibre perfectly bonded to the matrix, the shear stress concentration parallel to the interface is a maximum at the end of the fibre. If the shear strength of the interface or the surrounding matrix material is exceeded, fracture will occur at or close to the interface.

The fracture will start at the fibre end and grow along the fibre as the stress on the system increases. The main processes which can occur at the broken fibre are:-

(1) The crack in the fibre propagates into the surrounding matrix as a brittle crack.

(2) A yield zone is spread along the fibre as a result of the matrix being yielded.

(3) The interface or the matrix immediately adjacent to the fibre or the fibre immediately adjacent to the matrix failing in shear allowing the unloaded fibre to shrink back into the matrix (shear yielding or shear failure does not necessarily imply that the matrix is unable to transfer load to the fibre).

Also the frictional forces at the interface lead to a non-linear build-up in stress in the fibre from the broken ends. The relative importance of these processes depends on the properties of the fibres and the resin.

The relative amounts of interface failure and the magnitude of the frictional forces determine the overall appearance of the fracture surface. For strongly bonded carbon fibre-epoxy resin system with small tensile and shear values, there is only a small amount of debonding.

In contrast, the fracture surfaces of glass fibre-polyester resin with high tensile and shear values undergo massive debonding with large amounts of fibre pull-out.

Experimentally, it is found that for fibres embedded in epoxy matrices, the stress required to extract the fibre does not drop to zero after debonding has occurred because there are large frictional forces which resist the sliding of the

fibre out of the resin sheath.

In addition the reduction in the stress on the fibre at debonding resulted in an increase in fibre diameter owing to the poisson expansion and this leads to an increase in the pressure on the fibre surface [24]. The relative contribution of the interface bonding and frictional forces to the work required to pull the fibre out of the matrix depends on a large number of material parameters with frictional forces making a major contribution for a large pull-out distance. Before making an estimate of the work done in fibre debonding and fibre pull out, reference must be made to the stress distribution along the fibre after debonding has occurred. This debonding will initiate at the fibre ends and spread along the fibre not forbidding the frictional forces from operating and transferring stress to the fibre. This stress which is required to extract the fibre increases as the embedded length increases.

It was shown [25] & [26] that pull out is far more significant than debonding as an energy absorber.However, debonding must occur before pull out. If the shear stress for debonding is large then fibre fracture occurs before extensive debonding and the amount of pull out, and hence energy absorbed is small.

Fibres are the dominant constituent when considering most property characteristics and the same is true when assessing impact performance. For low velocity impact [27] the stored energy capability of the fibre is of key importance. Materials such as aramids and glass which have large areas under

their stress/strain curves, offer good performance. Composites made from these materials tend to fail in a progressive manner through delamination. Carbon fibre systems, in the other hand, can be brittle and fail suddenly at the maximum load.

In calculating delamination and its extent, one would consider the available strain energy per unit area at every point of a laminate interface. The region of highest energy is identified and compared to that of delamination (delamination can be viewed as a plane crack propagating in the interface between two adjacent plies parallel to the applied tension and resulting from the interlaminar stresses). If an area has an excess of energy, it is considered to be delaminated.

4.3 Impact Damage: A Closer Look.

Impact is a key issue in the design of composite structures and may be the limiting design issue in many cases. It is therefore essential that a complete understanding of the response of composite structures to impact be obtained. This comprises two separate areas:

(1) Damage Resistance. Where it is related directly to the impact as it measures the damage incurred by a material or a composite structure [28].

(2) Damage Tolerance. Where it has only a secondary relationship to the impact event since it is the amount and distribution of the damage present that directly determines the damage tolerance, not the details of

the impact event.

The impact event is related to damage tolerance through the damage resistance. Understanding and analyzing the damage resistance of composite structures is therefore important to determine the damage caused by a particular impact. This damage state can then be used to assess the damage tolerance and thus the capability of the structure to continue to meet performance requirements.

The damage that occurs during an impact is a progressive phenomenon. As damage occurs during the impact event, the parameters that govern the response may change. This can influence the overall response. This, in turn, can have an effect on the total amount of damage incurred during the impact event. It is therefore essential to understand how impact response parameters change as damage occurs.

This generally involves considering the global and local responses of the material promoted by the impactor. This will enable us to analyze the dynamic structural response and indentation in the material caused through impact damage. This damage was generally found to consist of small matrix cracks on

the back surface and internal damage, consisting of matrix cracks and delamination, about the size of the impactor.

Hence, a correlation between the composite stiffness and the induced local

stress at the point of impact exists due to the difference in contact area which results in indentations of various levels in relation to area of coverage. This results in the local damage not having a noticeable effect on the global structure response if the area of contact which is related to the impact energy is below a certain level and hence the damage size and depth of defect penetration.

In addition low-speed impact damage can degrade the compression strength of composite structures with transverse shear deformation possible depending on the mass ratio of impactor to sample under test which affects the response time and magnitude and phase of strain response. This strain is found to be lower for clamped specimens compared with the unsupported ones. Hence it is forecasted that boundary conditions significantly affect strain response of impacted structures.

The application of an impact can result in a dynamic stress system which when established can induce a damage that propagates at a number of sites within the material thickness. Composites with their low transverse tensile strength can be prone to this type of effect. In the case of carbon composites which can be opaque the damage may not be apparent without the application of sophisticated inspection method.

It has been reported [29] that upon impact shear failure is found to be the dominant mode of failure, followed by compression which can take the form of local crushing with glass reinforced systems superior to carbon reinforced

materials.

Conventional failure criteria for composites do not address all of the aspects of behaviour encountered in an impact. Both the different types of failure mode and the dynamics of the situation need to be accommodated in the analysis. Hence, any analysis which is intended to evaluate impact performance must consider energy dissipation in all failure processes. In addition, the residual strength which represent the load-carrying capability after an impact event. Such a value is often used as a means of quantifying material behaviour.

Matrix properties are, without a doubt, a key consideration for impact performance, as not only do they provide the mechanism of load transfer as mentioned before, but if damaged during the impact the resulting cracks could allow ingress of moisture which could cause degradation. The properties of the interface are also important, but more difficult to control given a preselected matrix/fibre combination. For weak interfaces failure is generally through large areas of delamination. Laminate construction and orientation can be an important factor in the design for impact performance. Simple unidirectional materials do not perform well, mainly because of high stresses generated transverse to the fibre direction. Also the tendency for delamination is increased where the disposition of individual plies leads to large discontinuities in stiffness. Adopting woven materials or three-dimensional stitched fabrics which tend to promote increased through-thickness tensile strength can be a positive factor.

For a number of applications, especially in the transport industry, the control of energy absorption under impact conditions is an important design feature. Because of this, there have been a number of attempts to improve the energy-absorbing characteristics of matrix materials.

These include the use of plasticizors, the addition of rubber or thermoplastic particles, control of cross-link density, the use of thermoplastic matrices and the use of interlayers within plies.

4.4 Impact Damage: An Energy Band Model

(ORIGINAL CONTRIBUTION)

Under normal conditions (no impact energy applied), material constituents are bound to their respective potential levels with relative stability under small vibrations. As impact energy is applied, shock waves (impulses) may cause damage such as fibre breakage or cracks (that can propagate over time).

When a defect is induced, the original energy distribution could be affected, hence, new energy levels and pockets of energy sub-levels may be formed. This energy re-mapping can be correlated to the applied force of impact via the proposed energy band model described below.

For a non-defective or practically acceptably defective component we will assume an energy level E_{th}. The impact will induce a large impulse such that the overall energy distribution in the material is raised in a manner that

subsequent impacts on the same area follows a power accumulative or exponential law in a context that will make the required impact energy for the same response lower locally but higher globally implying the formation of intermediate energy states or bands of energy in a less stable environment compared to the original structure, hence, propagation of a defect is a strong possibility over a much longer period of time relative to the impact contact time (as shown in Figure 4.1.)

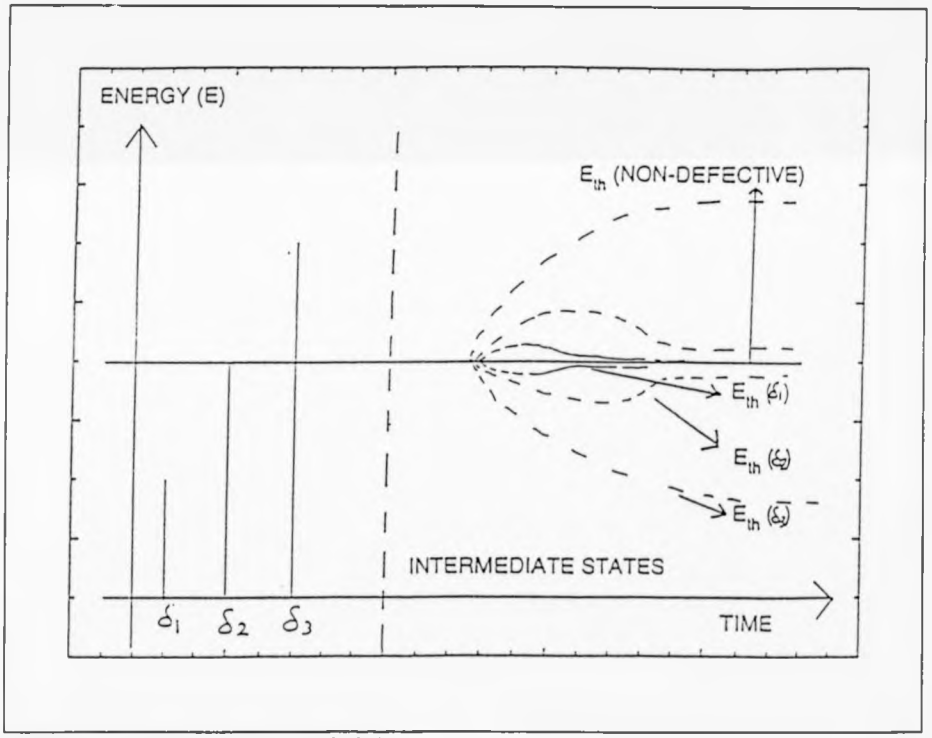

Figure 4.1: Energy Band Model.

From the graph, three cases can be established:

(1) Impact Energy (E_I) is much smaller than the Threshold Energy

($E_I << E_{th}$).

When induced E_I (δ_I) will initiate a response energy E_r ($\delta_1 + n\delta_1$) which contains two energy levels, defect energy (E_{dI}) and threshold energy (E_{th}) such that:

$$E_I = E_{dI} + \epsilon_1 \quad \ldots\ldots\ldots\ldots\ldots\ldots \quad 4.(1)$$

where ε_1 is a small balancing factor that accounts for frictional forces and energy conservation.

$$E_r = E_{th} - E_{dI} \quad \ldots\ldots\ldots\ldots\ldots\ldots \quad 4.(2)$$

Now substituting equation (1) into (2) yields:-

$$E_r = E_{th} + \epsilon_1 - E_I \qquad 4.(3)$$

And for $E_I << E_{th}$ we obtain:

$$E_r \cong E_{th} + \epsilon_1$$

$$\textit{hence} \quad \left| \frac{E_r}{E_{th} + \epsilon_1} \right| = 1 \qquad 4.(4)$$

In this case the applied impact had little or no effect on the structural integrity of the material.

(2) Impact Energy is less or equal to the Threshold Energy ($E_I \leq E_{th}$).

When applied E_I (δ_2) will cause an energy response E_r ($\delta_2 + K\delta_2$) which provoke a step like response with an absolute value below or equal to the critical energy level distributed within the material structure with both negative and positive

phase signal possible. If we now apply (1), (2) and (3) from the previous case with the new boundary condition, we obtain:

$$E_r = E_{th} + E_{d2} \qquad 4.(5)$$

$$E_r = E_{th} + \epsilon_2 - E_I = \epsilon_2 \qquad 4.(6)$$

so,

$$\left[\frac{E_r}{E_{th}} \right] = \left[\frac{\epsilon_2}{E_{th}} \right] \qquad 4.(7)$$

In this case the impact has created a new stable surface which is regarded as non-defective or acceptably defective locally with dependence on the magnitude of resistive forces.

(3) Impact Energy is much greater than the Threshold Energy ($E_I >> E_{th}$).

Upon application $E_I(\delta_3)$ will force an energy response $E_I(\delta_3 + M\delta_3)$ with a ramp characteristics having an absolute value above the resonant energy level within the composite structure.

Again, using equations (1), (2) and (3) we obtain:

$$E_r = E_{th} + E_{d3} \qquad 4.(8)$$

$$E_r = E_{th} + \epsilon_3 - E_I = \epsilon_3 - E_I \qquad 4.(9)$$

hence,

$$\left[\frac{E_r}{E_{th}} \right] = \left[\frac{\epsilon_3 - E_I}{E_{th}} \right] = \left[\frac{-E_I}{E_{th}} \right] \qquad 4.(10)$$

The expression 4.(10) indicates that above the essential energy level a

progressive band of energy states (microthreshold levels) are created and destroyed over a length of time (τ). At equilibrium a finite number of energy levels will be present as discrete energy pockets within an energy envelope. The expression also shows that since the energy distribution in response to this particular level in impact and above is extremely serious as it is controlled by the defect energy with possible phase reversal. In addition, interactions between these substates are possible and a mathematical model for their field interaction in space is possible using CONFORMAL TRANSFORMATION as outlined below [30-40].

A cross section of the energy envelope (energy pockets with difference in potential relative to each other and interactive field strength) is modelled as shown in Figure 4.2.

We will be using a form of bilinear transformation to transform a unit circle of the z-plane to the upper half (Im > 0) of the w-plane.

Consider the transformation:

$$z = x + jy = f(\zeta) = \left(j. \frac{1-\zeta}{1+\zeta} \right) \quad \ldots\ldots\ldots\ldots \quad 4.(11)$$

so,

$$t = \left(- \frac{z-j}{z+j} \right) \quad 4.(12)$$

Now, if x_1 is any general point on the x-axis of the z-plane and if it is

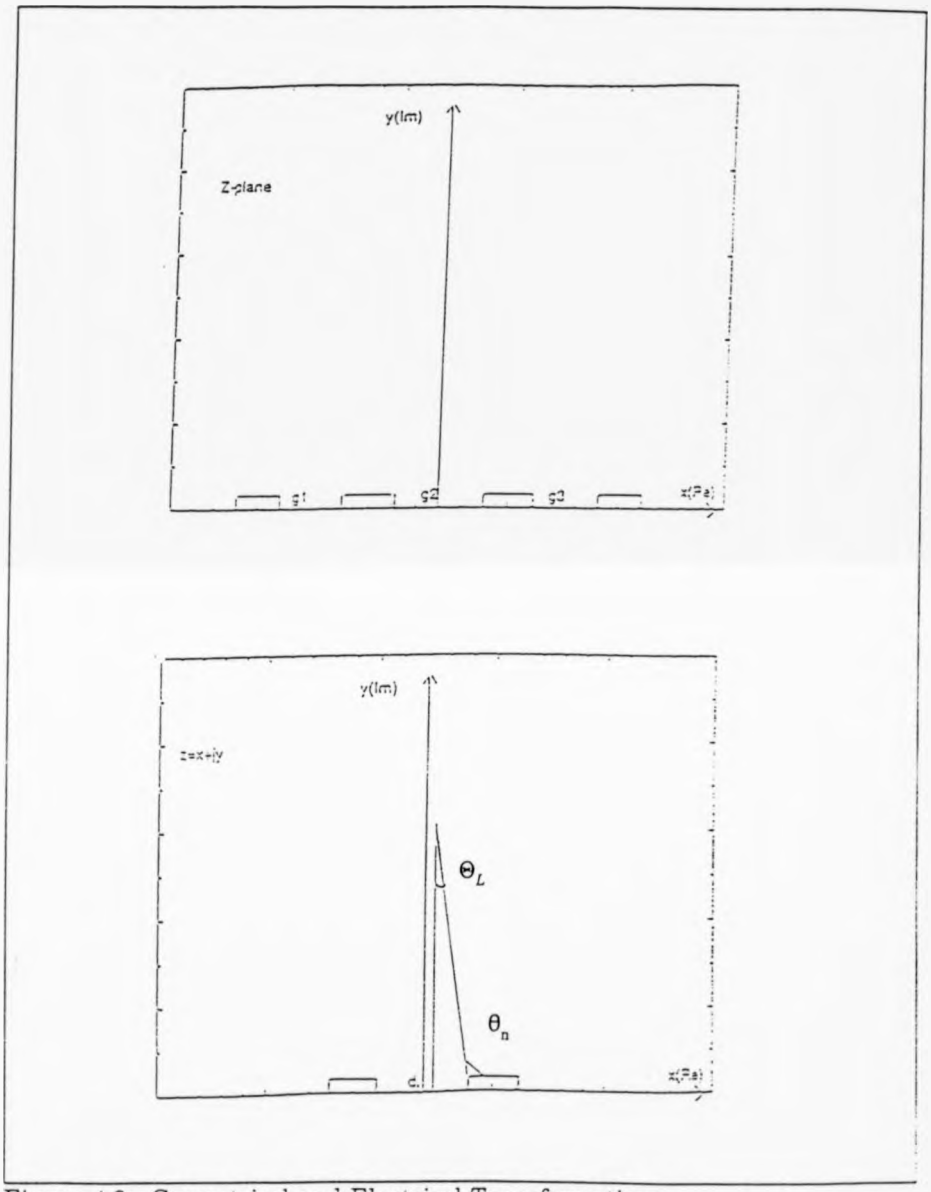

Figure 4.2: Geometrical and Electrical Transformations.

represented in its polar form with a corresponding angle of θ, then (4.12) can

be written as:

$$e^{j\theta_1} = \left(- \frac{x_1 - j}{x_1 + j} \right) \qquad 4.(13)$$

so,

$$\theta_1 = j\ln \left(\frac{x_1 - j}{x_1 + j} \right) \qquad 4.(14)$$

whence,

$$d\theta_1 = j \left(\frac{x_1 + i}{x_1 - j} \right) \left(\frac{- 2jdx_1}{(x_1 + j)^2} \right) = \left| \frac{2dx_1}{(1 + x_1^2)} \right| \qquad 4.(15)$$

Now the SCHWARZ complex potential solution $w = \phi + j\,\psi$ is obtained through the following evaluation.

$$w = \frac{1}{2\pi} \int_{-\infty}^{+\infty} \left(\frac{e^{j\theta_1} + t}{e^{j\theta_1} - t} \right) \varphi(x_1)\, d\theta_1 \qquad 4.(16)$$

Substitution of equations (12), (13) and (15) into (16) gives:

$$w = \frac{1}{2\pi} \int_{-\infty}^{+\infty} \left(\frac{- (1 + x_1 z)}{j (z - x_1)} \right) \cdot \left(\frac{2\, dx_1}{(1 + x_1^2)} \right) \varphi(x_1) \qquad 4.(17)$$

$$w = \frac{j}{\pi} \int_{-\infty}^{+\infty} \left(\frac{(1 + x_1 z)}{(1 + x_1^2)\,(z - x_1)} \right) \varphi(x_1)\, dx_1 \qquad 4.(18)$$

This is a solution of the first boundary value problem of the first kind in the upper half w-plane. The real part of (18) is:

This is POISSON'S integral formula for the upper half plane, and for a number

$$\varphi\ (x,y) = \frac{1}{\pi} \int_{-\infty}^{+\infty} \left(\frac{y}{(x - x_1)^2 + y^2} \right) \varphi(x_1)\ dx_1 \qquad 4.(19)$$

of energy pockets (i + 1) separated by gaps $g_1, g_2, \ldots, g_i$, equation (4.19) becomes:

$$\varphi(x,y) = \left[\frac{\varphi_0 y}{\pi} \int_{-\infty}^{+\infty} \left(\frac{dx_1}{(x-x_1^2)+y^2} \right) + \frac{\varphi_1 y}{\pi} \int_{g_1}^{g_2} \left(\frac{dx_2}{(x-x_2^2)+y^2} \right) + \ldots + \frac{\varphi_i y}{\pi} \int_{g_i}^{+\infty} \left(\frac{dx_i}{(x-x_i^2)+y^2} \right) \right] \qquad 4.(20)$$

Equation (20) describes the overall interaction of many energy pockets on a single point per cycle.

Hence:

$$\left(\frac{\varphi_o + \varphi_i}{2} \right) + \left(\frac{\varphi_o - \varphi_1}{\pi} \right) \tan^{-1} \left(\frac{d_1 - x}{y} \right) + \ldots$$

$$\left(\frac{\varphi_1 - \varphi_2}{\pi} \right) \tan^{-1} \left(\frac{d_2 - x}{y} \right) + \ldots + \left(\frac{\varphi_{i-1} - \varphi_i}{\pi} \right) \tan^{-1} \left(\frac{d_i - x}{y} \right) \qquad 4.(21)$$

To find the complex potential solution $w = \phi + j\,\psi$ and the field expression (21) is re-written in different form by considering Figure (4.2) which shows that:

$$\tan^{-1} \left(\frac{d_2 - x}{y} \right) = \phi_L = (\theta_L - \pi/_2) \qquad 4.(22)$$

where; $\theta_L = \arg (z - d_L)$ is the angle between $(z - d_L)$ and the positive x-axis.

Then:

$$\varphi\ (x,y) = \varphi_i + \left(\frac{\varphi_o - \varphi_1}{\pi} \right) \theta_1 + \ldots + \left(\frac{\varphi_{i-1} - \varphi_i}{\pi} \right) \theta_i$$

$$= \sum_{n=1}^{i} \varphi_i + \left(\frac{\varphi_{n-1} - \varphi_n}{\pi} \right) \theta_n \qquad 4.(23)$$

and

$$\varphi(x,y) = \varphi_i + \left(\frac{\varphi_i - \varphi_1}{\pi} \right) \arg (z - d_1) + \ldots + \left(\frac{\varphi_{i-1} - \varphi_i}{\pi} \right) \arg (z - d_i)$$

$$= \sum_{n=1}^{i} \varphi_i + \left(\frac{\varphi_{n-1} - \varphi_n}{\pi} \right) \arg (z - d_n) \qquad 4.(24)$$

Now equation (23) has the equivalent ELECTRICAL TRANSFORMATION:

$$\left[\varphi(x_1\ y) - \varphi_i \right]$$

$$= R_e \left[\frac{-j}{\pi} \sum_{n=1}^{i} (\varphi_{n-1} - \varphi_n) (\text{Ln } (R_n) + j\ \theta_n) \right] \qquad 4.(25)$$

where: R, θ are polar co-ordinates, and

$$R_L = \left[(x^2 - d_L^2) + y^2 \right]^{1/2}$$

$$\Theta_L = \tan^{-1} \left[\frac{d_L - x}{y} \right] \qquad 4.(26)$$

substituting (26) in (25) yields:

$$\varphi\ (x_1\ y) = \sum_{n=1}^{i} \varphi_i + \left(\frac{\varphi_{n-1} - \varphi_n}{\pi} \right) \theta_n \qquad 4.(27)$$

Now from equations (25), (26) and (27) we can deduce that the complex potential is given by:

$$w = \varphi + j\psi = \sum_{n=1}^{i} \varphi_i + \left(\frac{\varphi_{n-1}\ \varphi_n}{\pi} \right) \text{Ln } (z - d_n) \qquad 4.(28)$$

$$|f| = \left| -j\,\overline{\frac{dw}{dz}} \right| = \sum_{n=1}^{i} \left(\frac{\varphi_{n-1} - \varphi_n}{\pi} \right) \left(\overline{\frac{1}{(z - d_n)}} \right)$$

$$= \left| -j \sum_{n=1}^{i} \left(\frac{\varphi_{n-1} - \varphi_n}{\pi} \right) \left(\frac{(x - d_n) + jy}{(x - d_n)^2 + y^2} \right) \right| \qquad 4.(29)$$

Then:

$$|f| = \left| -j \sum_{n=1}^{i} \left(\frac{\varphi_{n-1} - \varphi_n}{\pi} \right) \left(\frac{(z - d_n)}{|z - d_n|^2} \right) \right|$$

$$= \sum_{n=1}^{i} \left(\frac{\varphi_{n-1} - \varphi_n}{\pi} \right) \left| \frac{(x - d_n) + y}{(x - d_n)^2 + y^2} \right| \qquad 4.(30)$$

The field function produced here in equation (30) represents an approximate model for the effect of potential differences created within a composite structure as a function of impact force which if exceed a certain limit, can create states acquiring different strain/stress energies and each of individual states in an envelope exercise a field effect by the others (Figure 4.3).

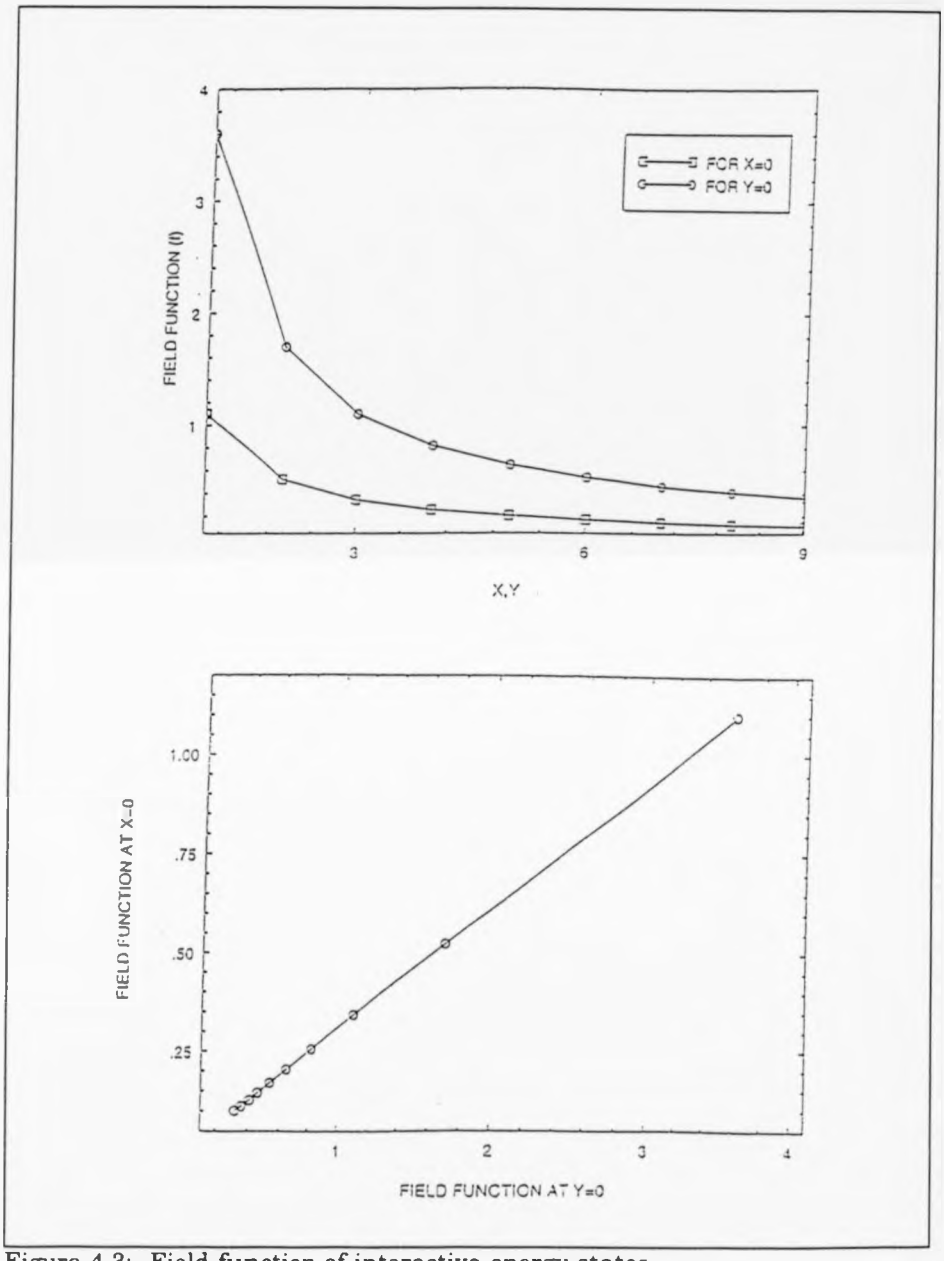

Figure 4.3: Field function of interactive energy states.

CHAPTER 5

DESTRUCTIVE AND NON-DESTRUCTIVE TEST TECHNIQUES

5.1 Introduction.

Composite materials depend on their structural arrangement to obtain their desired mechanical properties. The fibres on their own are generally of little practical use but with a well-designed combination of fibres and matrix a reliable component with good performance is produced and needed in demanding environments such as vehicles, airplanes and space craft industries.

Integrity of a material is based on quality of fabrication as the designed specifications are fulfilled not only the best available structural properties, but also any other combination of properties designed for a particular purpose. Hence, it is important to be able to control the manufacturing and to inspect the materials for their structural arrangements of fibres, matrix and defects which most often have a detrimental effect on the composite properties.

For practical and economical use of composites, it is very important to know not only the level of defect in the material but also its effect on the properties of the material, so that enough evidence will be available for accepting or rejecting a component.

A destructive testing of the mechanical properties is the most direct and

familiar way of accepting a material. But it is desirable to use non-destructive testing and inspection [41-43] to establish the soundness of a component. Two key areas for the application of NDT:

(1) The inspection and control of the manufactured components.

(2) The inspection during service with the object of detecting any damage to the material and thus predict a safe future-life of the component.

Both areas above are used to ensure the safety of a certain composite through inspection of its structural properties.

Until recently, there was no formal quantitative criterion for inspection of advanced composite materials. However over the past few years the need become more urgent to determine the allowed flaw limits and damage growth rates to establish inspection intervals and flaw characteristics. The technology which is being developed at the moment covers three main areas:-

(1) Critical damage identification and detection.

(2) Analysis and non-destructive monitoring of damage progression.

(3) Establishment of critical defect size as a function of stress levels, fatigue cycles and environment.

Thus, in order to develop the non-destructive inspection technology for fibre-reinforced composite materials, it is necessary that the development of detection capabilities be coupled with development of the technology that is capable of

assessing the influence of defect geometry upon strength and stiffness.

5.2 NDT: A Focus.

Testing is said to be non-destructive provided that any satisfactory specimen tested remains fit for service after the test. Changes in the tested specimen using contactable NDT techniques are expected but will not exceed a certain level. On the other hand, significant physical or chemical changes can take place in a destructive testing of a component. Such destructive tests can be useful for statistical analysis, also destructive testing would not be practical when it comes to applications in the nuclear industry and when large single expensive structures are involved.

Another type of testing which is halfway between destructive and non-destructive is proof testing where components are taken beyond the intended operating conditions. If they survive, they will be classified as acceptable and the test is actually regarded as non-destructive in nature even though during this extreme test certain defects could have started to grow and might contribute to the component future failure while in service.

Non-destructive testing helps to ensure that materials enter service in fit condition for the purpose for which they are meant to fulfil, and can check whether subsequent use or misuse has allowed the initiation or growth of defects. Yet, NDT would be a mere drain on resources if the tests themselves are unavailable. Too little sensitivity would allow failure to occur, and too

much sensitivity would waste perfectly good specimens. Clearly, one must distinguish between the capability of a technique and its day-to-day reliability in practice. This will be affected by both economical and human factors.

The basic contributions to the reliability of NDT arise from the nature of the structure itself, the environment in which the structure is expected to operate, and the kinds of defects expected to occur. From this information it is possible to estimate which are the defect types which might be expected to lead to failure and the maximum size of these defects which can be tolerated.

Having estimated the size and nature of the defect types which could lead to failure, a suitable NDT techniques based on understanding of the way in which defect detection is accomplished. The chosen technique needs to be calibrated using what is believed to be a standard calibration specimen. This includes non-defective samples and artificially defected ones.

Failure also involves the systematic relation of component failure and system failure. This leads to what is known as fitness for purpose concept which can take two different forms:

(1) To seek perfection in manufacturing by aiming for the best quality achievable with existing methods, irrespective of final application.

(2) To recognise the variations in significance of defects from one type to

another. The relevant quality is the extent to which the defect affects operating efficiency. This concept is a much more realistic and economic one in terms of industrial and commercial applications.

Current inspection techniques are neither able nor designed to detect all the different types of possible defect, but are restricted in their application to certain specific types of defect. Hence, a working knowledge of the types of defect which might occur and the identification of those which are most likely to be detrimental to the component in operation and how important they are for different types of component is essential when considering an NDT technique. This chosen technique needs to be able to detect defects at three major stages:-

(i) Raw Materials

(ii) During Manufacture

(iii) In Operation

This is essential since defects have the tendency to evolve with time and load application. The following two chapters touch on the essential principles behind NDT techniques.

CHAPTER 6

SONIC AND ULTRA-SONIC TEST TECHNIQUES.

During the past few years the industrial world has seen a massive growth in the use of NDT methods and techniques. In this section the application of physical principles for detecting defects in non-conductive fibre reinforced composite structures without impairing the usefulness of these materials are discussed with particular emphasis and elaboration on the NDT techniques used in this research.

6.1 Low Frequency Vibrational Techniques.

These can be divided into two types:

(i) Global tests (ii) Local tests

For (i) the test involves measurement of the natural frequencies and/or damping of the whole component. These quantities are properties of the whole structure and are independent of the position at which they are measured. Therefore a test at a single location can interrogate the whole component [44-45].

Since natural or resonant frequencies are very sensitive to dimensions, their use for the detection of small cracks at the production stage is limited to components which are produced to strict dimensional tolerances. Natural frequency measurements may also be used as an in-service test, measurements after a period of service being compared with base line taken on the same component. This means that the effect of dimensional variations across a production batch is removed so greater sensitivity to small defects is expected.

The application of natural frequency measurements for the production and quality control of fibre composites has been investigated by Cawley et al,[46-47]. Flexural vibration tests using the arrangement in Figure 6.1 were carried out on a series of filament wound carbon fibre reinforced plastic (CFRP) tubes, several of which had deliberate built-in defects. Some of the defective tubes had incorrect fibre volume fraction or winding angle, while others had localized defects such as siliconised paper inserts and cut fibres. Figure 6.2 shows a graph of first mode natural frequency versus second mode frequency for all the tested tubes.

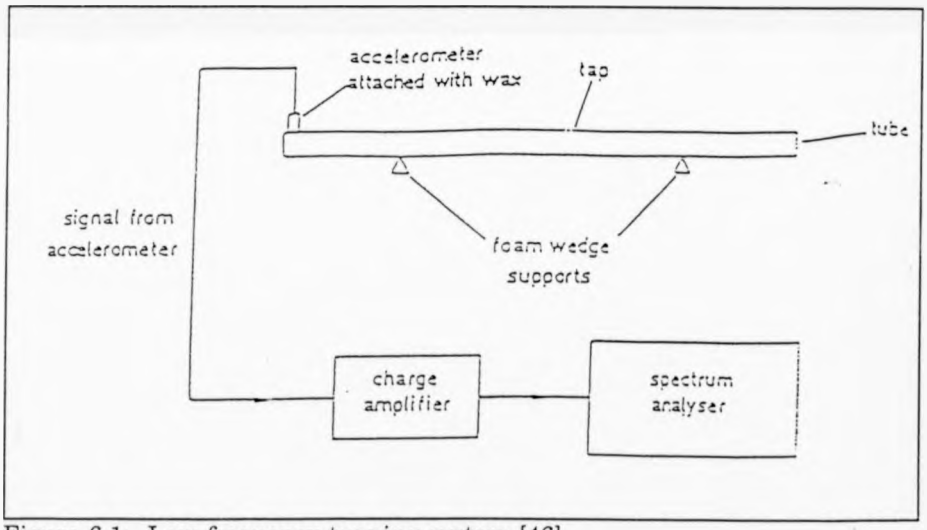

Figure 6.1: Low frequency tapping system [46].

From the graph, the generalized defects, low volume fraction and incorrect winding were readily detected except for small localized defects.

Structural damping is much less sensitive to dimensions compared to natural

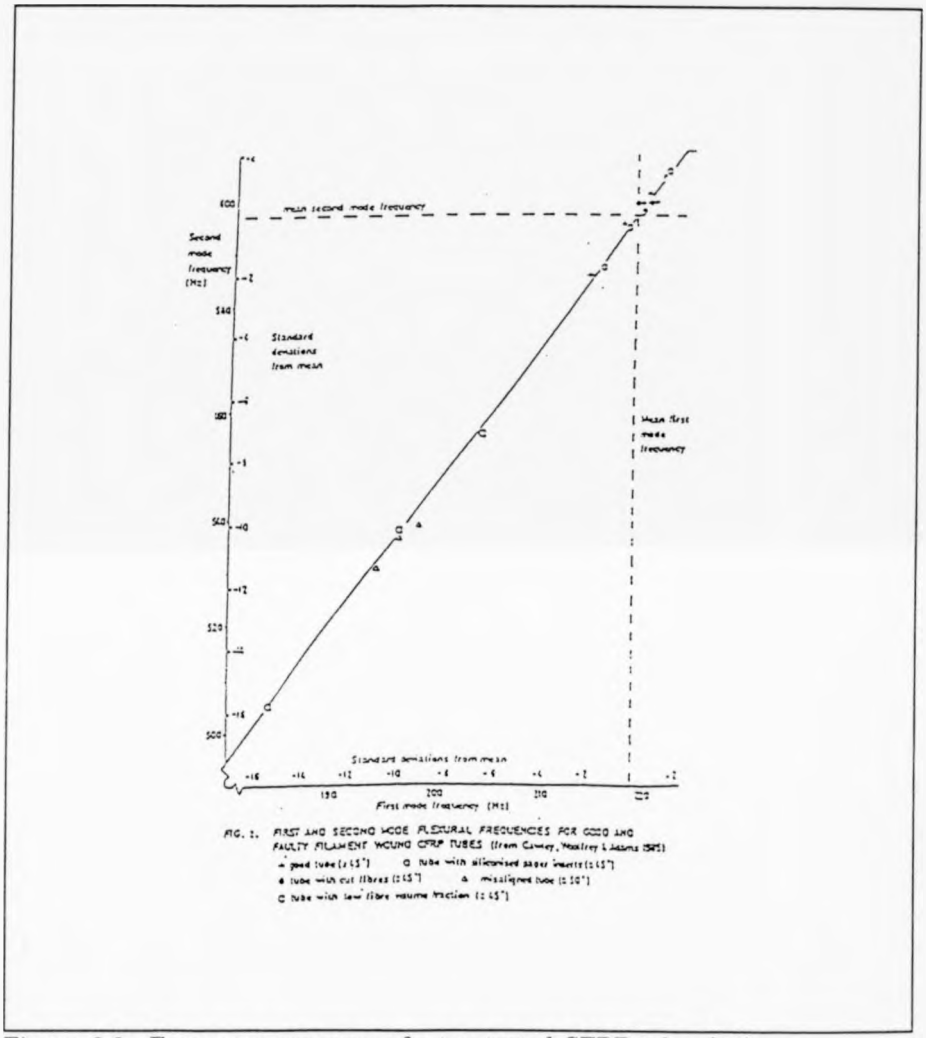

FIG. 1. FIRST AND SECOND MODE FLEXURAL FREQUENCIES FOR GOOD AND FAULTY FILAMENT WOUND CFRP TUBES (from Carney, Maxfield & Jessop [SP1])
+ good tube (± 45°) ○ tube with siliconised paper inserts (± 45°)
● tube with cut fibres (± 45°) △ misaligned tube (± 30°)
○ tube with low fibre resume fraction (± 45°)

Figure 6.2: Frequency response of a tap tested CFRP tubes [46].

frequencies [48]. Hence, damping measurements may therefore be used instead as a production quality control test. It can also be used as an in-service test similar to natural frequencies technique. However, even though damping is known to be more sensitive to damage, it is harder to measure accurately. In addition, when used to detect damage in fibre composite components,

localized defects will produce a very small percentage change in damping which is hard to detect and within the method limitations tend to confuse good components with bad ones.

For (ii) it involves vibrating the test structure (usually at its natural frequency) by applying an exciting force at a single point, and measuring a local property of the structure, in a particular mode of vibration, at all the points of interest. This type of test is thought to be more sensitive than the global one.

The presence of damage in composites leads to the formation of cracks and crazes. When cyclic stresses are applied to a damaged composite material, damping takes place between the sides of the cracks, resulting in the generation of heat.

The change in the overall level of damping in a structure is small, while localized damping can be large. This concept of defect detection is called VIBROTHERMOGRAPHY [51]. Using this technique, local temperature rise produced by local energy dissipation under cyclic stress which is produced by resonant vibration is measured. It is favourable that the structure has low thermal diffusivity to prevent rapid heat conduction from the damaged area. Vibrothermography is known to be more sensitive than transient thermography if transverse cracks are to be located but passive thermography is probably more suited to finding debonds and delaminations (thermography will be discussed later in this chapter).

However, local damage in a structure tends to distort the vibration mode shapes. With advances in laser holography systems, there has been a great interest in realizing this effect using NDT methods. The technique involves vibrating the test structure at resonance and producing a time-averaged hologram of the motion. The use of pulsed laser makes it possible to use the technique in the presence of background vibration. Using impulsive excitation produces holograms from views taken a few micro-seconds apart as the pulse propagates through the structure. This technique is still under development with expected high cost for the equipment and possibility for rapid inspection (more on this technique later in this chapter).

Application of vibrational excitation at each testing point is regarded as both locally and globally oriented. This technique is used for detection of defects such as debonds in adhesive joints, delaminations and voids in laminated structures and defective honeycomb constructions. These are all planar defects and this method is regarded as unsuitable for detecting transverse cracks.

Mechanical impedance is in general a function of frequency, when a delamination is present, the impedance of the structure in the direction normal to the surface is lower above the delamination compared to good areas. So defects can be detected by measuring the composite mechanical impedance as shown in Figure 6.3. At frequencies below 7KHz, the impedance over the defect is lower than that over good areas and reduces with increasing defect size. Over good areas the measured impedance is determined by the contact stiffness

between the probe and the structure, while over a defect it is governed by the stiffness of the layer(s) above the defect in series with the contact stiffness and is thought to be given by the following expression, Cawley et al & [46] :

$$K_{eff} = \left(\frac{K_c K_d}{K_c + K_d} \right) \qquad 6.(1)$$

and

$$K_d = \left(\frac{PEh^3}{d^2} \right) \qquad 6.(2)$$

Where:

K_{eff}	:	Effective contact stiffness
K_c	:	Stiffness over good area
K_d	:	Stiffness over defective area
d	:	Defect diameter
p	:	Constant depends on effective boundary conditions and poissons ratio of the layer(s) above the defect
E	:	Flexural modulus of the layer(s)
h	:	Depth of defect

The minimum defect depth as a function of its diameter is given by:

$$d_{min} = \upsilon h^{1.5} \qquad 6.(3)$$

The layers above a disbond or delamination may be reordered as a plate which is restrained around its edges. This plate can resonate, with the first mode being the membrane resonance in which the motion is similar to that of a diaphragm. Hence, if each point at which inspection is of an interest has been

excited at different frequencies then one of these frequencies will correspond to the membrane resonance frequency for a particular defect size which is expected to be larger than that over the good area. This resonance frequency is given by:

$$f_r = \frac{q\ (h/d^2)}{(E/_\rho)^{1/2}} \qquad 6.(4)$$

where: q: constant depends on effective boundary conditions and poissons ratio

ρ: Material density

and minimum diameter is given by:

$$d_{min} = \upsilon h^{1/2} \qquad 6.(5)$$

When however, an oscillating force is applied to a plate-like structure, bonding waves are produced which propagate away from the excitation point. The amplitude and velocity of the waves produced are a function of the material properties of the structure and its thickness. This constitutes a velocimetric technique which can be useful in checking component composition.

Excitation at each testing point using tapping techniques has been successfully used in this research. When a structure is tapped producing a sound, vibration at the major frequency modes of the structure at its fundamental values provides us with a way of characterizing the composite properties.

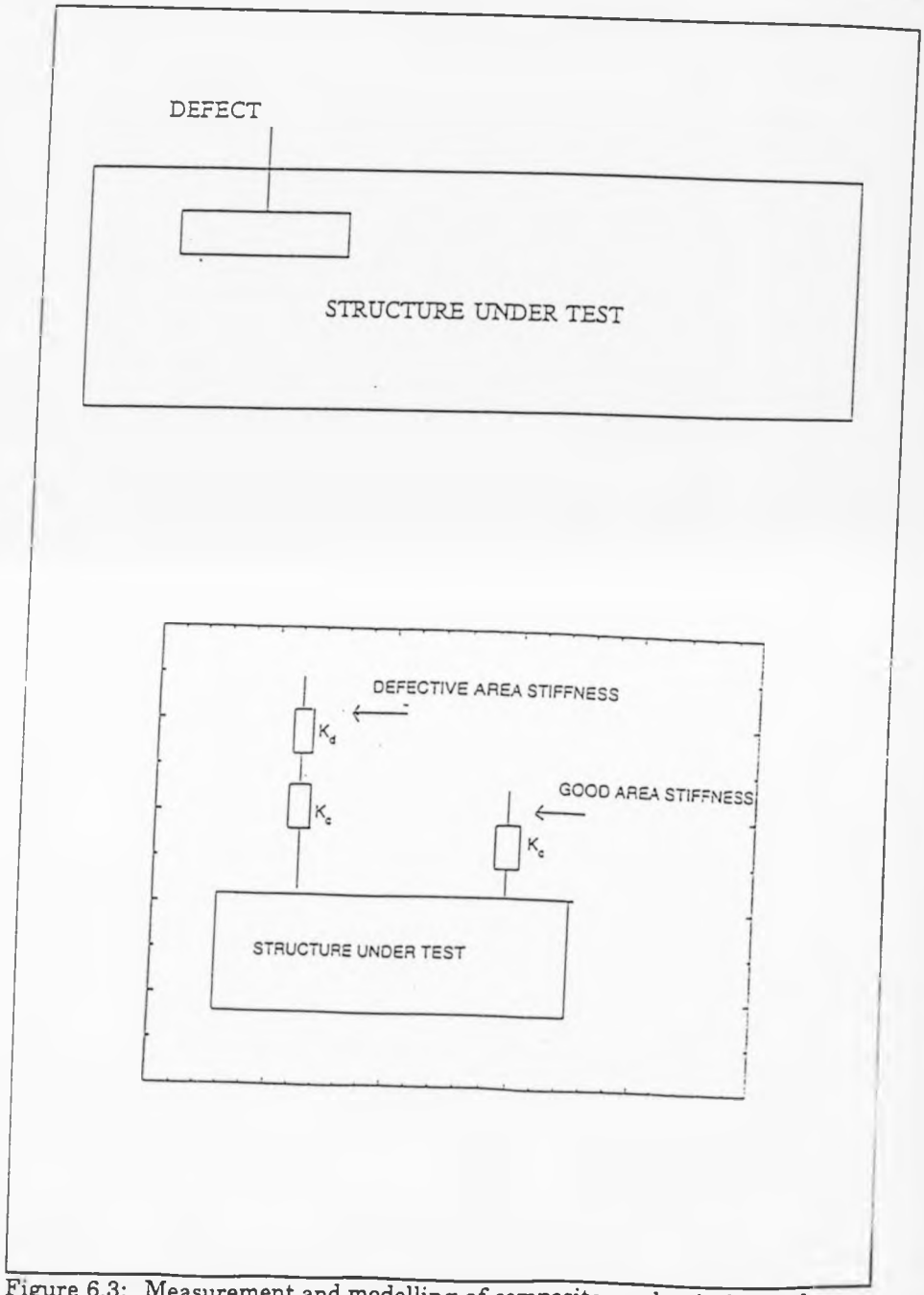

Figure 6.3: Measurement and modelling of composite mechanical impedance.

These structural characteristics are essentially independent of the position of excitation. When a structure is tapped, the characteristics of the impact are dependent on the local flexibility of the structure and the device used to strike it.

Damage such as delamination results in a local increase in the structural flexibility, and hence a change in the nature of the impact as shown in Figure 6.4. The impact over a good area is found to be more intense and of shorter duration than that on a damaged area.

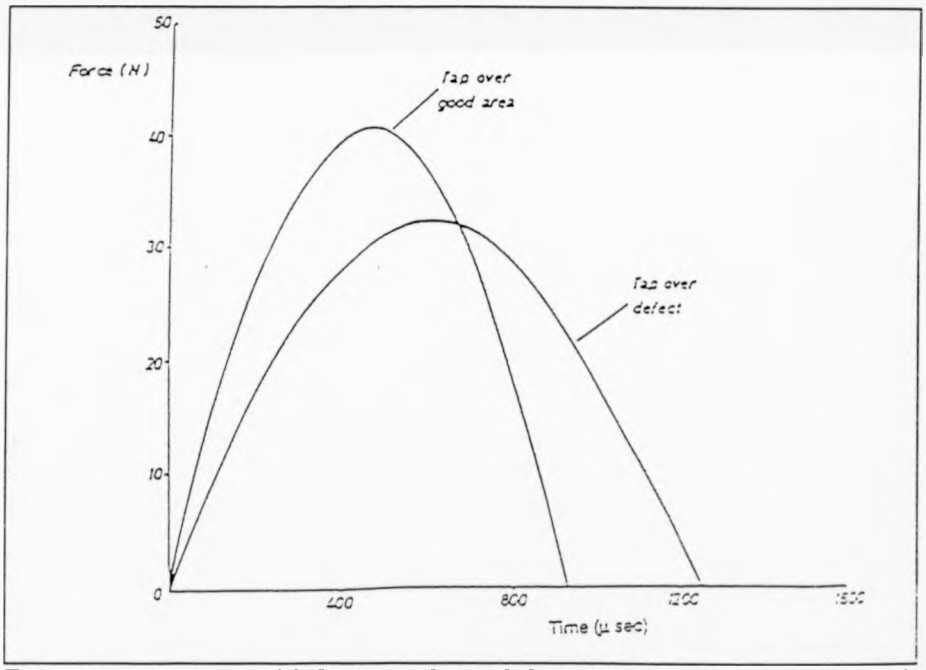

Figure 6.4: Response of defective and non-defective structures to tappings [46].

The difference in the sound produced is due to the frequency content of the force

pulse. The amplitude of the force input to the damaged area was found to fall off rapidly with increasing frequency. This means that the impact on the defective area will not excite the higher structural modes as strongly as the impact on the good zone. Therefore, the sound produced does not contain the higher frequencies and the structure sounds duller.

The change in the impact characteristic over a defect may be explained by considering the effect of the defect on the motion of the impactor. In the region of delamination, the flexibility of the structure in the direction normal to the surface is increased. This means that when an impactor strikes the structure above the defect, the surface "gives" more than over a good area. The damping effect also means that the impactor stays in contact with the surface for longer which results in a longer impact duration. Over a good area, the impact duration is controlled by the contact stiffness between the impactor and the structure. A delamination effectively reduces this contact stiffness.

The above findings were behind the design of an electronic tapping instrument which measures the force and time duration during the tap which makes this device insensitive to background noise.

6.2 Tapping Method: Mathematical Model (ORIGINAL CONTRIBUTION).

Based on the previous discussion and to be able to analyze and interpret the experimental data obtained from a device which implements such a function,

a model is devised to account for the response of a composite structure to the application of a fixed rate tapping with variable duration to an input impulse.

Figure 6.5 illustrates the principle of system response of an applied signal to a composite structure.

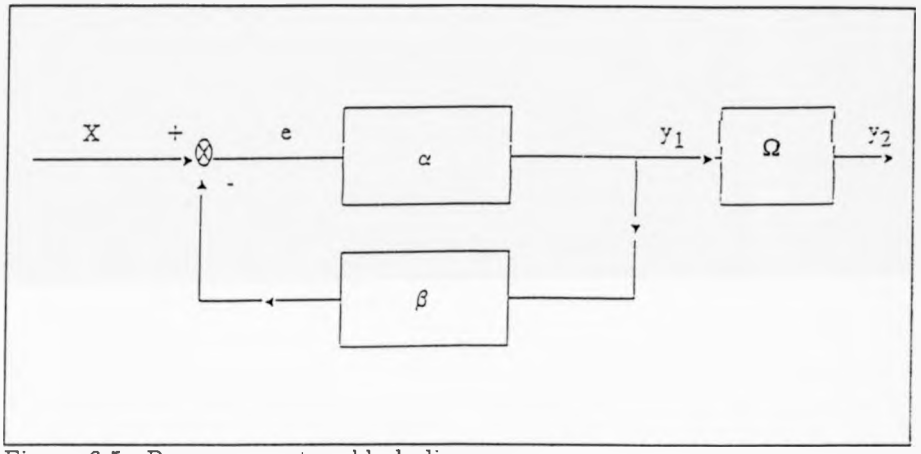

Figure 6.5: Response system block diagram.

From the closed-loop, feedback system block diagram we have:

$$x - \beta\, y_1 = e \qquad 6.(6)$$

$$y_1 = \alpha.e \qquad 6.(7)$$

$$\rightarrow \left(\frac{x}{y_1}\right) = K^{-1}_{General} = \left[\frac{1 + \alpha.\beta}{\alpha}\right] \qquad 6.(8)$$

For a direct contact (NO interface between the device and the structure , $\alpha \rightarrow$ 1.

Hence:

$$K_{General} = \left| \frac{1}{1 + \beta} \right| \qquad 6.(9)$$

and

$$y_2 = (\Omega . y_1) \qquad 6.(10)$$

From $K_{General}$, y_1, y_2 we obtain:

$$K_{ref} = \left| \frac{2}{1 + \beta} \right| \qquad 6.(11)$$

$$K_{avg} = \left| \frac{2\ \Omega}{1 + \beta} \right| \qquad 6.(12)$$

The factor of 2 appearing in equations (11) and (12) is to account for the signal transmission and reception which is a dual operation.

Where

$$\beta = \left(\frac{t_d}{t_{ref}} \right), \quad \Omega = \left(\frac{t_{avg}}{t_{ref}} \right) \qquad 6.(13)$$

By back substitution we obtain:

$$K_{ref} = \left| \frac{2.t_{ref}}{t_d + t_{ref}} \right| \qquad 6.(14)$$

$$K_{avg} = \left| \frac{2.t_{avg}}{t_d + t_{ref}} \right| \qquad 6.(15)$$

where:

t_{ref} : Reference response time.

t_{avg} : Average response time.

t_d : Defect response time.

K : Relative response factor.

From equations (14) and (15) we realized that the overall response time consists of two components:

(1) Defect introduced time delay.

(2) The original structure response (before damage).

The validity of this initial revelation can be established by examining three cases:

(1) $\mathbf{t_{ref} >> t_d}$

Here, the material is either non-defective or the defect level is much below the detectable damage for which the impact energy was well below the threshold. Hence:

$$\lim_{t_d \to 0} \left[\frac{2.t_{ref}}{t_d + t_{ref}} \right] = 2 \qquad 6.(16)$$

This limit of 2 could not be exceeded by any form of damage or change in material properties.

(2) $\mathbf{t_{ref} \simeq t_d}$

Here the structure is definitely defective and the time delay introduced is equivalent to the component original response but is not thought to be critically affecting the composite integrity. So:

(3) $\mathbf{t_d >> t_{ref}}$

$$\lim_{t_d \to t_{ref}} \left| \frac{2.t_{ref}}{t_d + t_{ref}} \right| = 1 \qquad 6.(17)$$

In this case the tested composition is severely damaged and at its serious or critical level. Hence:

$$\lim_{\left(\frac{t_{ref}}{t_d}\right) \to 0} \left[\frac{t_{ref}}{t_d + t_{ref}} \right] = 2. \left[\frac{t_{ref}}{t_d} \right] \qquad 6.(18)$$

This is always < 1.

In between the previous limits, the normalized function is mapped as in equation (14).

It is believed that averaging signal responses is one way of filtering out noise and obtaining a uniformity of composition characteristics. So, applying limits to equation (15) we obtain:

(4)

$$\lim_{t_d \to 0} \left[\frac{2.t_{avg}}{t_d + t_{ref}} \right] = 2. \left[\frac{t_{avg}}{t_{ref}} \right] \qquad 6.(19)$$

This describes a realistic, practical, non-defective or negligibly defective case due to instrument insensitivity or low damage level. Hence:

$$2 - \kappa < K_{avg} < 2 + \kappa$$

Where κ: small differential parameter.

In a perfect sample (ideal case): $t_{avg} = t_{ref} \Rightarrow K_{avg} = K_{ref} = 2$, i.e. no surface irregularities.

(5) $\mathbf{t_d = t_{ref}}$

$$\lim_{t_d \to t_{ref}} \left[\frac{2.t_{avg}}{t_d + t_{ref}} \right] = \left[\frac{t_{avg}}{t_{ref}} \right] \qquad 6.(20)$$

Here, the decision on the sample condition will be inclined strongly towards the defective part of the spectrum, where:

$$1 - \chi < K_{avg} < 1 + \chi$$

χ: Small differential parameter.

As before in a perfect sample $K_{avg} \rightarrow K_{ref} = 1$.

(6) $\mathbf{t_d >> t_{ref}}$

$$\rightarrow \left(\frac{t_{ref}}{t_d} \right) \lim_{\to 0} \left[\frac{2.t_{avg}}{t_d + t_{ref}} \right] = 2 \left[\frac{t_{avg}}{t_d} \right] \qquad 6.(21)$$

Always < 1.

As $t_{avg} \rightarrow t_{ref}$, $K_{avg} \rightarrow K_{ref}$, equation (21) becomes:

$$K_{avg} = K_{ref} = \left| \frac{t_{ref}}{t_d} \right| \text{ ideal case} \qquad 6.(22)$$

Always < 1.

(7) $t_d \simeq t_{avg}$

$$\lim_{t_d \to t_{avg}} \left[\frac{2.t_{avg}}{t_d + t_{ref}} \right] = \left[\frac{2}{1 + \left(\frac{t_{ref}}{t_{avg}} \right)} \right] \qquad 6.(23)$$

Equation (23) can approximate equations (17) and (20) under the right conditions ($t_{avg} \rightarrow t_{ref}$) and evaluates to the value of 1.

This indicates an evenly defective sample such that the whole of the structure is almost equally occupied by defects at similar energy levels.

It also indicates that at that specific impact level the impactor dimensions influenced the response in a way that enabled an almost equal energy propagation with minimal dissipation and reflection.

For a non-defective or acceptably defective structure we will assume an energy level E_{th}. When damaged the defect(s) within the structure will hinder the flow of energy from a tap, hence, including a propagation delay factor which modulates that initial applied energy of damage (E_I) to a form similar to the time response expression derived previously on the assumption that energy dissipation due to defects is proportional to the introduced time delay.

Hence, we can establish a correlating expression between time delay and applied defect energy and obtain the level of threshold necessary to overcome

for a structure to become defective. This is given by:

$$E_{th} = 2E_I \left(\frac{t_{ref}}{t_{def}} \right) = \left(E_I.K_{ref} \right) \qquad 6.(24)$$

$$E_{thg} = 2E_I \left(\frac{t_{avg}}{t_{def}} \right) = \left(E_I.K_{avg} \right) \qquad 6.(25)$$

Now to establish the shape function of such a response, we realize from equations (11) and (12) that:

$$\left(\frac{1}{K_{ref}} \right) = \frac{1}{2} \left(1 + \beta \right) = \phi_A \qquad 6.(26)$$

$$\left(\frac{1}{K_{avg}} \right) = \left[\frac{1}{2\Omega} + \frac{\beta}{2\Omega} \right] = \frac{1}{2\Omega} \left[1 + \beta \right] = \phi_B \qquad 6.(27)$$

By using Maclaurin's series expansion we obtain:

$$\phi_A = \left(\phi_1 + \phi_2 \right).\gamma \ , \phi_B = \left[\frac{\phi_A}{\Omega} \right] \qquad 6.(28)$$

Where $\phi_1 = \exp(\beta)$, $\phi_2 = \cosh(\beta)$, $\gamma = 0.5$.

E_{thg} : Average threshold energy.

E_{th} : Threshold energy.

Hence:

$$K_{ref} = \left| \frac{\cosh(\beta) + \exp(\beta)}{4} \right|^{-1} \qquad 6.(29)$$

$$K_{avg} = \Omega^{-1} \left| \frac{\cosh(\beta) + \exp(\beta)}{4} \right|^{-1} \qquad 6.(30)$$

$$\Rightarrow K_{ref} = \left| \frac{\cosh(t_d/t_{ref}) + \exp(t_d/t_{ref})}{4} \right|^{-1} \qquad 6.(31)$$

and

$$K_{avg} = \left| \frac{t_{avg}}{t_{ref}} \right|^{-1} \left| \frac{\cosh(t_d/t_{ref}) + \exp(t_d/t_{ref})}{4} \right|^{-1} \qquad 6.(32)$$

Hence:

$$E_{th} = (E_I.K_{ref}) \;,\; E_{thg} = (E_I.K_{avg}) \qquad 6.(33)$$

Using the above approximation, not only can we establish the response shape function and characteristics, but also allow a wider safety net for defective/non-defective decision making.

Figures (6.6), (6.7) illustrate the theoretical response of such a model.

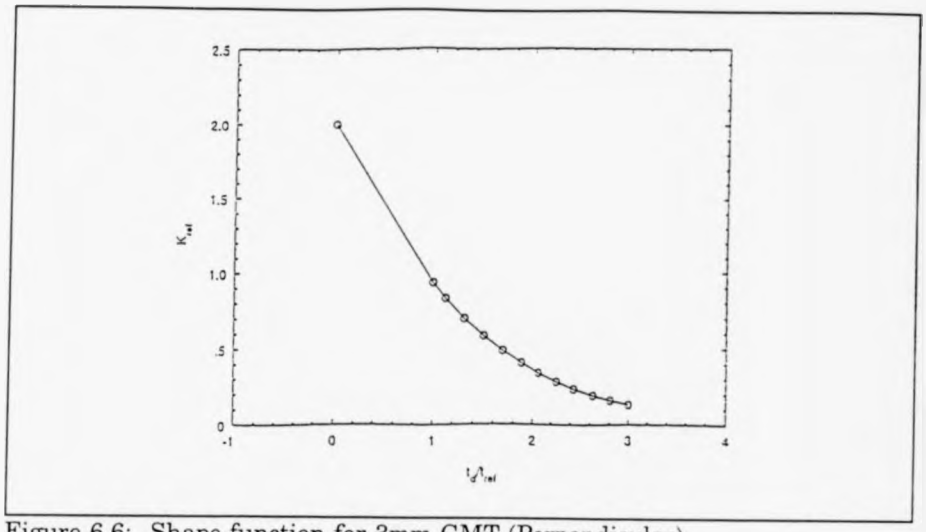

Figure 6.6: Shape function for 3mm GMT (Perpendicular).

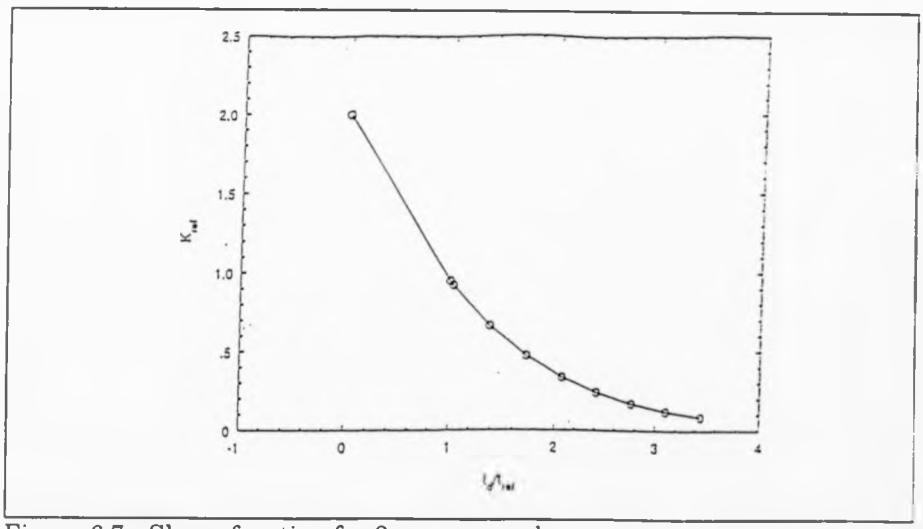

Figure 6.7: Shape function for 3mm woven glass.

6.3 Ultrasonic Techniques.

When considering ultrasonic technique for composites evaluation it is useful to review some of the properties of ultrasound waves [50-59] and the manner in which it is thought to interact with defects.

Ultrasound waves have frequencies above the upper limit of audibility which is approximately 20KHz, although the range of 1 to 50MHz is most often used for material evaluation. Ultrasound requires a medium to propagate and travel through in the form of stress waves. Several types of particle motion, or modes of propagation are supported in solid materials such as:

(a) Compressional waves, where the particle motion is parallel to the direction of propagation.

(b) Shear waves, where the particle motion is orthogonal to the direction of propagation.

(c) Surface waves, where the particle motion is elliptical and confined to a surface region of about one wavelength deep.

(d) Plate and Rod waves produced in bound, solid medium.

These types of waves propagate at different velocities, during their motion they tend to get modified by the encountered boundaries, by the material itself and

the presence of defects.

The nature of the interaction between the wave and materials and their defects depends on variables such as:

(a) Relative size of the defect to the wavelength of sound.

(b) The orientation of the defect.

(c) The mode in which the sound wave is propagating.

A material boundary constitutes a change in the acoustic impedance. For the case of normal incidence at the interface between two different environments, some sound is reflected and the rest is transmitted across the interface. The relative amplitude and phases of these waves depend upon the change in properties across the boundary. As the magnitude of the change in properties increases, a greater proportion of the incident energy is reflected and hence less is transmitted across the boundary.

However, when the sound wave is incident at some angle the amplitudes of the reflected and transmitted waves are also a function of the incident angle. The nature of wave-material interaction is complicated as one kind of incident wave can result in the generation of other types within a structure.

The material contribution in modifying the sound wave propagating through it can occur in a number of ways.

Energy can be lost due to dissipation mechanisms within the material or by scattering of sound from the structure by defects such as voids and inclusions. These mechanisms of energy loss are usually frequency-dependent, hence, modifying the shape of the propagating wave.

The change in sound velocities as a function of the elastic properties of materials can be given by:

$$C_{long} = \left[\frac{E}{\rho} \left(\frac{1 - \mu}{(1 + \mu)(1 - 2\mu)} \right) \right]^{1/2} \qquad 6.(34)$$

$$C_{trans} = \left[\frac{E}{\rho} \left(\frac{1}{2(1 + \mu)} \right) \right]^{1/2} \qquad 6.(35)$$

$$C_{surf} = \left[\frac{0.87 + 1.12\,\mu}{1 + \mu} \right] \left[\frac{E}{\rho} \left(\frac{1}{2(1 + \mu)} \right) \right] \qquad 6.(36)$$

Where:

E : modulus of elasticity

ρ : material density

μ : Poissons ratio

with sound exerting a pressure of relative amplitudes given by:

$$\frac{P(x)}{Po} = \exp(-\xi x) \qquad 6.(37)$$

Where: $p(x)$, p_o are pressure amplitude at points of origin and distance x.

ξ : Attenuation coefficient

The attenuation coefficient is given by:

$$\xi = \xi_a + \xi_s \qquad 6.(38)$$

Where: ξ_a : Absorption coefficient

ξ_s : Scattering coefficient

The acoustic impedance of any region is defined as:

$$z = \rho C \qquad 6.(39)$$

However for two different boundaries with acoustic impedances z_1 and z_2 a pressure amplitude reflection coefficient can be defined as:

$$r = \left| \frac{(z_2 - z_1)}{(z_2 + z_1)} \right| \qquad 6.(40)$$

and the pressure amplitude transmission coefficient is given by:

$$T = \left(\frac{2 z_2}{z_1 + z_2} \right) \qquad 6.(41)$$

Also, the relative intensities can be found from:

$$\left(\frac{I_r}{I_i} \right) = r^2 \qquad 6.(42)$$

and

$$\left(\frac{I_t}{I_i} \right) = \left(\frac{T^2 Z_1}{Z_2} \right) \qquad 6.(43)$$

where: I_r, I_t, I_i : Reflected, Transmitted and Incident energies.

As defects interact with ultrasound, that cause a change in acoustic impedance relative to the surroundings causing diffraction effects. These defects are overshadowed if the size of a defect is large compared to the sound wavelength causing sound reflection.

There are many different methods available for inspecting composite materials using ultrasound depending on the expected defects (Table 1).

A common factor of all techniques is the need for a couplant to interface the transducer to the structure to be tested. The efficiency of this coupling method depends on the elastic properties of the material involved. (A new approach has been developed which uses transducers that do not need coupling).

Basic ultrasonic testing systems use water as an interface where the specimen is immersed in a water tank and the transducer is held in position by a manipulator so that the orientation and distance from the specimen can be adjusted. The transducer can also be scanned relative to the specimen, usually automatically. Information can be obtained about the specimen condition and presented in a number of ways. The most usual being the A, B and C scans

which are also applicable to non-immersion systems.

(A) The A-Scan.

This technique is one of the simplest methods of presenting information. Figure 6.8 shows a schematic diagram of the equipment that can be used to perform such a test. The heart of the equipment is an ultrasonic test-set, which is an instrument that contains the necessary electronics to produce the signals that cause an ultrasonic transducer to generate sounds, to receive and amplify the signals generated by the transducer in response to incident ultrasonic energy, and to display the resulting information on an oscilloscope screen. The drive signal to the ultrasonic transducer will normally be a high amplitude voltage spike which the transducer converts into a pulse of ultrasonic energy. Ultrasonic waves are then interacted with the specimen, its boundaries and any defects through couplant.

In general, ultrasonic energy is both transmitted through the specimen and reflected from it. The transmitted energy may be detected by a separate transducer located on the far side of the specimen, in which case the process is called Through Transmission, alternatively the reflected energy may be detected by the same transducer acting as both transmitter and receiver and in this case the procedure is called Pulse Echo. In either case the received acoustic energy is converted into electrical energy by the receiving transducer, amplified and displayed by the test-set. Most production inspection of composite components is performed in the Through Transmission mode allowing

Property to be measured→ / Defect Type ↓	Reflections	Attenuation	Velocity	Backscattering	Polar Scan	Special Techniques
Incorrect cure		•	•			
Incorrect fibre volume fraction		•	•			
Voids		•	•			
Foreign bodies	•	•				
Fibre & ply misalignment				•	•	
Wavy fibres				•	•	
Ply cracking	•	•		•		
Delaminations	•	•				
Bonding defects	•	•				

Table 6.1 Ultrasonic Interaction.

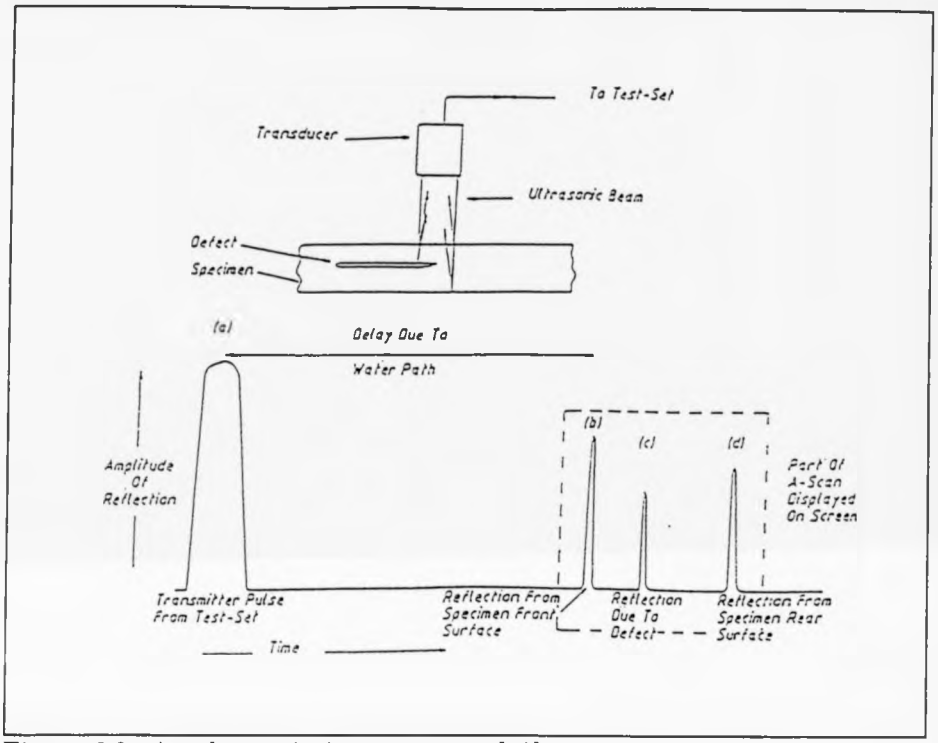

Figure 6.8: An ultrasonic A-scan system [50].

a greater thickness of material to be tested. In-service inspection due to physical constraints like access only being available from one side of a component may often need to be carried out using a Pulse Echo technique.

When the amplitude of the ultrasonic waves received by the transducer are displayed as the vertical deflection on an oscilloscope screen while the horizontal deflection corresponds to time, an A-scan display is produced. This consists of a series of spikes whose position along the horizontal axis can be calibrated in terms of depth in the sample under test so that the position of a reflection can be measured. The amplitude of each echo will give some

indication of the size and nature of the reflector, which might be a defect or a specimen boundary.

The A-scan type of display can also be used without an immersion tank when the ultrasonic transducer is coupled to the specimen by a thin grease or gel film. If a defect is present and of a type that reflects a large fraction of the incident sound-wave, then only a very small proportion will propagate beyond the defect. Any additional reflections will be small and pass undetected. The result is that the material in the shadow region behind the first defect will not be inspected and additional defects may not be found. This effect is important in determining damage.

(B) The B-Scan.

If the transducer used for recording A-scan is moved linearly, usually by a motor drive, in a plane parallel to that of the component, a number of A-scans can be recorded corresponding to different positions across the specimen. The basic principle is illustrated in Figure 6.9. The A-scans can be combined on a display device like a storage oscilloscope so that the horizontal deflection is proportional to the transducer position, the vertical deflection is proportional to time (or depth through the sample) and the stored intensity is modulated by the amplitude of the received reflections. This type of display is called a B-scan and corresponds to a slice taken through the sample, normal to the surface. With the B-scan type presentation it is possible to estimate the depth of reflections and their lateral extent along the axis of transducer movement.

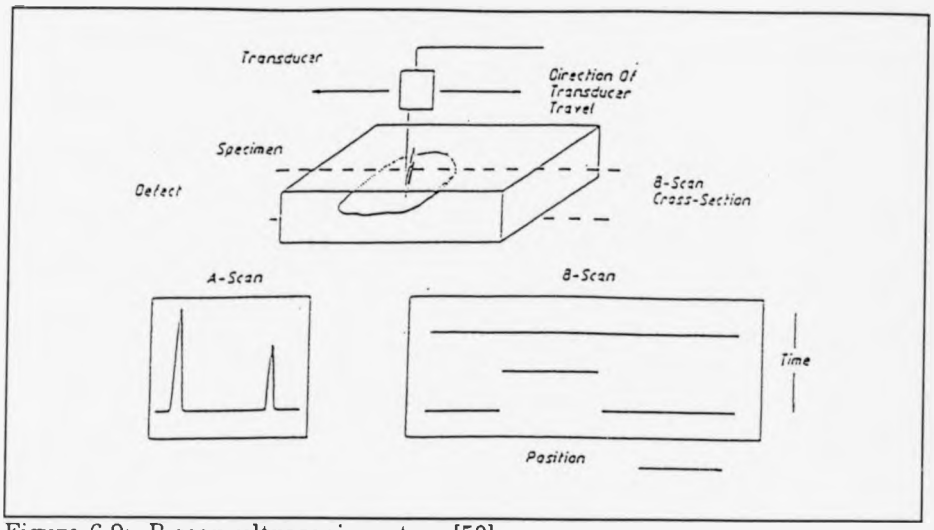

Figure 6.9: B-scan ultrasonic system [50].

(C) The C-Scan.

In this type of inspection, a more complex scanning system is used such that the transducer is scanned in a plane parallel to the sample in a rectilinear raster pattern as shown in Figure 6.10. In older systems a recorder pen is mechanically coupled to the transducer manipulator so that the pen produces the scanning pattern, normally on current sensitive paper. Modern systems are linked to computers allowing full colour graphics output to screen and plotter.

In an immersion system the transducer is scanned in the water tank above the sample. If a single transducer is employed in the pulse-echo configuration a glass reflector plate placed

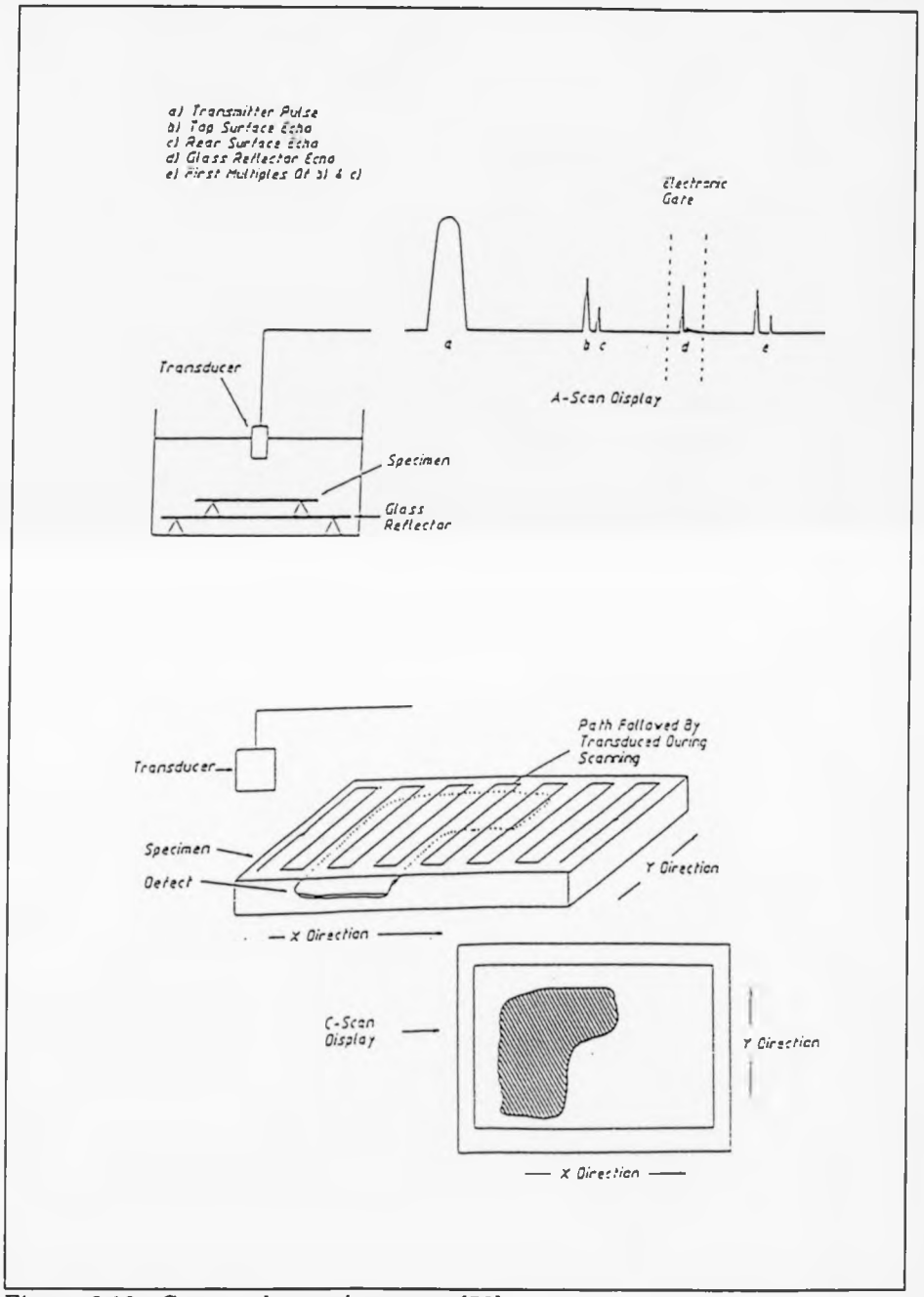

Figure 6.10: C-scan ultrasonic system [50].

behind the sample is often used. In this case the echo amplitude plotted corresponds to that of the ultrasonic pulse that has propagated through the sample, been reflected by the glass reflector plate, again propagated through the sample and returned to the transducer. Hence, the amplitude of this signal corresponds to that of a wave that has travelled through the sample twice so that it is called Double Through Transmission technique. Because the mismatch in acoustic impedance between the water and glass is so large, very little energy is transmitted through the glass and so in most cases it can be considered as a perfect reflector.

This system has the advantage that to a good approximation, neglecting, for example, changes in the sample reflectivity, the amplitude of the glass reflection can be considered as proportional to the attenuation of sound in the sample. This echo is also well separated in time from other reflections and hence is easy to monitor. This is done by using a time-gate which converts the amplitude of the largest reflection within a present time interval. Other gating techniques can be used such as back wall reflection where a more precise gating is required.

(D) Other Ultrasonic Techniques

(1) **Ultrasonic Jet Probes** A commonly used technique which still uses water as a couplant. Here the component is not immersed, instead the coupling water impinges onto the surface of the component in a jet along which the ultrasound travels. The water jet acts as a waveguide to the sound. The main difficulty is to make sure, by correct design of the probe

assembly, that the water flow is laminar. Because the sound is guided down the water jet considerable curvature can be tolerated in a specimen. This technique is generally used in through transmission and at frequencies below about 10MHz. For large components it is the most popular technique used in the aerospace industry for producing Through Transmission C-scans.

(2) **Roller Probes** In applications where the composite must not come into contact with water, roller probes can be used. The ultrasonic transducer element is held inside a wheel and the sound propagated into the specimen through a soft rubber tyre. This technique is generally used at low frequencies and can be used for the rapid detection of in-service damage but is not really suitable for its detailed characterization.

(3) **Laser Techniques**.

Ultrasound can be generated and detected in composites using lasers. Such a system has the following advantages:

(a) Transducers do not need to be in contact with the sample or coupled to it by a water path.

(b) The generation and reception of ultrasound is comparatively insensitive to the orientation of the sample relative to the laser beams.

(c) Scanning systems can be simple and fast.

(4) **Stress Wave Factor (SWF)** This technique seeks to characterise a composite by investigating the way in which it modifies an ultrasonic pulse that travels through it. Pulses of ultrasound are injected into the component from a pulser and transducer and are detected some distance away on the same side of the component. The pulses are seen as stimulated acoustic emissions and are detected and processed as such.

(5) **Acoustic Back Scattering**.

In this technique the scattering of sound waves back along their incident path is measured as a function of the orientations since a maximum is observed in the reflected amplitude when the ultrasound is incident normal to the fibre axis. Fibre waviness and cracks can also be detected.

(6) **Polar Scans**.

The polar scan displays the attenuation of a received signal as a brightness modulation on a polar display when the angle of incidence is varied to cover the angles of half a sphere. The resulting picture is rather complicated but it is thought to provide a unique fingerprint of a specific laminate being sensitive to ply stacking order and fibre orientation.

(7) **Velocity Measurement**.

This technique has the advantage of being simple to measure accurately in all but very thin specimens. It is thought that the velocity normal to the fibres is sensitive to fibre volume fraction and matrix porosity and also to the state of cure for some resin systems.

(8) **Imaging Systems**.

A considerable amount of work is being carried out into ultrasonic imaging systems with aims towards imaging damage in composites.

Defects Detected Using Ultrasonics

(1) **Surface-Breaking Defects**.

Often one finds a major division in ultrasonics between the detection of those defects which lie on the accessible surface and those on the back wall of the specimen. However, it is the latter which are most often and more easily located and sized.

(2) **Cracks** .

Crack-like defects are generally good specular reflectors of ultrasound. They may be readily detected if a near-normal incidence can be arranged. There are two basic problems, however. First the achievement of near-normal incidence implies some control over the test geometry, and this may not exist. In inspecting for near-surface cracks, for instance, it is very difficult to obtain a good reflection with a single probe and this inspection has traditionally a low success rate. On the other hand, a near-normal crack on the far surface can provide an almost perfect corner reflector, inspection with a single angled-probe is almost ideal for such a defect. The second problem is that cracks themselves may be semi-transparent so that the amplitude of reflection may be a misleading guide to the importance of the defect. Moreover, the degree of transparency may vary as a function of the life of the structure under

test, or with its loading, regardless of whether the defect has extended. In this way, repeat measurements can become confusing.

(3) **Wall Thinning, Denting**.

The detection of these defects is normally only a problem if they occur on the far side of the specimen. The ultrasonic test then becomes one of monitoring changes in wall thickness.

(4) **Surface Hardness**.

Surface treatments of materials can affect the local elastic properties. These effects may be monitored using ultrasonics.

(5) **Buried defects**.

Inclusions and laminates bonding are less easily monitored using ultrasonic techniques.

6.4 Acoustic Emission and Acousto-Ultra-Sonics.

Elastic stress waves are generated as vibrations within a structure when a rapid release of energy as a function of an acting process occurs. As these waves reach the surface via propagation they will produce small momentarily surface displacements [60-63]. In real components the surfaces play a vital role with waves such as longitudinal, shear, plate and rod ones possibly produced. Usually the produced stress waves are of low amplitude and high frequency outside of the audible range of the human ear, so sensitive transducers are required to detect and amplify the very small surface displacements associated with the waves.

The most popular type of transducers used to monitor this kind of stress wave

emission or acoustic emission (AE) [64-71] are piezoelectric ones which convert the surface displacement into an electric signal. Such a system is shown in Figure 6.11.

The electrical signal which approximates a decaying sinusoid from the transducer is amplified and digitized with the crystal left undamped. The analogue voltage (V) versus time (t) and its ring-down and event counting digital forms are shown in Figure 6.12. This signal can be approximated by the following expression:

$$V = \left[V_p \text{ Sin } (2\pi ft).\exp\ (-t/\tau) \right] \qquad 6.(44)$$

where:

f : Resonant frequency of the transducer

τ : Decay time

V_p : Peak voltage

The often encountered problem in (AE) is one of quantifying the numerous signals which may be detected during a test. The simplest method to obtain an indication of acoustic emission activity is to count the number of amplified pulses which exceed an arbitrary threshold voltage V_t. The number of ring-down counts can be computed from the following expression:

$$N_R = f.\tau.\ln\ (V_p/V_t) \qquad 6.(45)$$

It is sometimes convenient to record a count of unity instead of multiple counts obtained through ring-down counting. This can be achieved electronically by choice of dead times resulting in event counting. The previous two methods are the most frequency used techniques for monitoring composites under stress.

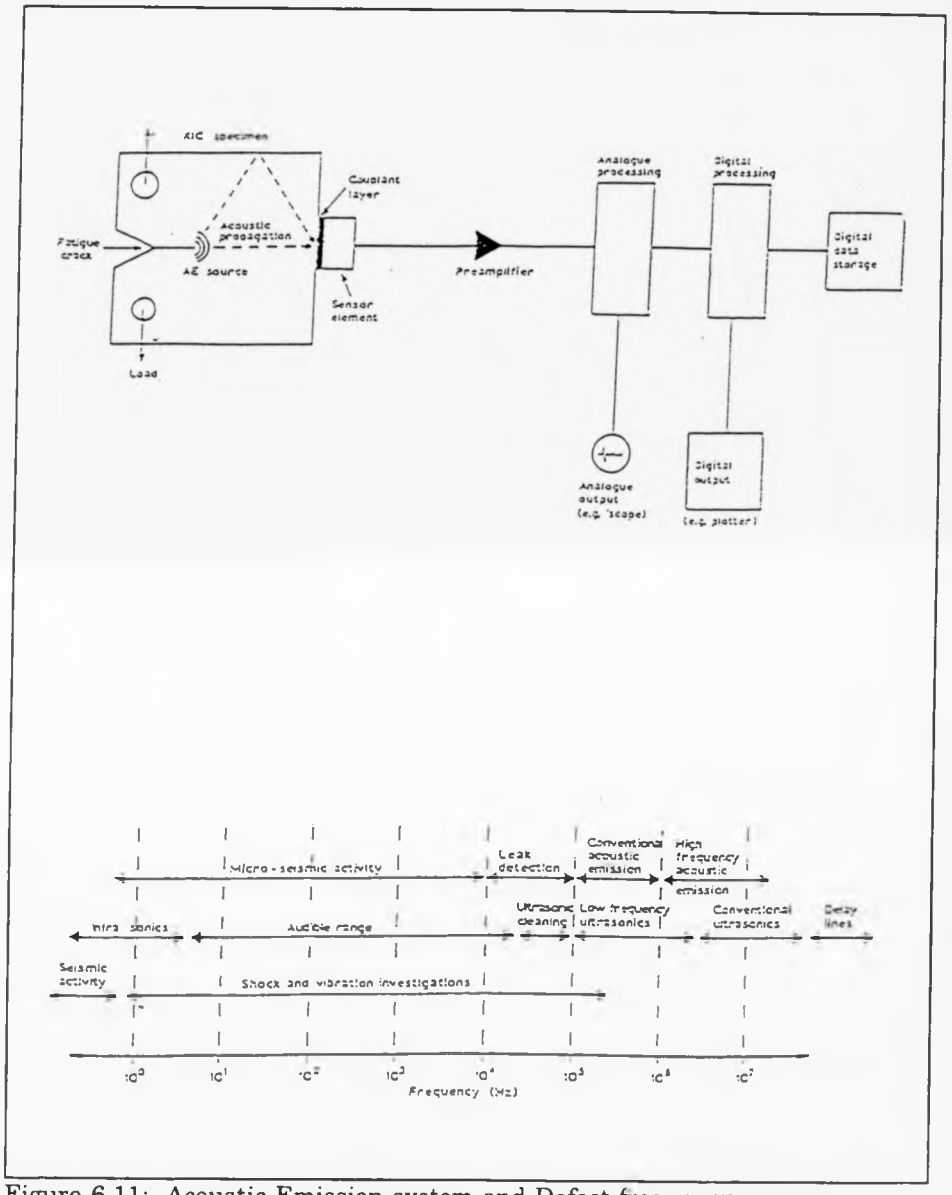

Figure 6.11: Acoustic Emission system and Defect frequency response spectrum [60-61].

A.E studies of polymeric matrix composites with aligned fibres and complex mat

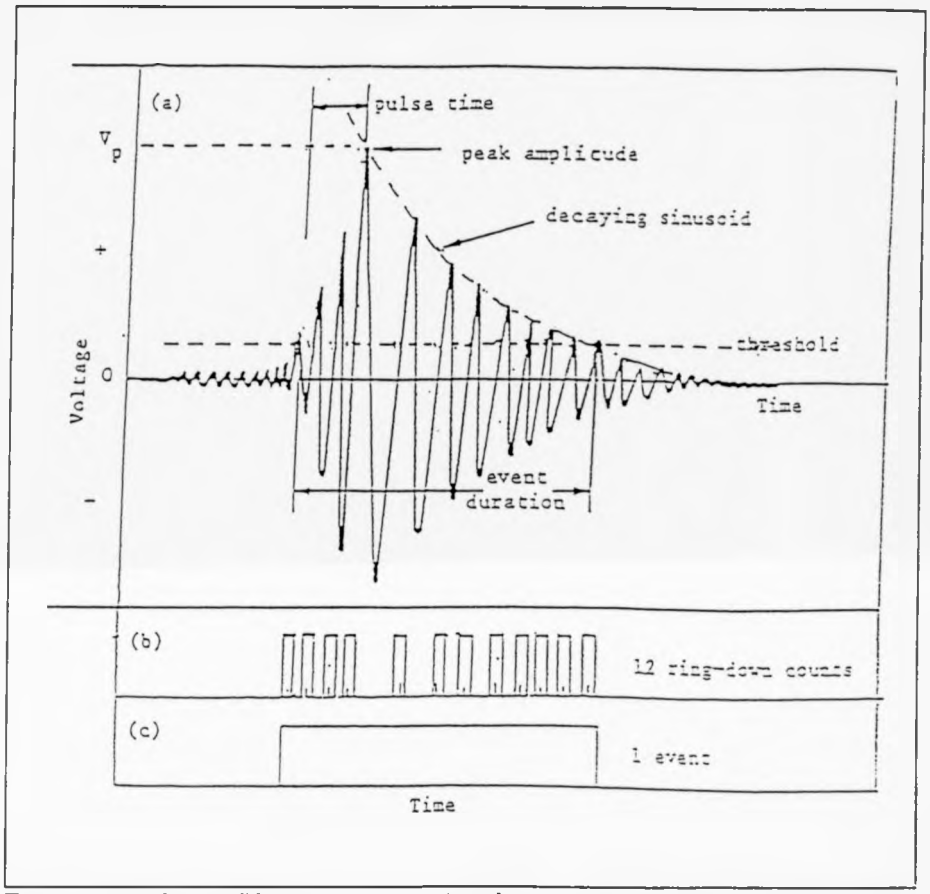

Figure 6.12: Stress Waves interpretation through ring and event counting [64].

configurations have demonstrated that emissions, indicating micro-damage can be detected at low stress as shown in Figure 6.13.

Counting techniques give some measure of damage. Often a specified number of counts must not be exceeded during pressurizing/loading for a component to be accepted and a test must be terminated if a sudden increase in the count rate occurs, which is an indication of gross damage and possibly impending failure. So, for a component to be accepted the count has to fall below a certain rate within a specific time limit.

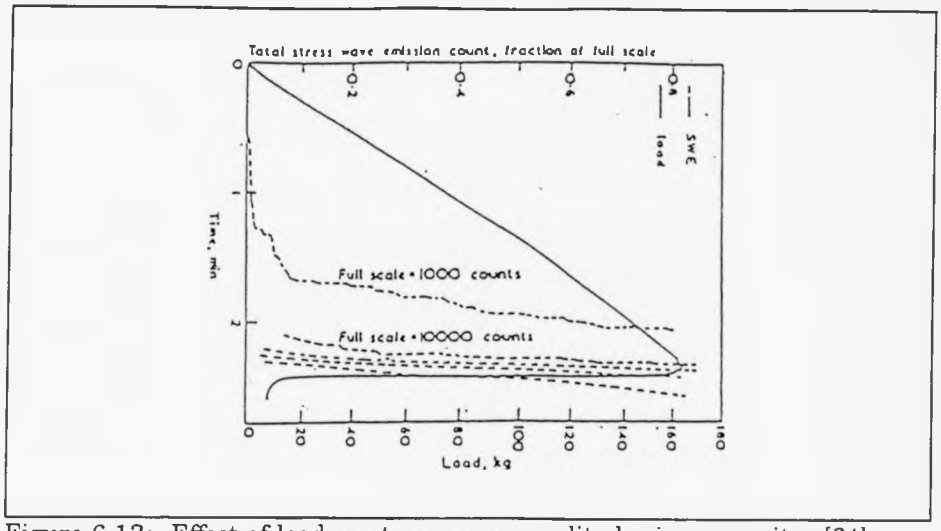

Figure 6.13: Effect of load on stress wave amplitudes in composites [64].

AE counting techniques have been successfully applied to composites under cyclic loading and it has been found that the onset of damage is accompanied by a sudden increase in count rate which is maintained during subsequent cycles as the fatigue cracks propagate. The sources of these emissions are thought to be:-

(a) Micro-damage mechanisms, such as matrix cracking and delamination as a function of fatigue cracking.

(b) Friction noise due to the rubbing together of the fracture surfaces during the unloading stage of each cycle.

A limitation of the counting techniques is that they cannot be used to determine the damage mechanisms. Damage mechanisms that can produce emissions in composites are:

(a) Fracture of fibres

(b) Fracture of matrix

(c) Fibre-matrix debonding

(d) Fibre pull-out

(e) Relaxation of fibre after failure

(f) Large flaws such as interlaminar defects

(g) Fracture of brittle interfacial layers

For detailed inspection the peak amplitude of the amplified acoustic signal (V_p) can be monitored. This peak voltage is a function of the acoustic emission energy (E_A) and is related through a constant (ϖ) when a narrow band instrumentation is used and expressed as:

$$E_A = \left[\varpi \, V_p^2 \right] \qquad 6.(46)$$

If only one type of source event is isolated over a monitoring period, the amplitude distribution is often found to obey a power law as:-

$$n_a = \left(V_a/V_o \right)^{-b} \qquad 6.(47)$$

Where:

n_a : Fraction of the emission population whose peak voltage exceeds V_a.

V_o : The lowest detectable voltage

b : Distribution characteristic constant

The amplitude distribution in a composite is complex, comprising a number of peaks, each can be attributed to a particular micro-damage mechanisms with

fibre fracture producing higher signal than matrix cracking and/or crack growth. However, under certain conditions other mechanisms may also produce events of high amplitude as shown in Figure 6.14. As well as identifying the operative micro-damage mechanisms, amplitude distributions can also assist in the detection of gross flaws in a composite.

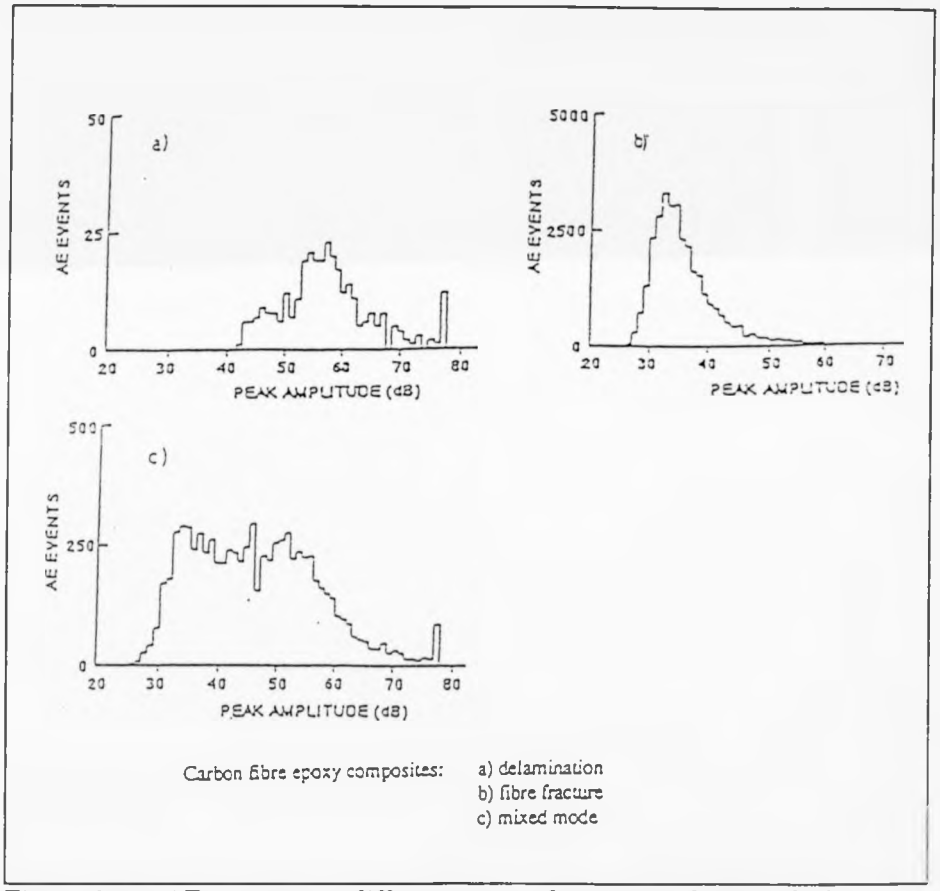

Figure 6.14: AE response to different types of composite damage [64].

Characterisation of an AE signal can also be done using event duration. It is thought that long duration events (LDE's) of medium amplitude may be the

result of delamination. Also bond failure and cracks can be identified with this method.

Locating the source of damage is also possible with AE by measuring the time of arrival of an emitted signal from a given source at different points using multi-transducer process, Figure 6.15.

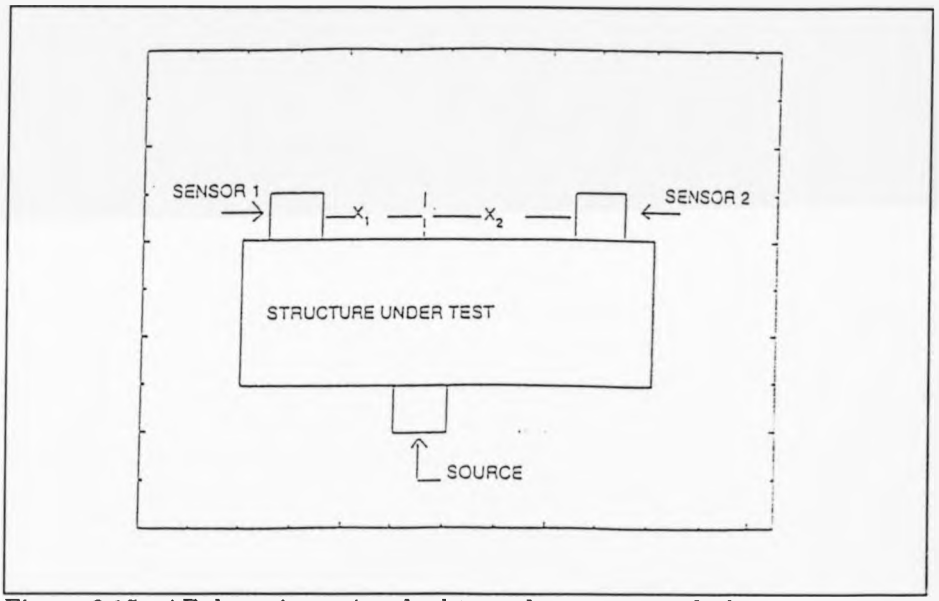

Figure 6.15: AE detection using dual transducer process [64].

However, the signal is expected, and does suffer attenuation which can be related to the following physical causes:

(a) Geometric spreading

(b) Energy absorption by the material

(c) Wave dispersion due to frequency dependence

In polymer matrix composites, two main problems are faced:

(a) High signal attenuation and acoustic mismatch.

(b) Directional velocity attenuation due to fibres alignment.

To measure the severity of damage in composites the Felicity ratio is used, which depends on loading and reloading a structure with no AE emission generated until the previous load is exceeded. The lower the ratio the greater the damage is thought to be.

AE can also be measured as a function of stress wave pulsed into the structure without the component being stressed itself. This is an acousto-ultrasonic method and it measures the integrated effect of the damage situated in the region between the pulser and the transducer. By scanning the pulser and the receiving AE transducer over a component it is possible to locate a defect. The received signal decreases with increasing flaw content and damage within a composite and the technique is used to inspect porosity content, fibre alignment, condition of resin, impact damage, fatigue damage and bonds.

CHAPTER 7

VISUAL AND OPTICAL TECHNIQUES

7.1 Introduction.

Visual inspection is the oldest known form of NDT. For a long time the human eye has been used to inspect products, observe symptoms and detect abnormalities.

Visual tests by human observers are usually employed to observe some potential change in a component and to verify, using a reflected or transmitted light if the modification of the component is critical. A significant flaw or component damage is the one that is unacceptable from safety and reliability points of view. Uniform results between observers can be difficult with traditional visual inspection. Special visual training and verification of each observer's visual capability are minimum requirements to provide a degree of confidence. A standard of critical capability for any given type of visual inspection would best be based on minimum allowable defect size, luminance, distance and other sight variables that must be considered.

Traditional visual inspection is the obvious choice when the need is for simple, direct examination of a component to verify its general surface characteristics and to scan for abnormal differences. The parameters being checked should be well within the average observers visual discriminating ability.

Access, noise, fatigue and consistency are factors that must be considered. The primary disadvantage of classic or traditional visual inspection technique is that conclusions are made regarding surface condition and not beyond, with some locations being hard, if not impossible to reach. In addition, the normal healthy eye perceives light best in the 550-560nm wavelength, which means that at these wavelengths the eye absorbs a given amount of energy as the brightest. As wavelengths increase or decrease from 500nm, it is more difficult for the eye to adjust. Below wavelengths of 400nm or above 700nm, the normal eye cannot perceive the radiation visually. Radiation in the 400-500nm and 570-700nm wavelength range requires larger amounts of energy in order for the normal eye to sense brightness than does radiation in the 500-560nm range.

The reciprocal value of the least amount of light at each wavelength required to produce equal brightness at all wavelengths can be plotted against wavelength to produce a graph of the luminosity function as shown in Figure 7.1.

Visual inspection is used in nondestructive automotive inspection through optics and visible light, ultra-violet and infrared. However, since any waveforms outside the visible range would pass undetected by the human eye, sophisticated instrumentation (hardware and software) have been developed to enable not only detection of particular wavelengths but also to convert the detected ones into the visible range for the operator to interpret for research and development and to feedback to the machine to determine the threshold of

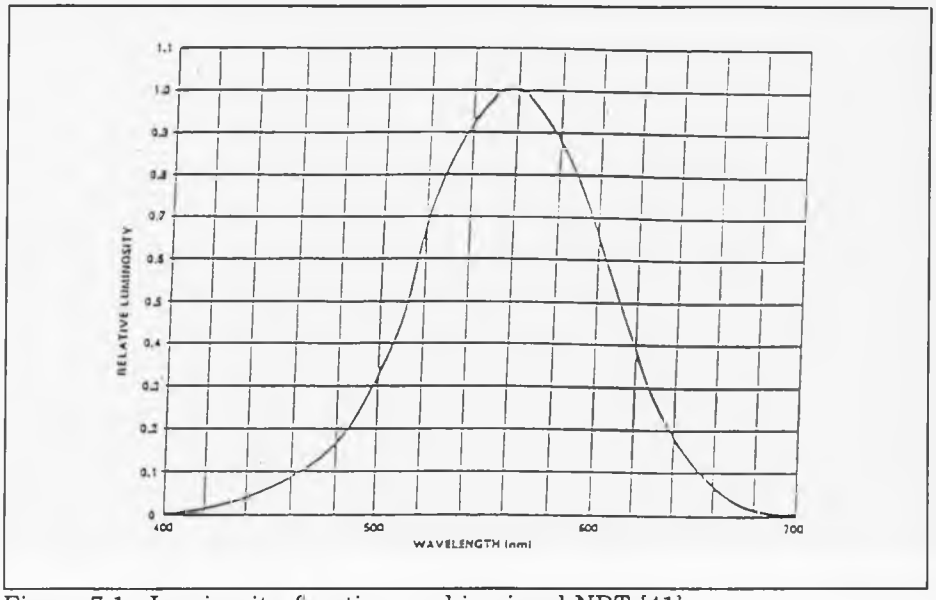

Figure 7.1: Luminosity function used in visual NDT [41].

defect levels and to assess the level of damage. The most favourable form of data display is in the form of an image which gives a comprehensive and effective way of on-line inspection.

7.2 Infrared and Thermal Recording

Infrared radiation differs from visible radiation mainly with regard to length of the electromagnetic waves. Red light has a longer wavelength than blue, and infrared radiation has a longer wavelength than either (Figure 7.2). In all other respects, these radiations behave similarly. They travel through space in the same wavefront configuration at the same speed. They can be reflected by appropriate mirrors, and their paths can be bent and focused by the proper refractive elements or lenses. The efficiency with which visible and infrared

radiations are transmitted or reflected by various materials can vary considerably.

At all temperatures above absolute zero (-273°C), every object emits energy from its surface in the form of a spectrum of differing wavelengths and intensities. The range of wavelengths emitted and the intensity of emission depends upon the absolute temperature and the emissivity of the surface. As the object becomes hotter, the amount of energy emitted at each wavelength increases. In addition, the range in which radiation occurs broadens to include shorter wavelengths. The peak moves from the long wavelength end of the infrared spectrum towards the short wavelength, and as the temperature increases below about 775K (500°C), the radiation is mostly infrared energy. At about 525K (250°C), enough near infrared energy radiation is present to be detected by sensitive recording materials.

Capturing images can be achieved through reflected infrared radiation and near infrared which can be produced from, for example, tungsten-filament lamp and infrared radiation directly emitted from objects that are themselves hot or even incandescent, and far infrared or longwave. Such recording is done by electronic detection and subsequent display at visible wave lengths.

Thermal nondestructive testing can be employed to detect inclusions and flaws that differ in their heat transfer properties from the undamaged structure. When external heat is applied, the presence of defects affect the normal heat

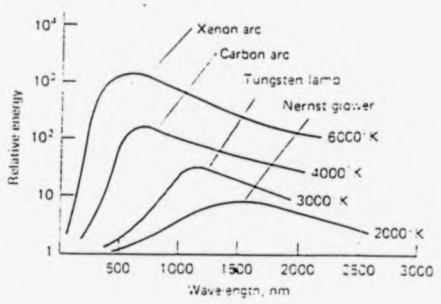

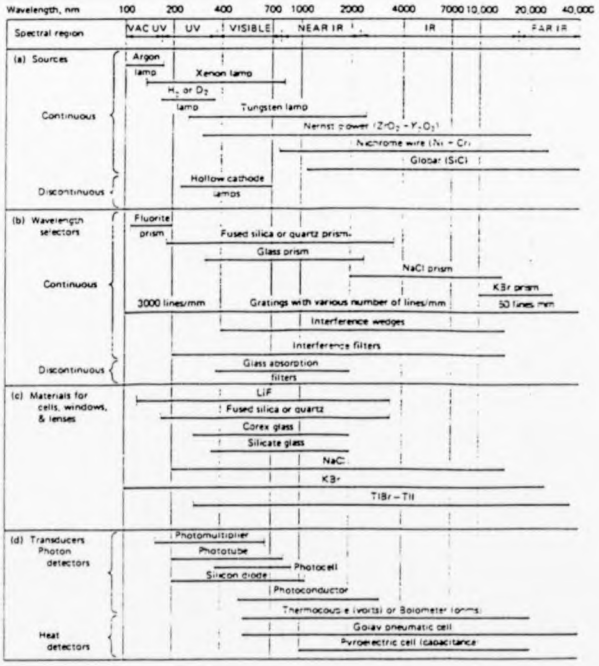

Figure 7.2: IR emissions and possible wavelengths recordings, reproduced from KODAK film company, U.K.

flow pattern of the structure. If this heat propagation is altered sufficiently, a temperature distribution profile can be realized. This distribution is then related to the existence of inclusion flaw. Infrared devices and temperature sensitive coatings (e.g. liquid crystals) are two of the most practical temperature classifiers.

(I) Liquid Crystals .

These are fluids consisting of stiff rod-like organic molecules which can form structures with some order. They therefore exhibit some of the properties of crystalline solids. Ordering of the rod-like molecules means that their bulk properties are highly anisotropic (Figure 7.3).

These organic molecules are blended with dyes to produce compounds that have colour transition temperatures at almost any temperature from -20°C to 250°C and colour play ranges of 1°C to 50°C. For most liquid crystals this process is reversible upon cooling. the colour indicating response ranges from 30mS to 0.1S. The colour is uniquely defined for a specific temperature range and temperature resolution can be within 0.1°C.

Liquid crystals can be modelled as multiple layers of two-dimensional crystals [103-106] in which layers are allowed to slide over one another. In a stack of liquid crystal layers, adjacent layers are rotated in the plane relative to each other in a helical manner. When, while light strikes the liquid crystals, a portion of the light, the particular wavelength being determined by the pitch of

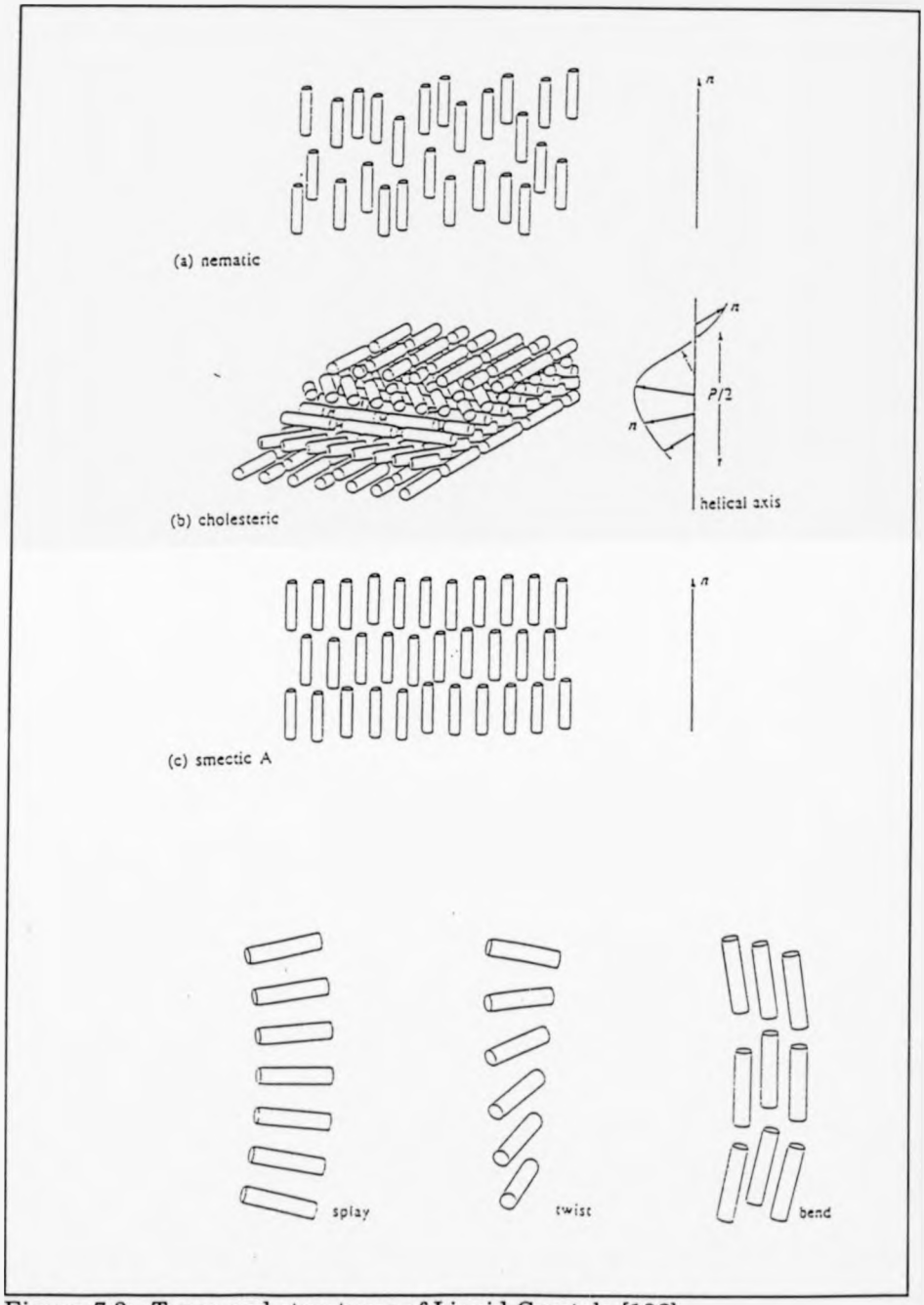

Figure 7.3: Types and structures of Liquid Crystals [106].

the helical structure, is reflected. Such a wavelength receives maximum reinforcement due to Bragg diffraction. Because the pitch of the helical structure is temperature dependent, the reflected wavelength is temperature dependent. If the wavelength is in the visible range, the crystals appear to change colour with variations in temperature.

A commercial new version of the above is the Thermal Colour OR. These reversible heat sensitive materials consist of two component substances:

(i) Electron Donor (ii) Electron Acceptor

These materials show a chromatic colour at the crystallized status by the interaction of these substances.

When a colour crystalline is heated, it becomes colourless as the electron acceptor is solved, and the radical interaction is stopped. This means it is possible to obtain the colour changes of/from colourless and to/from chromatic reversibility and repeatedly by the optional selection of electron acceptor with specific melting point. This choice also determines the type of colour transfer properties (Figure 7.4).

The typical thermal nondestructive testing procedure using liquid crystals involves applying an appropriate layer of liquid crystals. The object under test is then heated hence causing the deposited layer to emit colours when the temperature is within the colour-play range and results in mapping of the

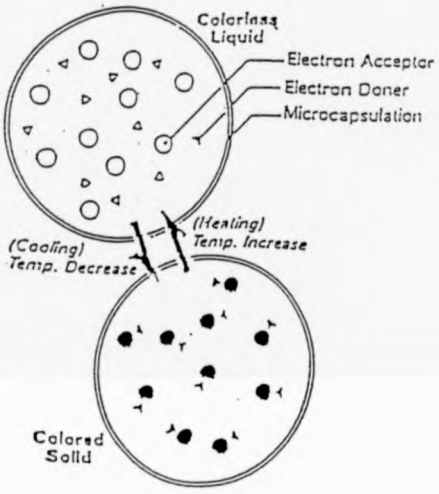

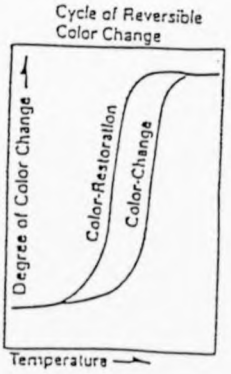

Figure 7.4: Concept of Thermal Colour OR and its response.Reproduced from the work at SIBER HEGNER Ltd, U.K.

surface temperature distribution of the tested structure.

For most fibre reinforced composites, slight variations in the fabrication procedures, curing cycles and rates of heat-up can have major effects on the mechanical properties without effect on the visual appearance.

Defects such as delaminations, cracks, voids, inclusions, improper resin to fibre ratio, and uncured resin. Such damage, if undetected may lead to service failures.

Liquid crystals are inexpensive thermal indicators that can operate over a wide range of temperatures and are found to be effective in detecting well defined inclusions. By using a video camera the surface temperature profile can be electronically processed and intelligently analyzed (Figure 7.5). However, the advantages of this thermal technique is undermined due to its contacting nature. Infrared thermo-imaging using an IR high resolution video camera interfaced to both video recorder and personal computer is non-contactable NDT technique but is preferred due to its speed, resolution and versatility even though it is a much more expensive technique to employ.

(II) IR Thermo-imaging.

(A) General

Thermoimaging (electronic thermography) is essentially an infrared radiation from the sample which subsequently converted into an electrical signal

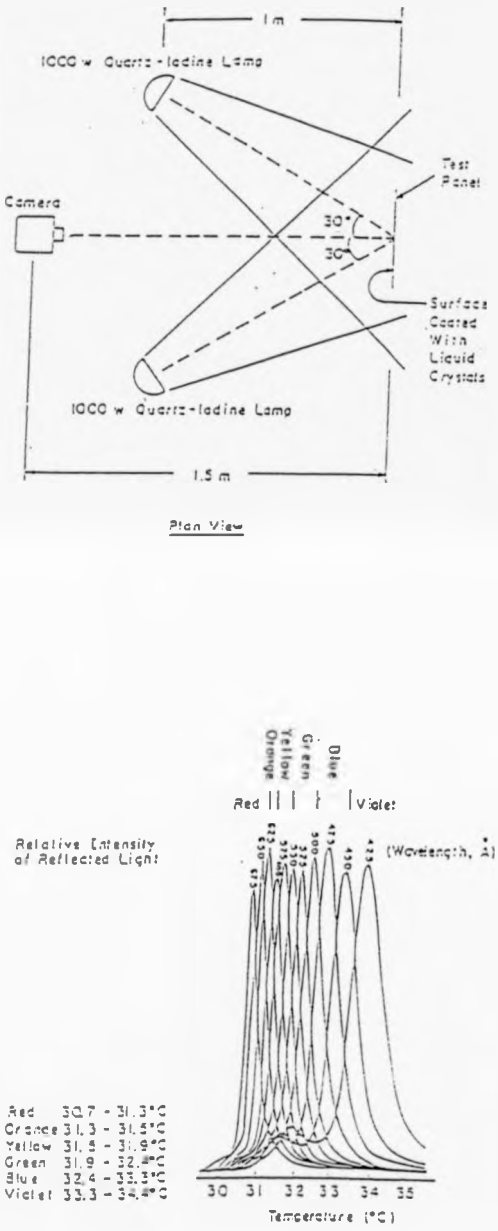

Figure 7.5: Visual processing of Liquid Crystals profile [103].

generating a real-time thermal image.

Two thermographic modes can be realized:

(i) Passive Mode:

Here the radiation is supplied by the sample which should possess an infrared temperature differential relative to the background.

(ii) Active Mode:

This is achieved through inducing of temperature differentials into the materials as it is subjected to a transient pulse of thermal energy on one side of the materials. This temperature across the surface of the material is a function of the material's internal structure.

As a result of defect presence, the thermal characteristics of the materials evidently affect the resulting image which has dynamic characteristics depending on the thermal diffusivity of the material.

The test structure can be inspected in two ways:-

(1) Examination in the reflection mode, where defects near the front surface restrict the rate of cooling and hence create "hot spots".

(2) Transmission mode: Defects near the surface appear as "cold spots" by impeding the flow of thermal energy.

Using thermoimaging we can obtain information regarding the following parameters:

(a) Thickness variation

(b) Material content homogeneity

(c) Porosity

(d) Defect dimensions

However, direct depth measurement is not possible and defects far from the surface have less effect than those near the surface. To provide sufficient temperature contrast, the material requires a sufficient quantity of heat. The actual temperature rise of a structure is affected by:

(1) The amount of energy incident on the material

(2) The rate of absorption

(3) The dynamic thermal properties of the material

Since the steepness of the temperature gradient provides the required "contrast" between defective and non-defective areas, a fast pulse as a source of heat must be used for a rapid temperature rise. This rapid rise is generated through discharging several kilojoules through xenon flash tubes which are directed at the area of interest.

The temperature differential across the surface of the material with a defective part is a function of the following:

(1) Defect dimensions

(2) Defect depth

(3) The initial rise in temperature

(4) The material thermal properties

Temperature difference is greatest shortly after the initial absorption of thermal energy and gradually decays with time. Therefore, it is necessary to measure temperature over an adequate time period which enables us to determine both thermal diffusivity and effusivity.

A matter of vital importance in detecting flaws in a structure is the thermal conductivity of the material. It was shown [84] that the thermal conductivity of glass fibre is in the same order of magnitude parallel as perpendicular to the fibre. In the case of carbon fibre there is quite a big difference in the conductivity. The conductivity parallel to the fibre was found to be much larger than the one perpendicular to it.

The most interesting parameter is the size of the defect. It was found that criteria to determine the size of a defect is the temperature derivative of the surface under observation. The derivative has its maximum at the edge of the defect.

The suggested criteria has proven to be able to determine the size of the defect effectively for the purpose of thermograms interpretation and that double sided technique (the heat source on one side and the detector on the other side) gives a better resolution in depth but the single sided technique gives a better spatial resolution.

Before tests with the IR scanning system can be conducted, temperature distribution through the panel needs to be investigated. If the core material is exposed to a temperature above the glass transition (T_g) temperature, the mechanical properties of the whole structure will be affected. But since it is very difficult to estimate the thermal properties of a particular material using calculations, it is recommended that thermocouples are used to determine the thermal properties of a healthy sample and set the basis for the rest of the experiments (insertion of thermocouples in the tested structure).

The parameters to be investigated to set the grounds for IR testing are:

(1) Time to reach a given temperature on the surface next to the heat source with given radiated energy from the heat source.

(2) Maximum temperature on the surface next to the heat source that would not cause a temperature greater than T_g anywhere in the structure.

(3) Maximum temperature on the side opposite to the heat source for a given temperature on the surface next to the heat source.

(4) The time interval during which the largest temperature gradient on the side opposite the heat source occurs.

Two obstacles are reported in thermo-imaging experiments:

(i) The air surrounding the test panels which absorbs energy by means of convective cooling which can give spurious contrasts that in turn cause difficulties in data interpretation when classical analysis algorithms are used.

(ii) Variability in surface emissivity that can cause confusing contrasts.

(B) Theoretical Considerations

Thermography received considerable attention as a medical diagnostic tool in the last few years. Engineering applications of thermography began to be seen in the early 1980's with energy conservation, electronic circuits, quality control and materials studies each receiving attention. This was motivated and encouraged by the improvements in thermal imaging systems having video recording and digital processing capabilities.

The use of thermography as a nondestructive testing technique for assessing structural integrity of fibre reinforced composites and monitoring plastics manufacturing process is growing rapidly.

Both passive technique, where the material does not itself produce thermal energy, but rather is subjected to heating (or cooling) by an external source, producing images which are transient in nature and harder to capture thermographically but provides the chance to fast test various geometries, and active technique, where the structure is cyclically stressed while its surface temperatures are monitored thermographically causing heat to dissipate from hysteretic and other effects leading to temperature distribution on the material surface which can be related to the distribution of stress within the material with loadings such as direct fatigue or vibration (vibrothermography).

Figure 7.6 shows the usual set up for passive (one and two sided) and active (vibrothermographical) techniques.

Various mathematical (analytical and numerical) models have been prepared by various researchers [79-82] to govern both heat distribution within a structure and the IR detection process. These findings are as follows:

(1) It is claimed that in pulse video thermography (PVT), based on the ability to measure temperatures over the full-time sequence of the thermal event that both thermal diffusivity (TD) and effusivity (TE) can be determined. TD is found to be described by:

$$TD = \left| \frac{0.14\ L^2}{t^{0.5}} \right| \qquad 7.(1)$$

where:

L : Material thickness

$$TD = \left(\frac{K}{\rho C} \right)$$

K : Thermal conductivity

$t^{0.5}$: Time at which material risen to half its final temperature

ρ : Material density

C : Material specific heat

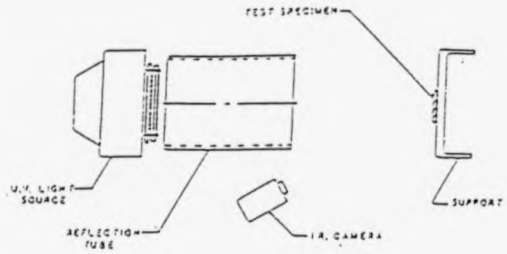

Experimental set-up, passive thermography. One-sided method.

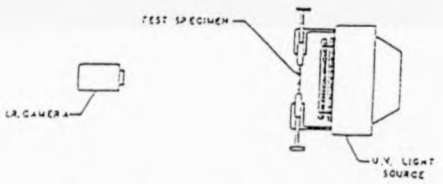

Experimental set-up, passive thermography. Two sided-method.

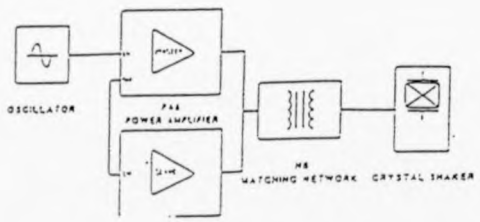

Block diagram of vibrothermography system.

Figure 7.6: Passive and Active Thermography [79-82].

This expression is used to describe the double sided thermoimaging technique.

Using a single-sided technique, it is found that the thermal effusivity (TE) of the material as a function of a square-pulse of constant heat flux (Q) applied to the surface from time t = 0 to t = t_0 is given by:-

$$TE = \left[\frac{0.637 \sqrt{Q^2 t}}{\Delta T} \right] \text{ for } 0 < t < t_0 \qquad 7.(3)$$

and

$$TE = \left[\frac{0.637 \left[\sqrt{Q^2 t} - \sqrt{Q^2 (t - t_0)}\right]}{\Delta T} \right], \; t > t_0 \qquad 7.(4)$$

The previous expressions are based on the following:

For a perfectly homogeneous material, the wavefront of heat passes through uniformly. However, where there are defects, such as delaminations, will create a higher thermal impedance to the passage of the wavefront. Physically when the defects are near to the surface, they restrict the cooling rate due to the diffusion process, and thereby produce "hot spots". When the surface is viewed, by a thermal imager, temperature differences arising from the presence of defects become clearly visible shortly after the deposition of heat pulse.

On the opposite (non-pulsed) side, because the defect impedes the passage of heat which warms the surface, the defect appears as "cold spot" against the background heat. The temperature rise of the heated surface is governed by the amount of energy deposited and the speed of application combined with the

thermal properties of the material surface. So, providing the pulse is fast enough, the diffusion process is totally controlled by the structure itself which also means that the rate and size of the heat rise at the appropriate surface is also governed by the material. The amount of contrast observed at either surface is a function of the defect dimensions and depth from the observed surface, the initial temperature rise and the materials thermal properties.

(2) Detection of the thermoimaging detection process of defects was modelled by various researchers, [88] . They attempted to establish depth of defect and the change in the structure thermal resistance based on heat wave function. Two expressions were obtained:-

(A) **The 'fundamental' equation of thermography:**

$$L' = (\tau_o \varepsilon_o L_o) + \tau_o (1-\varepsilon_o) \cdot L_a + (1-\tau_o) \cdot L_a t_m \qquad 7.(5)$$

where:

L'	:	Radiant emittance monitored by the camera
τ_o	:	Atmosphere transmission coefficient
ε_o	:	Object emissivity
$L_a t_m$	:	Atmosphere radiant emittance
L_a	:	Ambient radiant emittance
L_o	:	Object radiant emittance

For short distances < 2 metres, it is claimed that τ_o approaches 1 hence equation (5) becomes:-

From these expressions the authors highlighted the importance of measuring

$$L` = \epsilon_o L_o + (1 - \epsilon_o) L_a \qquad 7.(6)$$

both emissivity and ambient temperature to the determination of the object absolute temperature. The authors also suggested that the output signal from the IR camera is proportional to the maintained radiant emittance.

(B) **Thermal Characteristics:**

$$\epsilon_a + \rho_r + \tau_t = 1 \qquad 7.(7)$$

Where:

ϵ_a : Absorbed radiation

ρ_r : Reflected radiation

τ_t : Transmitted radiation

For an opaque, smooth and polished surface:

$$\epsilon_a + \rho_r = 1 \qquad 7.(8)$$

With this method, material emissivity can be obtained from measurement of reflected radiations. For practical, rough surfaces, the incident radiations are scattered, therefore, bidirectional spectral reflections measurements need to be performed.

The above technique and mathematical method was also used by other researchers [73] for the same NDT thermoimaging purpose.

(3) Flat plate and circular plate models (analytical and numerical) are used

in conjunction with diffusion, 1-D and 3-D expressions to characterise flaw detection .

7.3 Optical Techniques.

(a) Holography

Over the past few years, holography [122-124] has been successful in testing vehicle structures mainly in the aerospace industry. The availability of high speed holographic recording systems under computer control and recently the development of electronic speckle interferometry and electronic holography provided a useful tool for non-destructive testing. However, problems in such techniques are found due to the difficulty in interpreting the interference fringe, equipment set-up and other sides of development.

Holography uses coherent light from a laser source to illuminate the surface of an object. Conventional holography requires that all of the optical components from the beam splitter (Figure 7.7) through to the film, including the test object, to be held in a rigid manner to preserve path lengths between the reference and the object beam to within a fraction of the wavelength of the laser light during the exposure time. Except for pulsed laser application, holography must implement a stable air isolation test bench. Speckle reference beam holography is a technique that does not require the use of a mirror to reflect the reference beam to the hologram recording medium, instead the reference beam is focused to a spot on the object itself. Also, vibration isolation requirements of conventional holography are significantly relaxed with this technique and path

lengths between the recording medium and the test object are essentially phase-locked to the reference beam for changes in distances between the object and the centre line of the hologram. Object rotation and translation, however, are compensated only at the sight of the reference beam location on the test object. To avoid the superposition of the real and the conjugate images of the test object, the reference beam is directed to a point to one side of the illuminated area of interest (Figure 7.7). As seen in the diagram, the camera, laser and film processor are built into one unit, no vibration isolation is necessary. Real-time phase locked holograms using thermal loading have been used to evaluate composite structures. Vacuum-relaxation stressing is also used in holography to obtain a particular pattern. Phase-locked holography is used to detect damage such as cracks, moisture and unbonds.

(b) Shearography .

This technique is complementary to holography in the sense that it is used in NDT to measure derivatives of surface displacement while holography measures the displacements themselves. Based on laser principles, shearography was originally designed for strain measurements [125]. Figure 7.8 illustrates the practical arrangement for this technique.

A point source of coherent light illuminates the structure under test but multiple frequency and multiple laser sources can be used. The image is then captured by an image-shearing camera. When conventional shearography is used, a photographic film in the image plane is exposed twice with the object

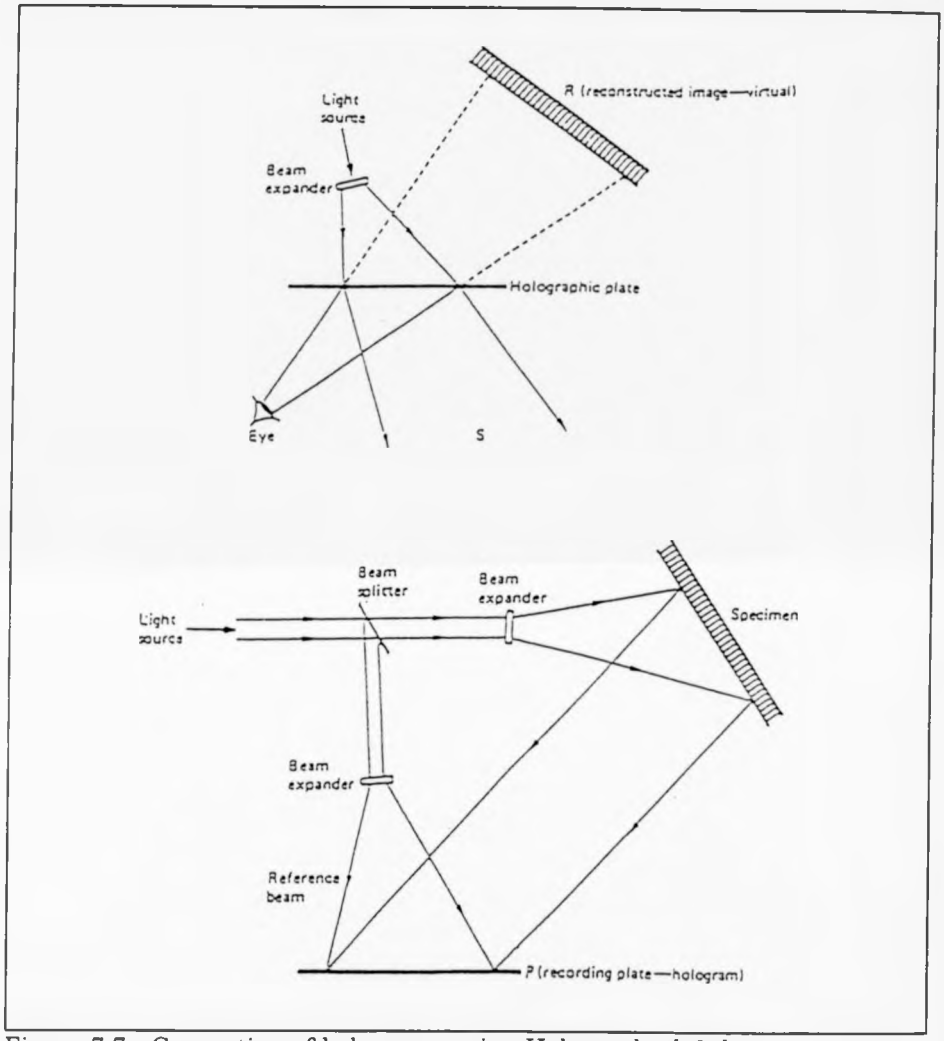

Figure 7.7: Generation of holograms using Holography [124].

being deformed between the exposures. The processed photograph yields a fringe pattern showing the derivatives of the surface displacements. This fringe pattern is not readily visible on the processed photographic film but can be made visible by a high-pass fourier filtering.

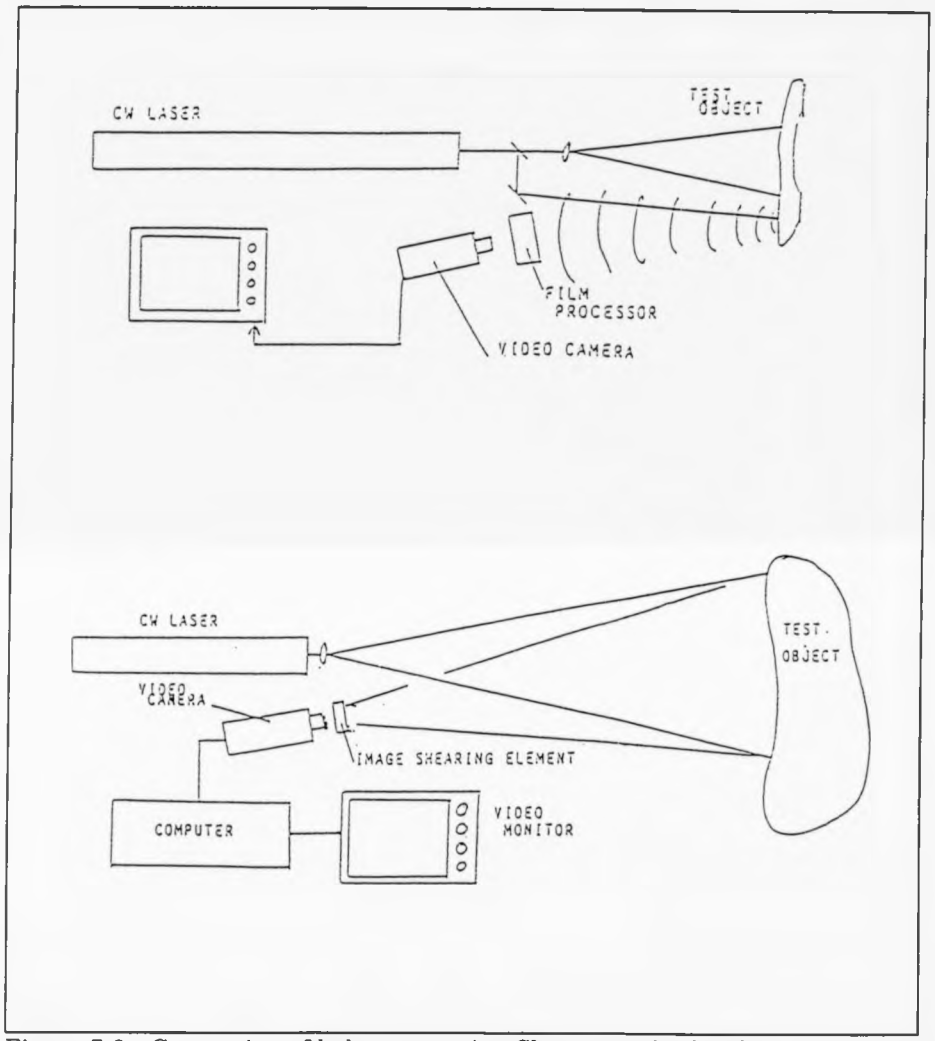

Figure 7.8: Generation of holograms using Shearography [124].

Electronic shearography provides instant, real-time shearographic imaging on a video monitor by using an image shearing element placed in front of a video camera. An image is stored in a video frame buffer. Subsequent video frames are subtracted in real time, and the resulting image is processed. Shearography can be applied to nondestructively inspect a wide range of composite structures,

and inspect voids, cracks and moisture.

In detecting flaws, shearography looks for flaw-induced strain anomalies with no concern for isolating vibration and simpler interpretation for the fringe patterns compared to holography that identifies flaws through flaw-induced displacement anomalies. Both techniques produce fringe patterns after measuring surface deformation and internal flaws which influence the deformation. Both techniques are used to inspect plates and shells with flaws close to the surface.

(c) Radiographical Techniques.

Radiography is a known and recognised technique for the assessment of materials and produced components. The technique is based on differential absorption of penetrating radiation (α, β, γ and X-rays) by the object under test. Because of differences in density and variation in thickness of the part or differences in absorption characteristics caused by variations in composition, different portions of a test piece absorb different amounts of radiation.

This very short wavelength electromagnetic radiation [137-142] can penetrate through solid structures but will partially be absorbed by the medium. The unabsorbed radiation passing through the part can be recorded on film, or photo sensitive paper, or monitored by various types of radiation detectors.

When an X-ray is absorbed a scattering process occurs due to atomic interaction with the incident beam. Four main types of scattering are possible:-

(1) Rayleigh scattering

(2) Compton scattering

(3) Photoelectric absorption

(4) Pair production

For most NDT applications the shortest wavelength X-rays are the important ones since they possess the highest penetrating power.

Radiographical methods are frequently employed in inspecting composite structures with particular emphasis on complex parts but insensitive to delaminations lying on a plane normal to the X-ray direction and the need for multiple exposures before the depth of the flaw is established. In addition, due to the low atomic number of composites, X-rays suffers little attenuation producing poor images. Hence, low energy X-rays are employed and development of ultralow voltage, high current X-ray tubes are also used to enhance both contrast and response time in film and real-time imaging.

Some of these low energy X-rays will be scattered at large angles which makes it possible to inspect the specimen from one side using the back scattering concept (Figure 7.9).

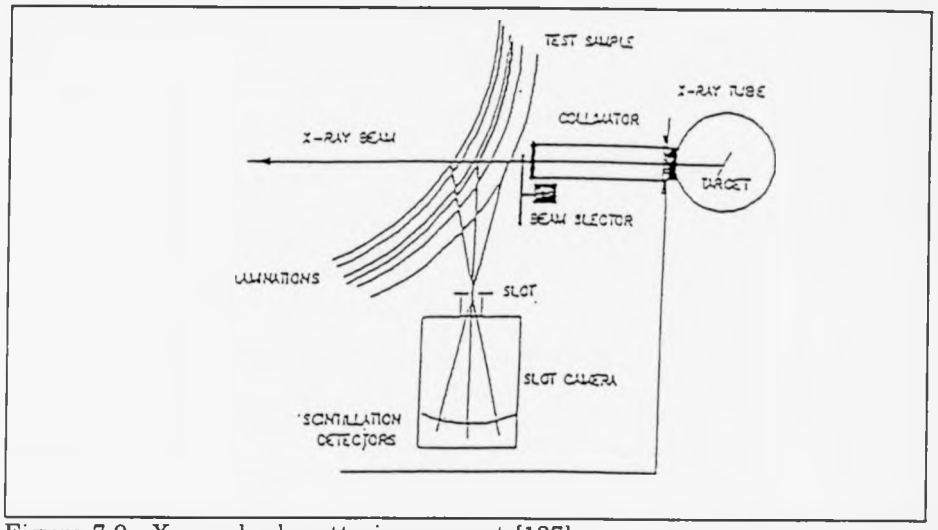

Figure 7.9: X-rays backscattering concept [137].

Back scattered X-rays are detected by an array of scintillation detectors. The back scatter intensity information is correlated with the detectors position, which in turn reveals data regarding the inspected depth. A void or inclusion will result in an abrupt change in the intensity enabling the whole object to be tested at once.

X-ray tomography (computerised axial tomography, CAT) [126] is another radiographical technique used nowadays in NDT inspection. The technique provides true cross-sectional images of the internal details of a component, with full through-thickness information which is not provided by conventional radiography. Also, it is possible to obtain a very sensitive X-ray absorption data as a by-product. This could be used to estimate fibre/resin ratio of a composite or the particle/matrix composition. Figure 7.10 shows the (CAT) system.

As the specimen is placed between a point X-ray source and the linear array of

detectors, the array is rotated around the specimen in small increments resulting in an output that is digitized and stored in a computer producing a scanned slice. The object can also be rotated and translated.

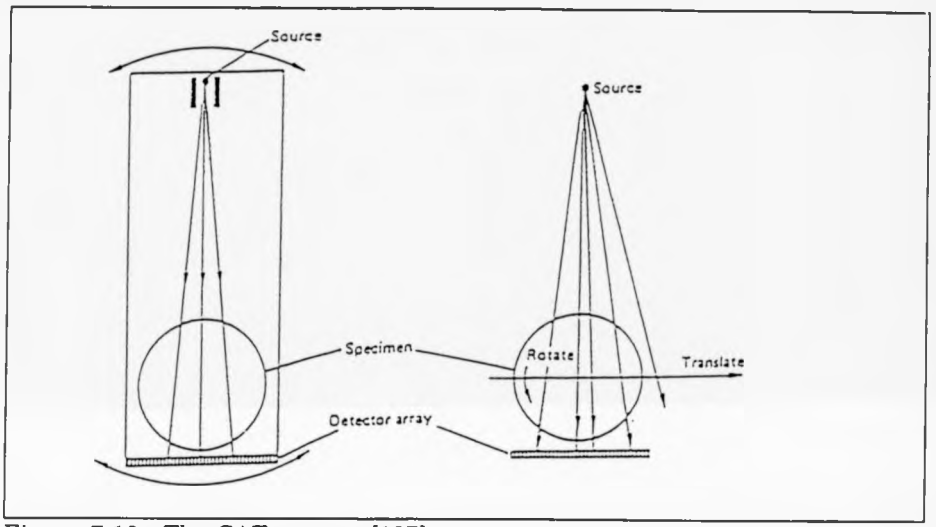

Figure 7.10: The CAT system [137].

7.4 Microwave Techniques.

This NDT technique which does not require direct coupling or contact with non-metallic structures under test uses microwave energy transducers that operate on electromagnetic waves at frequencies in the GHz region of the spectrum with wavelengths between 0.3mm to 1mm. The waves travel in straight lines and similar to light, reflect, refract, diffract and scatter.

The technique [127-132] allows rapid inspection which is limited by mechanical constraints and poor spatial resolution due to wide band implementation. However continuous wave, frequency modulated, amplitude modulated

microwaves are used in conjunction with polarization of transmission to determine structure properties, internal flaws, materials composition, density, homogeneity, moisture content and orientation.

The resolution of the received signal is a function of both band width and time duration. Due to their size, microwaves suffer little backscattering with surface roughness of a structure hard to detect when the discontinuities size is larger than applied wavelength.

When travelling through a structure electromagnetic waves are attenuated due to scattering from materials discontinuities and beam spreading. However, before it reaches the structure the transmitted EM microwaves suffer from the following energy losses:

(1) Antenna loss

(2) Antenna mismatch loss

(3) Transmission coupling loss

(4) Retransmission coupling loss

(5) Spreading loss

Where only one side of the material is accessible, reflection coefficient of the material can be measured (Figure 7.11). The technique uses the bridge technique which enables the measurements of material thickness to be carried out. Voids can be detected when the amplitude of the reflected signal undergoes a change. Also, phase change can be realized. Delaminations can

also be inspected by the same system when operating at different frequencies as well as inclusions and regions of porosity.

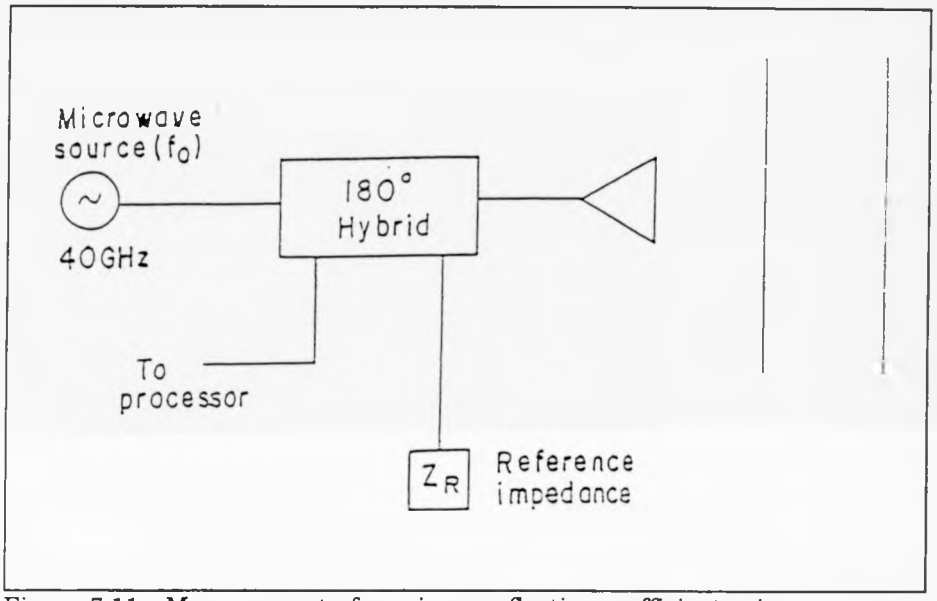

Figure 7.11: Measurement of specimen reflection coefficient using Microwaves [132].

Transmission mode NDT detection can be used to detect flaws in composites (7.12) with phase changes as the main approach. Moisture and state of cure of epoxy resin can be investigated with this approach. A look-into the material impulse radar system is developed to account for wideband backscattering concept in a reflected mode technique. The principle of such system is shown in Figure 7.13.

The system comprises antenna head, transmitter-receiver unit and a processing unit with computer interface. A train of pulses is applied via the transmit antenna to the material under test. The reflected signal is sampled and

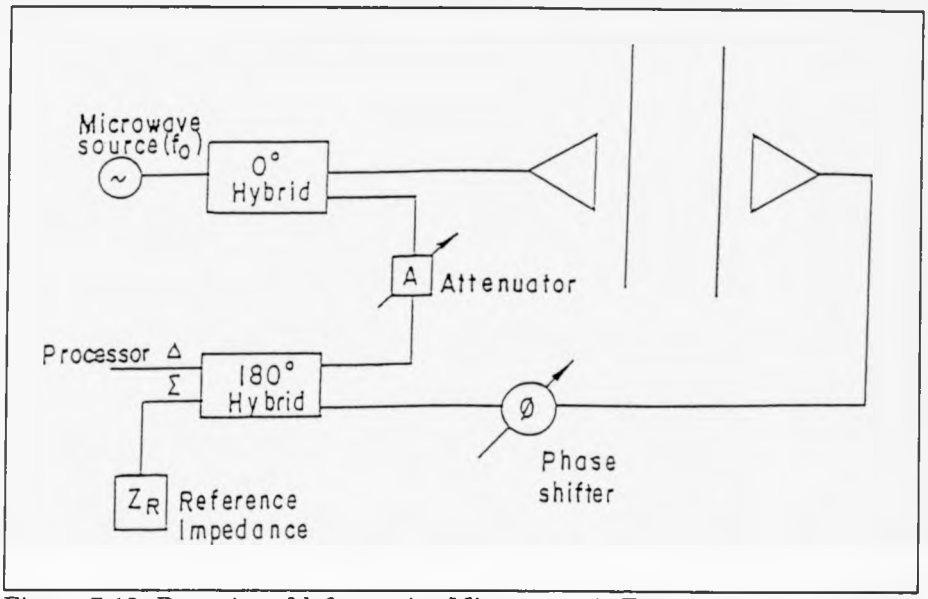

Figure 7.12: Detection of defects using Microwaves in Transmission mode [132].

processed. This provides an image of the structure cross-section and a two dimensional area picture with depth viewing. With this approach, voids, thickness and burried elements can be detected.

(A) Microwaves and Thermography.

Both in microwaves and infrared thermography radiation emitted by the body can be detected [133-134], hence the power received by the measuring instrument may be related to the temperature of the emitting source resulting in a microwave thermographical approach.

The intensity of radiation ($I(\upsilon)$) emitted by a structure at temperature (T) is expressed using Planck's radiation law:

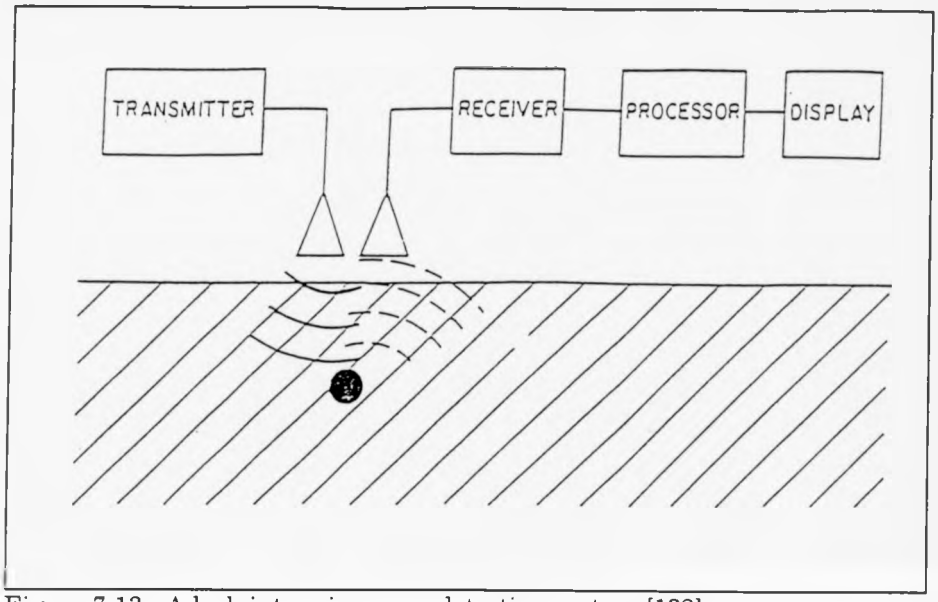

Figure 7.13: A look-into microwave detecting system [132].

$$I(\nu) = \frac{2h_p \nu^3}{c^2} \left(\exp\left(\frac{h_p \nu}{KT} \right) - 1 \right)^{-1} \qquad 7.(9)$$

where:

υ	:	Frequency of radiation
C	:	Velocity of propagation
h_p	:	Planck's constant
K	:	Boltzman's constant

In the infrared domain equation (9) is used as it stands relating the intensity of the detected radiation to temperature. In the microwave domain, the Rayleigh Jeans approximation is used since $h\upsilon << KT$ which reduces (9) to:

$$I(\nu) = \frac{2KT\ \nu^2}{C^2} \qquad 7.(10)$$

Thus, in the microwave region, radiation is directly proportional to emitting temperature. However, in practical cases both (9) and (10) must be multiplied by the emissivity factor e(υ), but can be approximated to 0.5 in case of microwaves and 0.9 in infrared.

Microwave thermography is a relatively new technique which requires waveguides, antennas, reflectors and other processing hardware and software to operate. But it is a very promising NDT approach.

(B) Microwaves and Holography.

The motivation for microwave holography [135] is based on the following factors:

(i) Propagation properties

Due to their high frequency and relatively long wavelengths, they can penetrate a variety of optically opaque structures providing a look-through capability unattainable at optical wavelengths.

(ii) Availability of a highly sophisticated microwave measurement techniques

Modern microwave measurement techniques provide efficient, sensitive and accurate means for the acquisition of microwave holographic (amplitude and phase) data over a broad range of frequencies (0.1-100 GHz). Computerized microwave network analyzers allow rapid

automated hologram data acquisition in the (0.1-40) GHz range particularly when used with spatial field mapping scanners. In addition, the availability of error correction routines and high spectral purity of phase-locked microwave sources allow any degree of coherent electromagnetic wavefields to be produced, and allow holographic images of larger bodies to be obtained.

(iii) Signal processing flexibility

Due to the two step nature of the holographic process i.e. recording and reconstruction, the raw hologram data, representing in some situations either the fresnel or fourier transform of the object, can be subjected to various preprocessing and filtering operations. In the scanned mode of microwave hologram data acquisition where the complex field amplitude over the hologram recording aperture is mapped and the data is available in an electronic signal form that lends itself to a variety of signal processing operations contrary to the limited optical processing operations.

(iv) Promising real-time processing

The density of fringes and consequently information content in microwave holograms are normally less than in optical holograms due to their long waves. This indicates that data retrieval should be feasible either digitally or in hybrid form (digital/optical).

(C) Microwaves and Tomography.

During the past few years computerized X-ray tomography or sometimes called computerized axial tomography (CT or CAT) was used. However an increased interest in the dangers of using ionizing radiation in the medical area of application resulted in efforts to find alternative techniques [136]. As an alternative, imaging of other forms of energy such as low-level microwaves are now used with a distinct feature of being able to reconstruct cross-sectional images of the molecular properties of the object.

Microwave tomography represents an attractive alternative to X-ray tomography. However, there is a fundamental difference between the two techniques. X-rays are non-diffracting, travel in straight lines, and therefore the transmission data measures the line integral of some object parameter along straight lines. This makes it possible to apply the fourier-slice theory by which a fourier transform of a projection is equal to a slice of the two-dimensional fourier transform of the object. On the other hand, when used for tomographical imaging, microwaves often do not propagate along straight lines. When the object's non-homogeneities are large compared to a wavelength, energy propagation is characterized by refraction and multi-path effects. Moderate amounts of ray bending induced by refraction can be taken into account by combining algebraic reconstruction algorithms with digital ray tracing and ray linking algorithms. When the object non-homogeneities become comparable in size to a wavelength, energy transmission would be analyzed in terms of wavefronts and scattered field. Polarization or vector fields can also

be used.

7.5 SUMMARY

Areas of application of NDT techniques are summarized in Table 7.1. More detailed discussion of NDT techniques as appropriate can be found in the references previously given.

Techniques	Detection Capability	Limitations/Disadvantages
Radiation X-ray	Inclusions, cracks	Older film dependent processes can be slow. Limited to crack size, must have access to both sides of the structure.
Gamma Radiation	Density variations	Must have access to both sides of the structure.
Electromagnetic Microwaves	Voids, delaminations, porosity, resin variables	Non-contacting. Requires expert interpretation.
Thermal Infra red	Voids, delaminations, unbonds	Sensitive to specimen surface emissivity. Sensitive to geometry of the part.
Liquid Crystals	Voids, delaminations, unbonds	Not useful for aluminium metals -to-aluminium honey structures.
Photo chromic coating	Voids, delaminations, unbonds	Very insensitive to small defects; useful for surface and near surface defects only.
Visual	Blisters, porosity, cracks, discolouration, surface defects, use in conjunction with dye penetrant	Limited to surface defects in opaque material.
Ultrasonics Pulse Echo	Delamination, porosity	Requires immersion in water. Requires expert interpretation.
Transmission	Delamination	Limited to access to both sides. Geometry of the part sensitive.

Table 7.2 Comparison Of NDT Techniques.

CHAPTER 8

NDT DATA: INTERPRETATION AND ANALYSIS TECHNIQUES

8.1 Introduction

Predictive and deterministic analysis is an important tool in reliability tests Components can experience a successful or unsuccessful performance. In both conventional and advanced interpreting systems, initial steps have to be taken to determine the parameters that governs the criteria under which a component can be ranked or classified. Typical considerations are:-

(1) Arranging defect types in terms of their significance in influencing failure.

(2) Arranging the tested components according to their theoretical propensity of failure.

(3) Arranging untested components according to their tendency of failure.

(4) Classification of the known test results into either success or failure population.

(5) Establishing a model and assess the model in terms of correct classifications.

(6) Modifying the manufacturing process to obtain less defective components.

(7) Testing of the new components and update the model as needed.

In conjunction with discriminating modelling, deterministic methods in the form of probabilistic analysis. There are various separate probability distributions involved, namely:

(1) The probability that a specific defect of certain size will result in a failure.

(2) The probability that inspection will succeed for those defects of importance.

(3) The probability that there is a flaw in the material or component prior to inspection.

Some model selection process is mainly based on statistical techniques such as discriminant analysis, canonical correlation, principal components, regression on principal component and stepwise procedures [143-147].

Thus it is important to review some of the methods used in classification and pattern recognition both conventional and adaptive.

8.2 Classification Techniques: A Review.

Classification techniques and pattern recognition can be categorized as:

(I) Numeric Techniques (II) Non-numeric Techniques

Numeric techniques use vectors for quantitative description and comprise deterministic and statistical measures applied to geometrical pattern space, while non-numeric ones use strings and trees for structural description and employ symbolic processing that is dealt with by methods such as fuzzy sets.

In deterministic methods [148-149], discriminant functions are employed and form the basis for the majority of pattern recognition techniques. Classification in general and discriminant classification is rarely performed using a single measurement, or feature from the input pattern. Normally, several measurements are needed to adequately distinguish between inputs that belong to different categories or classes. When a number of measurements on an input pattern are made, each of them represents a unique feature, a set of these features are created in a vector form.

By examining these feature vectors, we realize that they form distinct clusters which can be classified by assigning a class per cluster via a separating boundary like a line in simple systems Figure 8.1.

After establishing the decision boundary the process becomes simply a matter of deciding on which side of the boundary any new input falls by using the mathematical discriminant function to map the input features onto the classification space. To achieve such classification a number of decision based discriminant methods [150-151] can be used such as:

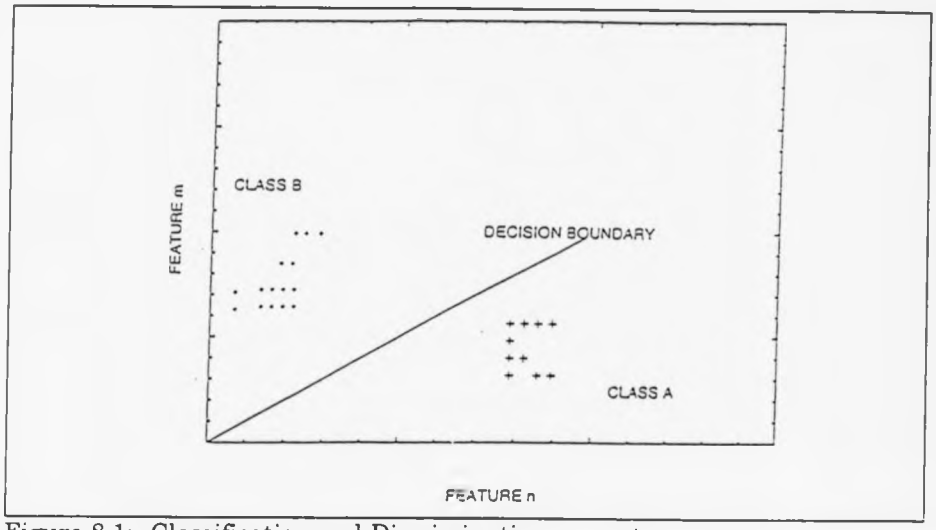

Figure 8.1: Classification and Discrimination concept.

(I.1) Linear Classifier (LC)

Consider Figure 8.2,

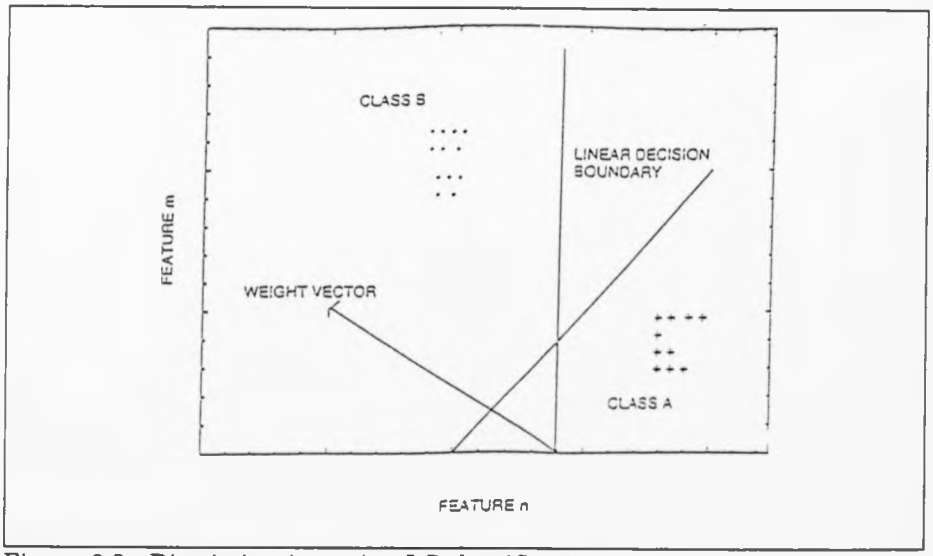

Figure 8.2: Discrimination using LC classification.

The diagram shows how Figure 8.1 is produced if (LC) is employed. In this technique the decision boundary comprises a discriminating function g(X) given by:

$$g(X) = \sum_{j=1}^{l} W_j X_j \qquad 8.(1)$$

Where:

X_j = j^{th} component of an input vector.

W_j = j^{th} component of a weight vector.

The expected output of the given function in equation (1) is either positive or negative depending on the values of weight and input vectors. Consider again Figure 8.2. Here positive output is classified as A-class and negative as B-class. This is a simple decision mechanism that uses the polarity of the function g(X), hence leading to the definition:

$$\begin{aligned} &\text{If } g(X) > 0 \Rightarrow \text{Decision} = \text{class A} \\ &\text{If } g(X) < 0 \Rightarrow \text{Decision} = \text{class B} \end{aligned} \qquad 8.(2)$$

By expanding the discriminant function we obtain:

$$\begin{aligned} g(X) &= \sum W_j X_j - \varpi \\ &= (| W | . | X | \cos \phi) - \varpi \end{aligned} \qquad 8.(3)$$

Where:

ϕ is the angle between the vector X and W.

ϖ is the bias value.

The above allows the required +/- classification to be achieved. To establish the position of the decision boundary in the pattern space we realize that at the boundary crossover point we have:

$$\sum_{j=1}^{l} W_j X_j - \varpi = 0 \qquad 8.(4)$$

and for l = 2 we obtain:

$$(X_1 W_1 + X_2 W_2) - \varpi = 0 \qquad 8.(5)$$

hence,

$$X_2 = \left[-\left(\frac{W_1}{W_2} \right) . X_1 \right] + \left(\frac{\varpi}{W_2} \right) \qquad 8.(6)$$

Equation (6) is equivalent to the equation of straight line:

$$y = m X + C$$

So,

$$m = \left(\frac{W_1}{W_2} \right), \quad C = \left(\frac{\varpi}{W_2} \right) \qquad 8.(7)$$

From equation (7) we can see that the decision line slope and intercept is controlled by the weights ratio and bias value. This indicates that we can perform a discriminating process providing we establish an appropriate value for the weight vector. To find a suitable value for the needed weight vector we use trial and error with a feed back line as an error function that compares the desired output with the required one.

This technique is mainly used to classify in a linear format for linearly separable classes. For more than two classes which are still linearly related

more than one hyperplane decision surface is required as shown in Figure 8.3.

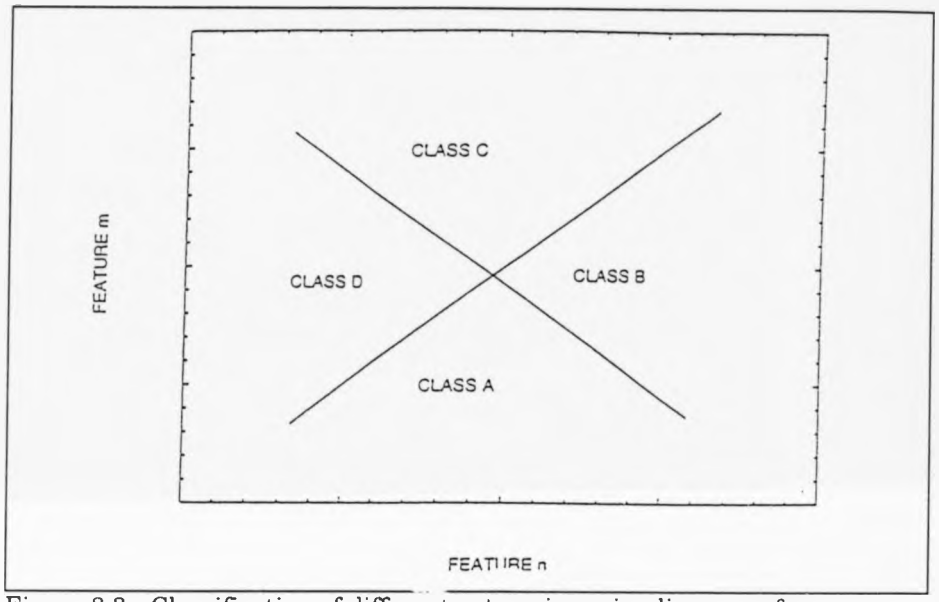

Figure 8.3: Classification of different categories using linear surfaces.

However, the process is lengthy and slow. For non-linearly separable classes, a transformation or mapping is carried out first before this technique can be used.

(I.2) Nearest Neighbour Classifier (NNC)

Also known as minimum distance classifier, is another classification technique which is slightly different from the previous [152]. Figure 8.4 illustrates the principle behind this technique.

In the figure we need to establish to which class pattern X belongs. The decision is made here as a function of the shortest distance to the neighbouring

class.

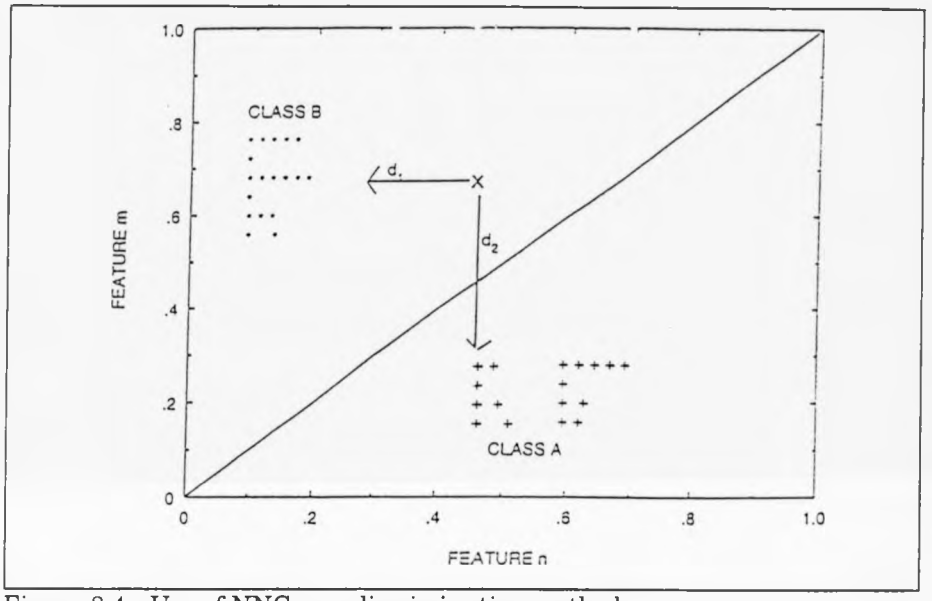

Figure 8.4: Use of NNC as a discriminating method.

From the diagram we can establish a classification function h(X) as:

$$h(X) = \text{Nearest (class A)} - \text{Nearest (class B)} \qquad 8.(8)$$

However, this technique can easily result in misclassification due to spread of one class that surround the unclassified sample and d_1 being equal to d_2 in other cases, Figure 8.5.

To overcome the problem of misclassification, several methods can be used like Hamming distance measures, Euclidean distance measure, City Block distance and Square distance measure.

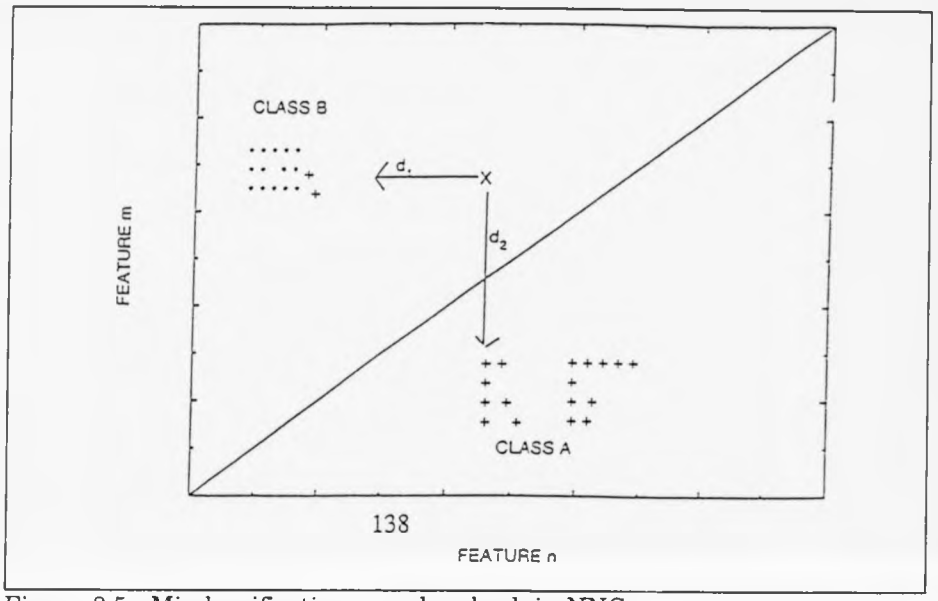

Figure 8.5: Misclassification as a drawback in NNC.

In practice, this technique works well when the distance between means is large compared to the spread or randomness of each class with respect to its mean.

(I.3) Statistical Techniques

Statistics play a vital role in pattern classification due to the randomness under which pattern classes are normally generated. It is possible to derive a classification approach that on average yields the lowest probability of classification errors when used.

Bayesian classification is an important technique that is widely used. It relies on the basic statistical theory and probabilities and conditional probabilities. For pattern classification we employ measurements from feature extracted

vectors and make an estimate of the probability that a pattern belongs to a specific class.

If we assume β_i for i = 1, 2, ..., K are the possible classes, then the probability of a pattern α_v belonging to β_i is:

$$p (\beta_i/\alpha_v) \quad (0 \leq p \leq 1) \qquad 8.(9)$$

Using conditional probability allows us to use a pre-captured knowledge about a pattern to improve the estimate of class membership. To assign a class to a feature vector using Bayer's rule we need to follow the condition:

$$p (\beta_i / \alpha_v) > p (\beta_j / \alpha_v) \text{ for } j = 1, 2, ..., n \quad i \neq j \qquad 8.(10)$$

for the pattern to belong to class β_i with the highest conditional probability.

The mathematics behind this concept and the one relating Bayes classifier to Gaussion distribution is complex and can be found in various publications [153-172]. Generally Bayesian classifiers can be optimised to perform very well with simple linear behaviour under certain conditions.

(II.1) Matching Shape Numbers

This is a structural technique (non-numeric) [153-154] that is equivalent to the nearest neighbour classifier discussed previously. The assignment of groups or classes is achieved here through region boundaries (shapes). To put the best match to

five different shapes (coded A, B, C, D, E), Figure 8.6, a similarity tree can be used.

From the diagram it is obvious that the best match is between C and F since they both have the highest score.

(II.2) String Matching

In this approach the region boundaries are coded into strings [155]. So for two boundaries A, B we have $a_1\ a_2 \ldots a_n$, $b_1\ b_2 \ldots b_n$. The similarity measure is given by:

$$R = \frac{S}{D} = \frac{S}{\max(|A|, |B|) - S} \qquad 8.(11)$$

where:

S : same or matching number of strings

D : different or not matching number of strings

and $R \Rightarrow \infty$ for a perfect match and 0 for no match.

(II.3) Syntactic Methods

These are fundamental in handling recognition of structural patterns [156]. The principle behind them is to specify a set of pattern primitives, a set of rules that governs their interconnections, and recognizes whose structure is determined by the set of rules in the form of a grammar.

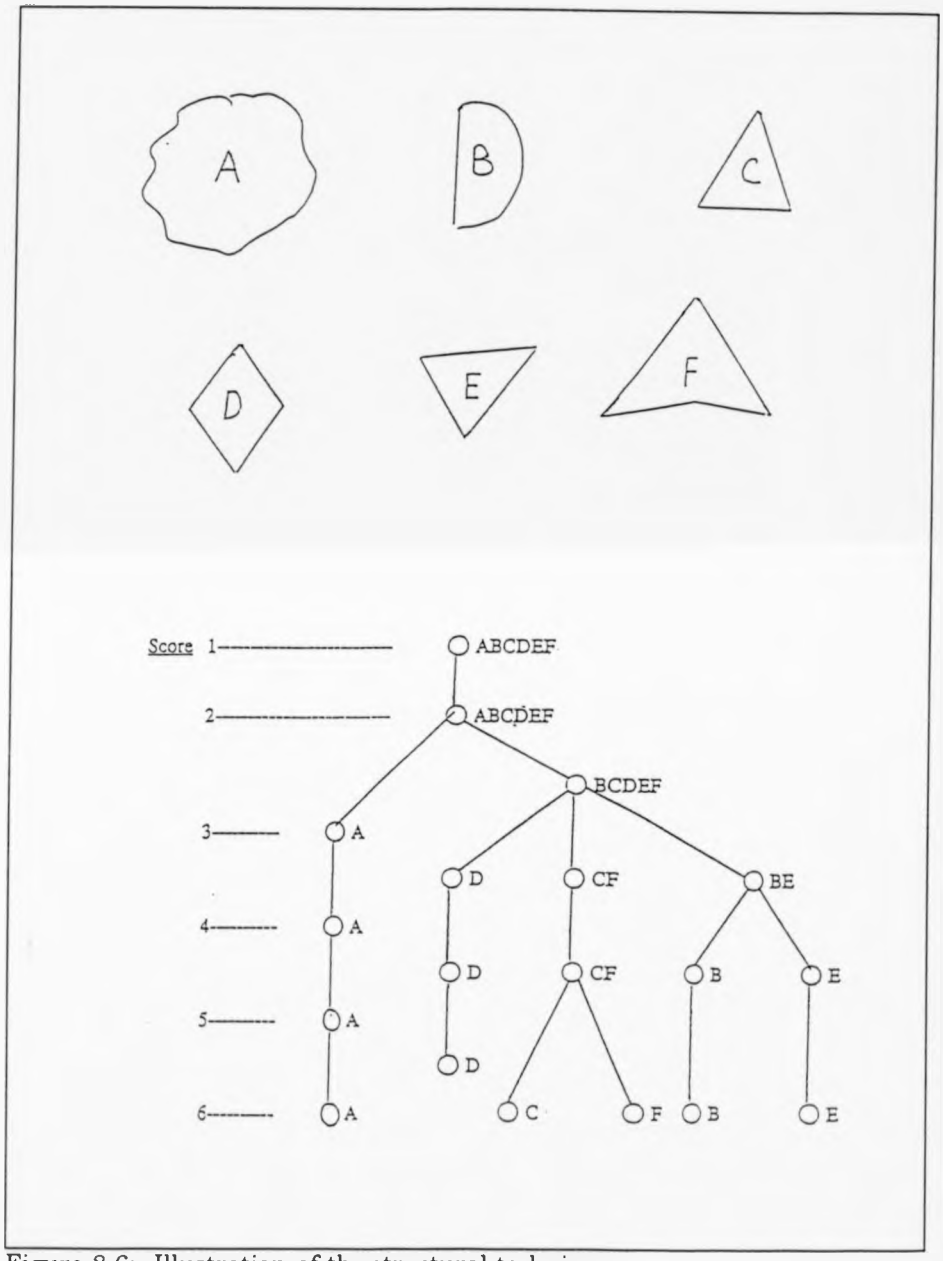

Figure 8.6: Illustration of the structural technique.

8.3 Adaptive Pattern Recognition Using Artificial Neural Networks.

(1) Purpose

The classification techniques presented in the previous section are based on finding a set of statistical parameters as a function of sample patterns and produce a pattern class. The nearest neighbour classifier is totally determined by the mean vector of each class. In the same way, the Bayes classifier for Gaussian distributions is specified by the mean vector and covariance matrix of each class.

Training is relatively simple using the previous methods as the training patterns of each training set (class) is used in a direct way to estimate the variables of the decision function relative to that class after which a fixed structure of the classifier is established with performance dependent on satisfying the boundary conditions [157-158].

However, what is really needed in an intelligent classification system is the flexibility to accommodate different boundary conditions with complex non-linear behaviour in a fast and accurate manner with capabilities of generalization, classification and prediction [159-165].

(2) General

Most existing pattern recognition systems originated from the study of artificial intelligence and are built on the principles of serial computing. These systems

suffer from the following drawbacks:-

(a) Lack of consistent ability to generalize from incomplete, noisy or distorted features.

(b) Lack of versatility in combining features into whole patterns.

(c) Time consuming in research and development.

(d) Suffers from weak associative rules or lack of them.

(e) Massive searching effort is needed to find a new pattern not stored in memory.

In recent years there has been a rediscovery and rapid development of models and intelligent systems for complex pattern recognition that depends on a large number of relatively simple processing elements which are highly interconnected and operate in parallel as an alternative to rule-based systems for data compression and automated solution of interpolation or classification problems [166-171].

The most marked feature of these processing elements is their inherent adaptability permitting fairly easy modification of the system to perform in a variety of applications. This kind of information processing system is based on a heavily simplified model of the physiological/ neurobiological system in the human brain and some other living organisms [172-179]. The principle follows that operations on primitive microstructures in large numbers will map and form a complex macrostructure with relevant operational characteristics for the

purpose of simulation of symbolic information processing on lower levels of abstraction. Due to certain similarities between these models and features of the central nervous system, they have come to be known as Neural Networks.

The basic design of such models contrast sharply with conventional digital computers where a highly complex central processing unit (CPU) carries out computation in a sequential, serial fashion. One of the principle reasons for interest in neural networks is the fact that many perform associative functions as a direct outcome of their architecture. These associative functions include reconstructing original learned patterns from inputs that are fragmented or distorted, the ability for novel patterns to extract outputs of related patterns that were previously stored in memory and the capability to link two or more unrelated patterns.

As a consequence of their associative properties, neural networks carry out direct distribution of inputs across the processing array and memory storage via alterations in the strengths of connections between the processing elements (connectionst networks) [180-183].

The state of a processing unit within the network is defined by its state of activation, usually a scalar value. Thus, neural information distribution and processing (communication) consists of switching patterns of activation within a neural complex. The processing elements are interconnected according to some pre-defined manner with individual connections participating in the

storage of many different patterns.

To simulate synaptic information transfer, each connection is associated with a weight as a measure of the influence exercised by one processing unit over another. The arrangement of weights is the sole means of knowledge representation within a neural network. Therefore, knowledge is not crystallized in the shape of symbols and symbol relationships; rather, it is represented on a sub-symbolic level and normally distributed among many connections. This eliminates the need to define a concise model of the required application. Also, compression of data is achieved and data size is reduced to a reasonable level by externally describing the input vector patterns.

Another feature of some neural networks is the ability to self-organize [184-186] by altering strengths of connections based mainly on local conditions. This allows these networks to develop their own internal representation of stored data. Neural network models of this form can be described as content-addressable since retrieval of data occurs when inputs directly extract output from the array of interconnected elements. This form of retrieval contrasts with that of digital computers where information is accessed by a code that is unrelated to the memory content (location addressable memory).

There are amazing similarities in architecture, operation and other features of certain artificial neural networks and the cerebral cortex. In addition to the brain-like, self organizing associative abilities, these networks display a relative

immunity to the effects of damage of individual processing elements (scale invariant) [187-192].

Also, to a large extent the function of artificial associative networks depends on a spatially distributed input system like that seen in the olfactory bulb projection to the piriform cortex [193-200].

The discriminative power of some of these networks is also similar to the piriform cortex in that it is greatly enhanced by positive feedback via interconnections between the processing elements that receive the distributed input. In piriform cortex, the interconnections between pyramidal cells (associational fibre systems) mediate a distributed positive feedback to cylindric segments that are immediately adjacent to the segments that receive the distributed input. Also, in associative memory models, individual inputs are typically weak relative to output threshold, which is also thought to be the case in olfactory cortex. The change that these inputs cause to the synaptic strengths (interconnections) are thought to be actively related [201-204].

There are various algorithms which are thought to be variations of the Hebb learning rule [205-212] that can be used to implement parallel distributed processing models as explained in the following part.

(3) Processing of Information

The weights (synapses) of the connections (neuron) hold the knowledge of a

neural network (Figure 8.7). The neuron is the basic processing element in a network, (Figure 8.8). Every neuron has one output reflecting the state of the neuron, i.e. its activation condition. This output is allowed as in a biological system to branch or fan out to interact with many other neurons. The inputs to these processing elements activate the neurons relative to the synaptic weights using a threshold function. The implemented activation function should possess a non-linear quality which restricts the output to lie between 0 and 1 for decision making and probability computing. Figure 8.9 illustrates some popular functions and their mathematical formulae.

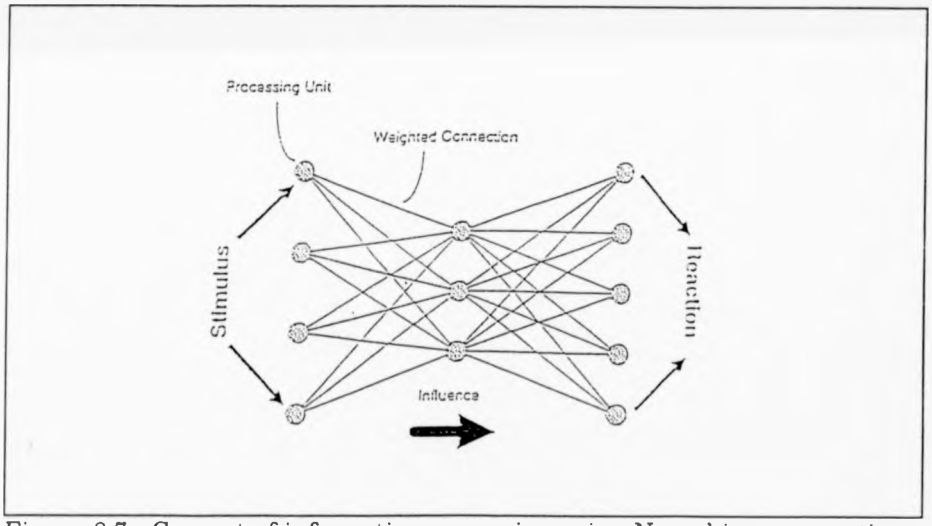

Figure 8.7: Concept of information processing using Neural interconnections.

When the synaptic weights acquire the necessary information, it is expected that the required output is produced once a pattern is presented to the inputs of the network. To achieve this, teaching the neural network is carried out via training techniques which comprise sequential presentation of patterns and weights adjustment with final fine tuning. This is done by employing a

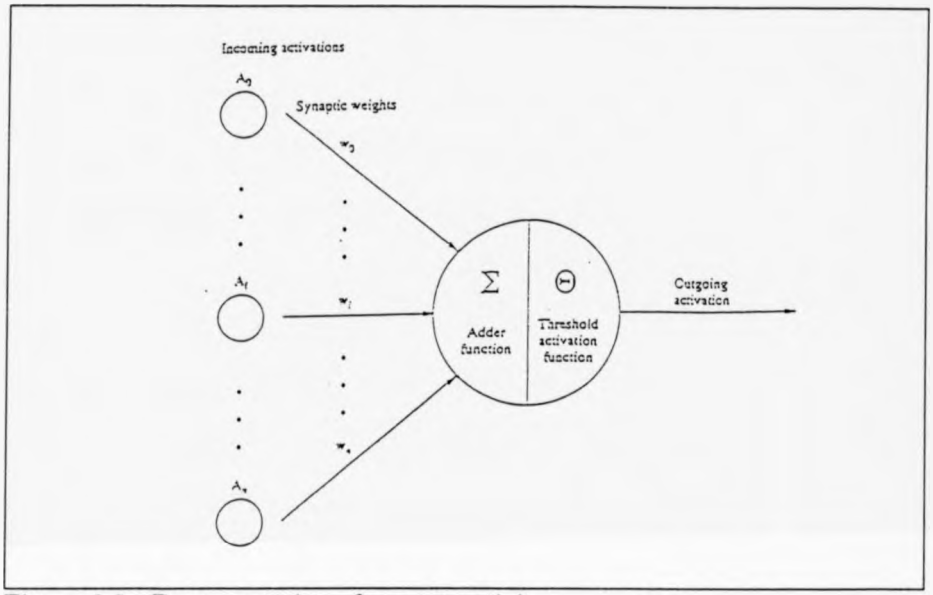

Figure 8.8: Representation of neuron activity.

learning rule that results in associative and correlative features originally based on Hebbion learning theory. Neural networks can learn through two types of teaching procedures:-

(1) **Unsupervised Learning**

Here, adjustment of weights is not related or a function of pre-designated or desired output. There is no comparison and correcting teaching signal and the network self-organises itself (Figure 8.10).

(2) **Supervised Learning**

The weights here are adjusted based on an error teaching signal produced after the network output pattern is compared to the desired output pattern. An error correction rule is used to activate this. Reinforcement learning is also a supervised learning, with variation on the correction technique. While supervised learning uses global correction algorithm, reinforcement learning

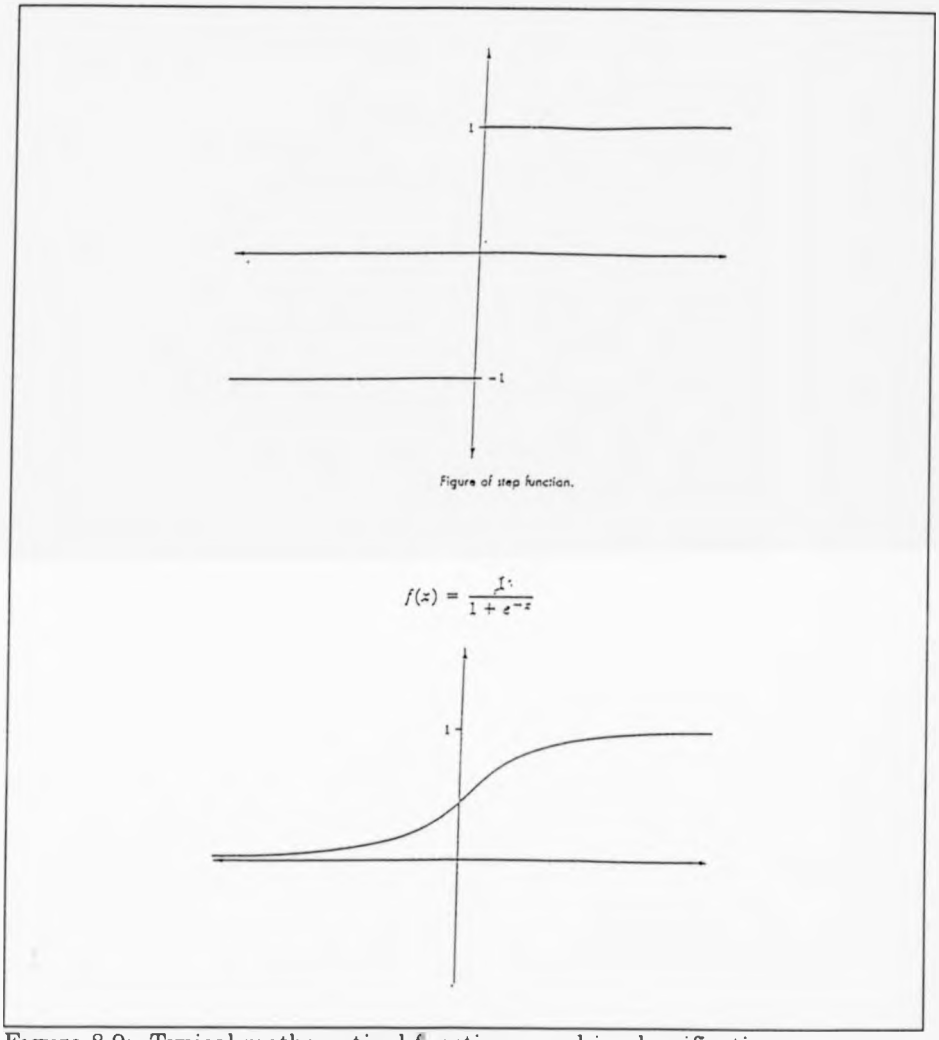

Figure 8.9: Typical mathematical functions used in classification.

employs more local and specific correction rule (Figure 8.11).

Multi-layer networks are often used in network implementation. Such a network would consist of:-

(a) Input layer with input units.

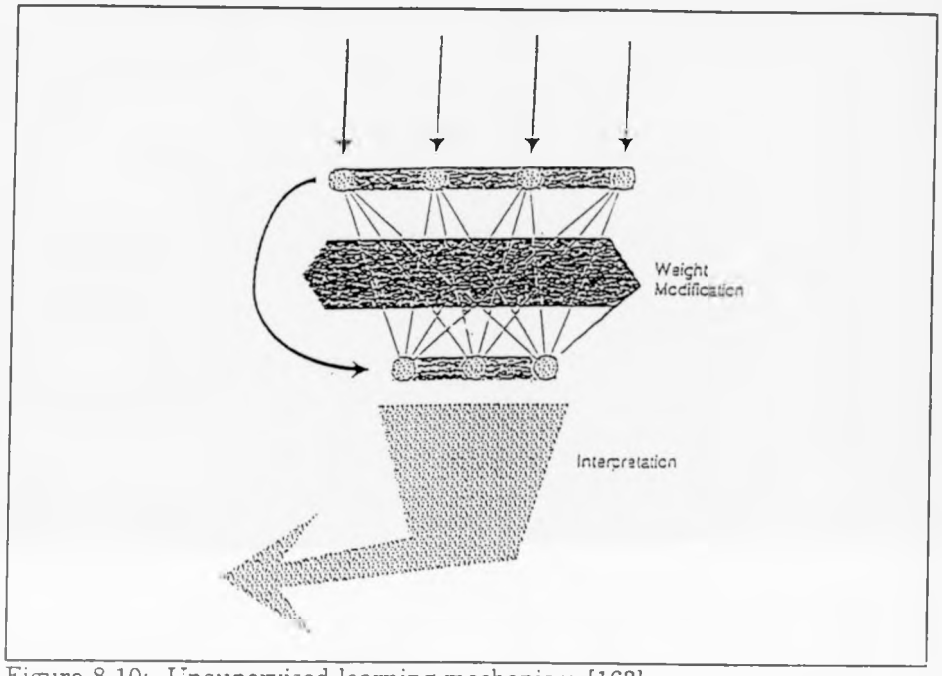

Figure 8.10: Unsupervised learning mechanism [163]

(b) Output layer with output units.

(c) One or more layers with hidden units in between.

The objective behind using a hidden layer is to allow the network to deal with non-linearly separable patterns and carry out non-linear mapping. This was discovered after a two layer network failed to emulate the behaviour of an XOR function. Figure 8.11 illustrates a general multi-layer network.

In information processing using neural networks, various multilayer network algorithms can be used for network training such as:

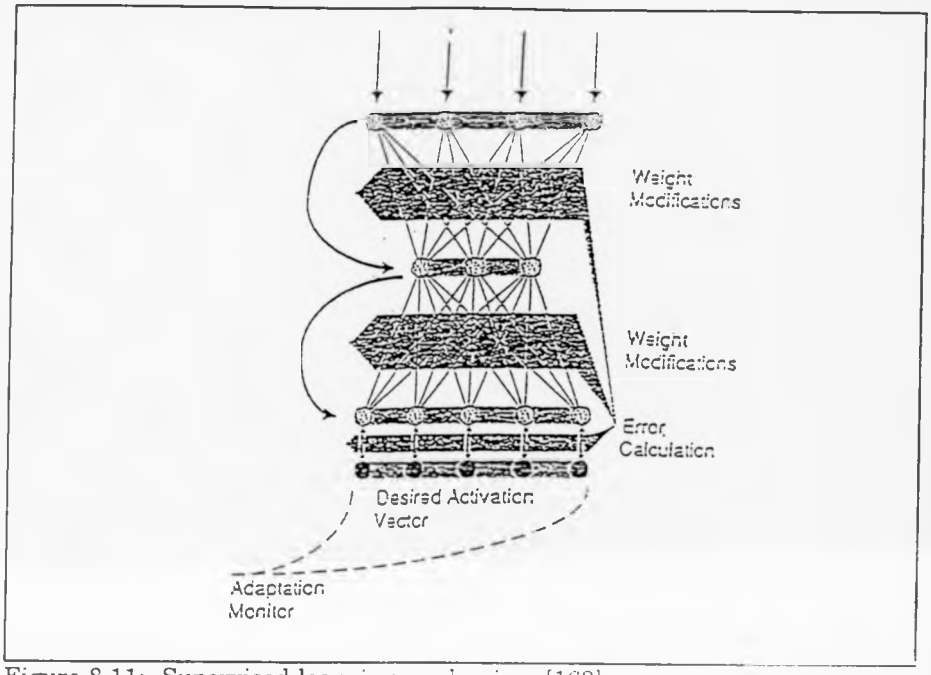

Figure 8.11: Supervised learning mechanism [163].

(a) Back propagation (BP)

(b) Counter propagation (CPN)

(c) Bidirectional associative memories and BAM systems

(d) Hopfield nets

8.4 Smart Classification and Neural Network Algorithms: Design, Modelling and Application to Defect Detection.

The objective of this approach is to try and implement some of the human senses into an intelligent automated NDT system.

The designed system is expected to produce data which will classify the tested specimen defects in N-dimensions, where N is the number of senses used. The purpose of incorporating more than one sensing device is to account for defects that cannot be detected using one single technique.

The general system block diagram is shown in Figure 8.12.

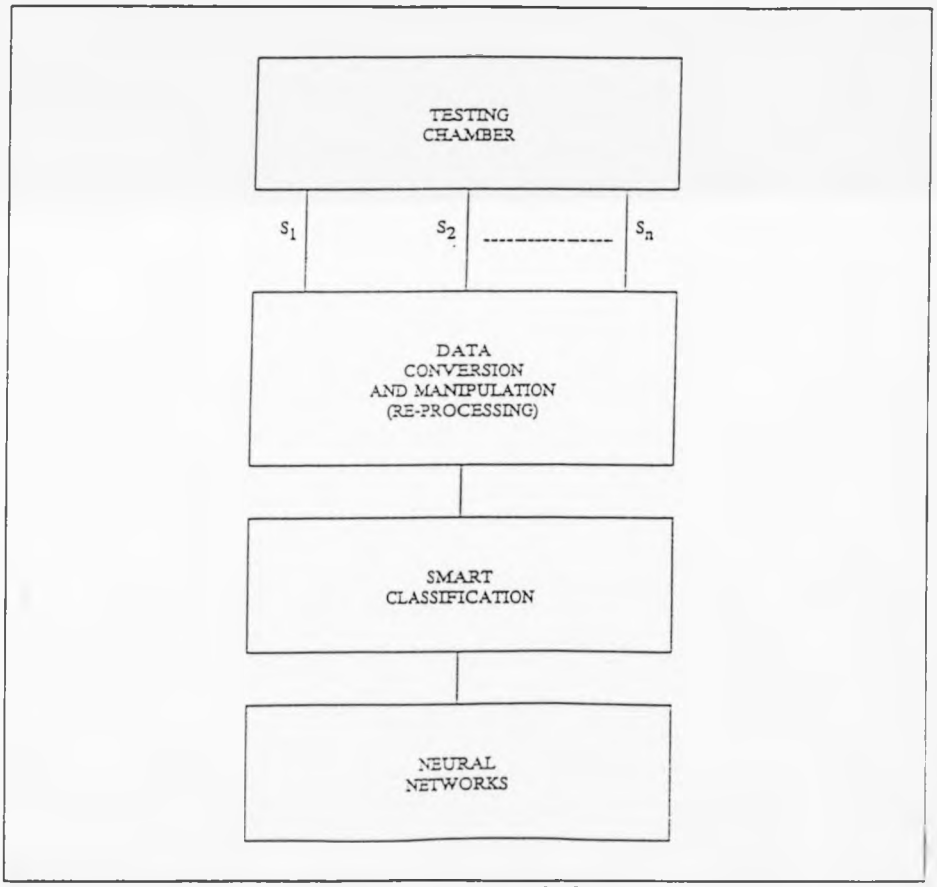

Figure 8.12: Smart classification system block diagram.

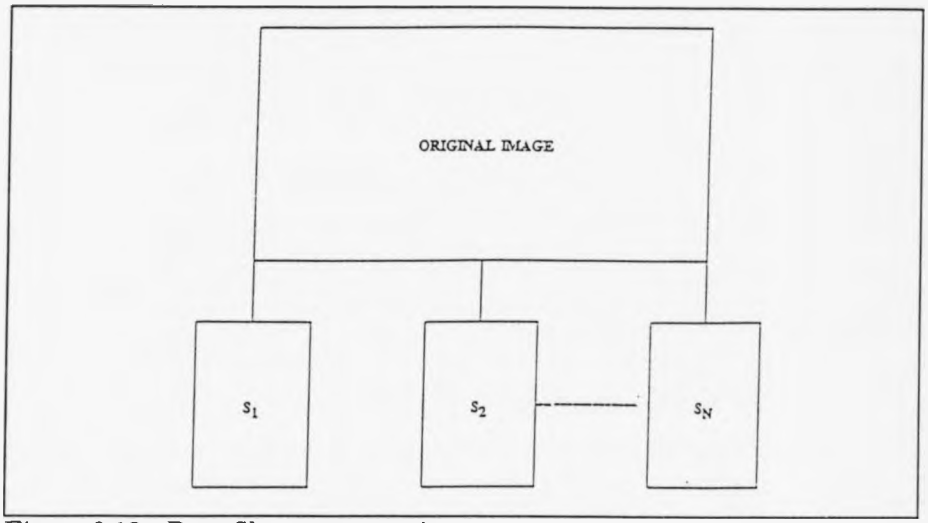

Figure 8.13: Data file source matrix.

(A) Matrix-Column Sensing System (ORIGINAL CONTRIBUTION)

In this model the sensing elements are placed in a matrix format and manipulated as follows:

The sequence S_1 to S_n consists of vectors of individual column matrices extracted from the original source matrix as shown in Figure 8.13.

The overall extracted matrix consists of the discrete combination of all column sequences, hence:

$$T_c = \begin{vmatrix} S_1 & S_2 & & S_n \\ a_{11}.r_{11} & a_{12}.r_{12} & \cdots & a_{1m}.r_{1m} \\ \vdots & \vdots & \cdots & \vdots \\ a_{n1}.r_{n1} & a_{n2}.r_{n2} & \cdots & a_{nm}.r_{nm} \end{vmatrix} \qquad 8.(12)$$

Where:

a_{ij} : original matrix elements

r_{ij} : Amplitude factor

From equation (12) we obtain:

$$S_1 = \begin{bmatrix} A_1 \\ \vdots \\ A_n \end{bmatrix}, \quad S_2 = \begin{bmatrix} B_1 \\ \vdots \\ B_n \end{bmatrix} \qquad 8.(13)$$

$$\ldots\ S_n \begin{bmatrix} X_1 \\ \vdots \\ X_n \end{bmatrix} \quad X : \text{General variable}$$

From equation (13) we obtain:

$$S_{1T} = \sum_{i=1}^{n} (A_i / \Xi)$$

$$S_{2T} = \sum_{i-1}^{n} (B_i / \Xi) \qquad 8.(14)$$

$$\vdots$$

$$S_{nT} = \sum_{i=1}^{n} (X_i / \Xi)$$

where Ξ : Normalizing factor

Now the original matrix is simplified (this is done for a fast yes/no or defective/non-defective decision), we can obtain the required hybrid column matrix for classification.

Thus:

$$T_h = \begin{bmatrix} S_{1T} \\ S_{2T} \\ \vdots \\ S_{nT} \end{bmatrix} \qquad 8.(15)$$

This expression in equation (15) is used for classification of complete data files. However, in the case of distorted, noisy or incomplete data files we need the algorithm to be able to predict and reproduce the original matrix thus giving a

defective/non-defective decision.

Two principles can be used for prediction:

(I) Prediction by elimination

Assume the total grouped sequences sum is S_T (Source Sequence); and the individual sequences are S_{1T}, S_{2T}, ..., S_{nT} then:

$$S_{nT} = S_T - [\, S_{1T} + S_{2T} + \ldots + S_{nT-1} \,]$$

$$[\, S_{nT} + S_{nT-1} \,] = S_T - [\, S_{1T} + S_{2T} + \ldots + S_{nT-2} \,]$$

where:

$$\sum_{i=1}^{n} S_{iT} = S_T \qquad 8.(16)$$

Hence, to find a missing column matrix we use:

$$S_{iT+1} = S_T - \sum_{\substack{i=1 \\ j=1}}^{n,k} q_j \, S_{iT} \qquad 8.(17)$$

where q_j is a quantizer vector.

(II) Principal Component Restriction

By examining a non-defective data file and obtaining the normalized sequences S_{1T} to S_{nT} we can concentrate on the change in one of these column matrices and apply a probability condition such that:

$$l_1 \le S_T \le l_2 \text{ and}$$

$$l_3 \le S_T - \sum_{i=1}^{n-1} S_{iT} \le l_4 \qquad 8.(18)$$

Then the specimen is defective/non-defective depending on the applied limits where:

$$l_1 * l_2 * l_3 * l_4 \qquad 8.(19)$$

To locate the defective area, classify different structures according to their composition and support the matrix-column classification and prediction algorithm (an algorithm based on the sequence grouping system that shelves data bits on corresponding states producing a specific spread pattern which is unique to the tested specimen, hence classifying the sample, Figure 8.14) another system is used, the Uniformity Factor Algorithm.

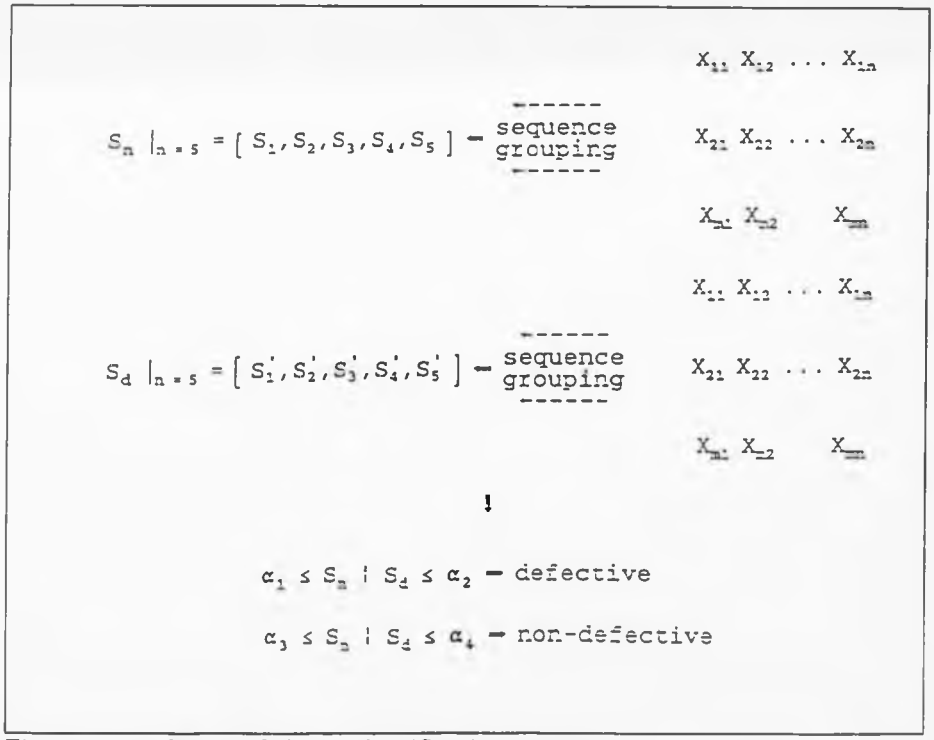

Figure 8.14: Matrix-Column classification concept.

Consider the data file (original matrix) shown in Figure 8.15:

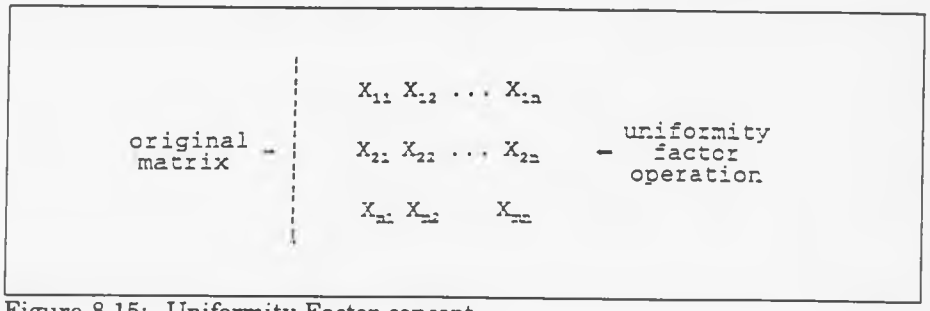

Figure 8.15: Uniformity Factor concept.

(i) Column Comparison:

A sequence of factors are produced such that if any two columns adjacent are similar, the factor is 1 otherwise it is zero producing.

$$f_T = \sum_{i=1}^{J} (f_i / \Xi) \qquad 8.(20)$$

If $f_T = 100$, this total or complete uniformity and composition is achieved column wise.

(ii) Row Comparison:

Similar to column comparison, each data bit in each row is compared to the one in the following row, hence:

$$h_T = \sum_{i=1}^{K} (h_i / \Xi) \qquad 8.(21)$$

Now if $f_T = h_T$ then data file is uniform in both directions and the sample is

non-defective. This is however, a very strict classification and prediction algorithm so, we can make it more flexible by introducing acceptable boundary conditions such that:

$$\text{if } f_T - \Delta X \neq h_T - \Delta y = \text{defective}$$
$$\text{if } f_T - \Delta X = h_T - \Delta y \leq \phi \qquad 8.(22)$$
$$= \text{Non-defective with different composition}$$

The complete smart classification block diagram is shown in Figure 8.16.

From the diagram we can compute the contribution each data bit makes towards the classification of the specimen response.

Stage 1

$$S_i = (W_{ssi} \cdot S) \qquad 8.(23)$$
$$\text{for } i = 1, 2, ..., n$$

where: S : Data source

W_{ssi} : Weight or response factor

S_i : Grouped sequence

Stage 2

$$C_{ij} = W_{s_i c_{ij}} \cdot S_i \qquad 8.(24)$$

where: C_{ij} : Grouped subsequences

From equations (23) and (24) we obtain:

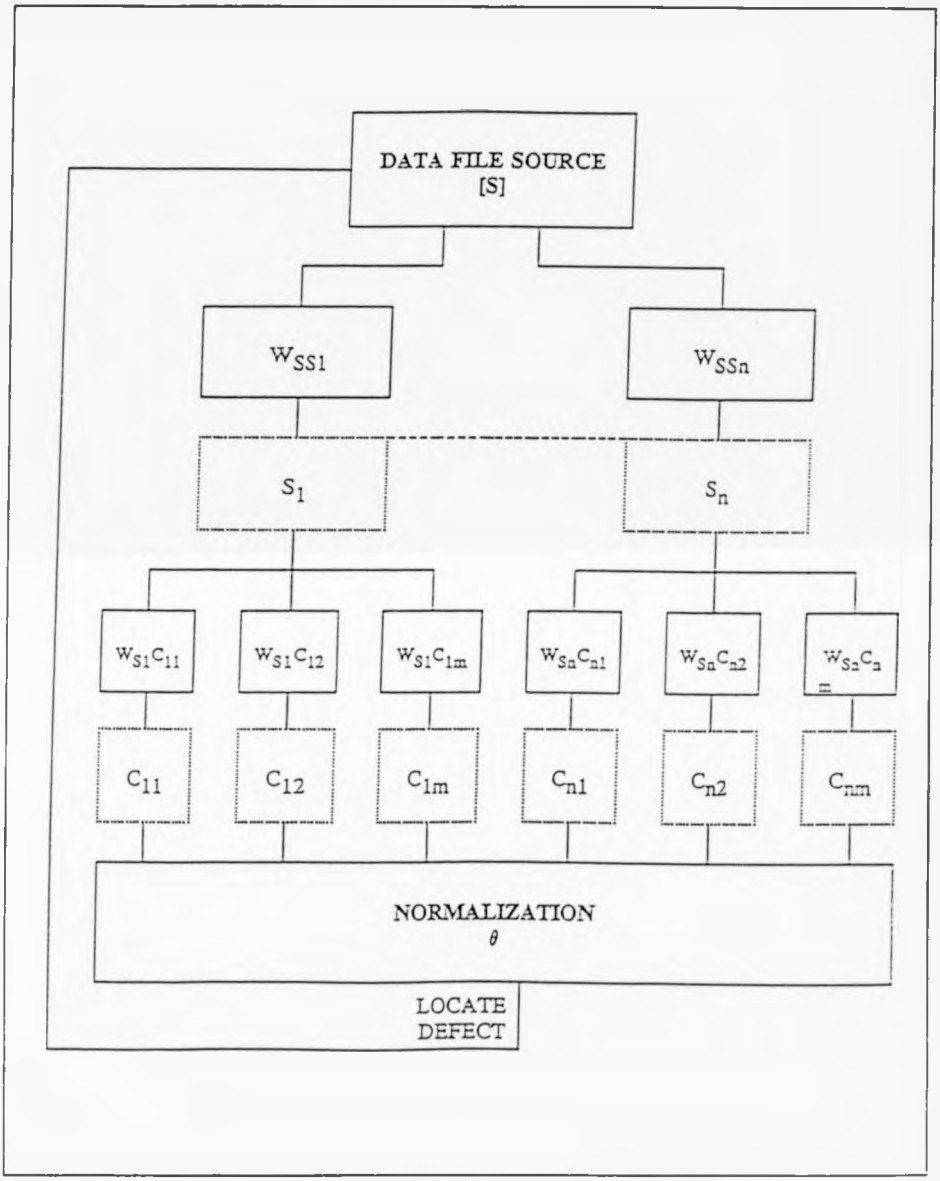

Figure 8.16: The overall Smart Classification block diagram.

$$C_{ij} = \left(W_{ssi} \cdot W_{s_i c_{ij}} \right) \cdot S \qquad 8.(25)$$

$$j = 1, 2, \ldots, m$$

and

$$\left(W_{ssi} \cdot W_{sc_{ij}} \right) = W_{sc_{ij}} = \left(\frac{C_{ij}}{S} \right) \qquad 8.(26)$$

The defective area can be located by using equation (25) and the normalizing factor Ξ

such that:

$$C_{ijN} = \left(\frac{C_{ij}}{\Xi} \right) = \left(\frac{(W_{ssi} \cdot W_{s_i c_{ij}}) \cdot S}{\Xi} \right) \qquad 8.(27)$$

and hence feed the result back to locate both the defect and determine its effect on the rest of the component.

For prediction and futuristic classification, a back propagation neural network algorithm is used.

The classical back propagation algorithm used is relatively generic technique which is applicable to a wide class of problems. As it is used as a supervised algorithm in this research a set of good patterns (healthy composite components data files) are used to train the network. The choice of network topology is critical and particular attention is paid to the hidden layers. Figure 8.17 illustrates the back propagation concept. The overall process of data prediction and decision making can be generally divided into two main parts:-

(A) Training

Here, random values are assigned to the connection (weights) between the input and hidden layers and the hidden and output (decision) layers. These could

take the values between -1 and 1. In addition the hidden layer(s) and output layer(s) thresholds should also be assigned.

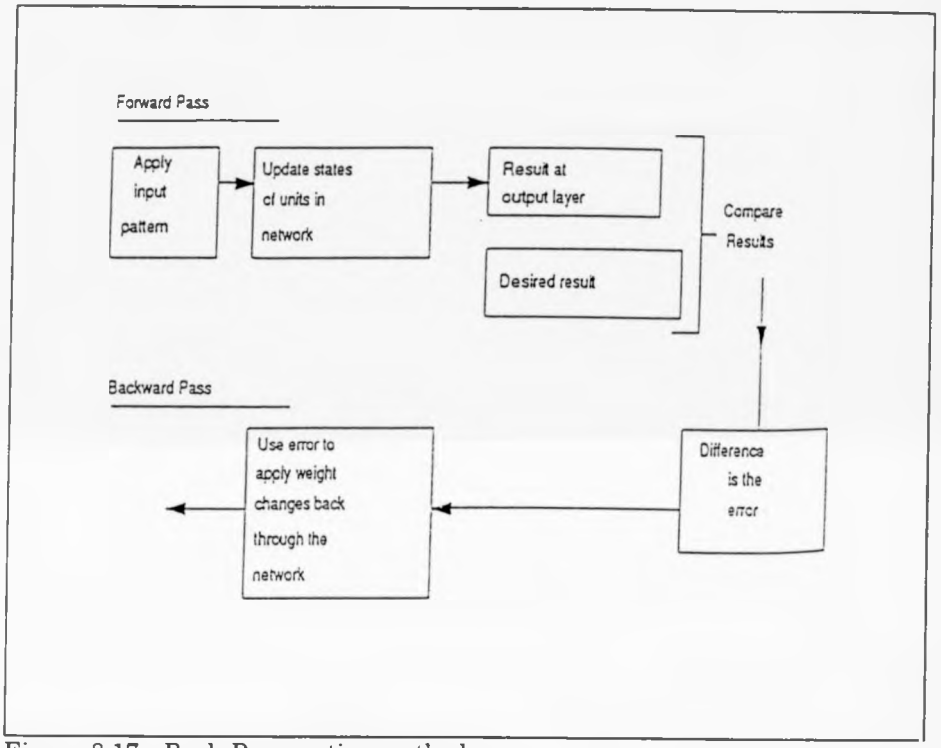

Figure 8.17: Back Propagation method.

When training the network, the following procedures are carried out:

FORWARD PROCESS:

(a) The hidden layer(s) neuron activations is computed as

$$h_l = g\ (i\ W_l) \qquad 8.(28)$$

Where:

h_l : Vector of hidden layer(s) neurons

i : Vector of input-layer neurons

W_1 : Weight matrix between the input and hidden layer(s)

(b) The output layer(s) neuron activations is computed as:

$$o = g\ (h_l\ W_2) \qquad 8.(29)$$

Where:

o : Represent the output layer(s)

h_l : Hidden layer(s)

W_2 : Matrix of synapses connection the hidden and output layers

g : Is an activation function in a sigmoid format given by:

$$g\ (x) = \left[\frac{1}{1 + \exp\ (-x)} \right] \qquad 8.(30)$$

BACKWARD PROCESS:

(c) The output layer(s) error is computed. This is the difference between the target and recorded outputs and it is computed as:

$$e_l = o\ (1 - o)\ (o - t_r) \qquad 8.(31)$$

Where:

e_l : Vector of errors for each output neuron.

o : Output layer(s) vector

t_r : Target (correct) activation of the output layer.

(d) The hidden layer(s) is also computed as:

Where:

$$e_2 = h_1 (1 - h_1) W_2 e_1 \qquad 8.(32)$$

e_2 : Vector of errors for each hidden layer neuron.

(e) The weights are adjusted for the last layer of synapsis (in this case we used two layers so L = 2). The adjustment factors the rule:

$$W_2 = W_2 + \Delta W_2 \qquad 8.(33)$$

Where:

ΔW_2 : Represents the change in matrix W_2

Δ is computed according to the expression:

$$\Delta W_2 (t) = \Gamma h_1 e_1 + \Theta \Delta W_2 (t_r - 1) \qquad 8.(34)$$

Where:

Γ : The learning rate

Θ : Momentum factor which allows the previous weight change to influence the weight change in the time period (t)

(f) The first layer weights are also adjusted according to:

$$W_1 = W_1 + W_1 (t) \qquad 8.(35)$$

Where:

$$W_1 (t) = \Gamma i e_2 + \Theta \Delta W_1 (t - 1) \qquad 8.(36)$$

The previous steps are repeated until the network converges to within a pre-specified tolerance.

(B) Interrogation

This is carried out when a network is fully trained and a fresh pattern is

presented to the network to be recognised.

During this operation the hidden and output layers activations are computed and the desired decision is made.

When a threshold function is used in computing hidden and output layers activates the expressions are:

$$h_1 = g\ (i\ W_1 + th_1) \qquad 8.(37)$$

$$o = g\ (h_1\ W_2 + th_2) \qquad 8.(38)$$

The thresholds are adjusted during training using the learning rate and error value of the particular layer under consideration according to:

$$th_i = th_i + \Gamma\ e_i \qquad 8.(39)$$

A threshold function is also used during the interrogation process.

The learning rate can be adjusted to affect the training process. Also the momentum rate can be changed to speed or slow the learning process. Both can take values between 0 and 1.

CHAPTER 9

EXPERIMENTAL ARRANGEMENTS

9.1 Introduction.

The general procedures for NDT of composites are discussed in Chapters 6 and 7. However, a more detailed discussion of the process employed will be presented here.

In all our experiments we emphasized on the following:

(1) Accuracy

(2) Simplicity

(3) Consistency

(4) Little or no human interference

(5) Portability and adaptability

9.2 Specimen Design and Structural Processing.

(I) Woven Glass: Tufnol Grade 10G/40.

(II) Glass Mat Thermoplastic (GMT): Random, Parallel, Perpendicular.

(III) Resin Injection Moulded (RIM): Out of the three types of composites tested, RIM was produced at the Advanced Technology Centre. Here will be discussing in detail the manufacturing process employed as follows:

(A) Equipment.

(1) An OHAUS, 700 series Triple Beam Balance Weighing machine is used for chemicals measurements.

(2) An oven.

(3) Reaction injection moulding machine (used as a press with manual resin injection or deposition).

(B) Materials.

(1) A 1153/72/A Epoxy Resin with a proven record of in-service durability supplied by Shell.

(2) A 1153/172/B Hardener.

(3) A U750/450 (Vetrotex) Glass Fibre (continuous fibre mat) with 7% thermo-plastic binder and random fibre orientation.

(4) Release agent and film.

(C) Production Process.

(1) The cutting edges of the mould blades of the press machine are cleaned for effective glass fibre sizing.

(2) The glass fibres are cut to 190 mm x 190 mm which fits the mould size on the pressing machine.

(3) The glass fibre mat is cut to the required size after cleaning the machine to prevent contamination and facilitate trimming.

(4) The top and bottom halves of the mould are brought together pneumatically with the bottom mould heating up the top mould to an equivalent temperature which is about 100°C with heating time of about 35 minutes.

(5) 200g of epoxy resin is placed in the oven which is set to between 70-80°C.

(6) After heating, the epoxy resin is mixed with 50g of hardener resulting in a 4 : 1 ratio.

(7) The top and bottom parts of the moulds are separated with release agent sprayed on their surfaces.

(8) A release film is placed on the bottom mould with layers of glass on the top of the film.

(9) The mixer of epoxy resin and hardener prepared earlier is then poured onto the glass fibre layers.

(10) The two moulds are brought together and left for approximately 5-10 minutes.

(11) The resulted component needs curing and further pressing for 1 hour.

The produced components contained 5 layers of glass fibre with percentage volume fraction of 65.4 and 34.6 resin for 2mm thickness, and 10 layers of glass fibre with percentage volume fraction of 64.4 and 35.6 resin for 5mm thickness. Selected samples were spray painted with either a reflecting or absorbing paint to determine their effect on damage detection.

9.3 Structural Damage: Impact Approach.

Forty specimens were prepared and cut into rectangular shapes with 130mm by 150mm dimensions with 2, 3, 4 and 5mm thicknesses. The composites were then subjected to impact loads using a drop weight impact system as illustrated in Figure 9.1.

The specimens were subjected to various levels of impact energy as shown in tables 10.4-10.6. These impact energies were achieved through usage of two principal loads of 1.35 Kg and 2.8 Kg dropped from different heights onto the specimen (Figure 9.2).

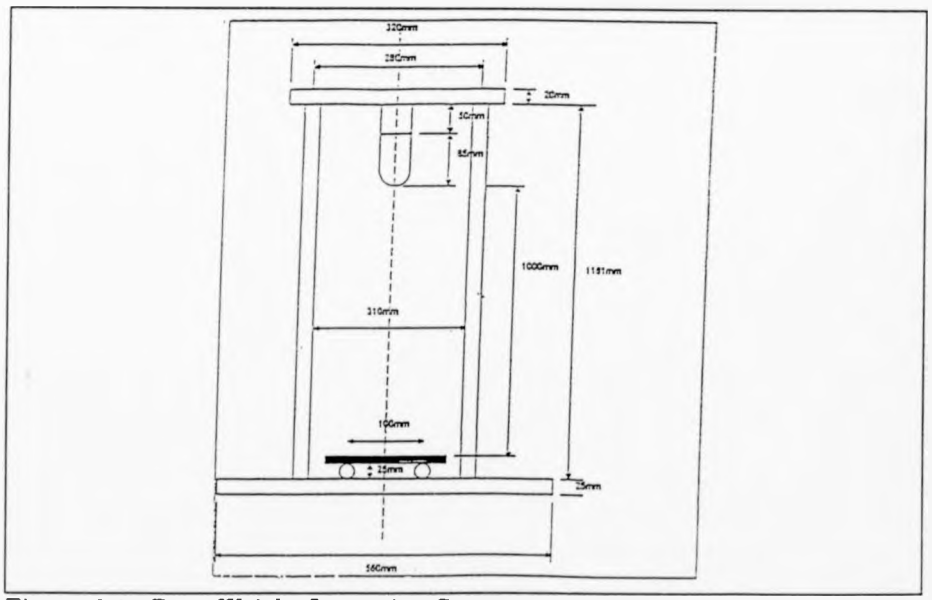

Figure 9.1: Drop Weight Impacting System.

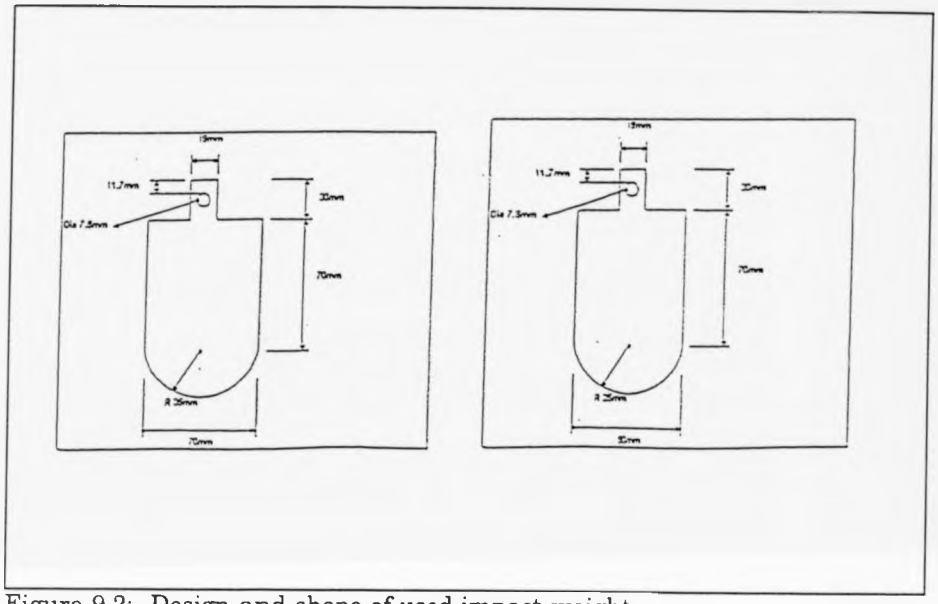

Figure 9.2: Design and shape of used impact weights.

9.4 Non-Destructive Testing Techniques.

(A) Low Frequency: Electronic Tapping

A hand-held Mitsui, WP632 tapping instrument, supplied by J.R. Technology Limited, is used for damage detection. This lightweight (400g) medium size (10 mm (H) x 46 mm (W) x 276 mm (L)) battery powered (1 watt consumption) device can be used in the following applications:

(1) Detection of exfoliation inside the honeycomb material.

(2) Detection of damage to core material connected to the surface of honeycomb boards.

(3) Checking of position and shape of core material.

(4) Detection of exfoliation in layers of composite material.

(5) Detection of exfoliation in connected parts of composite structure.

(6) Detection of position of a beam in the wall.

(7) Detection of exfoliation of tiles and clad steel.

With the WP632M data logger, the overall system eliminates the need to detect damage depending only on tone change by having the additional features of storing, displaying and plotting of the measured values. This in turn enables the device to be used in noisy places such as garages and production lines. The captured data can also be down loaded into a personal computer for further analysis and interface to intelligent classification system. For a fast defective/non-defective detection process, the tapping hammer which is driven by a solenoid is connected to a sensor within the device such that defects are interrogated though a blinking red or yellow LED display accompanied by a buzzing sound when a large defect is found.

Defect detection is carried out as follows:-

(1) Before starting the tapping process, a mode needs to be selected, for analysis purposes and research and development objectives, a low tapping frequency (4Hz) was selected with the number of averaged taps set to 8.

(2) A reference value needs to be obtained from a non-defective part of the component and/or a non-damaged sample. This is indicated through an illumination of green LED. The reference value is also stored in the

device memory for comparison purposes.

(3) The device is then held vertically and the component is scanned manually.

Figures 9.3 and 9.4 show the device and system with the scanning path adopted during testing process.

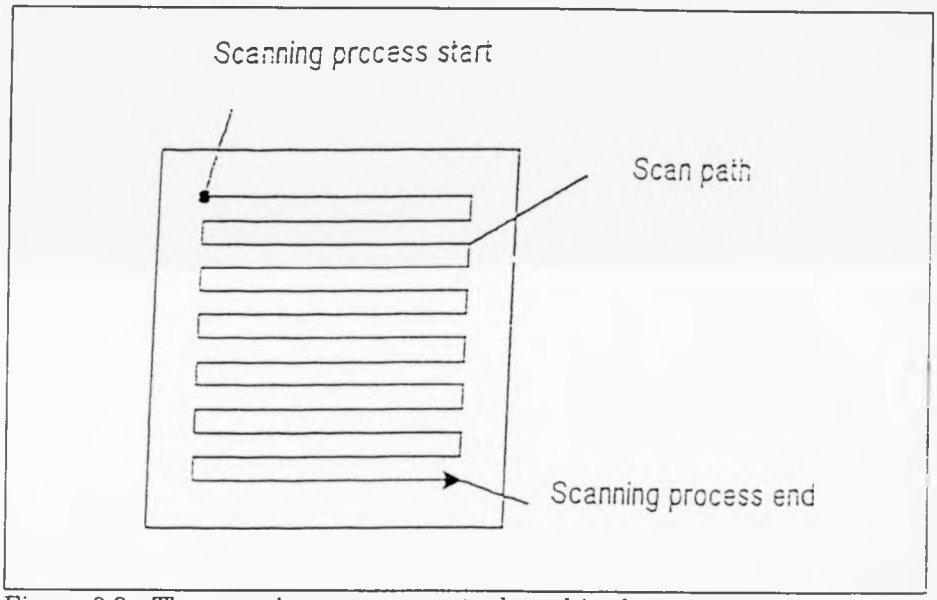

Figure 9.3: The scanning arrangement adopted in the experiments.

(B) Ultrasonic - C-Scan

The tests were carried out at SOFRATEST UK (Speedtronics Division). The equipment used was:

(1) SOFRATEST Ultrasonic Immersion Tank system, which comprises:

(a) Immersion Tank of approximate dimensions of 1 x 0.5 x 0.4 m with 3 motorised axes (X, Y, Z).

(b) Power controller cabinet with 3 power modules, PC-IDX/3 indexer card

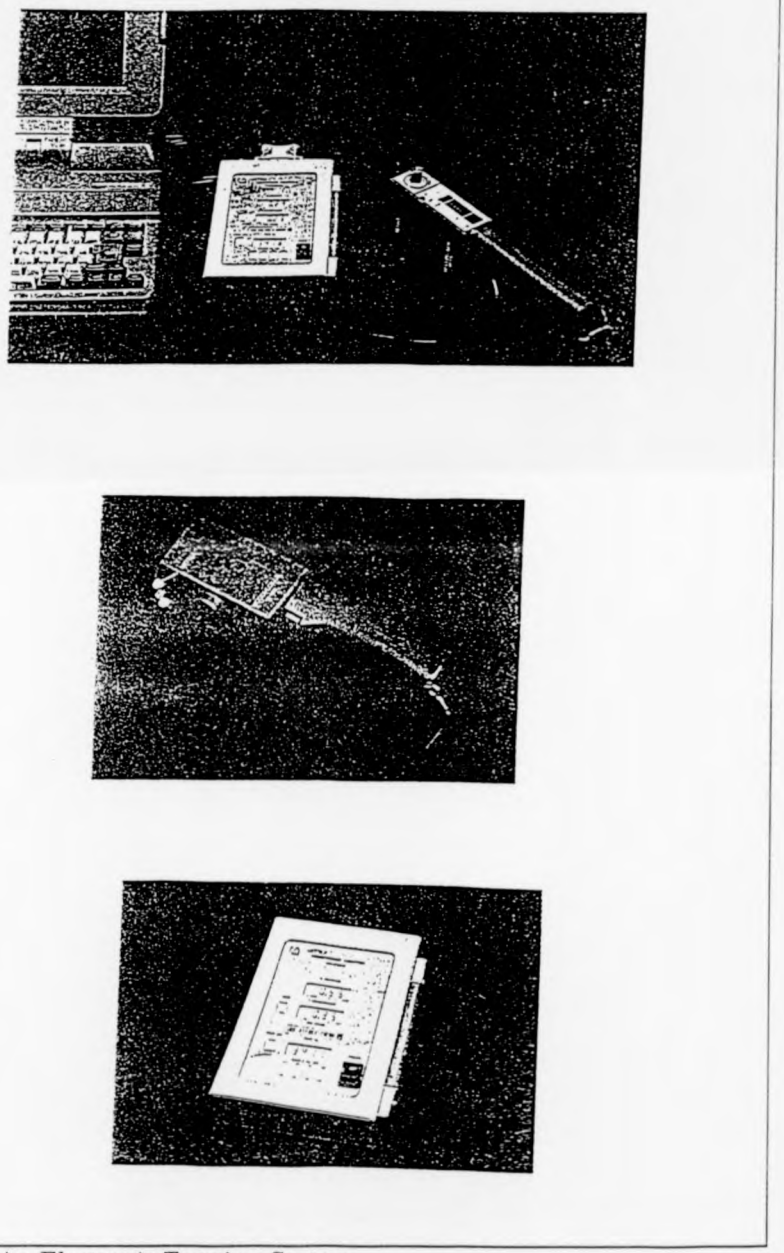

Figure 9.4: An Electronic Tapping System.

and 7.5 MHz immersion probes on two axes manipulator.

(2) IBM Compatible PC system box with Sofratest's SFT 4001C UT pulser/receiver card, SFT 4000 A/D card.

(3) The system is controlled by Sofratest ultrasoft 2000 A, B and C-Scan software.

The C-Scan system was set up to measure peak amplitude of the backwall echo through line scanning of the immersed composite component in the water tank. Figure 9.5 illustrates the experimental set up.

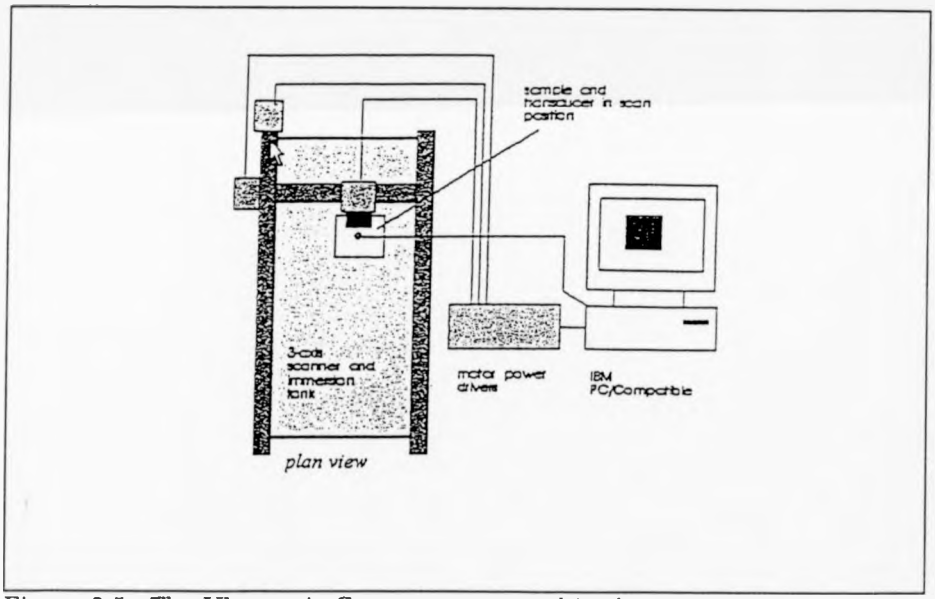

Figure 9.5: The Ultrasonic C-scan system used in the experiments.

(C) Low and High Temperature Imaging

The usual set up for both approaches is similar and shown in Figures 9.6-9.8 The only variation between low temperature, high temperature (static) and pulsed video thermography is the type of detecting camera used.

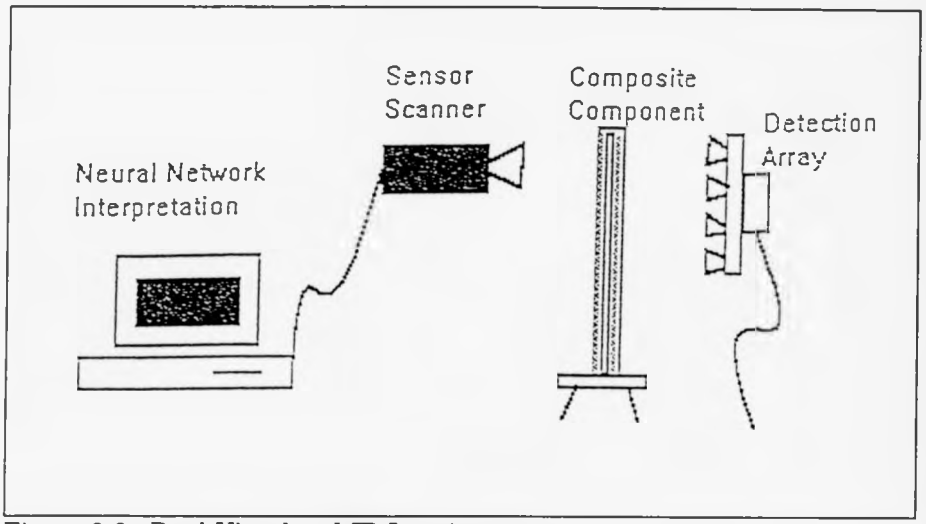

Figure 9.6: Dual Visual and IR Imaging setup.

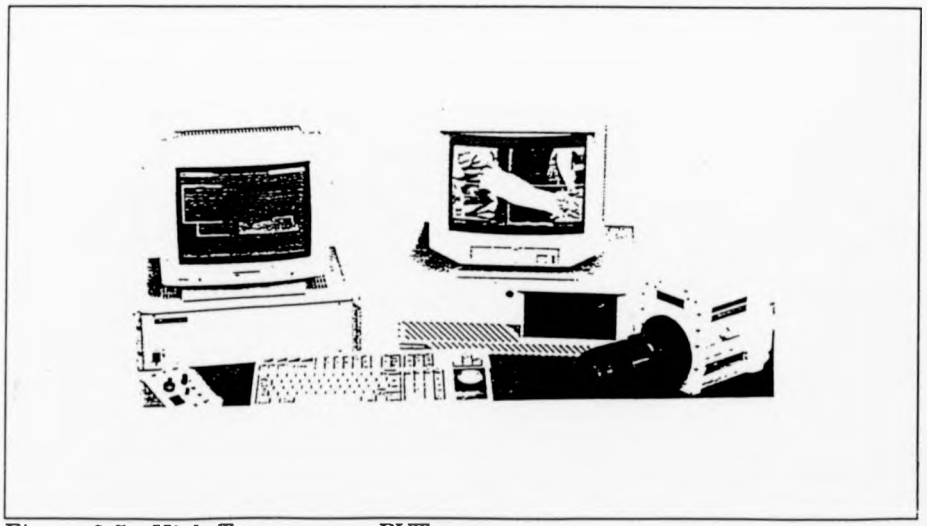

Figure 9.7: High Temperature PVT setup.

In the case of low temperature and high temperature (static) experiments a panosonic M10 video camera was used to defect detect a range of transmitted wavelengths from a pre-selected light source and pass the recorded images to a personal computer where it is stored, manipulated and input to a smart

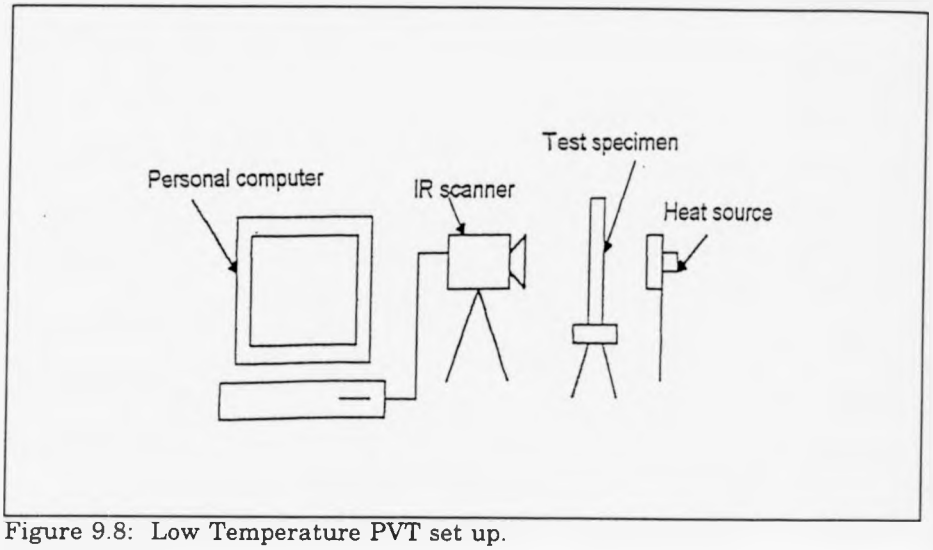

Figure 9.8: Low Temperature PVT set up.

classification and Neural Networks environment for analysis and interpretation. In the case of high temperature, a constant heating source is used to apply heat to the composite component. This heating source produces a far-field infrared heat waveform that travels through the sample with defects acting as obstacles to the flow of energy.

For pulse video thermography (PVT) the equipment used consisted of heat source and thermal imaging/analysis system. The heat source must be an adequately fast pulse, in order that there is a rapid temperature rise, since it is the steepness of the temperature gradient that provides the differential that is observed between defective and non-defective areas. This rapid rise is provided by discharging several Kilojoules of energy through each of two Xenon flash tubes, which are directed at the component under test. The thermal imaging part of the experiment was carried out using the TALYTHERM 90

system with the TICM 2B thermal imager produced by Rank Taylor Hobson. The thermal event was recorded directly on a video tape, and the analysis is then performed from the recorded image on a personal computer by interfacing the video recorder to the computing hardware.

The PVT experiments were carried out at AEA Technology, Harwell, Oxfordshire.

9.5 Processing and Analysis System.

(A) Image Processing

Image capture and digitization from all image producing NDT techniques was carried out using the MICROEYE 1C MK2 hardware and software which operates within the windows software environment. This image processing system was supplied by Digithurst Limited. This system is versatile and allows the following choices:

(1) Electronic focusing of the image to be captured.

(2) Brightness, saturation, contrast, hue and threshold adjustment.

(3) Displaying in:

(a) Diffused (b) Mono (c) Optimised

(d) Black and White

(4) Size bitmap stretching.

(5) Compatible with PAL, NTSC and Canon ION

(6) Operates on both RGB and composite signals.

(7) Operate on either single field or frame.

(8) Having the facility of filtering signals and address selection.

(B) Data Processing and Interpretation

For all the digitized images and other types of data inputs from other detecting instruments, a software in C-language is written for both data processing and smart classification which also work in conjunction with a standard Neural Network software package supplied by NCS Limited. The Neural Network software provides the following options:

(1) An interface program that provides the facility to design, train and run a neural net automatically from a set of data input in spreadsheet format.

(2) A network editor with which a design can manually be created and existing neural nets edited.

(3) A run time processor, controlled by external programs such as a database or spreadsheet, which supervises the processing and interfacing of the neural net.

CHAPTER 10

EXPERIMENTAL RESULTS.

In this chapter important results are presented and referred to in the next chapter for the purpose of discussion. In the table below are the spread or deviation values of the mean of data used for analysis with all curves fitted to a second order Quadratic equation. The search through of images was carried out from -255 to +255 instead of 0 to 511.

APPLICATION (NDT TECHNIQUE)	**NO. OF SAMPLES PER DATA POINT.**	**DEVIATION OR ERROR.**
LOW FREQUENCY.	30 POINTS.	+/- 4.5%
C-SCAN.	06 IMAGES.	+/- 4.0%
VISUAL IMAGING.	06 IMAGES.	+/- 3.5%
H.T.P.V.T.	06 IMAGES.	+/- 3.1%
L.T.P.V.T.	06 IMAGES.	+/- 2.6%

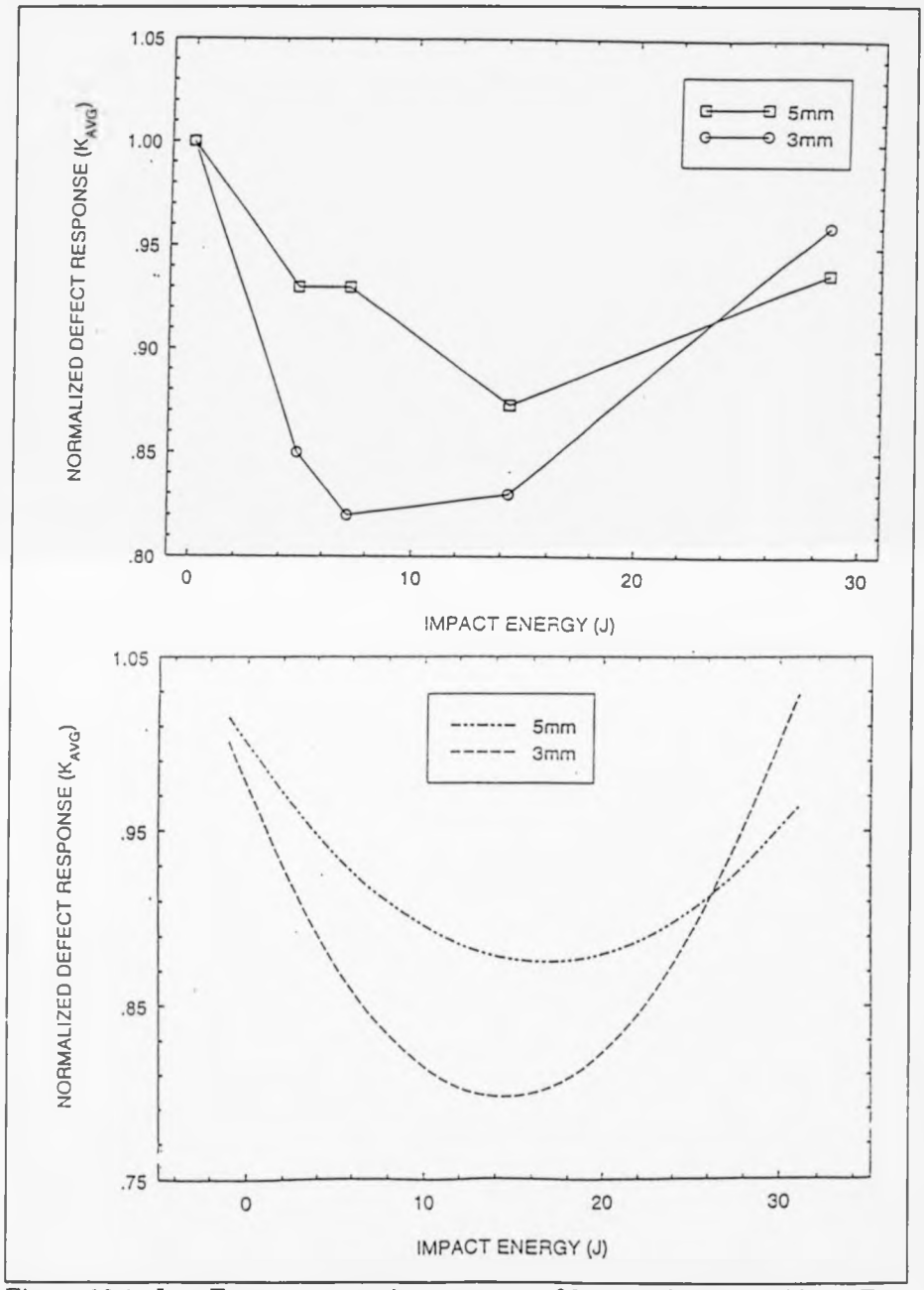

Figure 10.1: Low Frequency tapping response of 3mm and 5mm W.Glass. Top: Experimental. Bottom: Fitted. (Mean of 30 points).

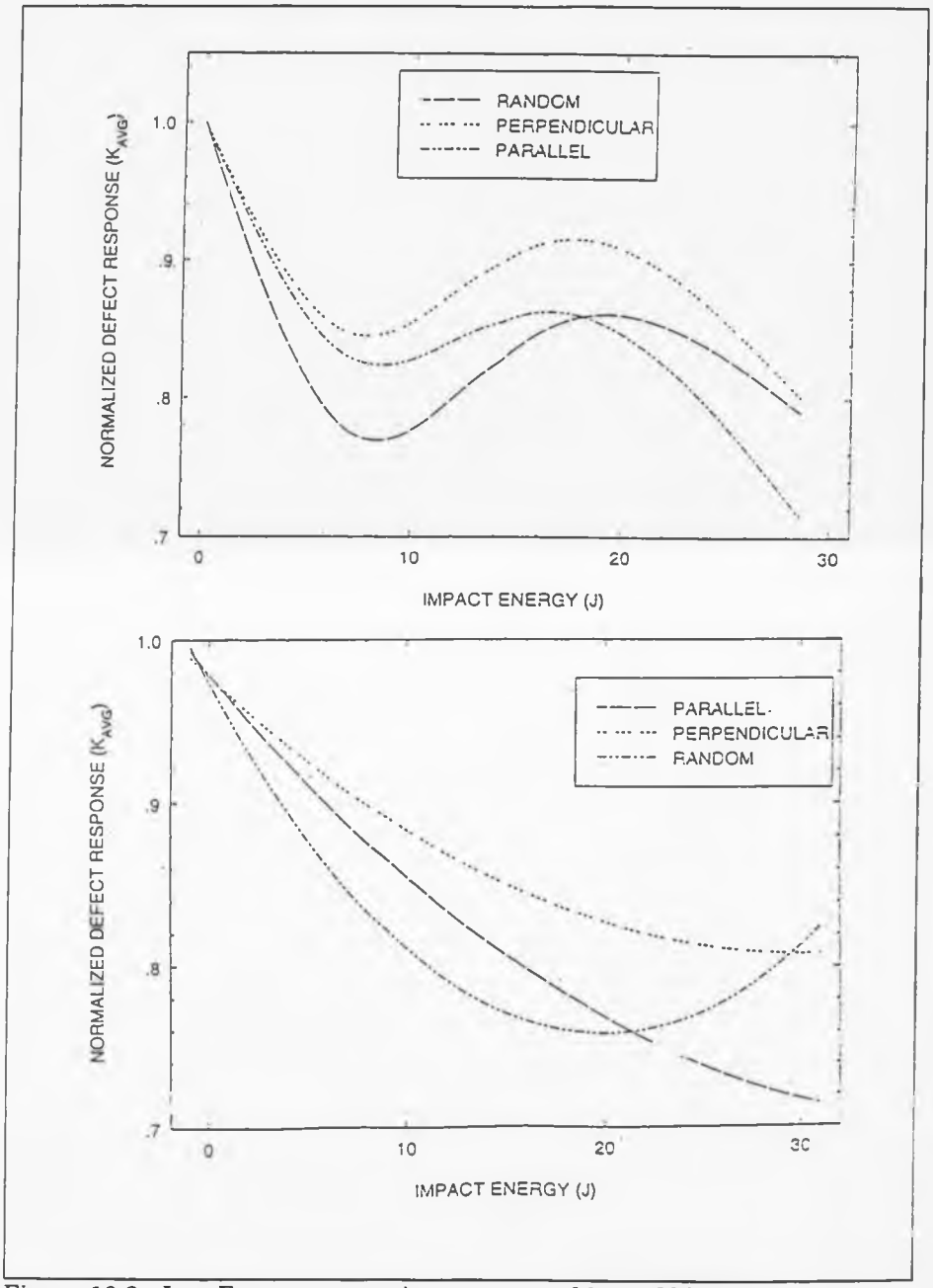

Figure 10.2: Low Frequency tapping response of 3mm GMT. Top: Experimental. Bottom: Fitted. (Mean of 30 points).

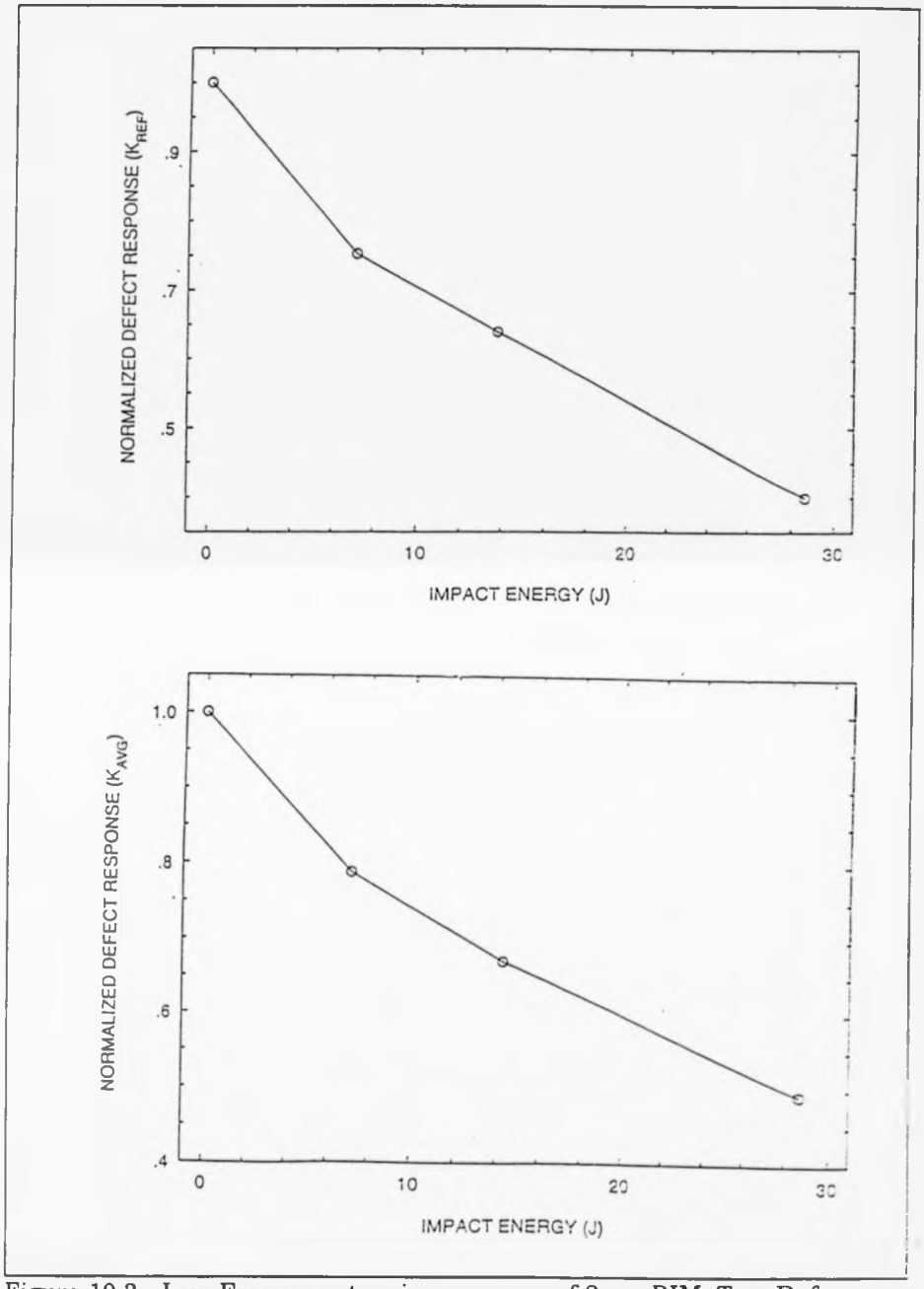

Figure 10.3: Low Frequency tapping response of 2mm RIM. Top: Reference factor. Bottom: Average factor. (Mean of 30 points).

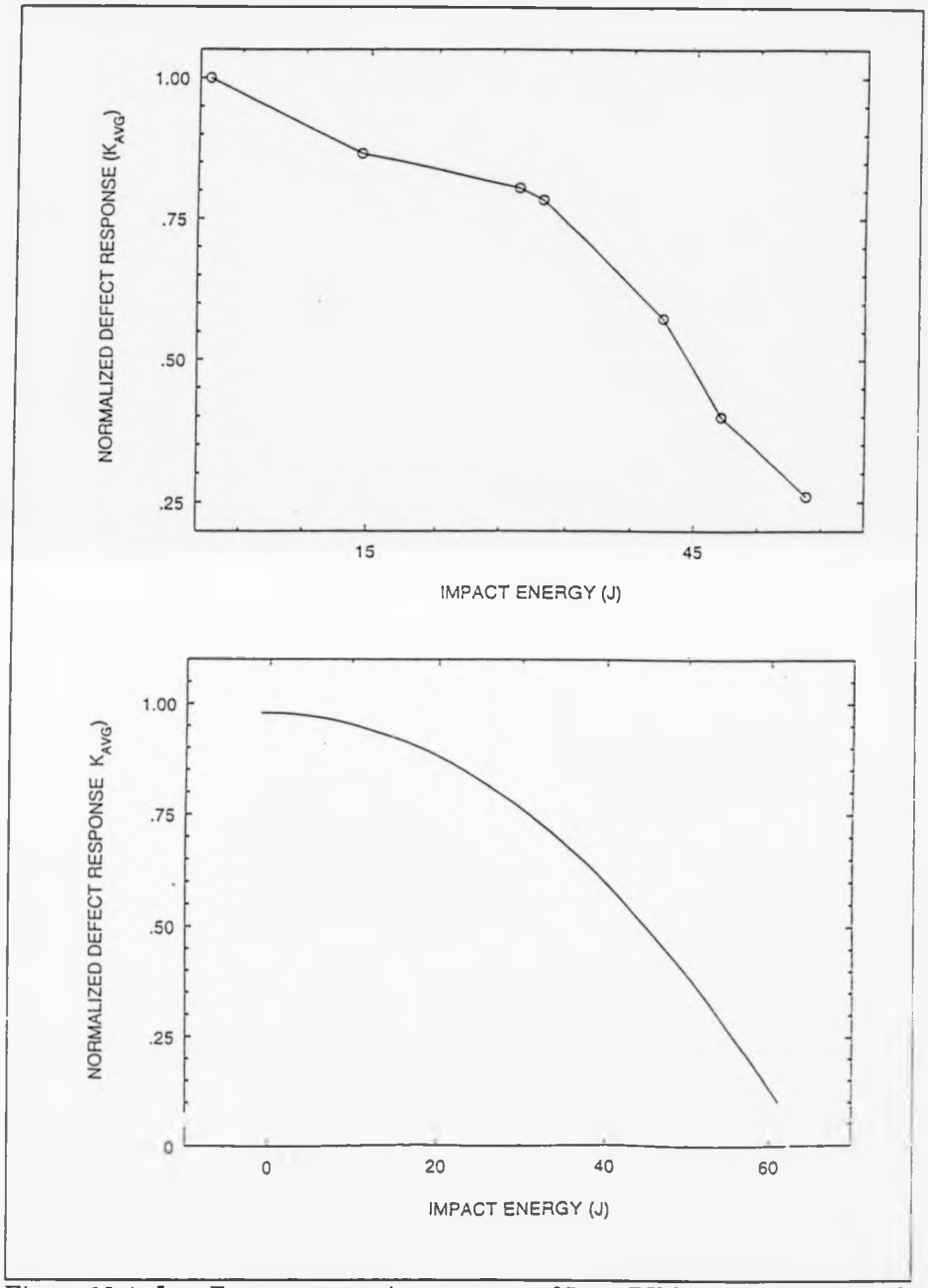

Figure 10.4: Low Frequency tapping response of 5mm RIM. Top: Experimental. Bottom: Fitted. (Mean of 30 points).

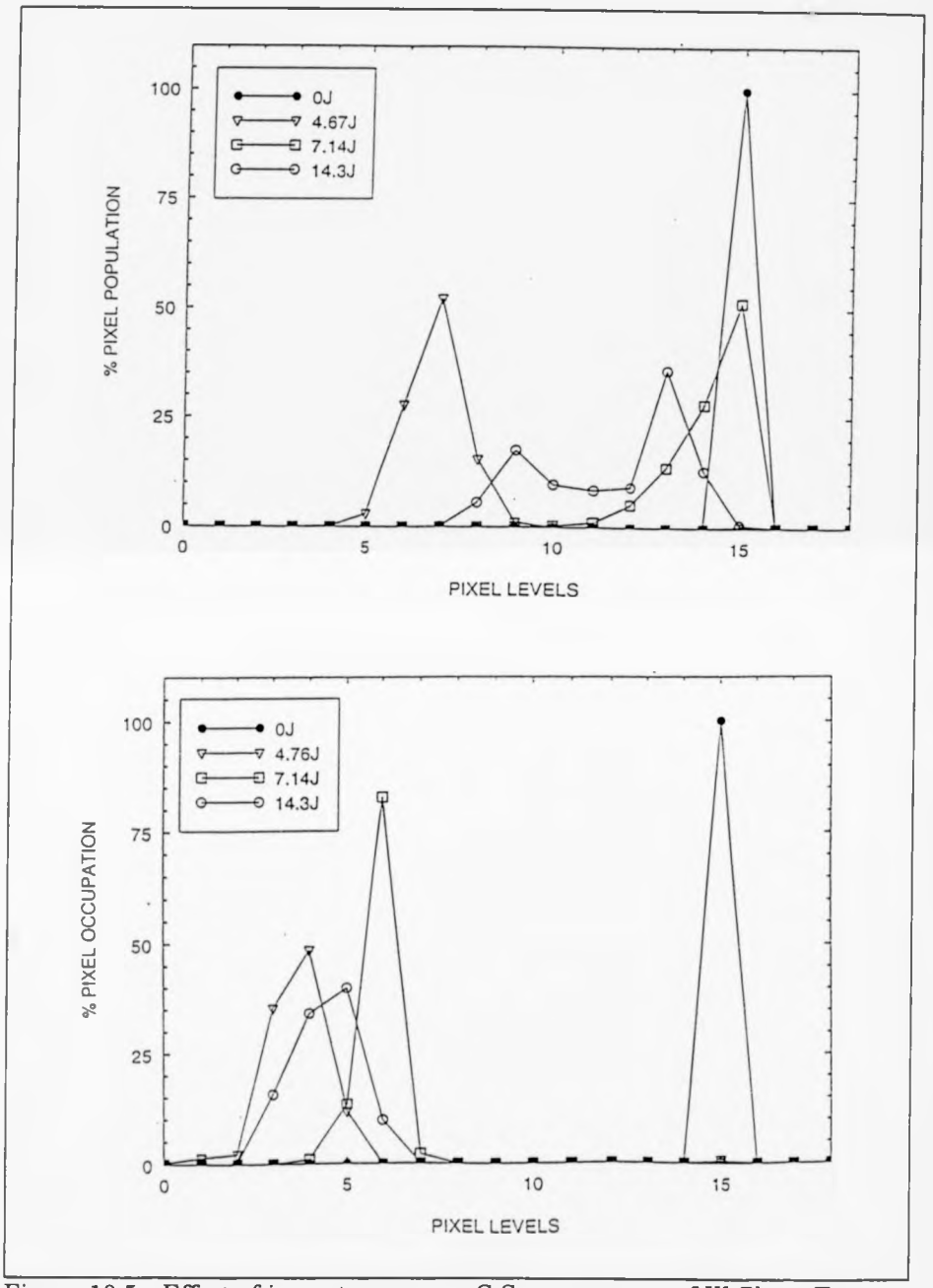

Figure 10.5: Effect of impact energy on C-Scan response of W.Glass. Top: 3mm. Bottom: 5mm. (Mean of 6 images).

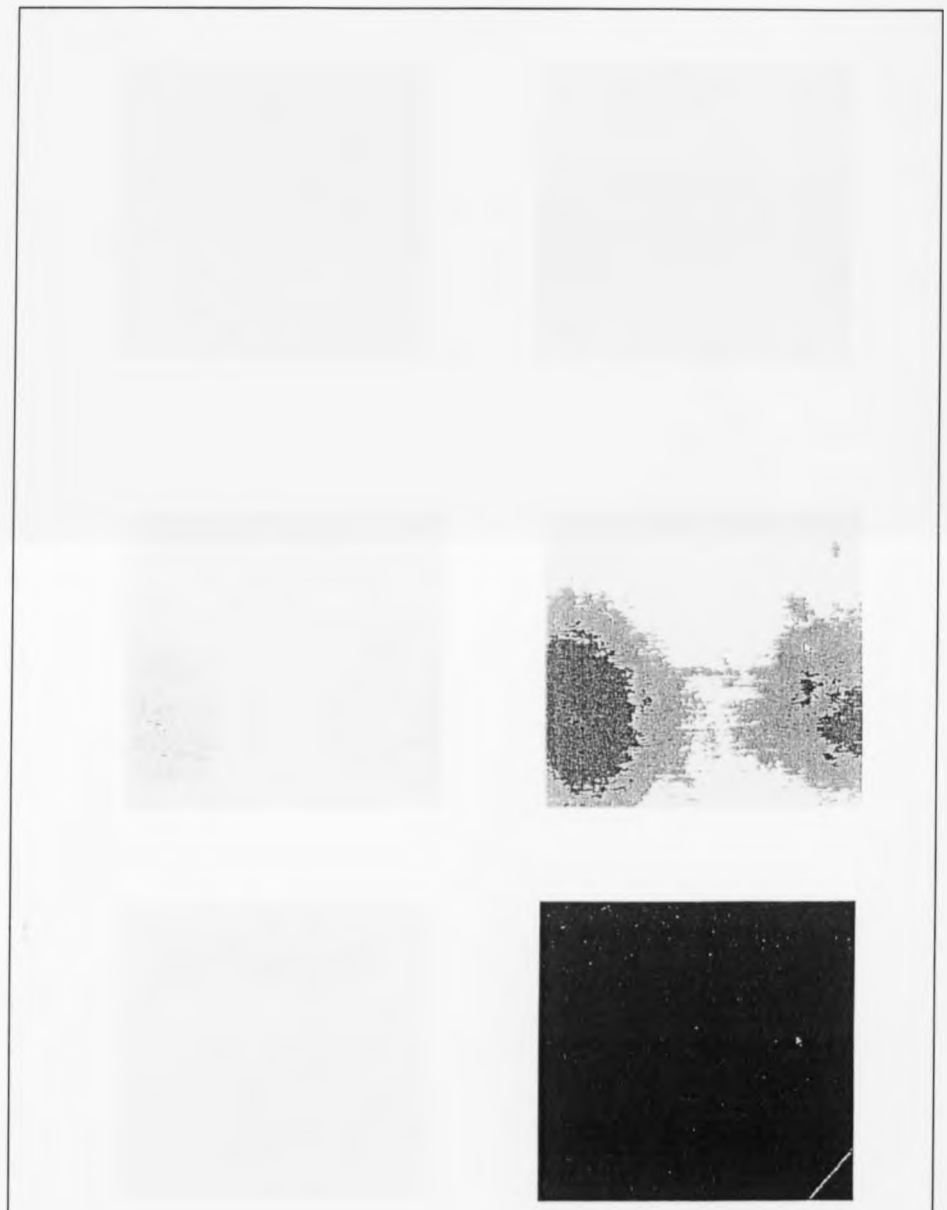

Figure 10.6: C-Scan images of 5mm W.Glass impacted at 14.3J using Search Through Technique. (Cycles 1-6, left to right).

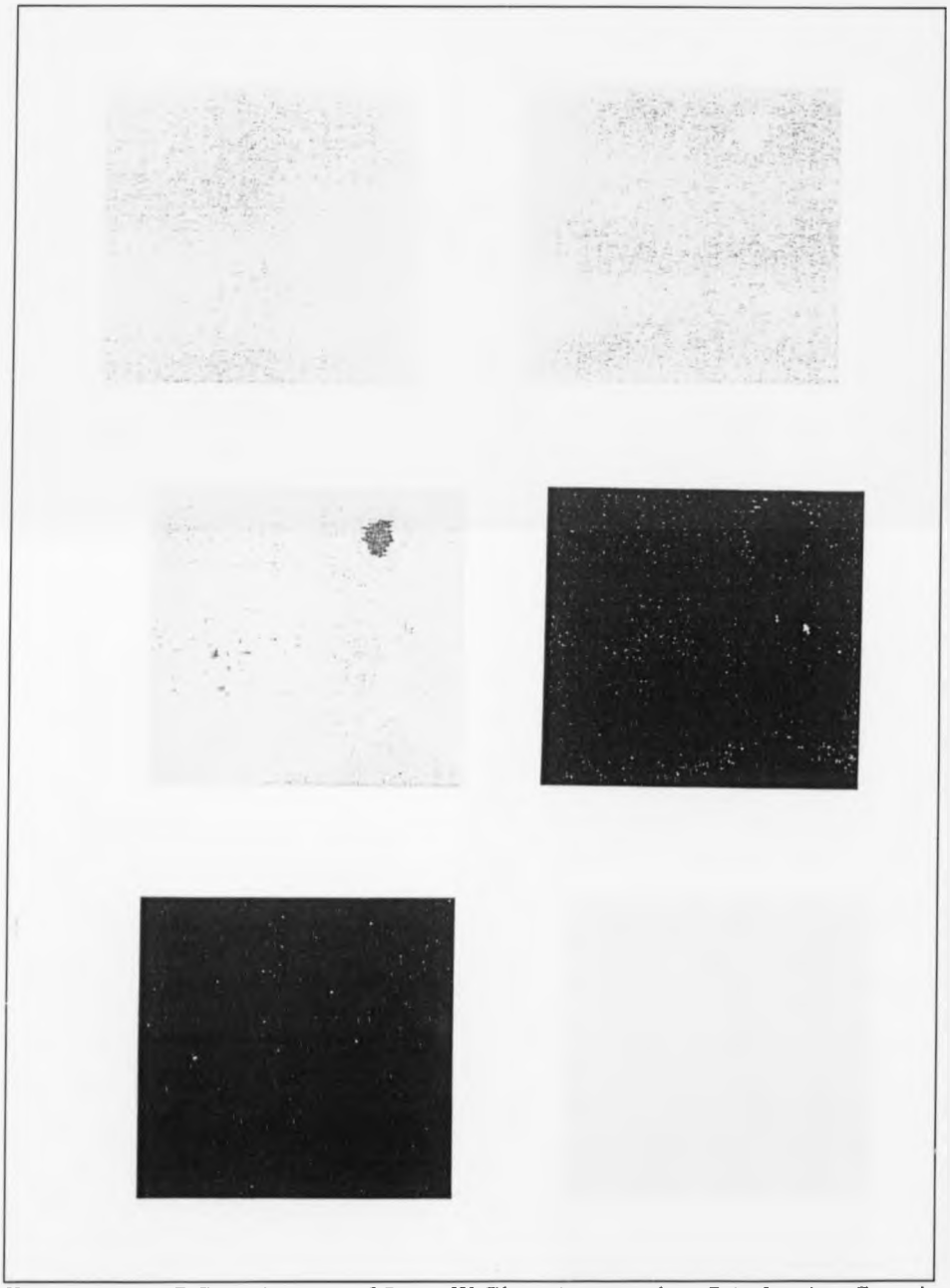

Figure 10.7: C-Scan images of 5mm W.Glass impacted at 7.14J using Search Through technique. (Cycles 1-6, left to right).

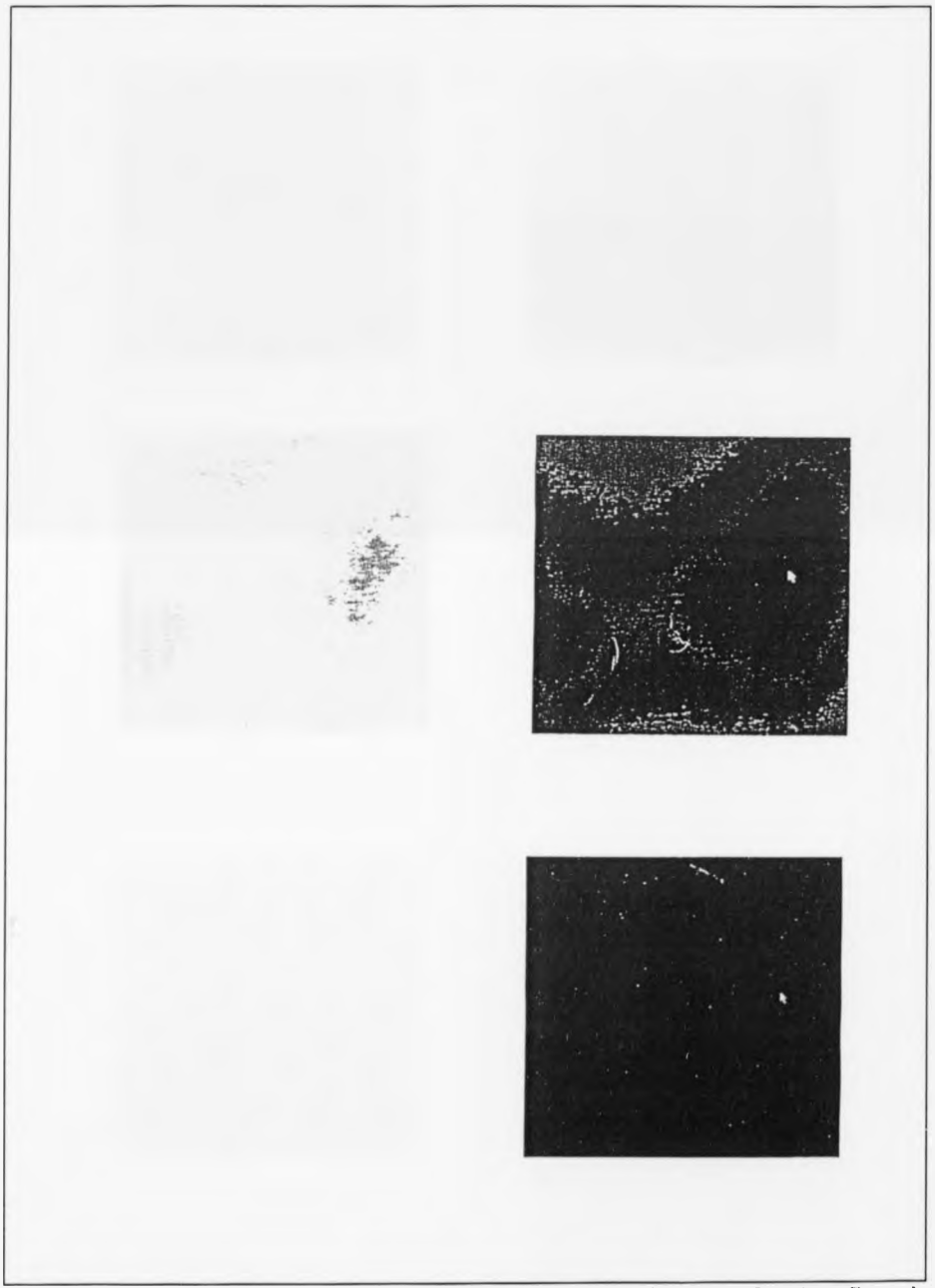

Figure 10.8: C-Scan images of 5mm W.Glass impacted at 4.76J using Search Through technique. (Cycles 1-6, left to right).

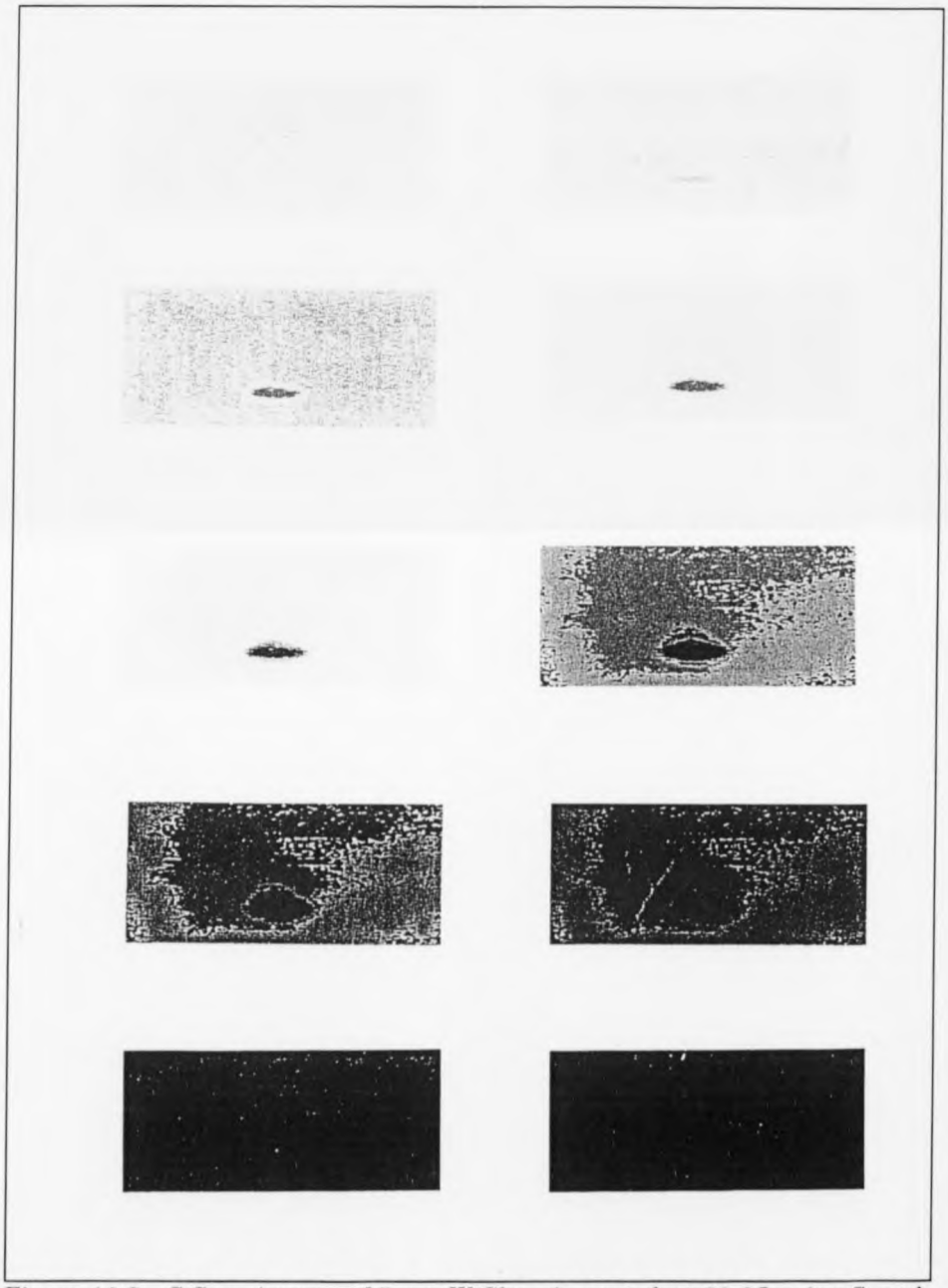

Figure 10.9: C-Scan images of 5mm W.Glass impacted at 28.6J using Search Through technique. (Cycles 1-10, left to right).

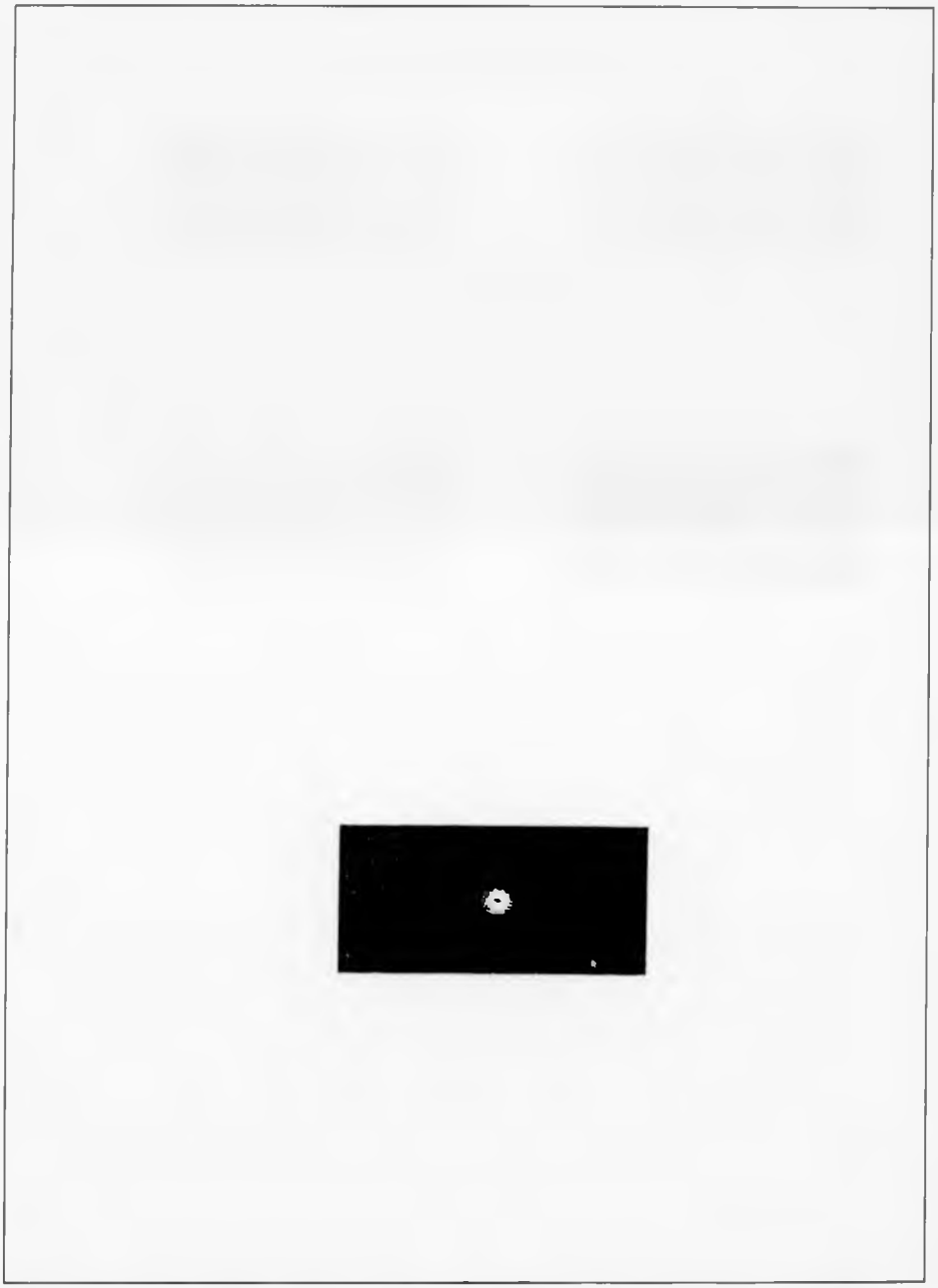

Figure 10.10: C-Scan images of 5mm W.Glass with a hole using Search Through technique. (Cycles 1-5, left to right).

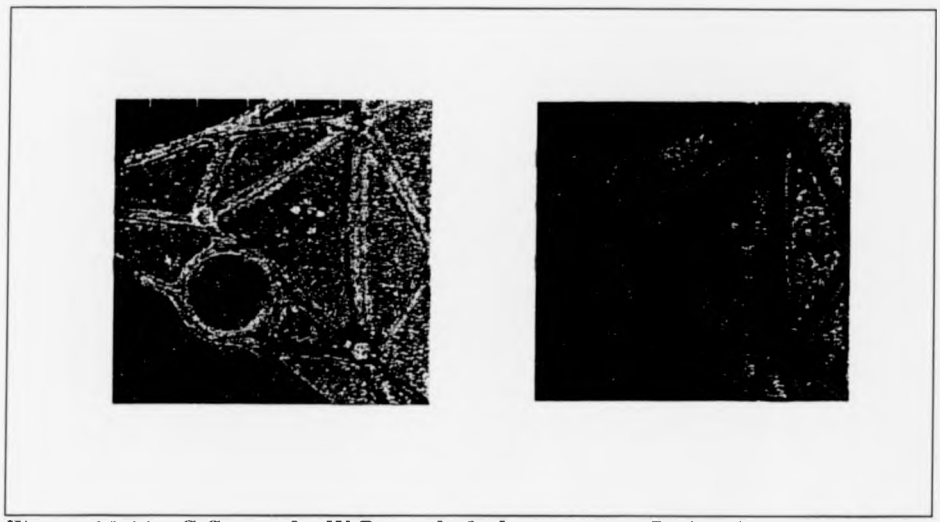

Figure 10.11: C-Scan of a W.Bone. Left: Inner parts. Right: Outer parts. (6 images mean).

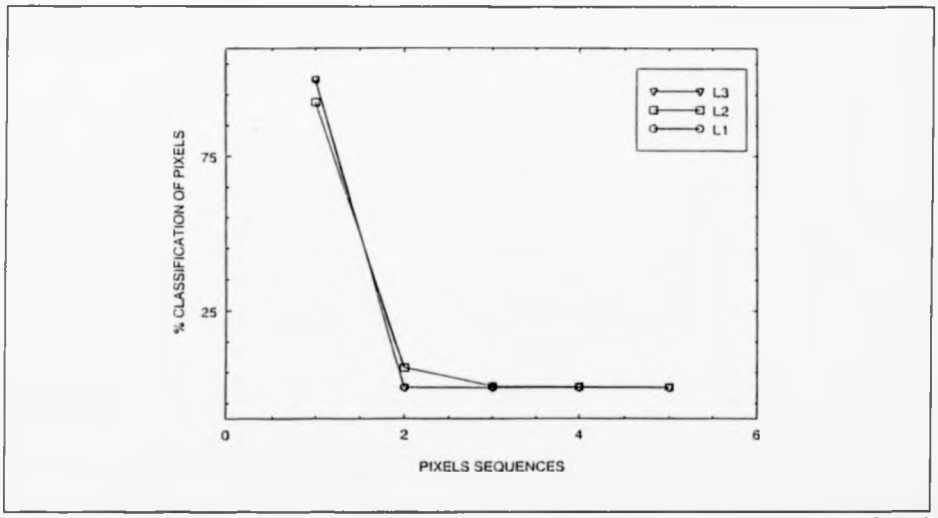

Figure 10.12: First stage classification of 5mm W.Glass impacted at 4.76J and tested using Low Temperature Visual Camera. (Mean of 6 images)

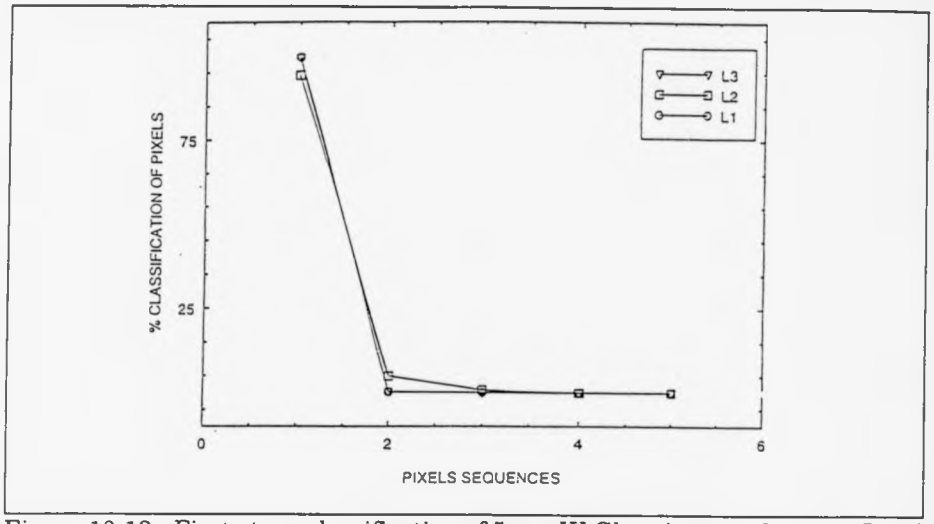

Figure 10.13: First stage classification of 5mm W.Glass impacted at 7.14J and tested using Low Temperature Visual Camera. (6 images mean).

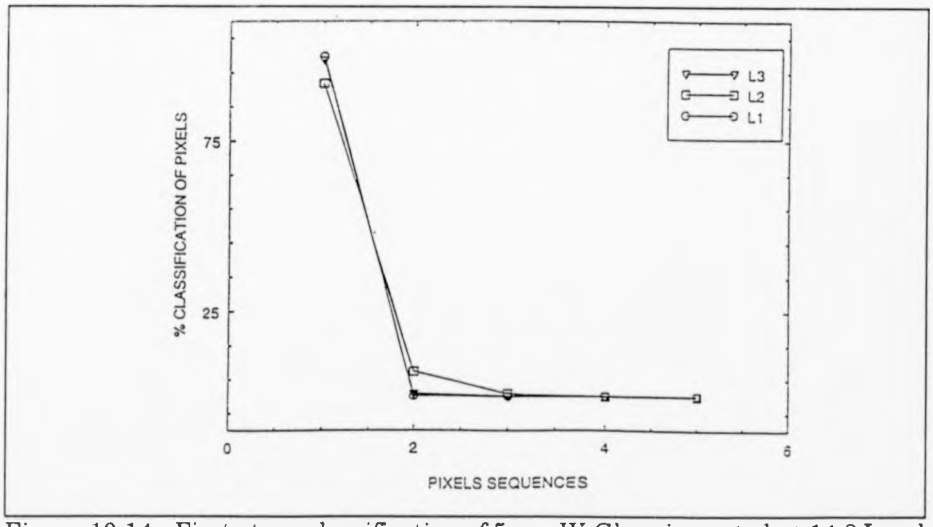

Figure 10.14: First stage classification of 5mm W.Glass impacted at 14.3J and tested using Low Temperature Visual Camera. (6 images mean.)

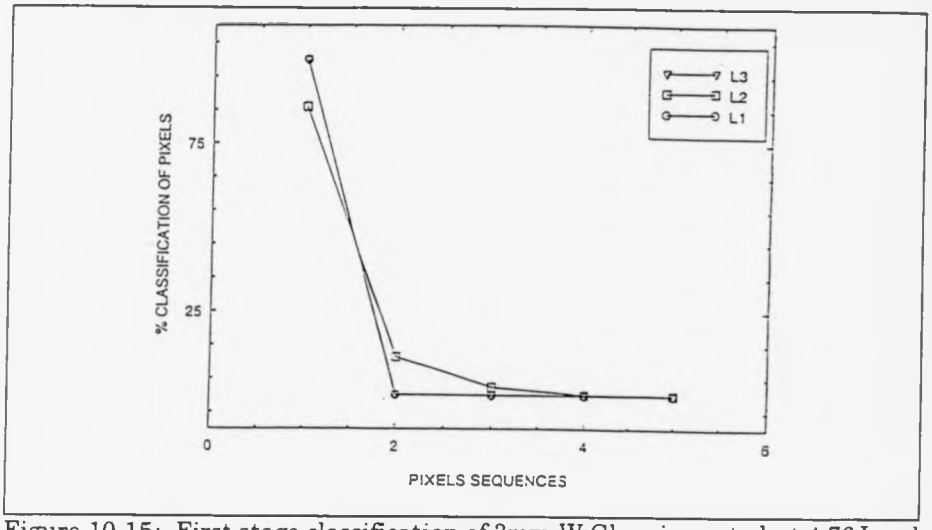

Figure 10.15: First stage classification of 3mm W.Glass impacted at 4.76J and tested using Low Temperature Visual Camera. (6 images mean).

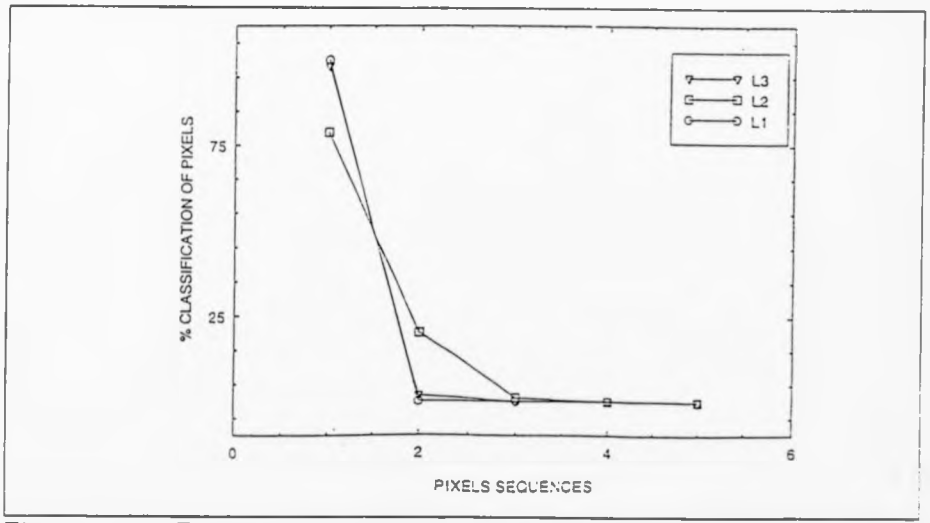

Figure 10.16: First stage classification of 3mm W.Glass impacted at 7.14J and tested using Low Temperature Visual Camera. (6 images mean).

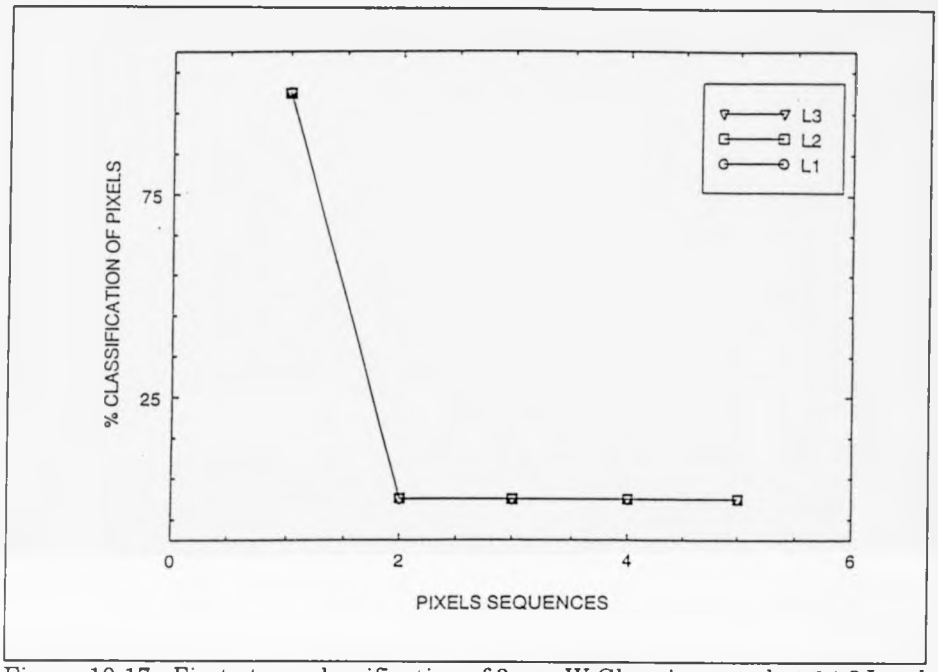

Figure 10.17: First stage classification of 3mm W.Glass impacted at 14.3J and tested using Low Temperature Visual Camera. (6 images mean).

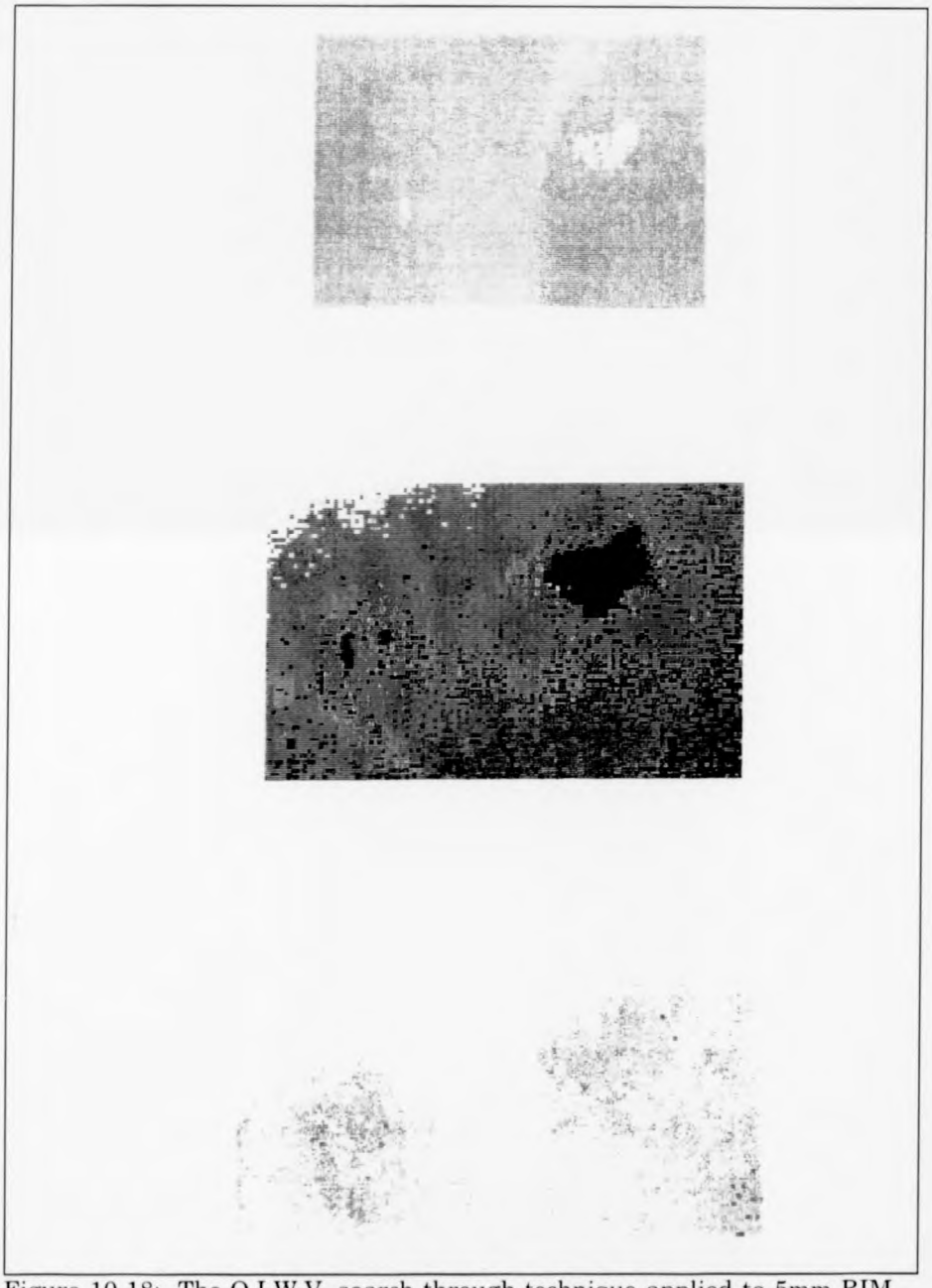

Figure 10.18: The O.I.W.V. search through technique applied to 5mm RIM impacted at 28.6J and 42J. (Cycles 1-3).

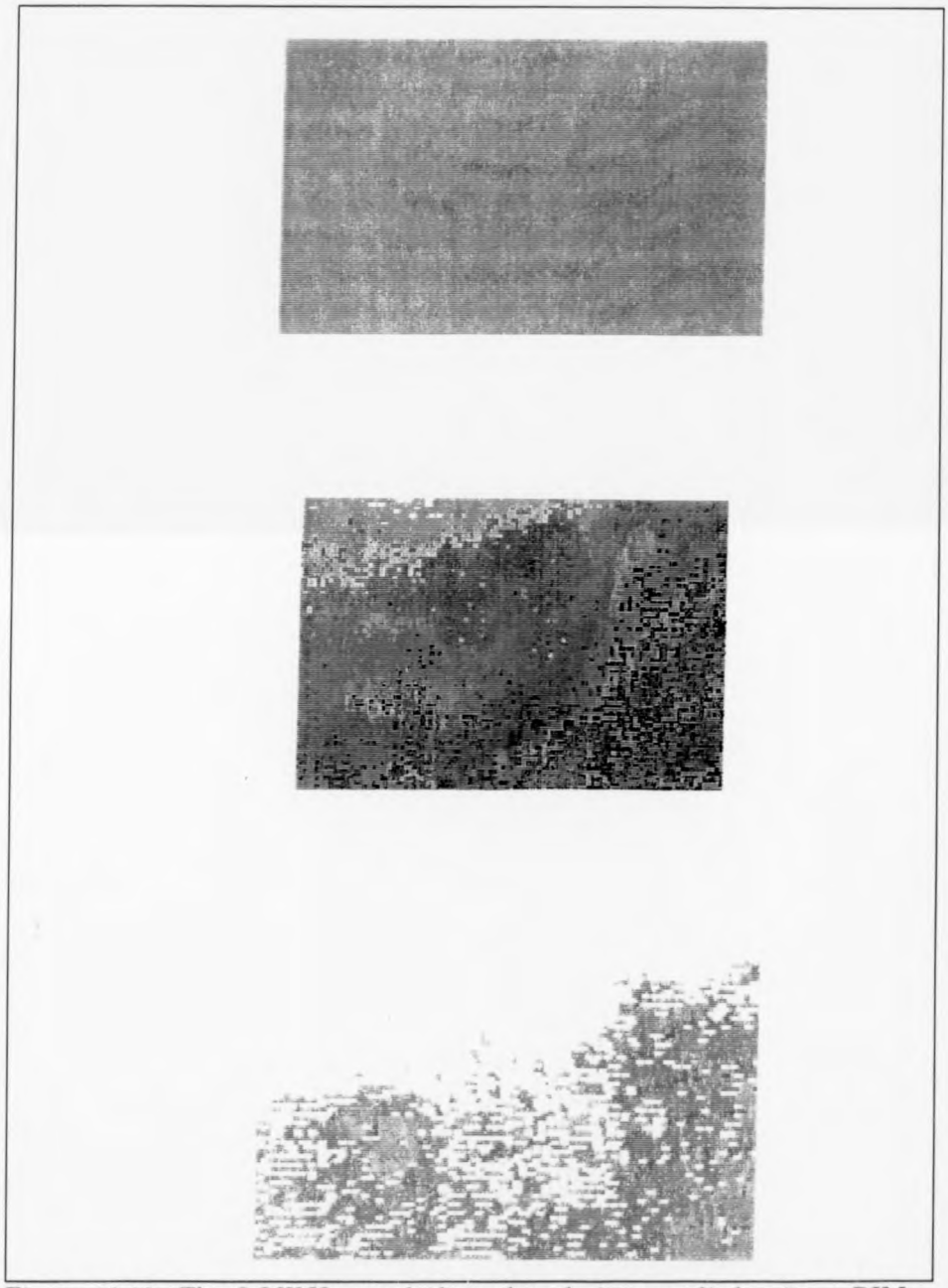

Figure 10.19: The O.I.W.V. search through technique applied to 5mm RIM impacted at 14.3J and 30.8J. (Cycles 1-3).

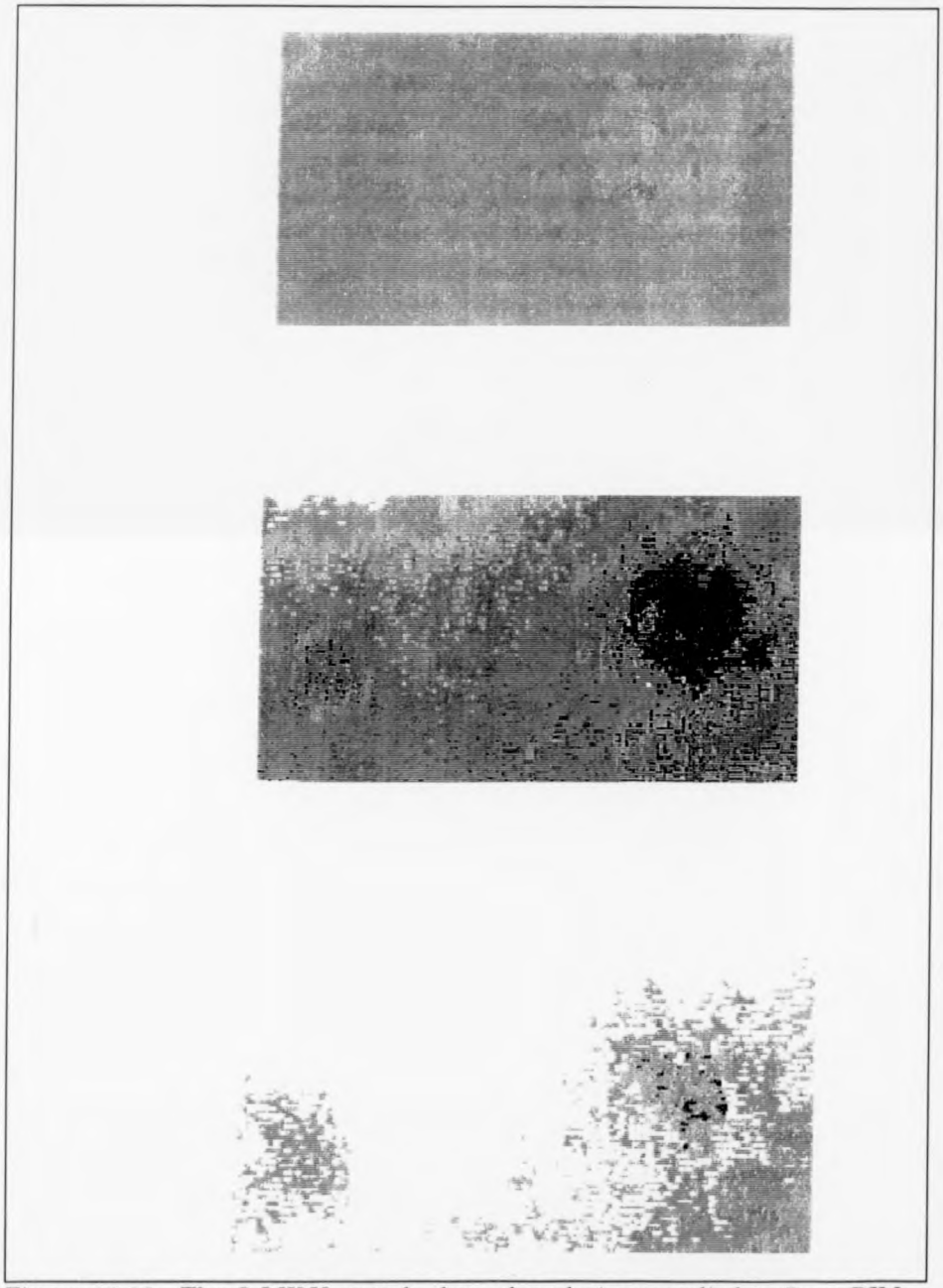

Figure 10.20: The O.I.W.V. search through technique applied to 5mm RIM impacted at 28.6J and 28.6J with angle. (Cycles 1-3).

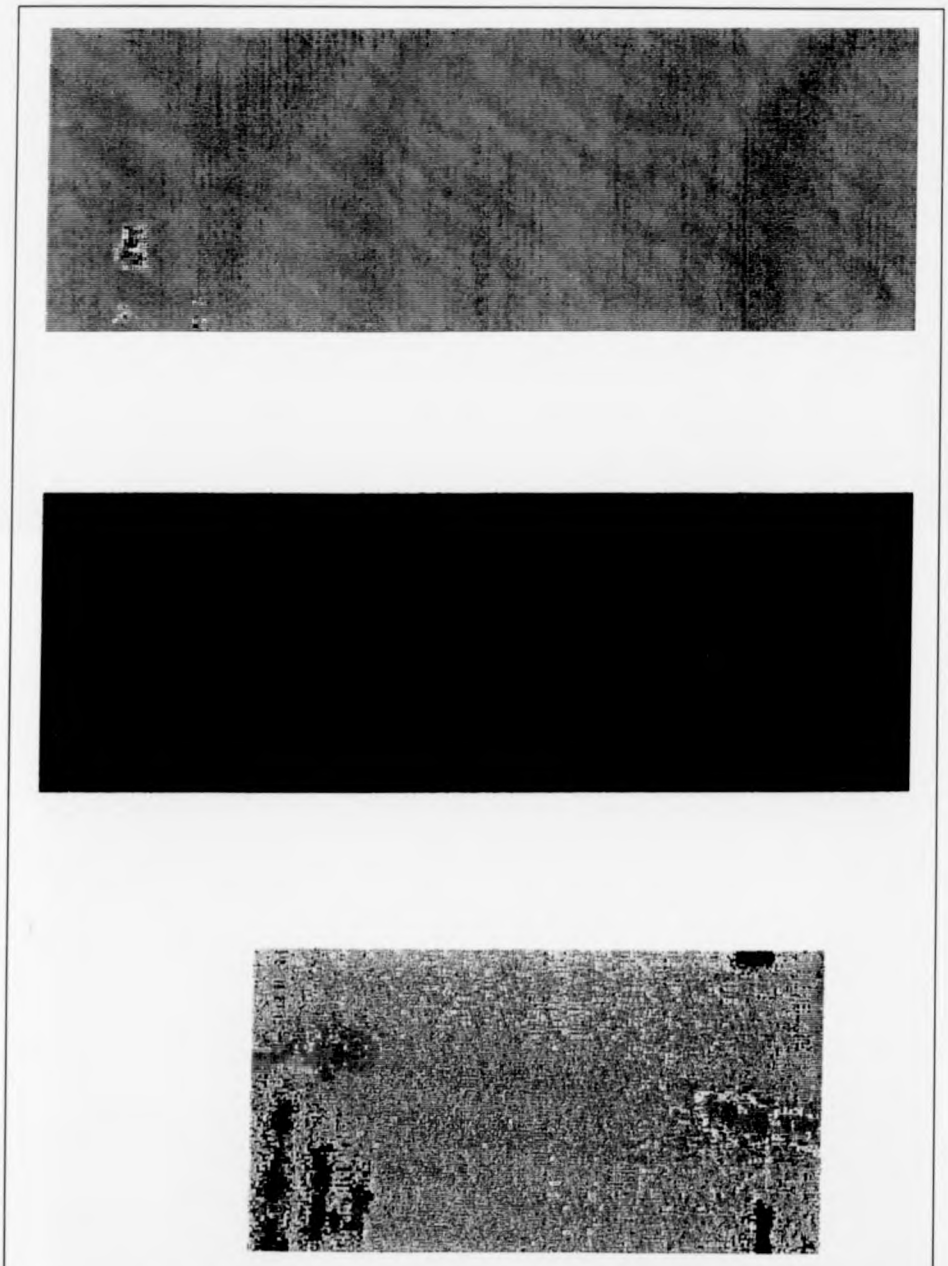

Figure 10.21: The O.I.W.V. search through technique applied to 5mm RIM impacted at 47.6J with reflective paint. (Cycles 1-3).

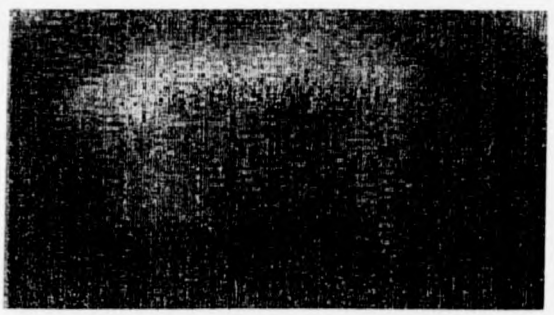

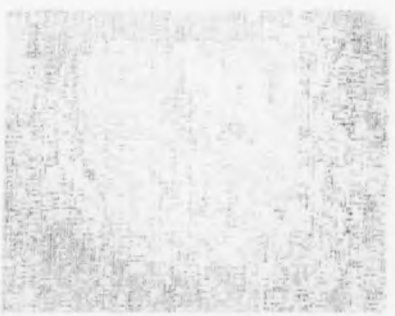

Figure 10.22: The O.I.W.V. search through technique applied to 5mm RIM impacted at 55.6J with reflective paint and part extraction. (Cycles 1-3).

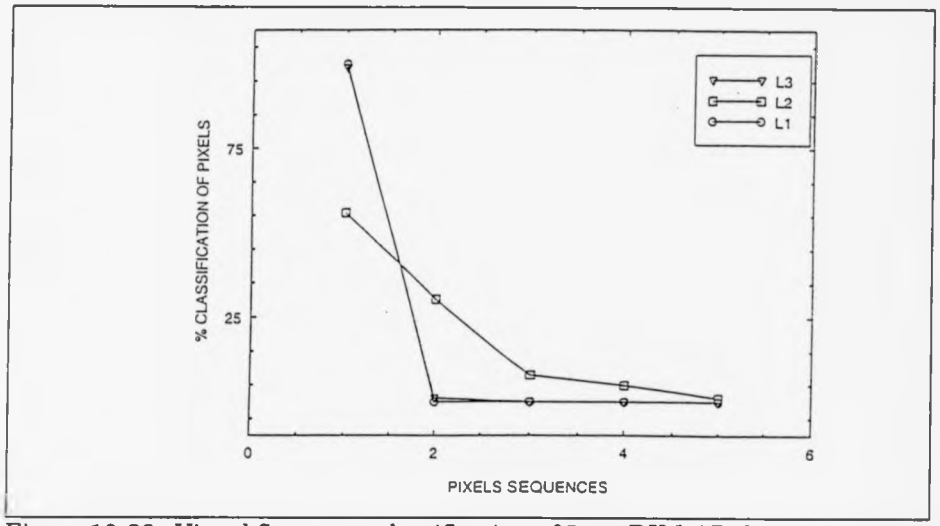

Figure 10.23: Visual first stage classification of 5mm RIM. (Reference sample). (Mean of 6 images).

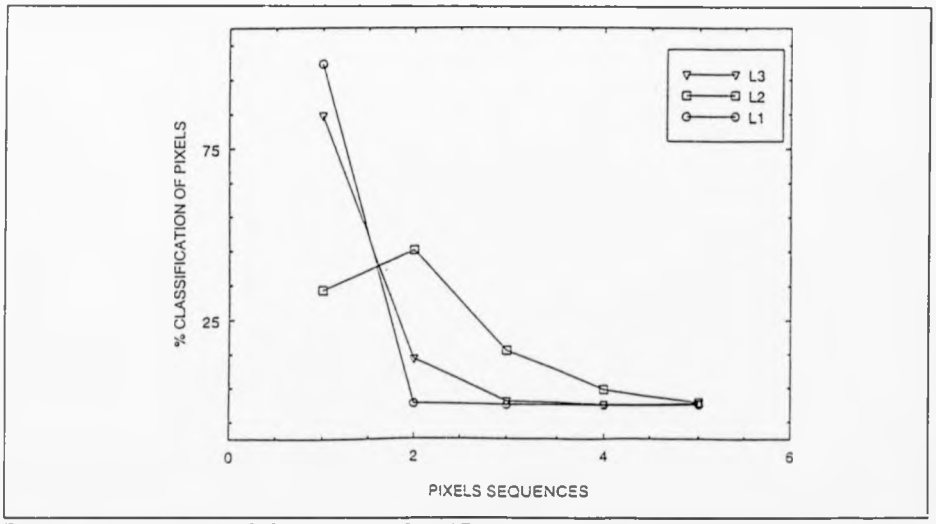

Figure 10.24: Visual first stage classification of 5mm RIM impacted at 14.3J and 30.8J. (Mean of 6 images).

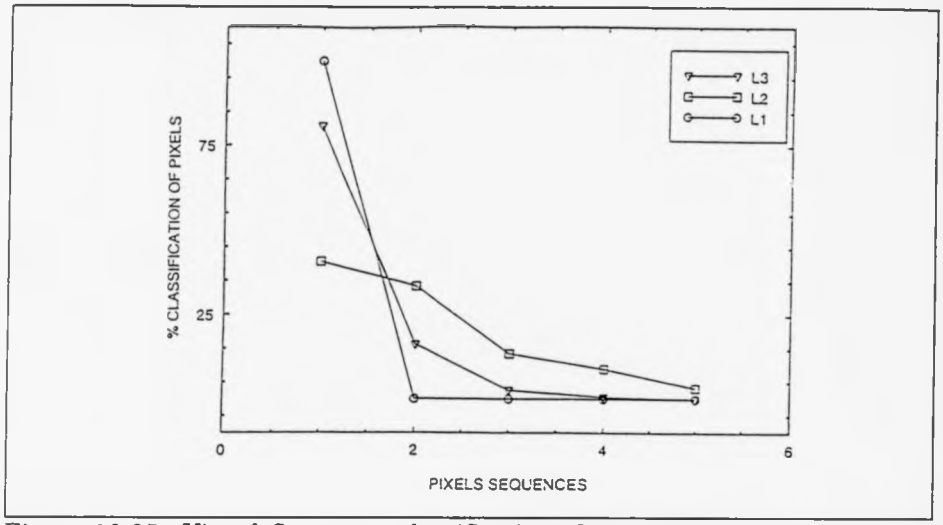

Figure 10.25: Visual first stage classification of 5mm RIM impacted at 28.6J and 28.6J with load angle. (Mean of 6 images).

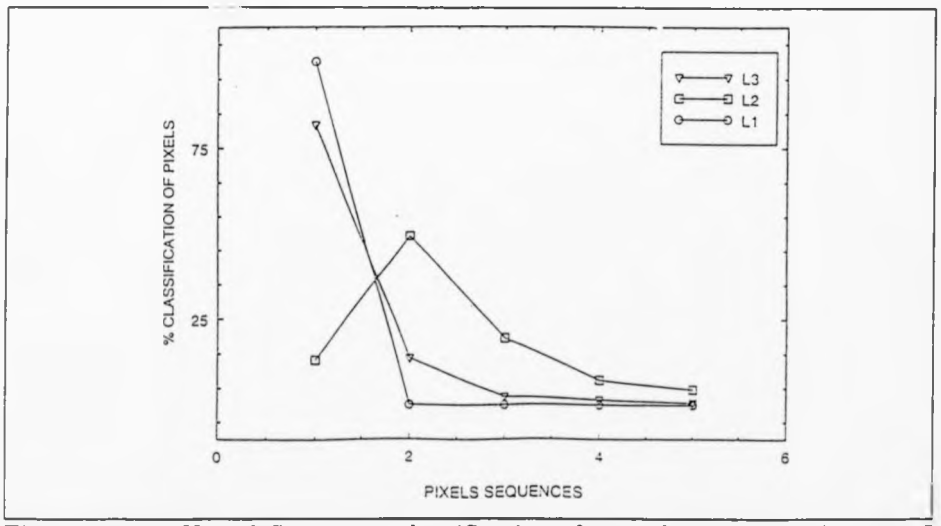

Figure 10.26: Visual first stage classification of 5mm RIM impacted at 28.6J and 42J. (Mean of 6 images).

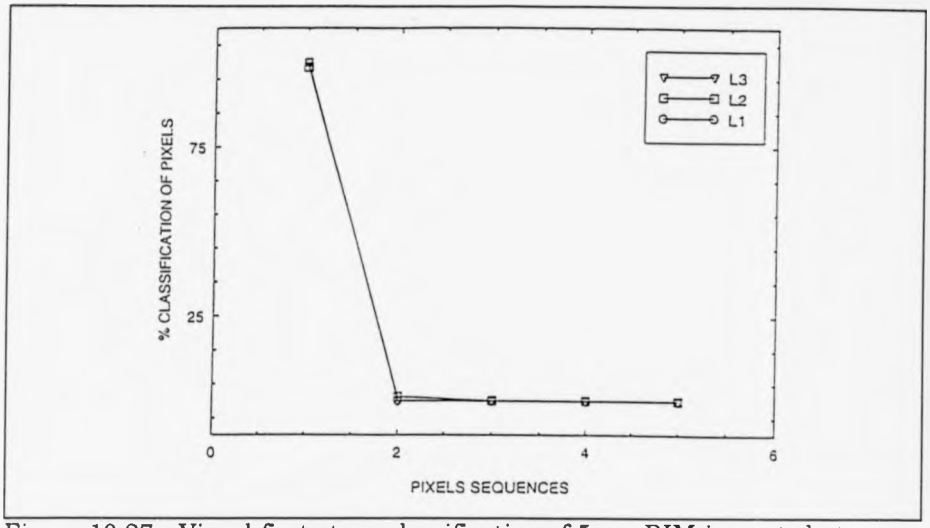

Figure 10.27: Visual first stage classification of 5mm RIM impacted at 47.6J and 47.6J. (Mean of 6 images).

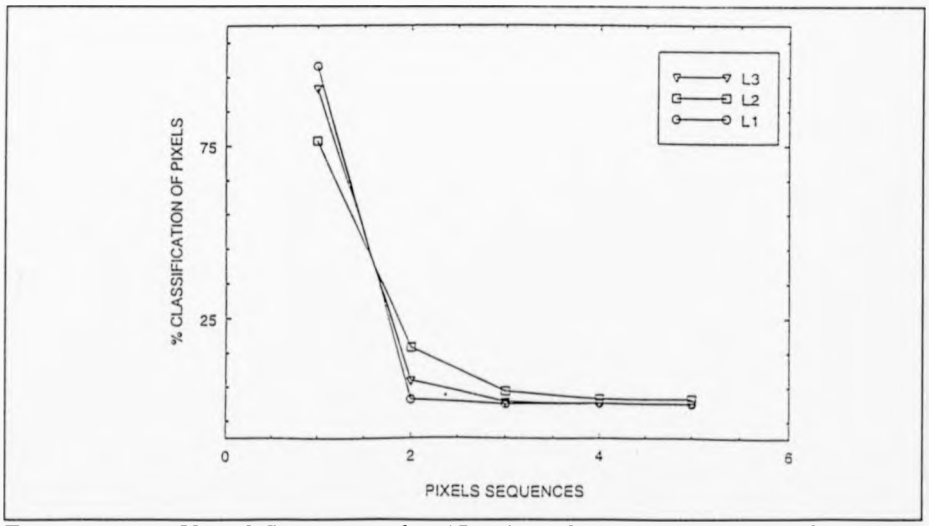

Figure 10.28: Visual first stage classification of 5mm RIM impacted at 55.6J with reflective paint and part extraction. (6 images mean).

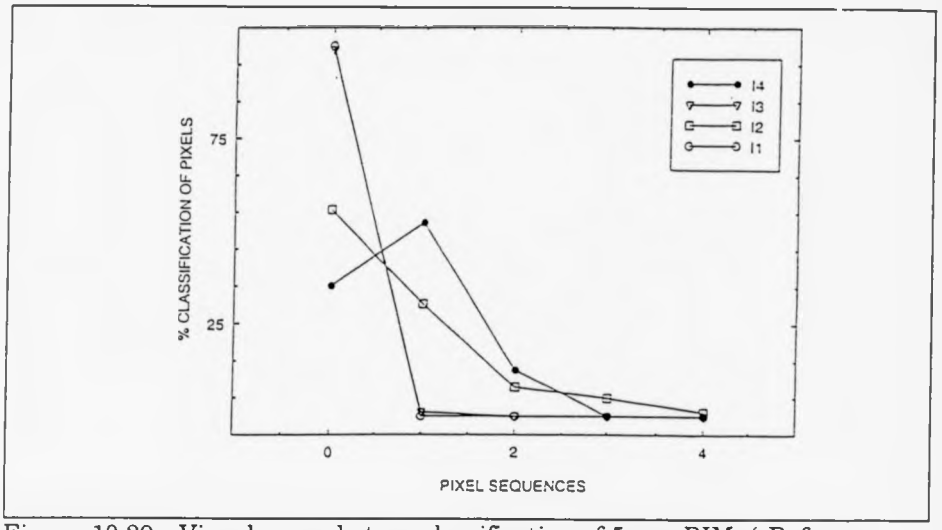

Figure 10.29: Visual second stage classification of 5mm RIM. (Reference sample). (Mean of 6 images).

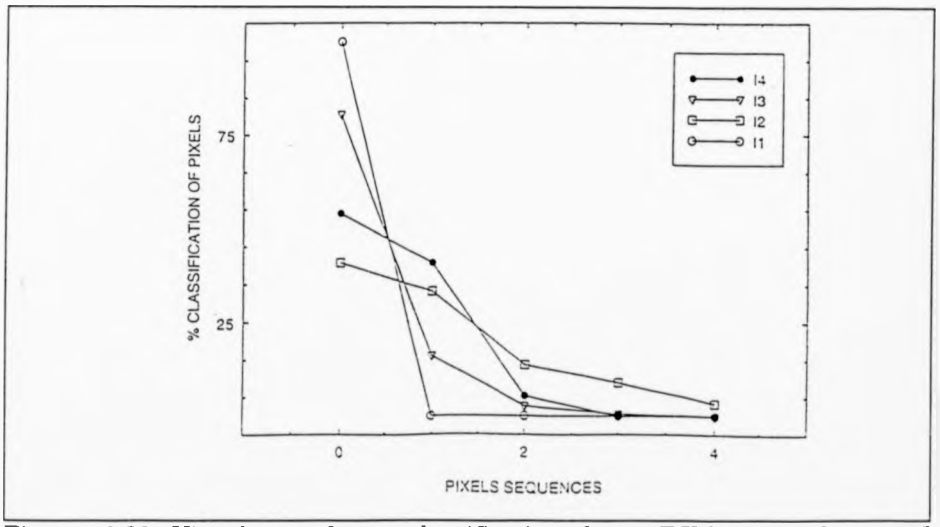

Figure 10.30: Visual second stage classification of 5mm RIM impacted at 14.3J and 30.8J. (Mean of 6 images).

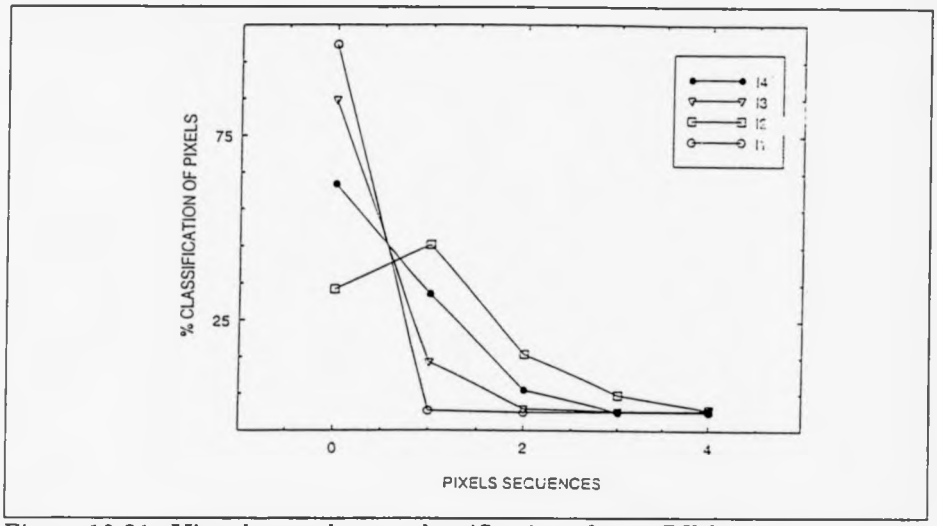

Figure 10.31: Visual second stage classification of 5mm RIM impacted at 28.6J and 28.6J with load angle. (Mean of 6 images).

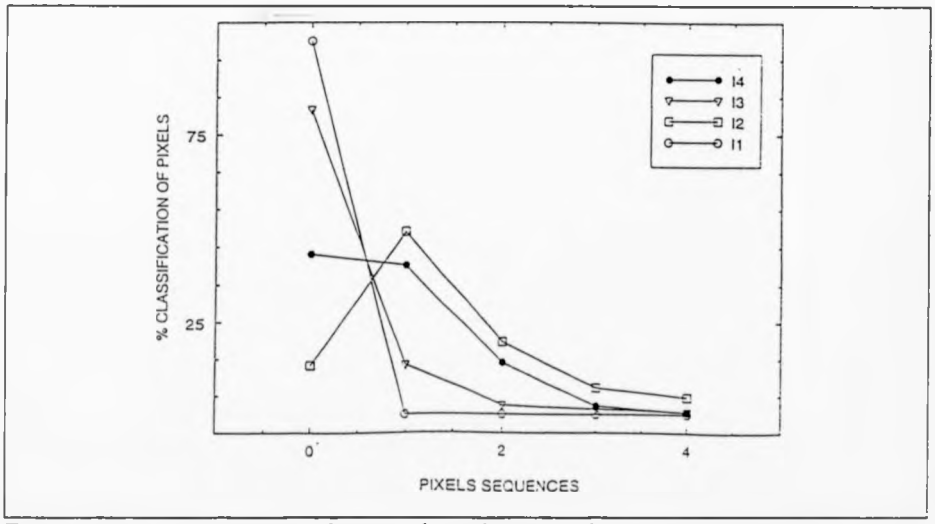

Figure 10.32: Visual second stage classification of 5mm RIM impacted at 28.6J and 42J. (Mean of 6 images).

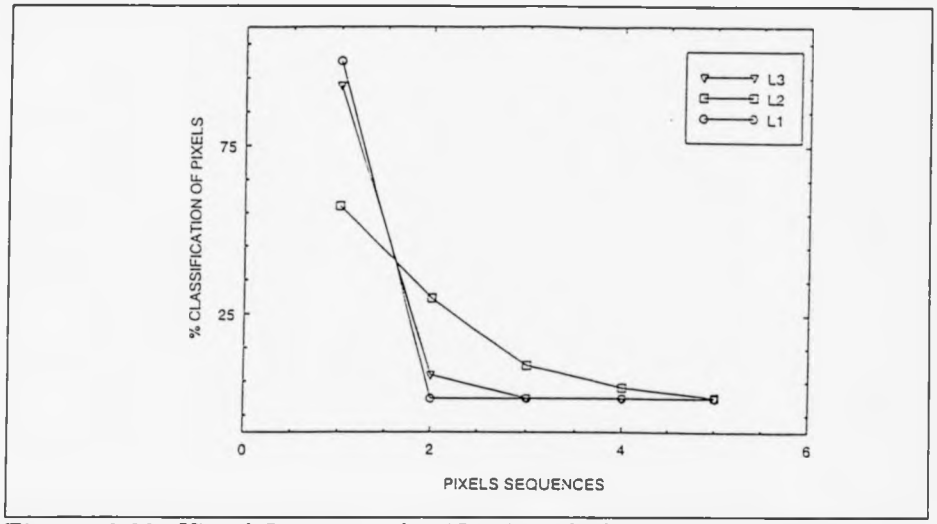

Figure 10.33: Visual first stage classification of 5-layers, 5mm RIM. (Mean of 6 images)

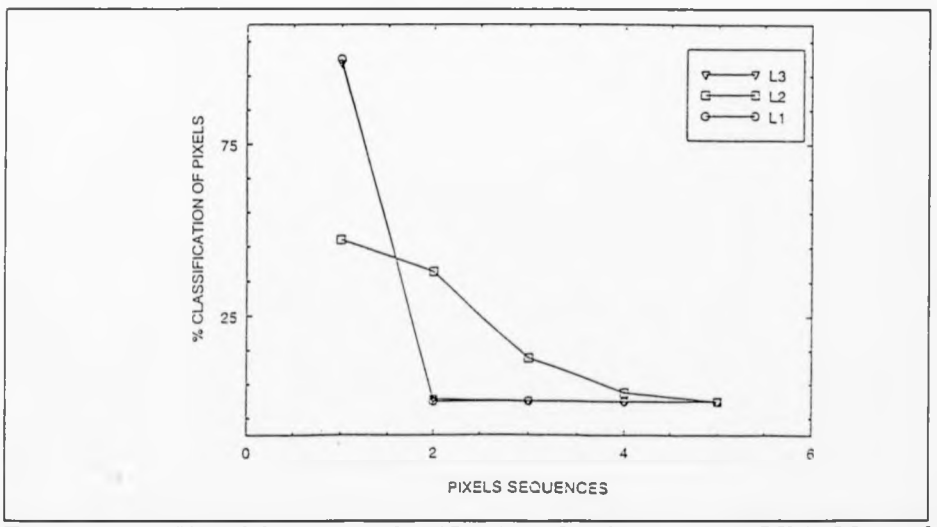

Figure 10.34: Visual first stage classification of 10-layers, 5mm RIM. (Mean of 6 images).

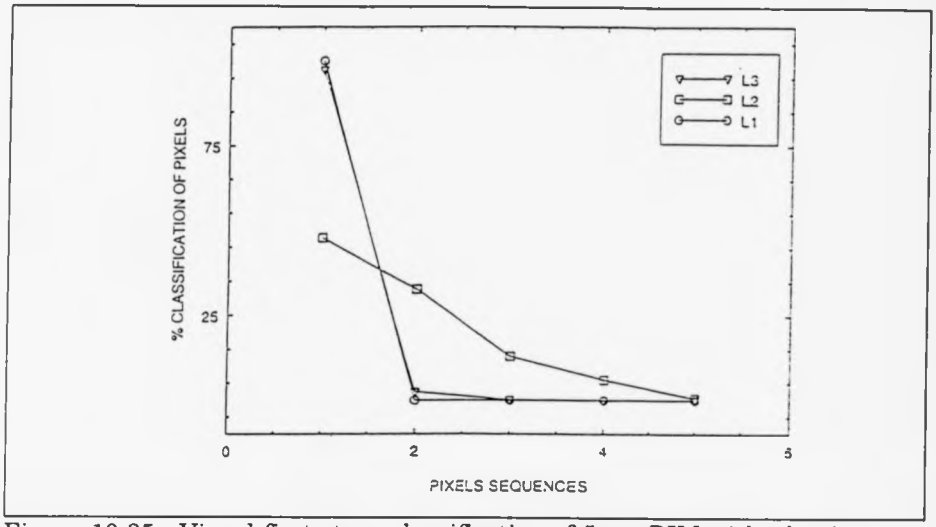

Figure 10.35: Visual first stage classification of 5mm RIM with plastic inclusions. (Mean of 6 images).

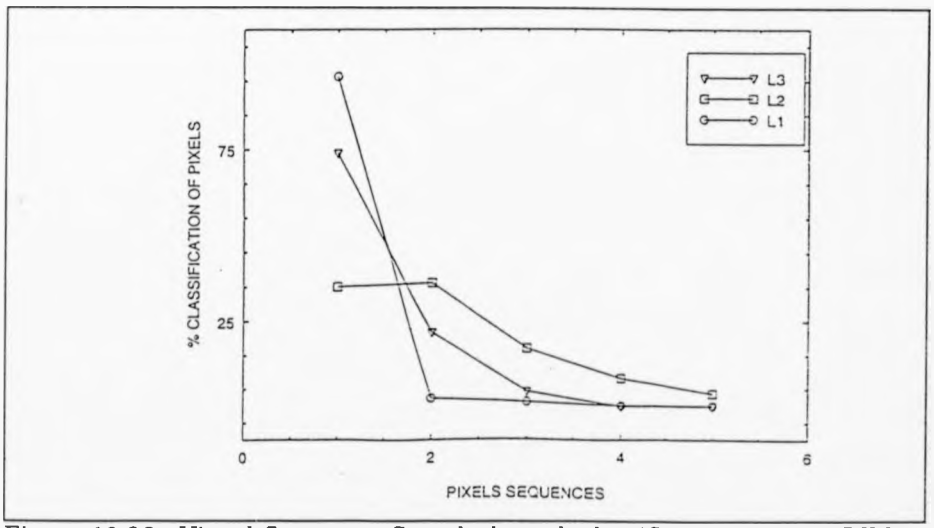

Figure 10.36: Visual first stage Search through classification of 2mm RIM impacted at 4.76J. (Mean of 6 images).

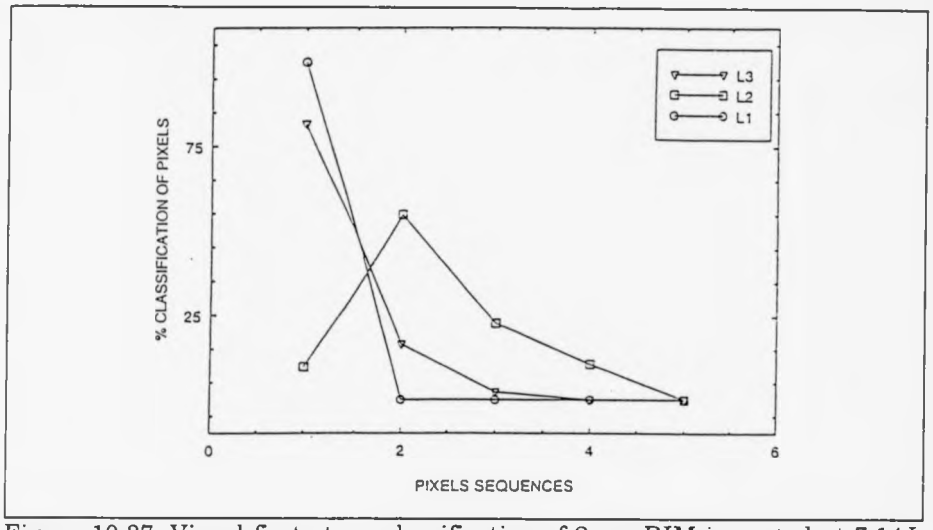

Figure 10.37: Visual first stage classification of 2mm RIM impacted at 7.14J. (Mean of 6 images).

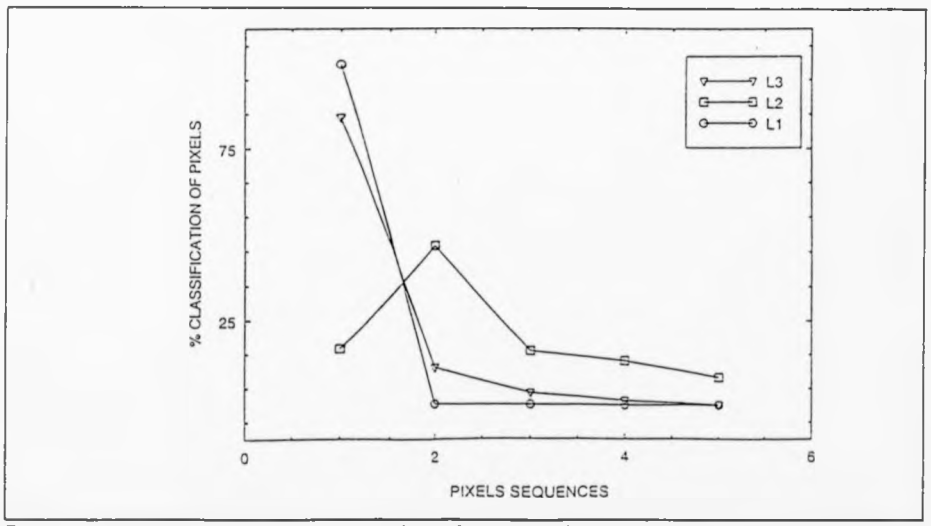

Figure 10.38: Visual first stage classification of 2mm RIM impacted at 14.3J. (Mean of 6 images).

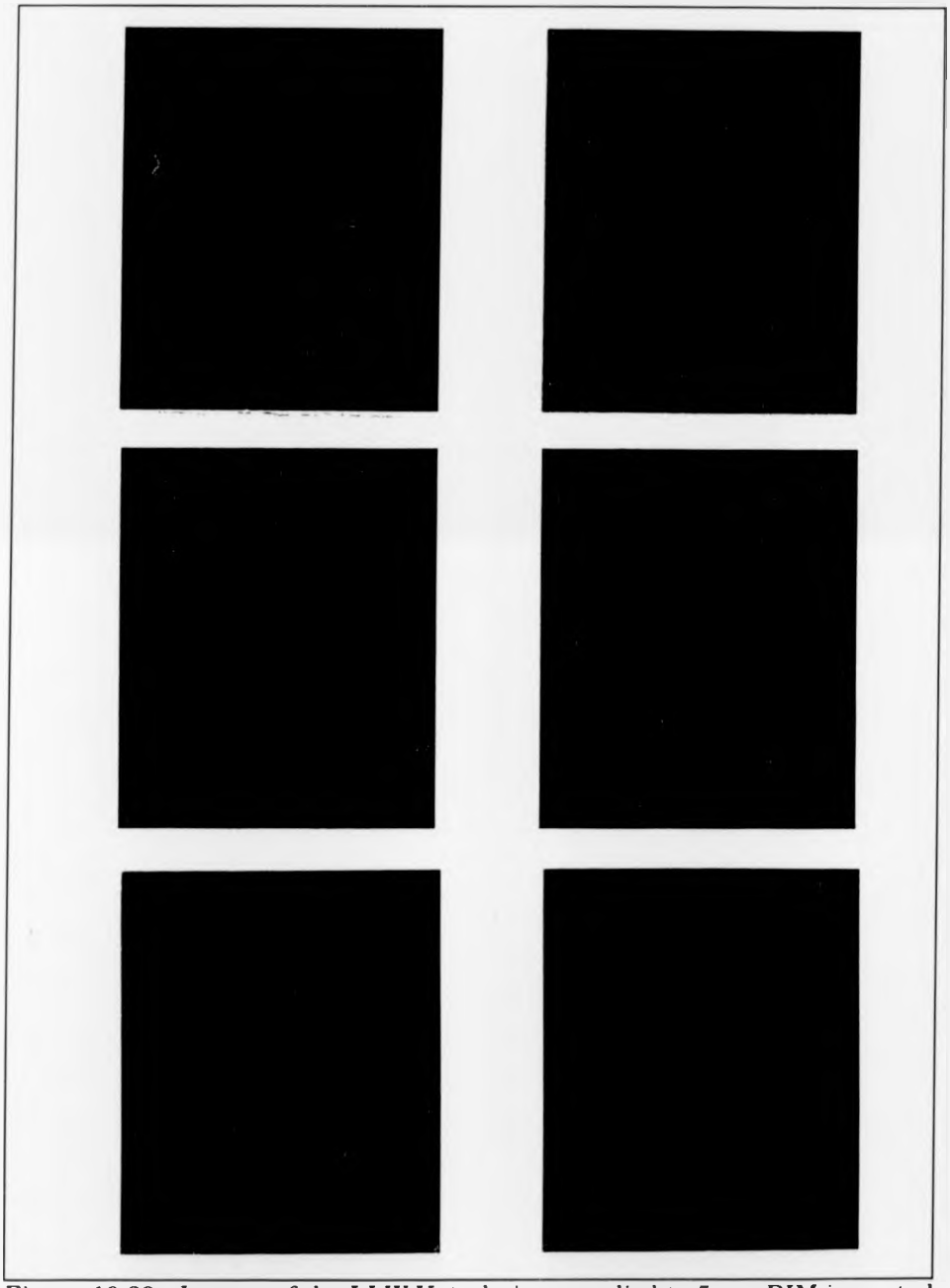

Figure 10.39: Images of the I.I.W.V. technique applied to 5mm RIM impacted at 28.6J and 42J. (Light source 1, cycles 1-6, left to right).

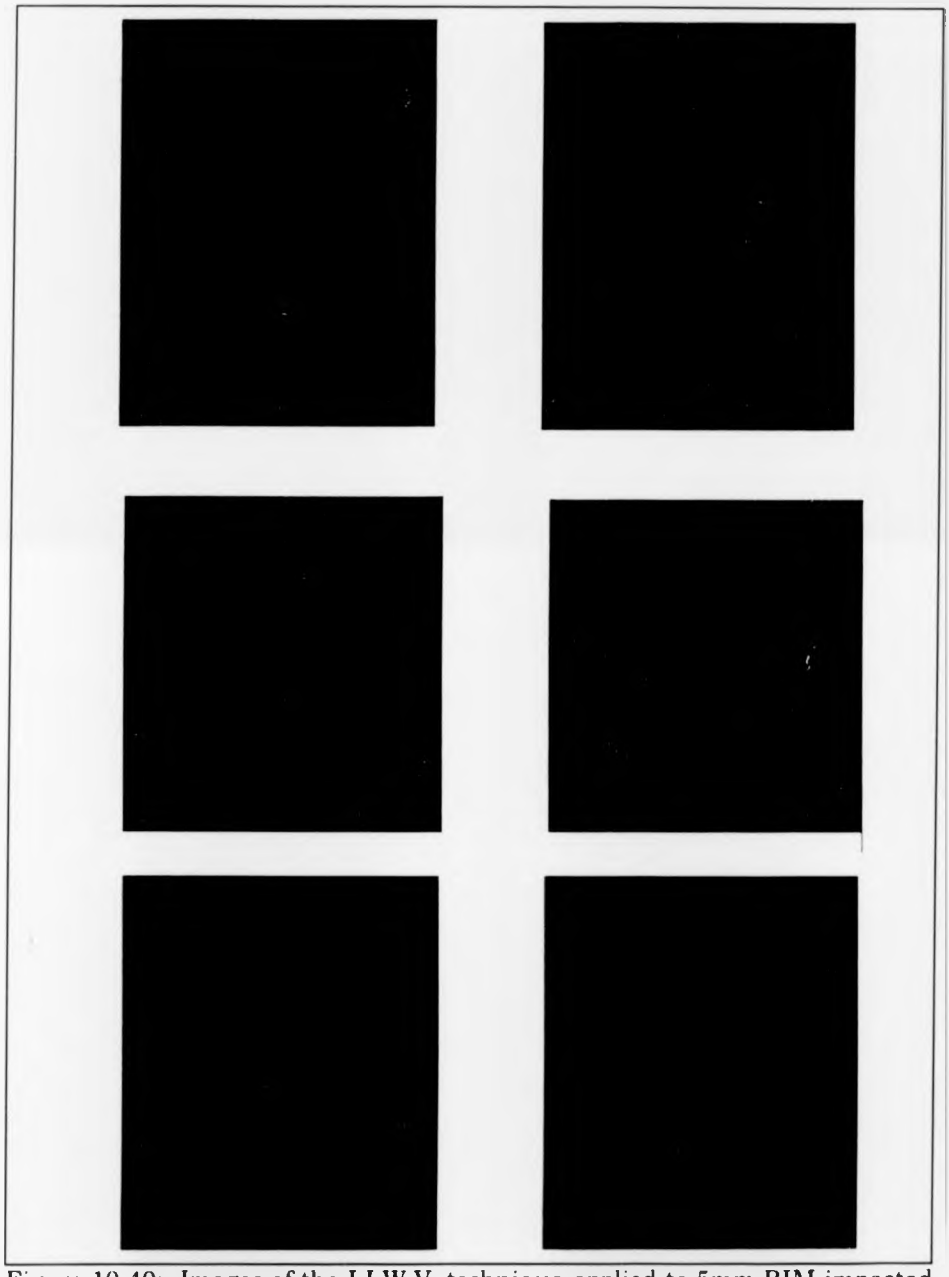

Figure 10.40: Images of the I.I.W.V. technique applied to 5mm RIM impacted at 14.3J and 30.8J (shown). (Light source 1, cycles 1-6, left to right).

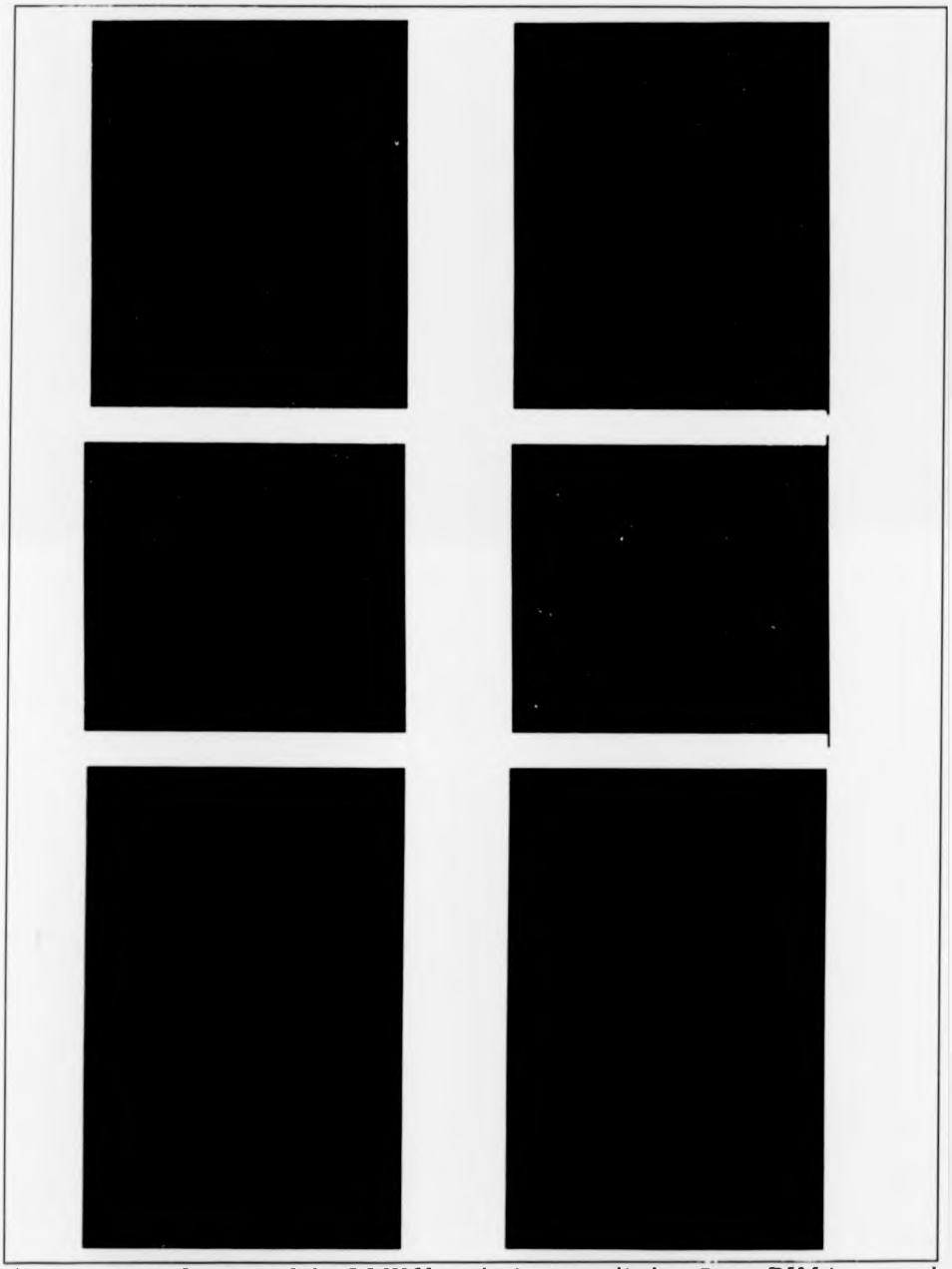

Figure 10.41: Images of the I.I.W.V. technique applied to 5mm RIM impacted at 28.6J and 28.6J with load angle (shown). (Light source 1, cycles 1-6, left to right).

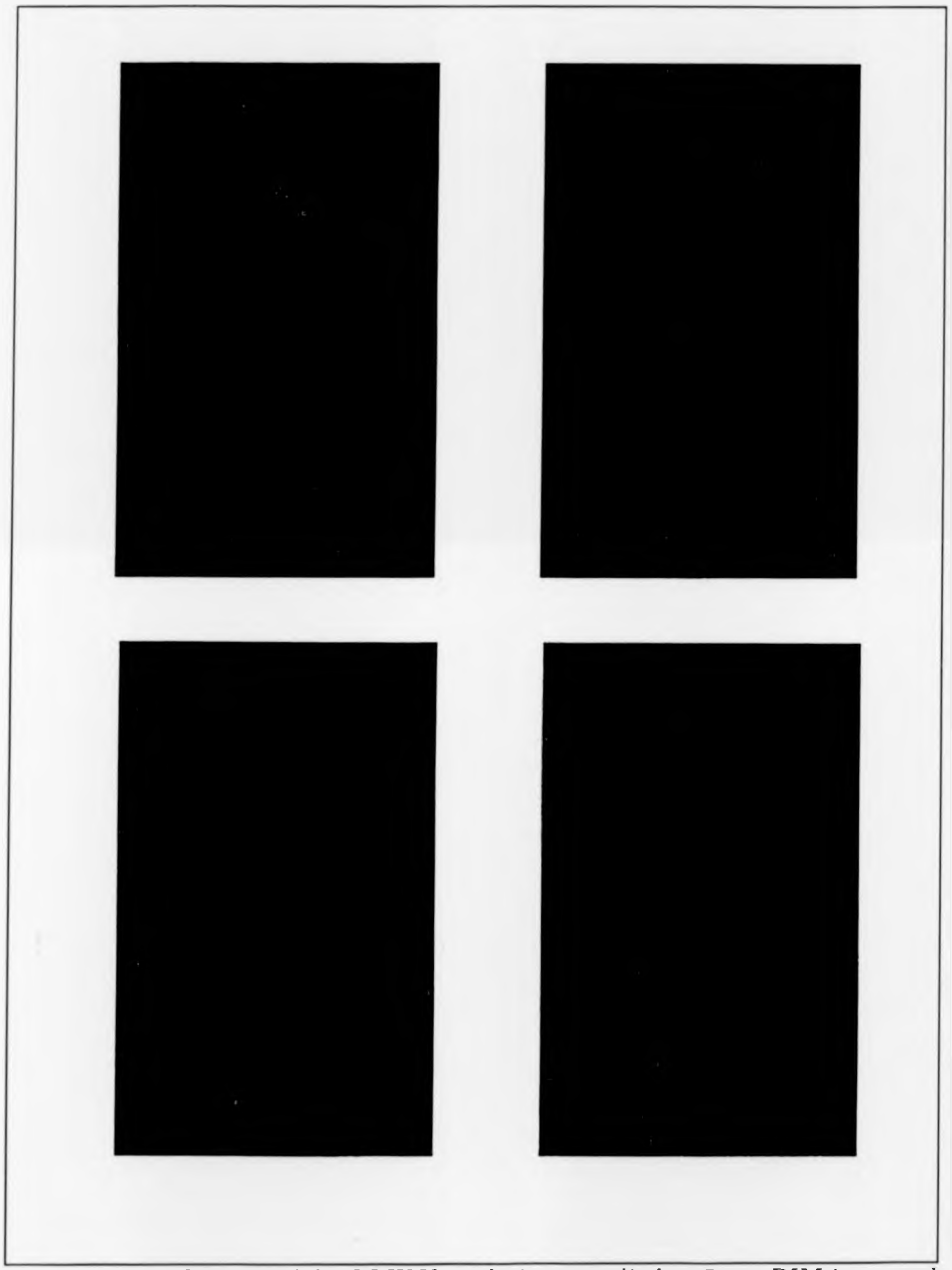

Figure 10.42: Images of the I.I.W.V. technique applied to 5mm RIM impacted at 28.6J and 28.6J with load angle (both shown). (Light source 2, cycles 1-4, left to right).

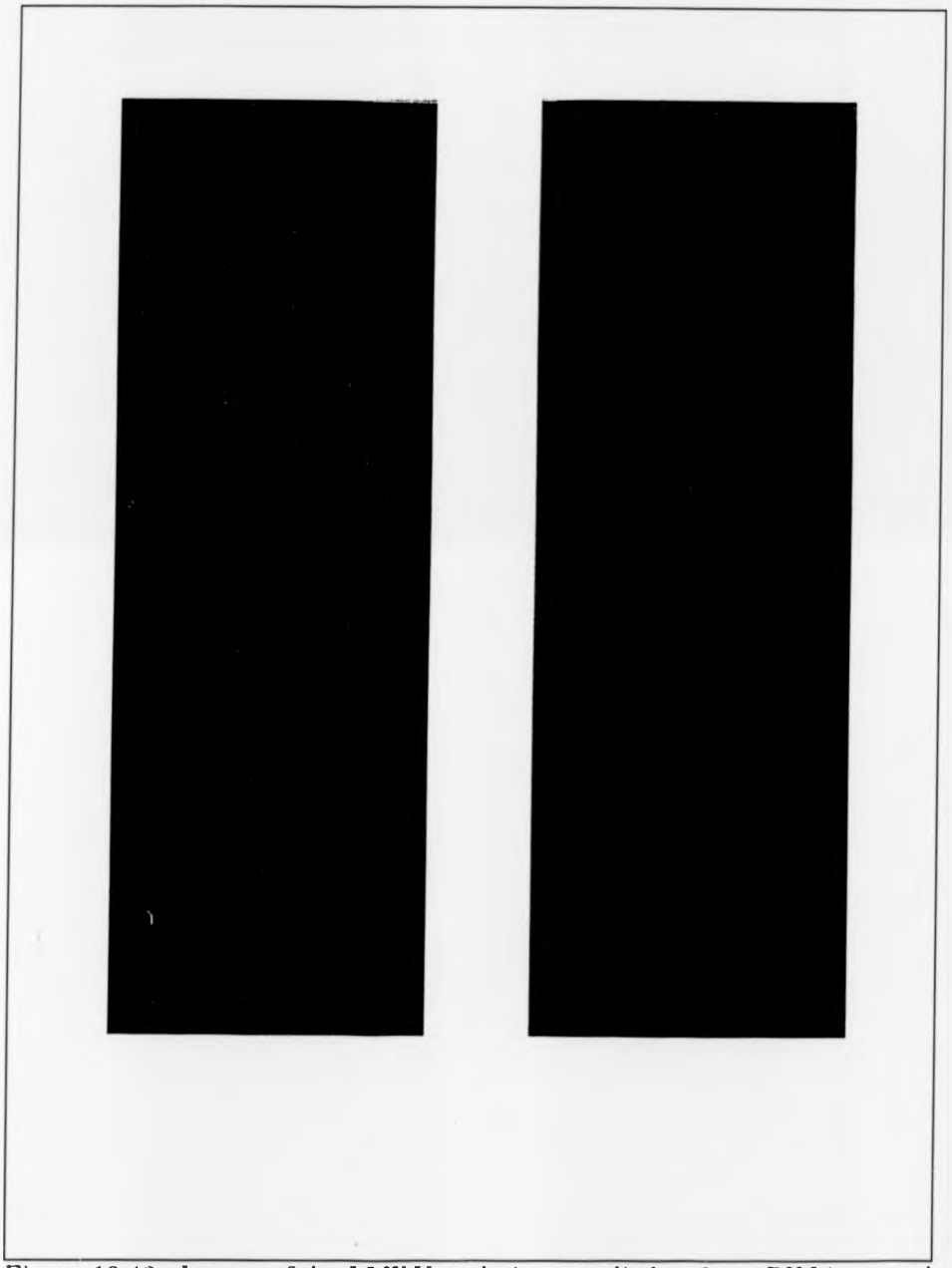

Figure 10.43: Images of the I.I.W.V. technique applied to 5mm RIM impacted at 47.6J and 47.6J with reflective paint. (Light source 1, cycles 1-2, left to right).

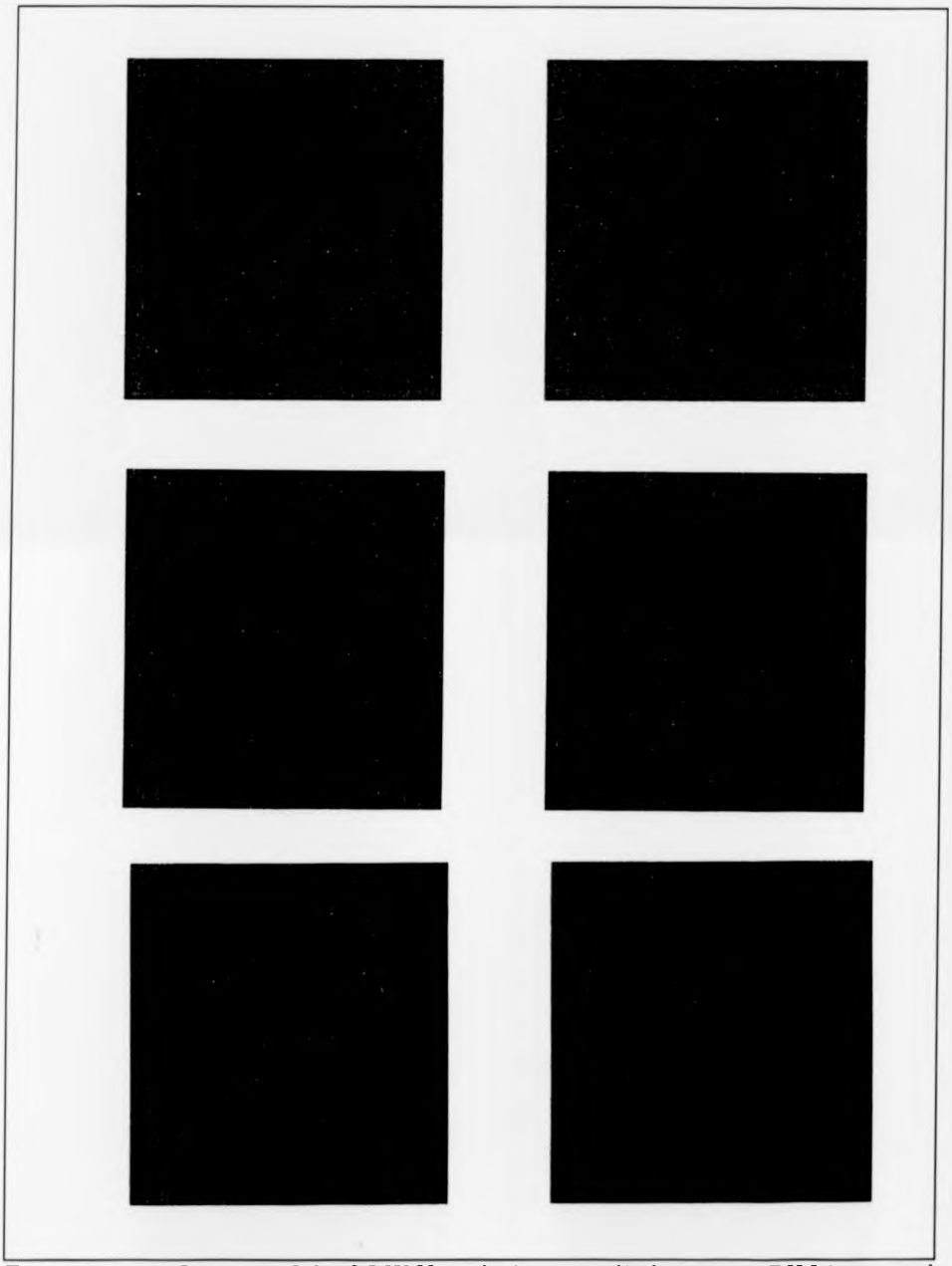

Figure 10.44: Images of the I.I.W.V. technique applied to 5mm RIM impacted at 55.6J with reflective paint and part extraction. (Light source 1, cycles 1-6, left to right).

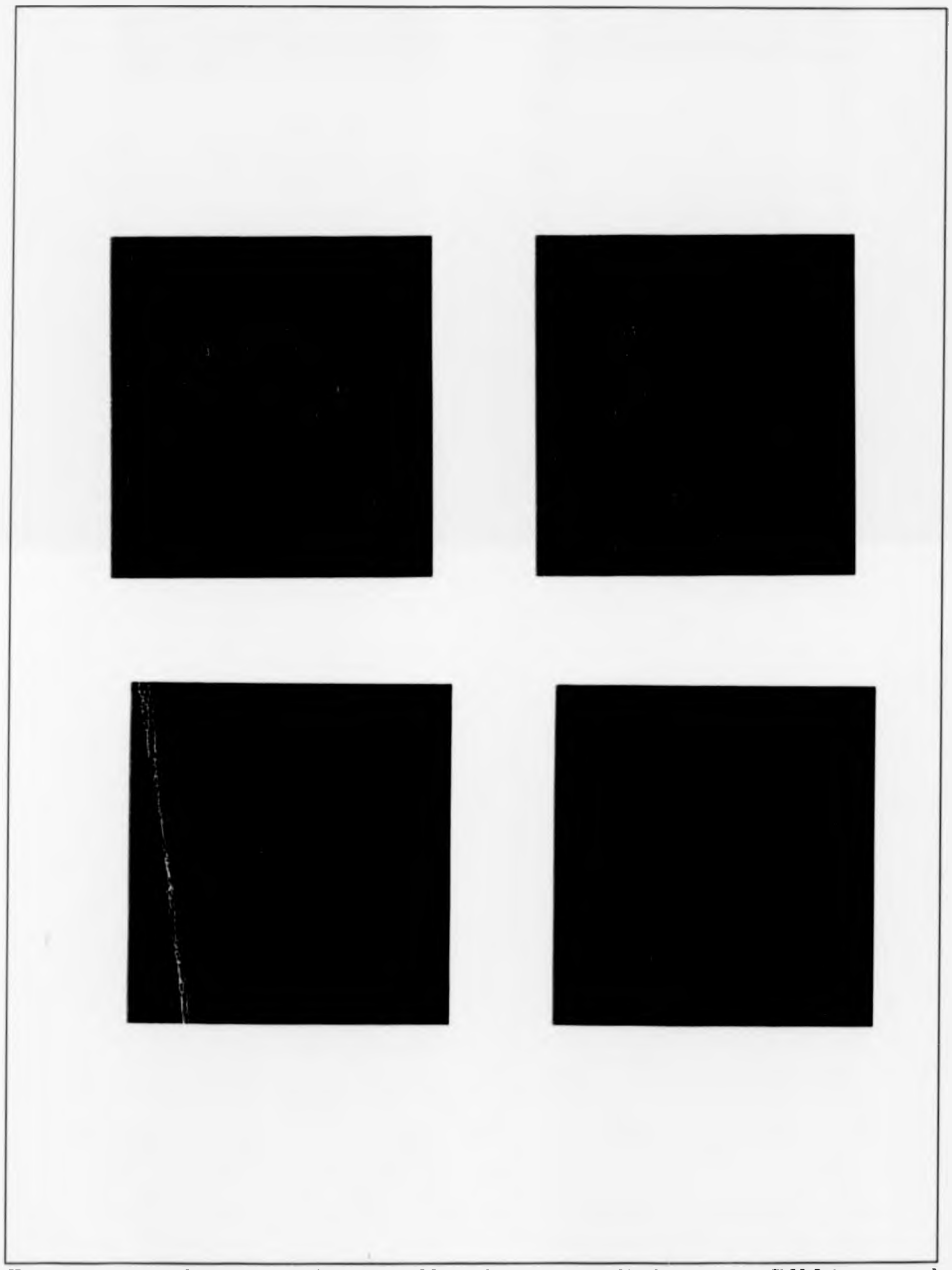

Figure 10.45: Images of the I.I.W.V. technique applied to 5mm RIM impacted at 55.6J with reflective paint and part extraction. (Light source 1, cycles 7-12, left to right).

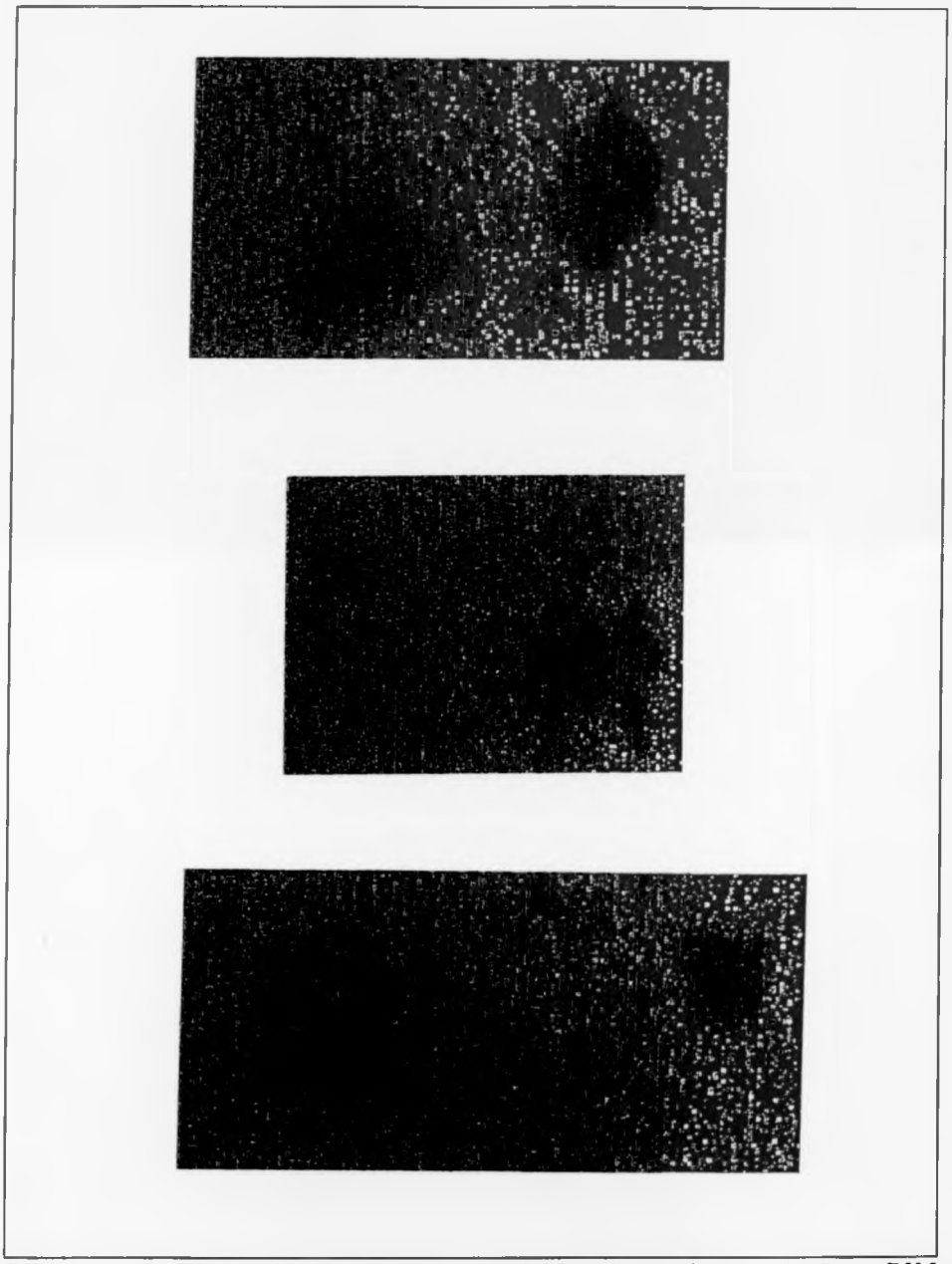

Figure 10.46: Thermal Visual Imaging applied to detect damage in 5mm RIM impacted at 28.6J & 42J(top), 14.3J & 30.8J(middle), 28.6J & 28.6J with load angle(bottom).

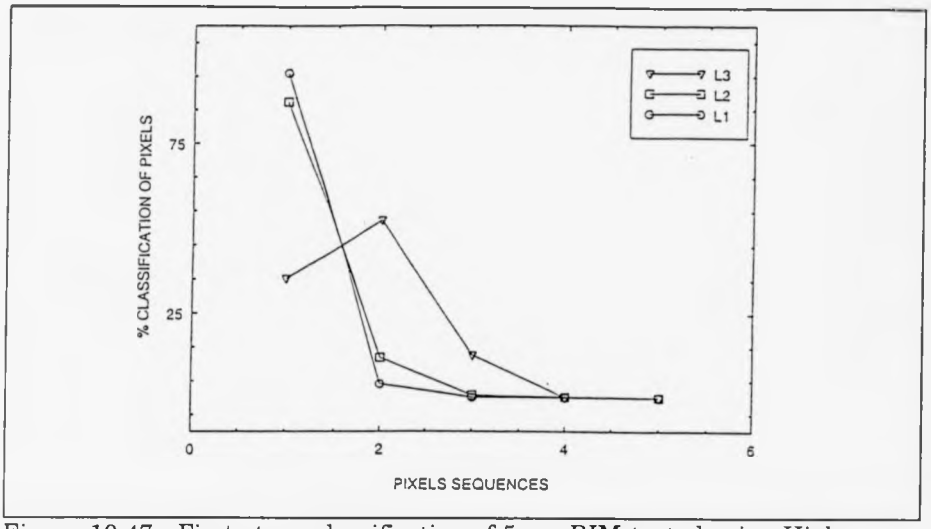

Figure 10.47: First stage classification of 5mm RIM tested using High Temperature Visual Imaging. (Reference sample). (Mean of 6 images).

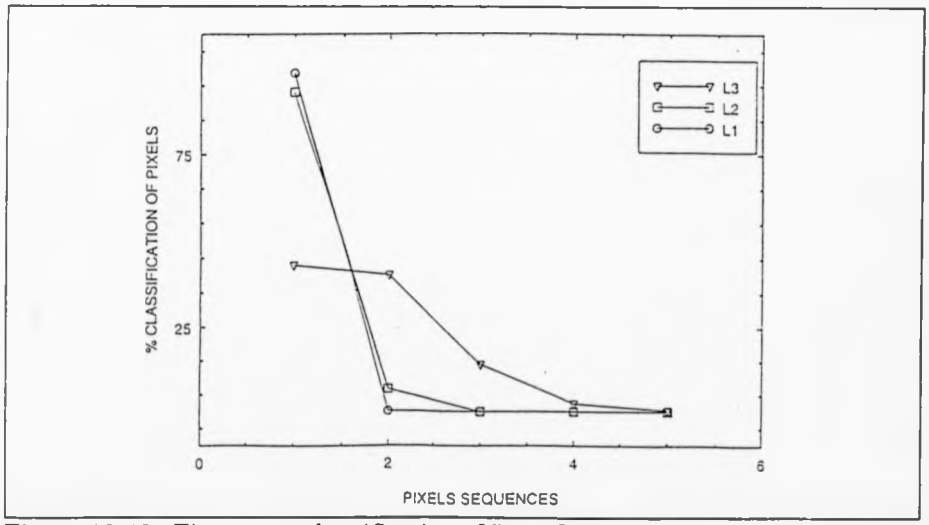

Figure 10.48: First stage classification of 5mm RIM impacted at 28.6J and 42J and tested using High Temperature Visual Imaging. (Mean of 6 images).

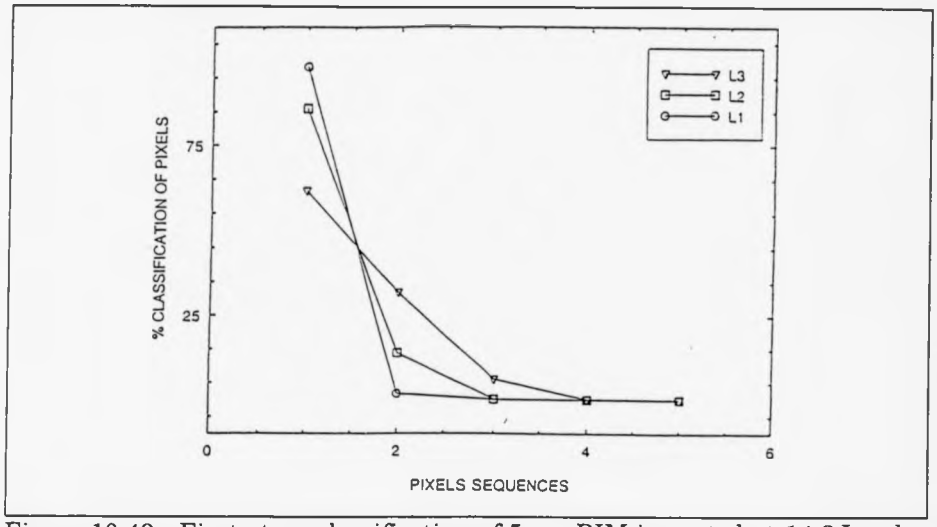

Figure 10.49: First stage classification of 5mm RIM impacted at 14.3J and 30.8J and tested using High Temperature Visual Imaging. (Mean of 6 images).

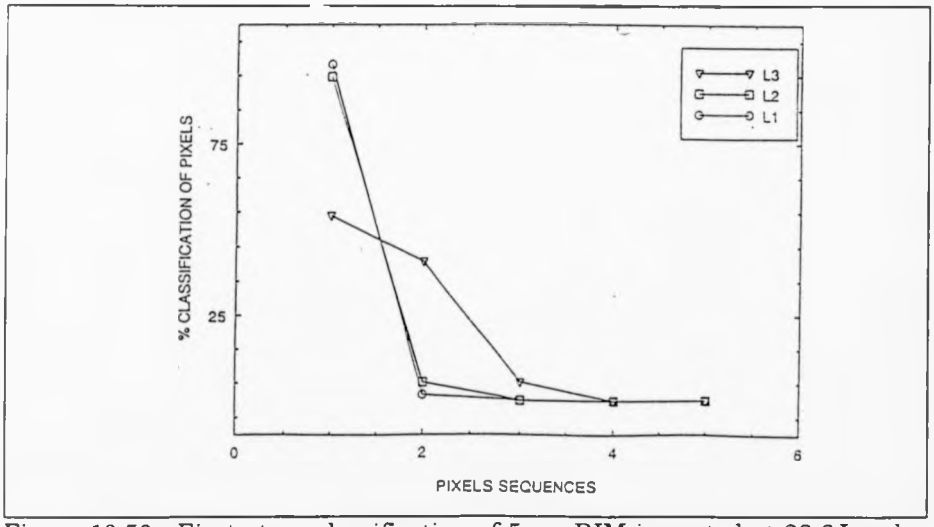

Figure 10.50: First stage classification of 5mm RIM impacted at 28.6J and 28.6J with load angle and tested using High Temperature Visual Imaging. (Mean of 6 images).

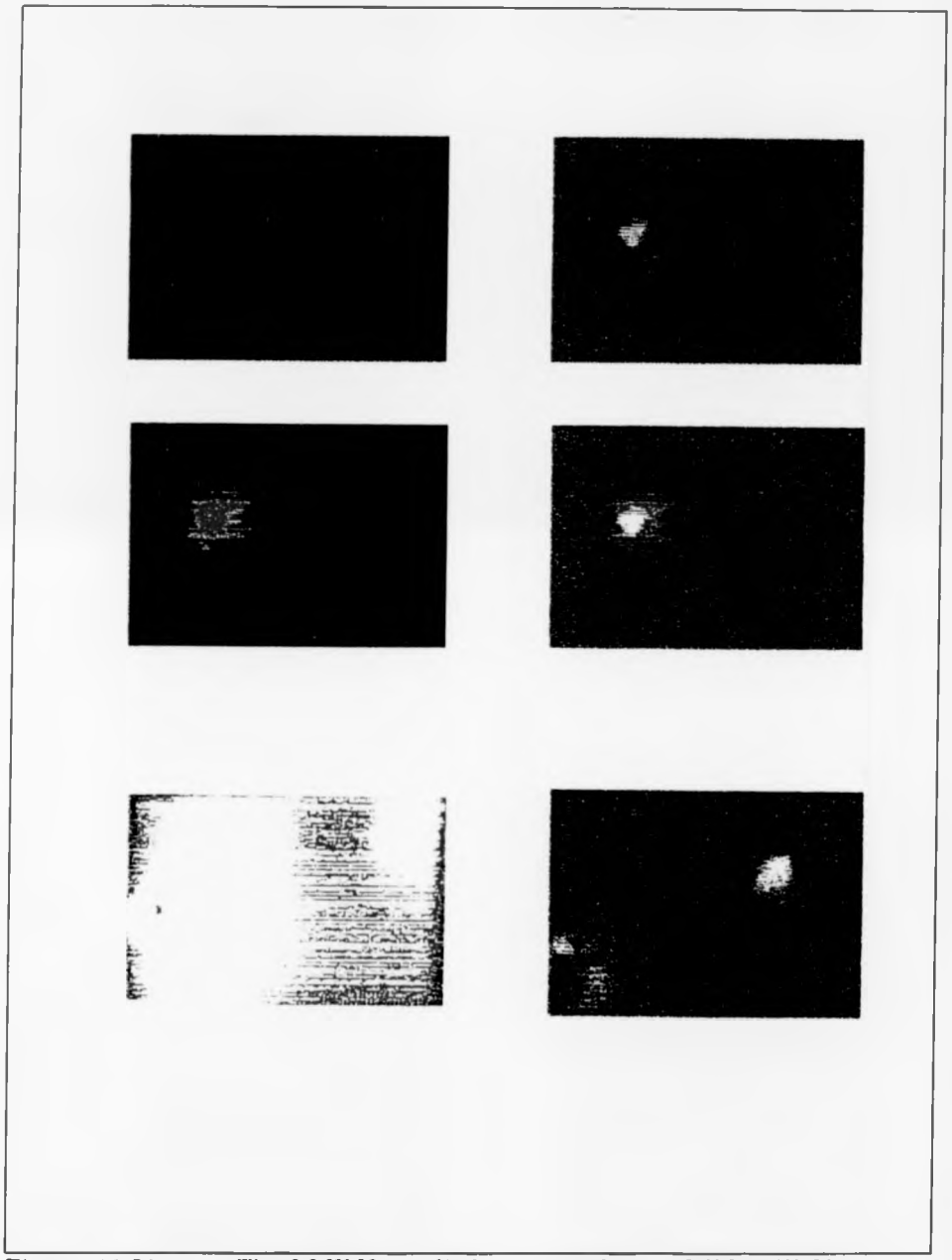

Figure 10.51: The I.I.W.V. applied to painted 5mm RIM & W.Glass, impacted at 55.6J & 28.6J, tested using HTPT. (Cycles 1-4,1-2, left to right).

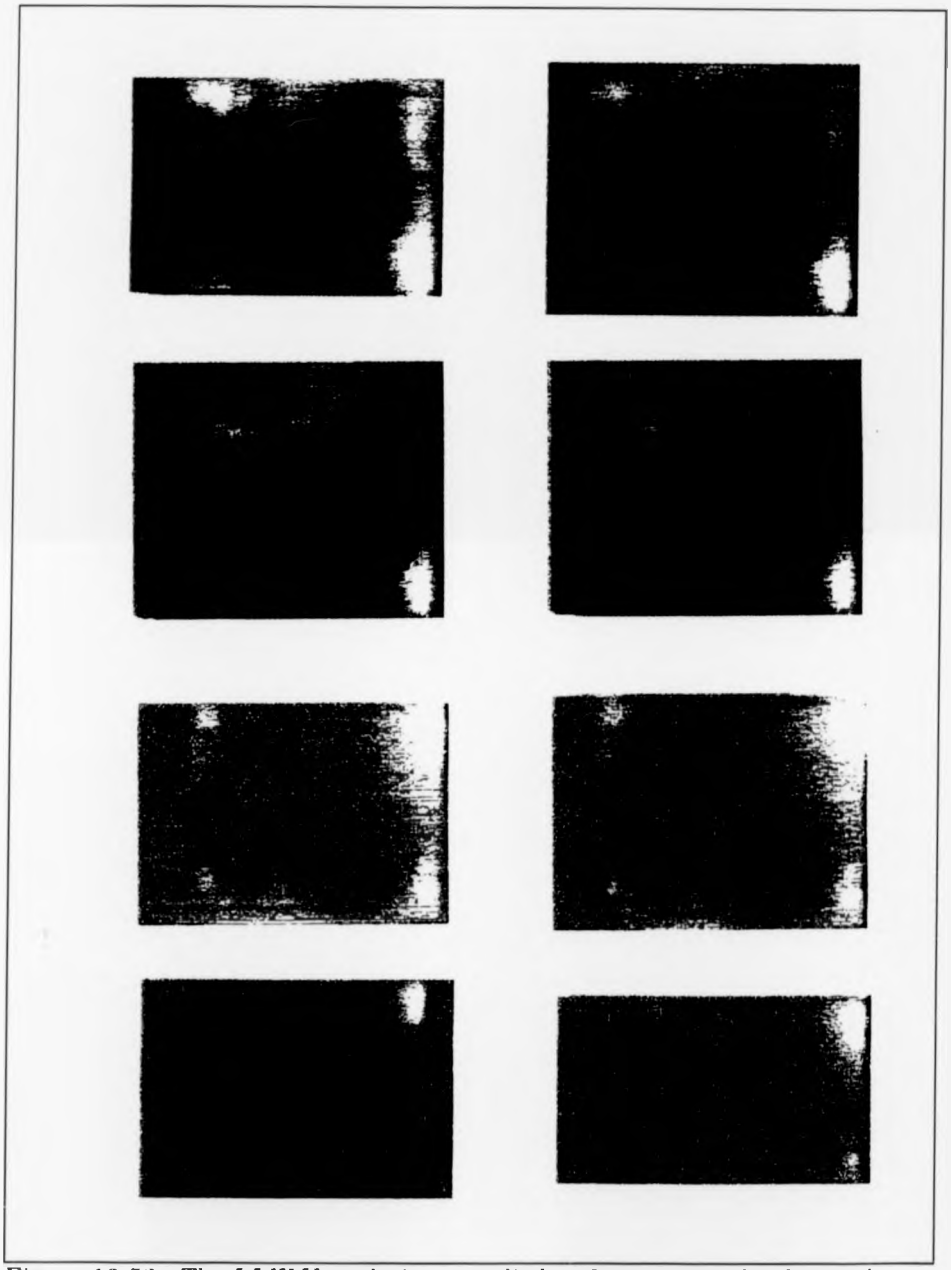

Figure 10.52: The I.I.W.V. technique applied to 3mm perpendicular and parallel GMT impacted at 14.3J and tested using High Temperature PVT.(Cycles 1-8, left to right).

Figure 10.53: The I.I.W.V. technique applied to W.Bone tested using High Temperature PVT. (Cycles 1-4, left to right).

IMAGE	SIZE	D_1	D_2	D_3	D_4	D_5
Mnonb	14880	1	1	1	1	1
Mnonbl	12540	1	1	1	1	1
MnonblR	12869	1	1	1	1	1
Mnonf	14602	1	1	1	1	1
Mnonfl	16647	1	1	1	1	1
MnonflR	14600	1	1	1	1	1
VS_1mb	11495	1	1	1	1	1
VS_1mbl	9086	0	0	0	0	0
VS_1mblR	8330	1	1	1	1	1
VS_1mf	7280	1	1	1	1	1
VS_1mfl	8160	0	0	0	0	0
VS_1mflR	6630	1	1	1	1	1
VS_2mb	14214	1	1	1	1	1
VS_2mbl	12300	0	0	0	0	0
VS_2mblR	8610	1	1	1	1	1
VS_2mf	8176	1	1	1	1	1
VS_2mfl	8008	0	0	0	0	0
VS_2mflR	7344	1	1	1	1	1
VS_3mb	16932	1	1	1	1	1
VS_3mbl	13770	0	0	0	0	0
VS_3mblR	13588	1	1	1	1	1
VS_3mf	15300	1	1	1	1	1
VS_3mfl	16700	0	0	0	0	0
VS_3mflR	15264	1	1	1	1	1

IMAGE	SIZE	D_1	D_2	D_3	D_4	D_5
S_1D_1mb	5428	1	1	1	1	1
S_1D_2mb	5640	1	1	1	1	1
S_1D_1mbl	4650	0	0	0	0	0
S_1D_2mbl	3416	0	0	0	0	0
S_1D_1mblR	4284	1	1	1	1	1
S_1D_2mblR	3933	1	1	1	1	1
S_1D_1mf	4002	1	1	1	1	1
S_1D_2mf	3242	1	1	1	1	1
S_1D_1mfl	4160	0	0	0	0	0
S_1D_2mfl	4108	0	0	0	0	0
S_1D_1mflR	3648	1	1	1	1	1
S_1D_2mflR	2880	1	1	1	1	1
S_2D_1mb	6767	1	1	1	1	1
S_2D_2mb	5353	1	1	1	1	1
S_2D_1mbl	6305	0	0	0	0	0
S_2D_2mbl	5643	0	0	0	0	0
S_2D_1mblR	4131	1	1	1	1	1
S_2D_2mblR	4050	1	1	1	1	1
S_2D_1mf	4118	1	1	1	1	1
S_2D_2mf	3796	1	1	1	1	1
S_2D_1mfl	3952	0	0	0	0	0
S_2D_2mfl	3750	0	0	0	0	0
S_2D_1mflR	3953	1	1	1	1	1
S_2D_2mflR	3149	1	1	1	1	1

IMAGE	SIZE	D_1	D_2	D_3	D_4	D_5
S_3D_1mb	9292	1	1	1	1	1
S_3D_2mb	7575	1	1	1	1	1
S_3D_1mbl	6942	0	0	0	0	0
S_3D_2mbl	4891	0	0	0	0	0
S_3D_1mblR	7140	1	1	1	1	1
S_3D_2mblR	5930	1	1	1	1	1
S_3D_1mf	7920	1	1	1	1	1
S_3D_2mf	7029	1	1	1	1	1
S_3D_1mfl	8500	0	0	0	0	0
S_3D_2mfl	7425	0	0	0	0	0
S_3D_1mflR	8372	1	1	1	1	1
S_3D_2mflR	6825	1	1	1	1	1

Table 10.1: Image Decision Data (RIM).

IMAGE	SIZE	D_1	D_2	D_3	D_4	D_5
Va_1mb	24700	1	1	1	1	1
Va_1mbl	27084	0	0	0	0	0
Va_1mblR	31496	1	1	1	1	1
Va_1mf	30222	1	1	1	1	1
Va_1mfl	23228	0	0	0	0	0
Va_1mflR	21630	1	1	1	1	1
Va_2mb	25164	1	1	1	1	1
Va_2mbl	23128	0	0	0	0	0
Va_2mblR	22656	1	1	1	1	1
Va_2mf	23571	1	1	1	1	1
Va_2mfl	22654	0	0	0	0	0
Va_2mflR	22278	1	1	1	1	1
Va_3mb	26643	1	1	1	1	1
Va_3mbl	25480	0	0	0	0	0
Va_3mblR	26108	1	1	1	1	1
Va_3mf	26532	1	1	1	1	1
Va_3mfl	24304	1	1	1	1	1
Va_3mflR	23504	0	0	0	0	0
VX_1mb	22852	1	1	1	1	1
VX_1mbl	10998	0	0	0	0	0
VX_1mbl	16171	1	1	1	1	1
VX_1mf	17304	1	1	1	1	1
VX_1mfl	9543	0	0	0	0	0
VX_1mflR	14259	1	1	1	1	1

IMAGE	SIZE	D_1	D_2	D_3	D_4	D_5
Vx_2mb	10300	1	1	1	1	1
Vx_2mbl	4840	0	0	0	0	0
Vx_2mblR	9006	1	1	1	1	1
Vx_2mf	9563	1	1	1	1	1
Vx_2mfl	9680	0	0	0	0	0
Vx_2mflR	10396	1	1	1	1	1
Vx_1mb	9156	1	1	1	1	1
Vx_1mbl	9396	0	0	0	0	0
Vx_1mblR	12240	1	1	1	1	1
Vx_1mf	9605	1	1	1	1	1
Vx_1mfl	8855	0	0	0	0	0
Vx_1mflR	10137	1	1	1	1	1

Table 10.2: Image Decision Data (W.Glass).

MATERIAL TYPE	THICKNESS	IMPACT ENERGY	IMPACT DIAMETER	t_{ref}	t_{avg}	t_{def}	$\%S_1$	$\%S_2$	$\%S_3$	$\%S_4$	$\%S_5$
3	5	7.14	0.57	0.2795	0.2904	0.3747	18.16	-13.17	-3.35	-0.866	-0.651
3	5	14.3	0.87	0.2871	0.2977	0.4032	31.84	-21.16	-6.61	-2.28	-1.96
3	5	28.6	1.54	0.3016	0.3123	0.4694	56.70	-34.34	-11.98	-5.83	-5.188
3	5	42	1.95	0.3095	0.32201	0.5292	64.53	-38.19	-13.94	-7.42	-6.64
4	5	47.6	2.72	0.3220	0.3924	1.241	8.057	-5.08	-2.42	-0.56	-0.676
4	5	55.6	2.75	0.3200	0.3923	1.265	6.432	-4.12	-2.08	-0.384	-0.50
3	2	4.76	0.04250	0.5685	0.6345	0.9253	47.76	-24.60	-8.55	-7.38	-6.85
3	2	7.14	0.0428	0.5856	0.6445	0.9071	54.10	-28.35	-9.28	-8.32	-7.66
3	2	14.3	0.0463	0.6259	0.6688	0.8518	58.62	-37.55	-13.3	-10.37	-9.42
2	3	4.76	0.0996	0.4753	0.5350	0.6310	0.9261	-0.4986	0.191	-0.1	-0.0416
2	3	7.14	0.0955	0.4800	0.5385	0.6353	0.2053	-0.108	0.337	-0.011	0.0448
2	3	14.3	0.068	0.4880	0.5445	0.6580	-1.456	0.786	0.661	0.207	0.258
2	3	28.6	0.109	0.4821	0.5400	0.7501	-2.25	1.194	0.772	0.327	0.3601
2.1	3	7.14	0.0103	0.5030	0.5613	0.6622	0.3610	-0.1005	0.356	-0.111	-0.065
2.1	3	14.3	0.0737	0.5115	0.5672	0.6825	-0.865	0.545	0.597	0.049	0.089
2.1	3	28.6	0.1242	0.5072	0.5633	0.7775	-0.585	0.3519	0.50	0.005	0.0196

MATERIAL TYPE	THICKNESS	IMPACT ENERGY	IMPACT DIAMETER	t_{ref}	t_{avg}	t_{def}	$\%S_1$	$\%S_2$	$\%S_3$	$\%S_4$	$\%S_5$
2.2	3	7.14	0.110	0.5245	0.5815	0.5839	0.9373	-0.319	0.3044	-0.279	-0.241
2.2	3	14.3	0.078	0.5337	0.5876	0.7021	0.2425	0.036	0.451	-0.200	-0.171
2.2	3	28.6	0.142	0.5315	0.5847	0.7990	2.177	-1.026	0.072	-0.50	-0.50
1	5	4.76	0.041	0.2551	0.2603	0.7556	4.41	-4.89	-0.99	0.445	0.623
1	5	7.04	0.031	0.2559	0.2610	0.2548	4.50	-4.95	-1.03	0.408	0.59
1	5	14.3	0.0311	0.2582	0.2626	0.2531	4.79	-5.15	-1.19	0.329	0.518
1	5	28.6	0.0022	0.2612	0.2648	0.2518	5.743	-5.795	-3.16	-0.58	-0.36
1	3	4.76	0.0017	0.2774	0.2977	0.3364	14.57	-10.40	-2.74	-0.45	-0.24
1	3	17.14	0.0066	0.2810	0.3008	0.3361	12.81	-9.31	-1.69	-0.09	0.086
1	3	14.3	0.0066	0.2902	0.3088	0.3383	8.150	-6.382	-1.69	-0.092	0.086
1	3	28.6	0.0176	0.2993	0.3176	0.3572	1.667	-2.20	-0.294	0.427	0.564

Table 10.3: Neural Network Prediction Data.

SPECIMEN CODE	SPECIMEN THICKNESS (mm)	IMPACT HEIGHT (cm)	IMPACT WEIGHT (Kg)	IMPACT ENERGY (J)	N	ΔS_1 %	ΔS_2 %	ΔS_3 %	ΔS_4 %	ΔS_5 %	t_{avg}	t_{ref}	t_{def}	K_{avg}	K_{ref}	D
$(VX_{1,1})$	3	102	1.4	14.3	1	0	0	0	0	0	0.295	0.29	0.355	0.83	0.82	
$(VX_{1,2})$	3	102	1.4	14.3	1	+0.35	-0.35	0	0	0	0.295	0.29	0.355	0.83	0.82	
$(VX_{1,3})$	3	102	1.4	14.3	1	-0.35	+0.35	0	0	0	0.295	0.29	0.355	0.83	0.82	
$(VX_{4,1})$	3	51	1.4	7.14	1	-2.0	+2.0	-0.1	+0.2	-0.1	0.315	0.315	0.385	0.82	0.82	
$(VX_{4,2})$	3	51	1.4	7.14	1	+20.54	-16.96	+4.26	+0.24	+0.44	0.315	0.315	0.385	0.82	0.82	
$(VX_{4,3})$	3	51	1.4	7.14	1	-22.54	+18.96	+4.26	-0.24	-0.54	0.315	0.315	0.385	0.82	0.82	
$(VX_{3,1})$	3	34	1.4	4.76	1	-0.4	+0.6	-0.2	0	0	0.34	0.315	0.40	0.85	0.79	
$(VX_{3,2})$	3	34	1.4	4.76	1	+14.0	-10.7	-2.6	-0.4	-0.3	0.34	0.315	0.40	0.85	0.79	
$(VX_{3,3})$	3	34	1.4	4.76	1	-14.4	+11.3	+2.4	+0.4	+0.3	0.34	0.315	0.40	0.85	0.79	
$(VX_{4,[1]})$	3	102	2.8	28.8	1						0.25	0.24	0.26	0.96	0.92	
$(VX_{4,[2]})$	3	102	2.8	28.6	1						0.25	0.24	0.26	0.96	0.92	
$(VX_{4,[3]})$	3	102	2.8	28.6	1						0.25	0.24	0.26	0.96	0.92	

SPECIMEN CODE	SPECIMEN THICKNESS (mm)	IMPACT HEIGHT (cm)	IMPACT WEIGHT (Kg)	IMPACT ENERGY (J)	N	ΔS_1 %	ΔS_2 %	ΔS_3 %	ΔS_4 %	ΔS_5 %	t_{avg}	t_{ref}	t_{def}	K_{avg}	K_{ref}	D
$(V_{6\times}X_{[1]})$	5	102	1.4	14.3	1	-1.22	+0.38	+0.18	+0.36	+0.28	0.275	0.265	0.315	0.873	0.841	
$(V_{6\times}X_{[2]})$	5	102	1.4	14.3	1	+7.26	-7.04	-0.74	+0.36	+0.46	0.275	0.265	0.315	0.873	0.841	
$(V_{6\times}X_{[3]})$	5	102	1.4	14.3	1	-6.26	+7.62	+0.92	+0.92	-0.18	0.275	0.265	0.315	0.873	0.841	
$(V_{6\times})$	5	51	1.35	7.14	1	+0.04	+0.14	-0.06	-0.26	-0.06	0.27	0.265	0.29	0.93	0.91	
$(V_{6\times})$	5	51	1.35	7.14	1	+5.66	-5.14	-0.74	-0.54	+0.26	0.27	0.265	0.29	0.93	0.91	
$(V_{6\times})$	5	51	1.33	7.14	1	5.62	+5.28	+0.68	+0.72	+0.22	0.27	0.265	0.29	0.93	0.91	
$(V_{6\times})$	5	34	1.35	4.76	1	+0.06	+0.26	+0.14	+0.24	+0.14	0.265	0.265	0.285	0.93	0.93	
$(V_{6\times})$	5	34	1.35	4.76	1	+7.5	-6.5	-0.5	+0.3	+0.2	0.265	0.265	0.285	0.93	0.93	
$(V_{6\times})$	5	34	1.33	4.76	1	-7.34	+6.46	+0.86	+0.86	+0.06	0.265	0.265	0.285	0.93	0.93	
$(V_{6\times}X_{[1]}X_{[1]})$	5	102	2.8	28.6	1						0.253	0.245	0.27	0.937	0.91	
$(V_{6\times}X_{[1]}X_{[2]})$	5	102	2.8	28.6	1						0.253	0.245	0.27	0.937	0.91	
$(V_{6\times}X_{[1]}X_{[3]})$	5	102	2.8	28.6	1						0.253	0.245	0.27	0.937	0.91	

SPECIMEN CODE	SPECIMEN THICKNESS (mm)	IMPACT HEIGHT (cm)	IMPACT WEIGHT (Kg)	IMPACT ENERGY (J)	N	ΔS_1 %	ΔS_2 %	ΔS_3 %	ΔS_4 %	ΔS_5 %	t_{avg}	t_{ref}	t_{def}	K_{avg}	K_{ref}	D
$(VX34_{,1})$	3	102	1.4	14.3	1						0.24	0.22	0.26	0.844	0.888	
$(VX34_{,2})$	3	102	1.4	14.3	1						0.24	0.22	0.26	0.844	0.888	
$(VX34_{,3})$	3	102	1.4	14.3	1						0.24	0.22	0.26	0.844	0.888	
$(VX32_{,1})$	3	102	2.8	28.6	1						0.265	0.23	0.445	0.828	0.741	
$(VX32_{,2})$	3	102	2.8	28.6	1						0.265	0.23	0.445	0.828	0.741	
$(VX32_{,3})$	3	102	2.8	28.6	1						0.265	0.23	0.445	0.828	0.741	
$(VX35_{,1})$	3	102	1.4	14.3	1						0.255	0.235	0.275	0.927	0.854	
$(VX35_{,2})$	3	102	1.4	14.3	1						0.255	0.235	0.275	0.927	0.854	
$(VX35_{,3})$	3	102	1.4	14.3	1						0.255	0.235	0.275	0.927	0.854	
$(VX31_{,33,[1]})$	3	102	2.8	28.6	1						0.25	0.24	0.268	0.953	0.896	
$(VX31_{,33,[2]})$	3	102	2.8	28.6	1						0.25	0.24	0.268	0.953	0.896	
$(VX31_{,33,[3]})$	3	102	2.8	28.6	1						0.25	0.24	0.268	0.953	0.896	

Table 10.4: Neural Network Training Data (W.Glass).

SPECIMEN	SPECIMEN	IMPACT	IMPACT	IMPACT	N	ΔS_1 %	ΔS_2 %	ΔS_3 %	ΔS_4 %	ν_{avg}	ν_{ref}	ν_{ref}	K_{avg}	K_{ref}	D
$(VS_1,1)$	5	102	2.8	28.6	2	-18.64	+13.26	+3.66	+0.76	+0.86	0.31	0.30	0.285	0.805	0.779
$(VS_1,2)$	5	102	2.8	28.6	2	+68.8	-35.2	-15.2	-10.2	4.2	0.31	0.30	0.285	0.805	0.779
$(VS_1,3)$	5	102	2.8	28.6	2	-47.44	+48.56	+18.86	+10.96	+9.36	0.31	0.30	0.285	0.805	0.779
$(VS_2,1)$	5	102	1.4	14.3	2	-15.28	+12.72	+0.82	+1.22	+0.22	0.29	0.275	0.235	0.866	0.821
$(VS_2,2)$	5	102	1.4	14.3	2	+51.14	-31.56	-14.26	-3.66	-1.46	0.29	0.275	0.235	0.866	0.821
$(VS_2,3)$	5	102	1.4	14.3	2	-66.42	+44.58	+15.18	+4.38	+1.58	0.29	0.275	0.235	0.866	0.821
$(VS_3,1)$	5	102	2.8	28.6	2	-19.5	+16.3	+2.6	+2.3	+0.1	0.26	0.24	0.605	0.595	0.562
$(VS_3,2)$	5	102	2.8	28.6	2	+40.24	-16.26	-10.26	-7.96	-5.66	0.26	0.24	0.605	0.595	0.562
$(VS_3,3)$	5	102	2.8	28.6	2	-39.84	+22.66	+12.96	+5.46	+5.76	0.26	0.24	0.605	0.595	0.562
$(VS_4,1)$	5	170	2.8	47.6	2	-5	+3.4	+1.2	+0.2	+0.2	0.325	0.285	0.85	0.382	0.335
$(VS_4,2)$	5	170	2.8	47.6	2	-2	+1	+1	0	0	0.325	0.285	0.85	0.382	0.335
$(VS_4,3)$	5	170	2.8	47.6	2	-3	+2.4	+0.2	+0.2	+0.2	0.325	0.285	0.85	0.382	0.335

SPECIMEN CODE	SPECIMEN THICKNESS (mm)	IMPACT HEIGHT (cm)	IMPACT WEIGHT (Kg)	IMPACT ENERGY (J)	N	ΔS_1 %	ΔS_2 %	ΔS_3 %	ΔS_4 %	ΔS_5 %	ν_{avg}	ν_{ref}	ν_{ref}	K_{avg}	K_{ref}	D
$(VS_5,1)$	5	200	2.8	55.6	1	-6.45	+5.63	+0.7	+0.25	+0.13	0.45	0.36	1.78	0.26	0.21	
$(VS_5,2)$	5	200	2.8	55.6	1	+15.29	-9.46	-2.81	-1.81	-1.41	0.45	0.36	1.78	0.26	0.21	
$(VS_5,3)$	5	200	2.8	55.6	1	-21.74	+15.11	+2.11	+1.26	+1.26	0.45	0.36	1.78	0.26	0.21	
(Mean,1)	5	-	-	-	-	+0.74	+2.26	-3.44	-2.24	-0.14	0.38	0.30	0.30	1	1	
(Mean,2)	5	-	-	-	-	+43.7	-27.8	8.3	-5.7	-2.2	0.38	0.30	0.30	1	1	
(Mean,3)	5	-	-	-	-	-44.44	+29.86	-7.26	+5.26	+1.86	0.38	0.30	0.30	1	1	

SPECIMEN CODE	SPECIMEN THICKNESS (mm)	IMPACT HEIGHT (cm)	IMPACT WEIGHT (Kg)	IMPACT ENERGY (J)	N	ΔS_1 %	ΔS_2 %	ΔS_3 %	ΔS_4 %	ΔS_5 %	ν_{avg}	ν_{ref}	ν_{ref}	K_{avg}	K_{ref}	D
$(S_1D_1,1)$	5	150	2.8	42	1.2	-21.48	+11.54	+3.24	+2.24	+2.24	0.31	0.30	0.34	0.574	0.556	
$(S_1D_1,2)$	5	150	2.8	42	1.2	-48.44	+40.46	-17.16	-6.16	-6.16	0.31	0.30	0.34	0.574	0.556	
$(S_1D_1,3)$	5	150	2.8	42	1.2	68.1	+52.2	-18.4	-8.2	-8	0.31	0.30	0.34	0.574	0.556	
$(S_1D_1S_2D_1D_1,1)$	5	102	2.8	28.6	1.2	-19.6	+12.8	+4.0	+1.8	+1.2	0.31	0.30	0.285	0.805	0.779	
$(S_1D_1S_2D_1D_1,2)$	5	102	2.8	28.6	1.2	+48.32	-28.8	-9.78	-7.78	-4.78	0.31	0.30	0.285	0.805	0.779	
$(S_1D_1S_2D_1D_1,3)$	5	102	2.8	28.6	1.2	-47.92	+27.78	+17.78	+8.28	+6.18	0.31	0.30	0.285	0.805	0.779	
$(S_2D_1,1)$	5	110	2.8	30.8	1.2	-12.8	+11.1	+0.8	+0.7	+0.2	0.29	0.275	0.33	0.784	0.745	
$(S_2D_1,2)$	5	110	2.8	30.8	1.2	+61.68	-35.42	-17.72	-6.72	-1.82	0.29	0.275	0.33	0.784	0.745	
$(S_2D_1,3)$	5	110	2.8	30.8	1.2	-74.48	+46.52	+18.53	+7.42	+2.72	0.29	0.275	0.33	0.784	0.745	
$(S_2D_2,1)$	5	102	1.4	14.3	1.2	-8.84	+10.29	+1.36	+2.36	-0.56	0.29	0.275	0.235	0.866	0.821	
$(S_2D_2,2)$	5	102	1.4	14.3	1.2	-28.66	-26.81	-10.31	-3.81	-3.46	0.29	0.275	0.235	0.866	0.821	
$(S_2D_2,3)$	5	102	1.4	14.3	1.2	38.2	+46	+10.8	+1.2	+3.2	0.29	0.275	0.235	0.866	0.821	

Table 10.5: Neural Network training Data (RIM).

SPECIMEN CODE	SPECIMEN THICKNESS (mm)	IMPACT HEIGHT (cm)	IMPACT WEIGHT (Kg)	IMPACT ENERGY (J)	N	ΔS_1 %	ΔS_2 %	ΔS_3 %	ΔS_4 %	ΔS_5 %	ν_{neg}	ν_{ref}	ν_{def}	K_{neg}	K_{ref}	D
$(S_2D_1D_{r1})$	5	170	2.8	47.6	1.2	-1.25	+1.25	+0.4	+0.20	+0.10	0.325	0.285	0.878	0.37	0.325	
$(S_2D_1D_{r2})$	5	170	2.8	47.6	1.2	-1	+0.25	+0.25	+0.20	+0.1	0.325	0.285	0.878	0.37	0.325	
$(S_2D_1D_{r3})$	5	170	2.8	47.6	1.2	-1.25	+1.2	+0.05	0	0	0.325	0.285	0.876	0.37	0.325	
$(S_2D_1D_{r1})$	5	200	2.8	55.6	1.2	-3.75	+6	+1	+0.4	+0.25	3.45	0.36	1.7	0.265	0.212	
$(S_2D_1D_{r2})$	5	200	2.8	55.6	1.2	+16.5	-10.5	-3	-1.2	-1.2	0.45	0.36	1.7	0.265	0.212	
$(S_2D_1D_{r3})$	5	200	2.8	55.6	1.2	-24.25	+16.5	+4	+1.9	+1.85	0.45	0.36	1.7	0.265	0.212	

SPECIMEN CODE	SPECIMEN THICKNESS (mm)	IMPACT HEIGHT (cm)	IMPACT WEIGHT (Kg)	IMPACT ENERGY (J)	N	ΔS_1 %	ΔS_2 %	ΔS_3 %	ΔS_4 %	ΔS_5 %	ν_{neg}	ν_{ref}	ν_{def}	K_{neg}	K_{ref}	D
(VX_{r1})	2	102	1.4	14.3	1	-15.42	+7.68	+5.68	+1.68	+0.28	0.67	0.64	1	0.67	1.64	
(VX_{r2})	2	102	1.4	14.3	1	+75.12	-41.78	-10.78	-10.78	-6.78	0.67	0.64	1	0.67	1.64	
(VX_{r3})	2	102	1.4	14.3	1	88.34	+49.66	+16.46	+12.46	+10.16	0.67	0.64	1	0.67	1.64	
(VX_{r1})	2	51	1.4	7.14	1	-13.107	+6.328	+4.828	+1.428	+0.128	0.67	0.64	0.85	0.788	0.713	
(VX_{r2})	2	51	1.4	7.14	1	+62.152	-35.313	-9.163	-9.163	-6.313	0.67	0.64	0.85	0.788	0.713	
(VX_{r3})	2	51	1.4	7.14	1	-75.259	+42.041	+13.991	+10.391	+8.636	0.67	0.64	0.85	0.788	0.713	
(VX_{r1})	2	30	1.4	4.76	1.2	-24.72	+18.88	+4.68	+0.28	+0.68	0.615	0.5	0.823	0.745	0.606	
(VX_{r2})	2	30	1.4	4.76	1.2	+37.76	-16.24	-10.24	-6.84	-6.24	0.615	0.5	0.823	0.745	0.606	
(VX_{r3})	2	30	1.4	4.76	1.2	-43.48	+33.22	+15.02	+7.22	+7.02	0.615	0.5	0.823	0.745	0.606	
(VX_{r1})	2	102	2.8	28.6	1.2	-8.3625	+7.0425	-8.875	-0.365	+0.475	0.615	0.5	1.25	0.492	0.4	
(VX_{r2})	2	102	2.8	28.6	1.2	+18.25	-11.825	-3.3125	-2.0125	-1.705	0.615	0.5	1.25	0.492	0.4	
(VX_{r3})	2	102	2.8	28.6	1.2	-27.175	+18.887	+3.9875	+1.95	+1.95	0.615	0.5	1.25	0.492	0.4	

SPECIMEN CODE	SPECIMEN THICKNESS (mm)	IMPACT HEIGHT (cm)	IMPACT WEIGHT (Kg)	IMPACT ENERGY (J)	N	ΔS_1 %	ΔS_2 %	ΔS_3 %	ΔS_4 %	ΔS_5 %	ν_{neg}	ν_{ref}	ν_{def}	K_{neg}	K_{ref}	D
(VX_{r1})	5	102	1.4	14.3	1	-1.38	+1.32	+0.12	-0.02	-0.04	0.315	0.36	0.36	0.875	0.833	
(VX_{r2})	5	102	1.4	14.3	1	+14.7	-10.8	+0.3	+1.1	+0.74	0.315	0.36	0.36	0.875	0.833	
(VX_{r3})	5	102	1.4	14.3	1	-16.28	+10.32	-0.18	-1.08	-0.78	0.315	0.36	0.36	0.875	0.833	
(VX_{r1})	5	51	1.4	7.14	1	0.36	+7.24	+0.64	+0.24	+0.24	0.335	0.295	0.35	0.957	0.843	
(VX_{r2})	5	51	1.4	7.14	1	+16.68	-14.02	-1.92	-0.72	-0.12	0.335	0.295	0.35	0.957	0.843	
(VX_{r3})	5	51	1.4	7.14	1	-25.04	+21.26	+2.46	+0.96	+0.36	0.335	0.295	0.35	0.957	0.843	
(VX_{r1})	5	34	1.4	4.76	1	-2.25	+1.38	+0.48	+0.18	+0.18	0.315	0.305	0.345	0.915	0.884	
(VX_{r2})	5	34	1.4	4.76	1	+37.6	-22.8	-3.8	-1.3	+0.1	0.315	0.305	0.345	0.915	0.884	
(VX_{r3})	5	34	1.4	4.76	1	-29.82	+24.26	+3.98	+0.68	+0.08	0.315	0.305	0.345	0.915	0.884	

Table 10.5: Neural Network Training Data (RIM).

SPECIMEN CODE	SPECIMEN THICKNESS (mm)	IMPACT HEIGHT (cm)	IMPACT WEIGHT (Kg)	IMPACT ENERGY (J)	N	ΔS_1 %	ΔS_2 %	ΔS_3 %	ΔS_4 %	ΔS_5 %	I_{avg}	I_{ref}	I_{def}	K_{avg}	K_{ref}	D
$(VX_{19,1})$	4	102	1.4	14.3	1						0.515	0.48	0.625	0.824	0.768	
$(VX_{19,2})$	4	102	1.4	14.3	1						0.515	0.48	0.625	0.824	0.768	
$(VX_{19,3})$	4	102	1.4	14.3	1						0.515	0.48	0.625	0.824	0.768	
$(VX_{20,1})$	4	51	1.4	7.14	1						0.505	0.465	0.58	0.871	0.801	
$(VX_{20,2})$	4	51	1.4	7.14	1						0.505	0.465	0.58	0.871	0.801	
$(VX_{20,3})$	4	51	1.4	7.14	1						0.505	0.465	0.58	0.871	0.801	
$(VX_{21,1})$	4	34	1.4	4.76	1						0.515	0.48	0.625	0.824	0.768	
$(VX_{21,2})$	4	34	1.4	4.76	1						0.515	0.48	0.625	0.824	0.768	
$(VX_{21,3})$	4	34	1.4	4.76	1						0.515	0.48	0.625	0.824	0.768	
$(VX_{18,1})$	4	102	0.7	7.14	1						0.495	0.415	0.605	0.818	0.686	
$(VX_{18,2})$	4	102	0.7	7.14	1						0.495	0.415	0.605	0.818	0.686	
$(VX_{18,3})$	4	102	0.7	7.14	1						0.495	0.415	0.605	0.818	0.686	

SPECIMEN CODE	SPECIMEN THICKNESS (mm)	IMPACT HEIGHT (cm)	IMPACT WEIGHT (Kg)	IMPACT ENERGY (J)	N	ΔS_1 %	ΔS_2 %	ΔS_3 %	ΔS_4 %	ΔS_5 %	I_{avg}	I_{ref}	I_{def}	K_{avg}	K_{ref}	D
$(VX_{49,1})$	4	51	0.7	3.7	1						0.445	0.425	0.545	0.817	0.780	
$(VX_{49,2})$	4	51	0.7	3.7	1						0.445	0.425	0.545	0.817	0.780	
$(VX_{49,3})$	4	51	0.7	3.7	1						0.445	0.425	0.545	0.817	0.780	
$(VX_{50,1})$	4	34	0.7	2.38	1						0.48	0.455	0.595	0.807	0.765	
$(VX_{50,2})$	4	34	0.7	2.38	1						0.48	0.455	0.595	0.807	0.765	
$(VX_{50,3})$	4	34	0.7	2.38	1						0.48	0.455	0.595	0.807	0.765	

SPECIMEN CODE	SPECIMEN THICKNESS (mm)	IMPACT HEIGHT (cm)	IMPACT WEIGHT (Kg)	IMPACT ENERGY (J)	N	ΔS_1 %	ΔS_2 %	ΔS_3 %	ΔS_4 %	ΔS_5 %	I_{avg}	I_{ref}	I_{def}	K_{avg}	K_{ref}	D
$(VX_{15,56,1})$ [5]	5	-	-	-	-	-7.56	+7.12	+0.44	-0.22	3	0.255	0.245	810 R5	0.94	0.86	
$(VX_{15,56,2})$ [5]	5	-	-	-	-	+35.38	-22.22	-9.92	-3.52	-1.32	0.255	0.245	810 R5	0.94	0.86	
$(VX_{15,56,3})$ [5]	5	-	-	-	-	-43.44	+29.34	+9.44	+3.24	+1.32	0.255	0.245	810 R5	0.94	0.86	
$(VX_{17,1})$ [10]	5	-	-	-	-	-1.3	+0.8	+0.2	0	0	0.275	0.31	810 R5	0.94	0.86	
$(VX_{17,2})$ [10]	5	-	-	-	-	+53.24	-35.76	-11.26	-4.26	-1.96	0.275	0.31	810 R5	0.94	0.86	
$(VX_{17,3})$ [10]	5	-	-	-	-	-54.24	+36.56	+11.46	+4.26	+1.96	0.275	0.31	810 R5	0.94	0.86	
$(VX_{16,37,1})$	5	-	-	-	-	-1.48	+0.58	-0.62	-0.72	-0.72	0.253	0.283	0.35	0.923	0.809	
$(VX_{16,37,2})$	5	-	-	-	-	+50.46	-30.64	-12.04	-5.74	-2.54	0.253	0.283	0.35	0.923	0.809	
$(VX_{16,37,3})$	5	-	-	-	-	-48.98	+31.22	+11.42	+5.32	+2.52	0.253	0.283	0.35	0.923	0.809	
$(VX_{17,45,1})$	10	$VX_{16,37}$: Contains Plastic Inclusions												0.37	0.35	
$(VX_{17,45,2})$	10	-	-	-	-									0.37	0.35	
$(VX_{17,45,3})$	10	-	-	-	-									0.37	0.35	

Table 10.5: Neural Networks Training Data (RIM).

SPECIMEN CODE	SPECIMEN THICKNESS (mm)	IMPACT HEIGHT (cm)	IMPACT WEIGHT (Kg)	IMPACT ENERGY (J)	N	ΔS_1 %	ΔS_2 %	ΔS_3 %	ΔS_4 %	ΔS_5 %	t_{exp}	t_{ref}	t_{def}	K_{exp}	K_{ref}	D
$(VX_{1,1},1)$	31	1.4	102	14.3	1						0.28	0.53	3.665	0.899	3.821	
$(VX_{1,1},2)$	31	1.4	102	14.3	1						0.28	0.53	3.665	0.899	3.821	
$(VX_{1,1},3)$	31	1.4	102	14.3	1						0.28	0.53	3.665	0.899	3.821	
$(VX_{1,3},1)$	31	1.4	102	14.3	1						0.595	0.283	3.665	0.856	3.842	
$(VX_{1,3},2)$	31	1.4	102	14.3	1						0.595	0.283	3.665	0.856	3.842	
$(VX_{1,3},3)$	31	1.4	102	14.3	1						0.595	0.283	3.665	0.856	3.842	
$(VX_{1,4},1)$	31	1.4	51	7.14	1						0.58	0.283	0.665	0.847	0.854	
$(VX_{1,4},2)$	31	1.4	51	7.14	1						0.58	0.283	0.665	0.847	0.854	
$(VX_{1,4},3)$	31	1.4	51	7.14	1						0.58	0.283	0.665	0.847	0.854	
$(VX_{1,5},1)$	31	1.4	51	7.14	1						0.58	0.56	0.70	0.829	0.714	
$(VX_{1,5},2)$	31	1.4	51	7.14	1						0.58	0.56	0.70	0.829	0.714	
$(VX_{1,5},3)$	31	1.4	51	7.14	1						0.58	0.56	0.70	0.829	0.714	

SPECIMEN CODE	SPECIMEN THICKNESS (mm)	IMPACT HEIGHT (cm)	IMPACT WEIGHT (Kg)	IMPACT ENERGY (J)	N	ΔS_1 %	ΔS_2 %	ΔS_3 %	ΔS_4 %	ΔS_5 %	t_{exp}	t_{ref}	t_{def}	K_{exp}	K_{ref}	D
$(VX_{2,1},1)$	31	102	2.8	28.6	1						0.565	0.485	0.705	0.901	0.668	
$(VX_{2,1},2)$	31	102	2.8	28.6	1						0.565	0.485	0.705	0.901	0.668	
$(VX_{2,1},3)$	31	102	2.8	28.6	1						0.565	0.485	0.705	0.901	0.668	
$(VX_{2,2},1)$	31	102	2.8	28.6	1						0.59	0.54	0.825	0.715	0.633	
$(VX_{2,2},2)$	31	102	2.8	28.6	1						0.59	0.54	0.825	0.715	0.633	
$(VX_{2,2},3)$	31	102	2.8	28.6	1						0.59	0.54	0.825	0.715	0.633	
$(VX_{AB},1)$	3.R	34	1.4	4.76	1						0.505	0.43	0.665	0.753	0.613	
$(VX_{AB},2)$	3.R	34	1.4	4.76	1						0.505	0.43	0.665	0.753	0.613	
$(VX_{AB},3)$	3.R	34	1.4	4.76	1						0.505	0.43	0.665	0.753	0.613	
$(VX_{61},1)$	3.R	51	1.4	7.14	1						0.50	0.43	0.665	0.775	0.698	
$(VX_{61},2)$	3.R	51	1.4	7.14	1						0.50	0.43	0.665	0.775	0.698	
$(VX_{61},3)$	3.R	51	1.4	7.14	1						0.50	0.43	0.665	0.775	0.698	

SPECIMEN CODE	SPECIMEN THICKNESS (mm)	IMPACT HEIGHT (cm)	IMPACT WEIGHT (Kg)	IMPACT ENERGY (J)	N	ΔS_1 %	ΔS_2 %	ΔS_3 %	ΔS_4 %	ΔS_5 %	t_{exp}	t_{ref}	t_{def}	K_{exp}	K_{ref}	D
$(VX_{62},1)$	3.R	102	1.4	14.3	1						0.53	0.445	0.64	0.828	0.695	
$(VX_{62},2)$	3.R	102	1.4	14.3	1						0.53	0.445	0.64	0.828	0.695	
$(VX_{62},3)$	3.R	102	1.4	14.3	1						0.53	0.445	0.64	0.828	0.695	
$(VX_{63},1)$	3.R	102	2.8	28.6	1						0.585	0.51	0.74	0.790	0.649	
$(VX_{63},2)$	3.R	102	2.8	28.6	1						0.585	0.51	0.74	0.790	0.649	
$(VX_{63},3)$	3.R	102	2.8	28.6	1						0.585	0.51	0.74	0.790	0.649	

Table 10.6: Neural Networks Training Data (GMT).

CHAPTER 11

ANALYSIS AND DISCUSSION

11.1 Introduction.

In this chapter, images, plots and tables will provide the required evidence to firstly support some of the existing NDT techniques and their findings through new models, secondly to confirm the validity of the novel ideas, theories and mathematical models presented through out this research.

11.2 Low Frequency Techniques - Electronic Tap Testing.

(A) Woven Glass

Figure 10.1 shows plots for both the obtained experimental data and the curve fitted ones based on practical results for both 3 mm and 5 mm thick samples.The plots correlates time response (through the normalized response factors) with impact energy.

From the plots, the following can be deduced:

(1) The greater effect impact energy has on the 3 mm components compared to the same order energy applied to 5 mm ones. This enables the distinction between different thickness using this method of time

response measurement.

(2) The characteristic curve shape that is unique to this particular woven glass specimen.

(3) A point of intersection between 3 mm and 5 mm curves as they change at different rates.

(1) The damage caused due to impact will act as an obstacle affecting the propagation characteristics of an applied signal and behaving as a sub-station that receives the original signal and re-transmits it after modulating its amplitude, phase and time duration. (Refer to Chapter 6, Sections 6.1 and 6.2).

This spatial and temporal modulation is a function of both material properties and specimen dimensions in relation to the impactor ones. Hence, for the same impactor weight, shape and size the tone and sharpness of the received feedback tap signal that is fed to the electronic tap sensor would be damped at a rate controlled by the previous factors, impact energy and specimen thickness.

(2) By tracing the curves in Figure 10.1 we realize that at zero impact energy (reference undamaged sample), the normalized response is found from practical measurements of the electronic tap instrument to be unity. As the impact energy is applied the normalized response is reduced indicating the start of the damage cycle.

This reduction is consistent with equations 6.(14) and 6.(15) which include the time delay factor t_d. When increased, the impact energy tends to have the general effect of changing the tone of the received signal such that a general trend of reduction in the normalized response in the first half of the cycle is observed as the response is thought to be mainly controlled by damage caused as a result of impact with negligible surface effects. This is also consistent with equations 6.(14) and 6.(15). In the second half of the cycle, an increase is noticed in the normalized response as the time delay factor t_d moves from above t_{ref}, t_{avg} towards t_{ref}, t_{avg} indicating a redistribution of energy and a contribution of other mechanisms such as surface effects in the process in a way that the induced time delay becomes comparable to the reference and average specimen time responses. This is consistent with 6.(17) and 6.(20). This 'saddle' point leads to the formation of what we call the 'cup' function which causes the concavity of the response curve to change in direction and sign at a specific critical point. This turning point is found to be 7.14 J for 3 mm components and 14.3 J for 5 mm components with both curves intersecting at 23.8 J impact energy. The lowest points in the normalized response for both 3 mm and 5 mm (turning points) and their equivalent impact energies conform to our expectations.

It is clear that the effect of impact on a structure is a function that is related directly through a factor to the specimen thickness.

As mentioned before, both 3 mm and 5 mm curves intersect at 23.8 J which is

the start of energy levels redistribution scheme that almost eliminates the effect of component thickness as the curves normalized response approach each other before making an increase towards unity. As these curves approach a unity value and enter the saddle region and pass a certain peak point their phase and amplitude changes again under the combined influence of impact energy level, thickness and the amount of reversible or irreversible energy levels alteration.

This influence is believed to initiate another cycle through which a decrease in the normalized response is expected with increasing impact energy which can proceed in two ways, depending on material properties:

(1) Reaching another saddle point and thereby starting yet another cycle.

(2) Continue to decrease steadily in consistence with 6.(18) and 6.(21).

For (1) we would expect that at a certain saddle point X_1 and after a number of cycles N a sudden reduction in the normalized response factor due to complete structural damage to be observed. For (2) we anticipate a smooth reduction in the component integrity but within slow and acceptable rates of change. The number of cycles is a function of component shape, size, mechanical property, impactor dimensions, frequency of impact and its energy.

However, not all the experimental data agreed with the derived mathematical model as in the case of undamaged (Reference) sample where the instrument would give a unity normalized response factor at the same time as it gives near

unity factor for a damaged sample in a saddle region of defection. Hence, our mathematical model which is implemented in the analysis software would take the electronically measured values and provide a wider margin of classification and defect/non-defect detection given a value of 2 for non-defective samples while the defective one varies between zero and unity. Hence 6.(16) and 6.(19) are used mainly for decision making.

The flow chart in Figure 11.1 illustrates how the model is used in classification.

(B) GMT

Figure 10.2 illustrates normalized response of three different forms of GMT composite structures, namely:

Random: The fibre is randomly oriented within the matrix.

Perpendicular: The fibre is at right angles within the matrix.

Parallel: The fibre is at zero angle within the matrix.

From the graph the following is observed:

(1) The ability to distinguish between the three different types of composites due to their responses to impact energy.

(2) The effect of fibre orientation on the normalized response of such materials.

(3) The evidence of cyclic mechanism due to the presence of equilibrium points within the normalized response spectrum.

(4) The intersection points at different rates between random and perpendicular, parallel structural responses.

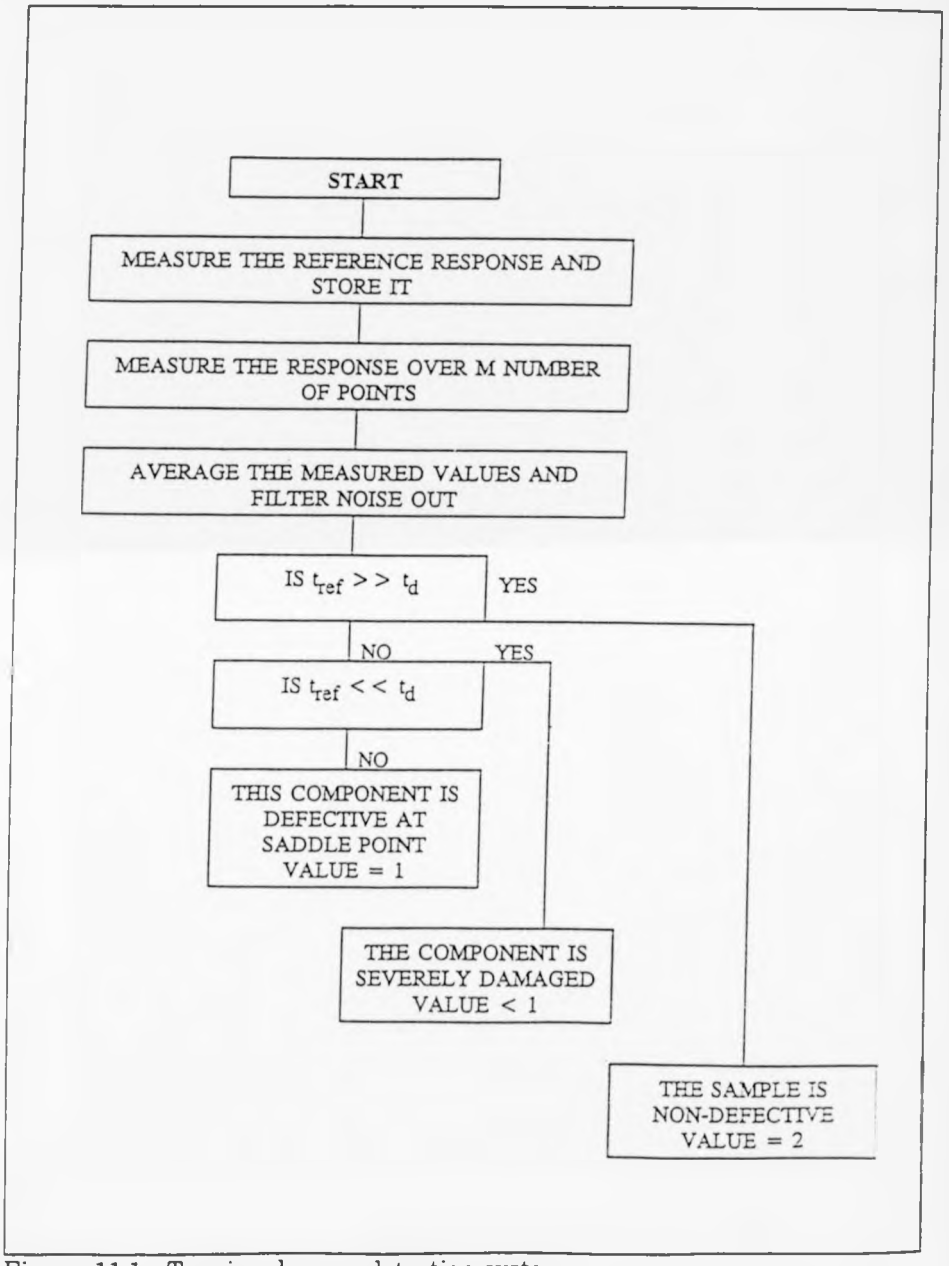

Figure 11.1: Tapping damage detection system.

By following the three curves from their starting point at unity (no damage) we immediately establish that a difference in frequency and time response (tone modulation) exists between each type of structure.

As the impact energy is applied, a reduction in the normalized response is recognised. This decrease is more marked in the case of the randomly oriented fibres component, followed by the parallel structure then the perpendicular samples which suffers the least impact effect for the same energy and thickness. The first cycle comes to an end when the curves reach their first saddle point at the same impact energy level (confirming that all curves belong to the same original composite) but different amplitude of response. It is observed (Figure 11.2) that GMT components enter their equilibrium energy region ($t_d \simeq t_{ref}$) at a much lower energy than woven glass, hence having a shorter cycle duration with the consequences of doubling the number of cycles for the same sample thickness and range of impact energies (Table 11.1). This difference in material response between GMT and woven glass is accompanied by phase reversal which is a feature that is worth further research and analysis.

As impact energy is further increased it is noted that the curves leave their saddle region as t_d starts to increase above t_{ref}, t_{avg} and enter a second cycle with a significant decrease in their normalized response with the random response intersects with the parallel one at almost half the impact energy it needed to intersect with the perpendicular response curve with the random component normalized response changing direction at a slower rate than the other two due to its original higher level of energy state restructuring with the parallel components rate of change as fastest indicating very slow energy levels recovery

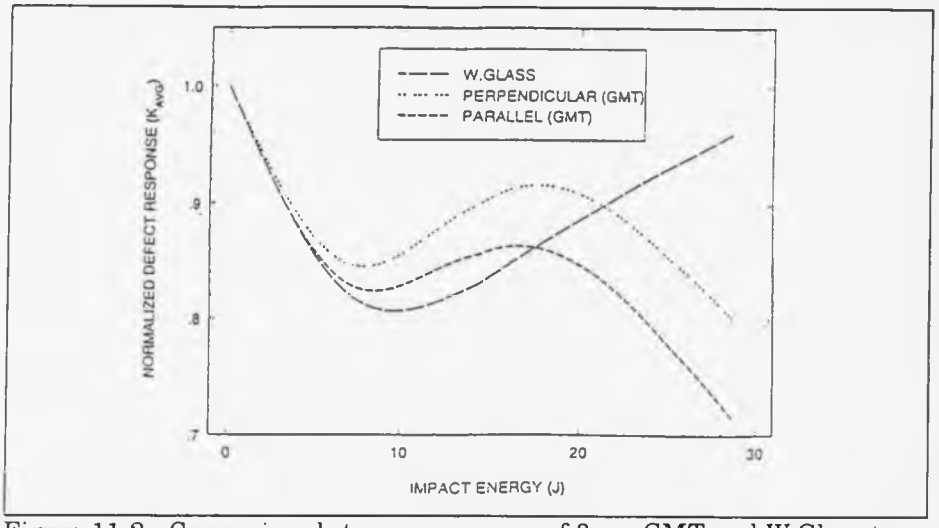

Figure 11.2: Comparison between responses of 3mm GMT and W.Glass to tapping. (Mean of 30 measurements per point).

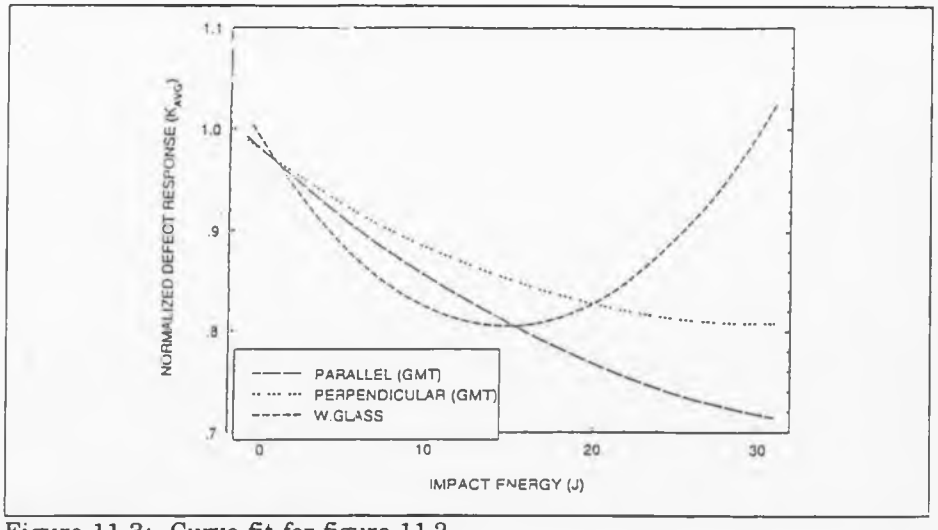

Figure 11.3: Curve fit for figure 11.2.

and marked damage compared to the other two types, hence anticipating less numbers of cycles. The perpendicular specimen is thought to be the most stable among all GMT tested components due to its relatively steady level of switching

MATERIAL.	THICKNESS.	FIRST TURNING POINT.
WOVEN GLASS	3mm	7.14J
WOVEN GLASS	5mm	14.3J
GMT	3mm	7.14J
RIM	2mm	None
RIM	3mm	None
RIM	5mm	None

Table 11.1: Comparison of composites.(Energy and Thickness).

and phase and amplitude change. For the same impact energy spectrum it is observed that as the GMT samples reach their second minimum point in the second response cycle, woven glass reaches its first saddle point which implies a ratio of 2 between the number of cycles obtained in GMT relative to woven glass for the same thickness, making woven glass a more reliable material to use. The GMT response curves also agrees with the feedback mathematical model developed in Chapter 6, sections 6.1 & 6.2.

(C) RIM

Figures 10.3-10.4 illustrate the normalized response for 2 mm and 5 mm thick specimens.

From the plots we observe:

(1) The bigger effect impact has on 2 mm components compared to 5 mm ones.

(2) The absence of any saddle regions within the response (2mm case).

(3) The effect thickness has on the response phase.

(4) The effect of paint coating the components on the normalized response.

For the 2 mm components, they are noticeably affected in a stronger way than the 5 mm ones with phase reversal in the medium part of the impact energy spectrum and expected phase reversal in the high part of the spectrum if one type of component is not painted or suffered an harmonic distortion in its tone modulation. This normalized response is consistently decreases with increasing impact energy in a much sharper and faster manner. This thickness effect agrees with the findings in both woven glass and GMT cases discussed previously.

The phase agreement between the 2 mm and 5 mm normalized response in the high region of the impact energy spectrum which is due to the difference in thickness being compensated by the increase in impact energy is parallel and comparable to the one governing the very low part of the spectrum. This is due to painting the 5 mm samples which affected their response and characteristics causing a change in the curve concavity as it converges towards its minimum limit. The parallel phase is observed after a slower decrease in the 5 mm normalized response compared to 2 mm ones which corresponds to the sample

thickness and uniformity variation in its composition. The previous also agrees with the mathematical model developed in Chapter 6 and discussed earlier in Part A.

From this analysis we realise the marked effect covering, painting or clamping can have on the phase response of a composite structure. This phenomenon needs much more research and analysis to enable both component designers and fault finders to be more accurate regarding defect detection.Figure 11.3 shows a comparison between the three tap tested types of composites, all of 3 mm thickness.

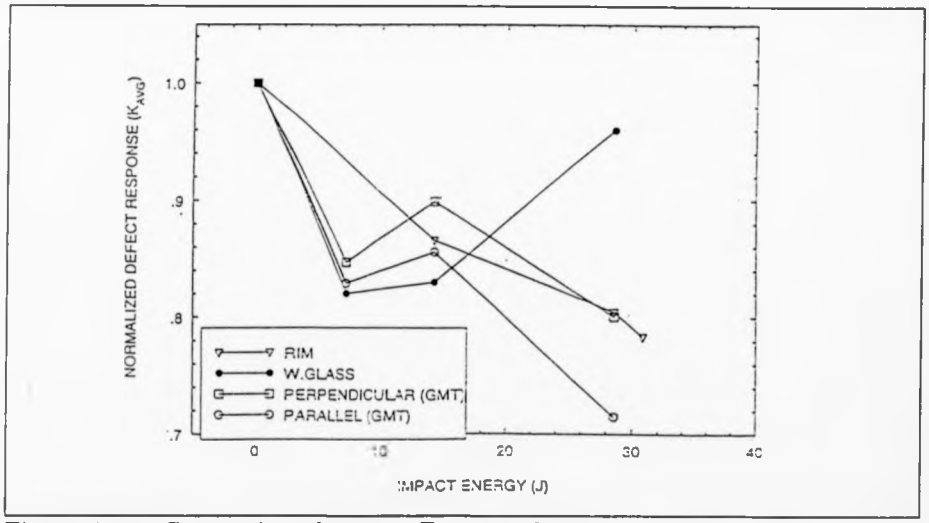

Figure 11.4: Comparison between Tap tested 3mm composites. (Mean of 30 measurements per point).

Although all curves emanate from the same point of no-damage, not far into the energy spectrum before a clear distinction between them is established. These

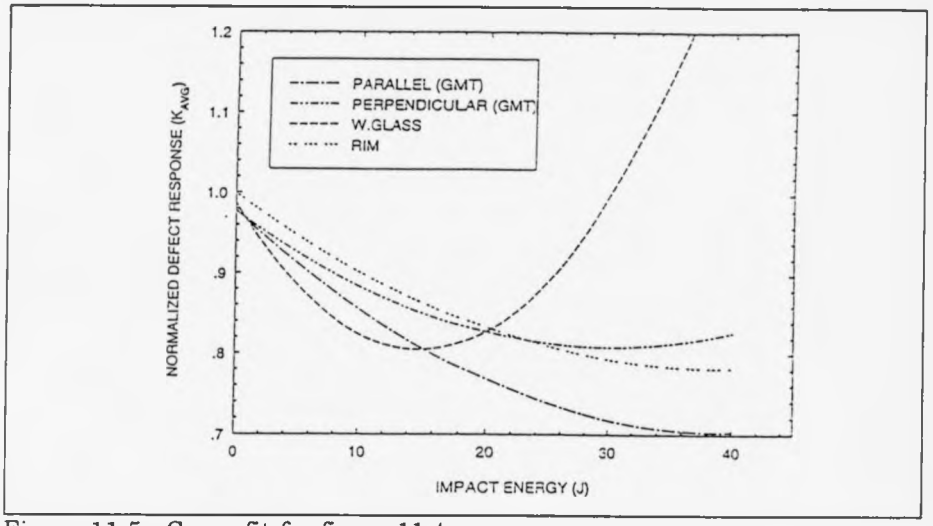

Figure 11.5: Curve fit for figure 11.4.

observations are the building block in the software classification system which is taken into account and the type and dimensions of composite tested when making a defective/non-defective decision. The flowchart in Figure 11.6 illustrates this concept.

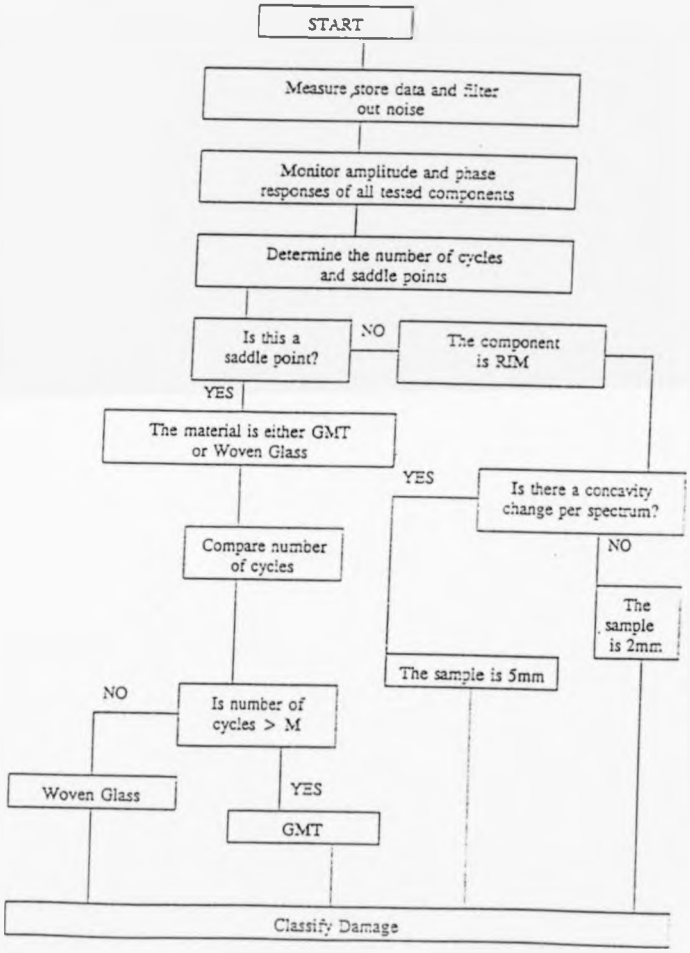

Figure 11.6: The complete tap testing and classification system.

11.2 High Frequency Techniques: Ultrasonic C-Scan.

(I) Sequential Search Through Classifier (ORIGINAL CONTRIBUTION)

(A) Woven Glass

Figure 10.5 shows a sequential classification of 3mm and 5mm woven glass components as a function of impact energy. Two major aspects of these plots are immediately noticed:

(1) The number of empty pixel levels between an undamaged component and damaged ones.

(2) The difference in pixel population per level as inversely proportional to impact energy.

For (1) it is a confirmation of thickness role in structural damage where in the 3mm case and for the same impact energies a stronger effect is observed both in amplitude of response and the creation of intermediate levels. (Refer to Chapter 4, Section 4.4 - Energy Band Model.) This leads to the conclusion that higher impact energies are needed for the 5mm components to create similar levels. These findings also agree and correlate to the observations regarding amplitude, phase and rate of change of tap response discussed in the previous section.

For (2) as the impact energy is increased, the pixel population per level is reduced and either transferred to an existing occupied one if the sample thickness to impact energy ratio is less than a certain factor, say f_t, or pixel transfer and creation of new states are observed if the ratio is greater than f_t. Figures 11.7-11.9 show a comparison in response to impact energy between 3mm and 5 mm samples for individual impact energy levels. From the plots we observe that at low impact energy (4.76J) both 3mm and 5mm specimen are similarly classified in amplitude but at different levels, where the 3mm component peak value is at twice the level height of the 5mm one. Again the thickness factor plays its role. As we move higher within the impact energy spectrum, the damage in the 3mm samples is noticeably more than the one in the 5mm samples per single impact with clear separation and classification of both in the sequential spectrum. Intermediate levels of energy and microstates are created within the 3mm components at impact energy of 14.3J which is consistent with the findings in the previous section when the electronic tap test was employed and also corresponds to the structural response entering its saddle point region with evident correlation to the thickness factor.

Using C-scan and the sequential classifier we can also distinguish between normal impact damaged samples and controlled cuts into components as shown in Figure 11.10 and also in car wishbones as complicated surfaces as illustrated in Figure 11.11. The sequential classification software is used to extract the necessary information from the converted C-scan coloured images. This software and its application to classification of images is discussed next in conjunction with our novel search through technique.

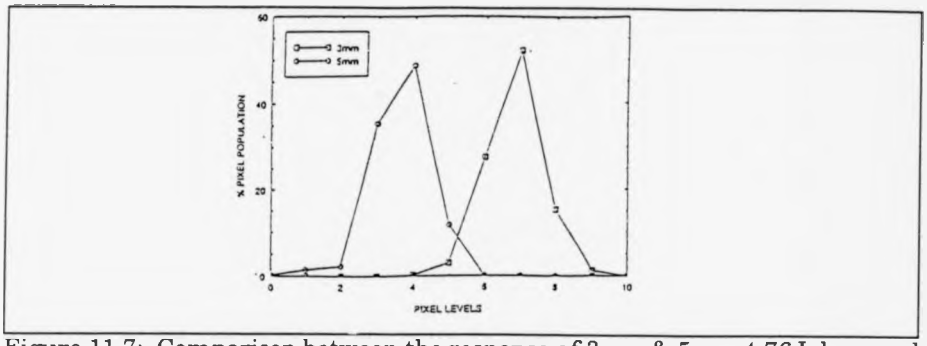

Figure 11.7: Comparison between the response of 3mm & 5mm 4.76J damaged W.Glass to C-scan. (Mean of 6 images).

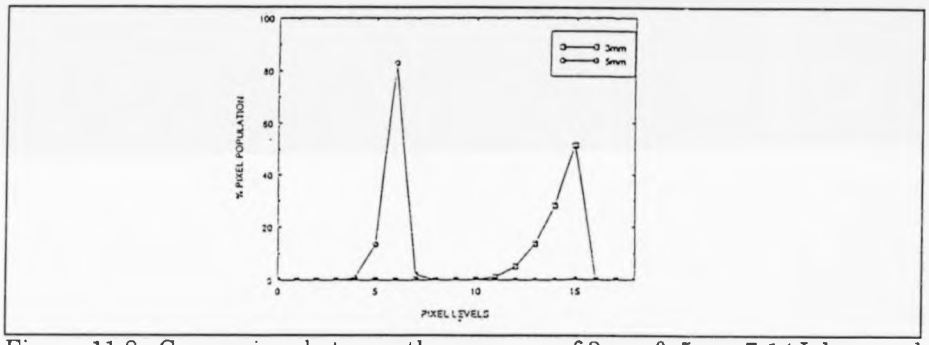

Figure 11.8: Comparison between the response of 3mm & 5mm 7.14J damaged W.Glass to C-scan. (Mean of 6 images).

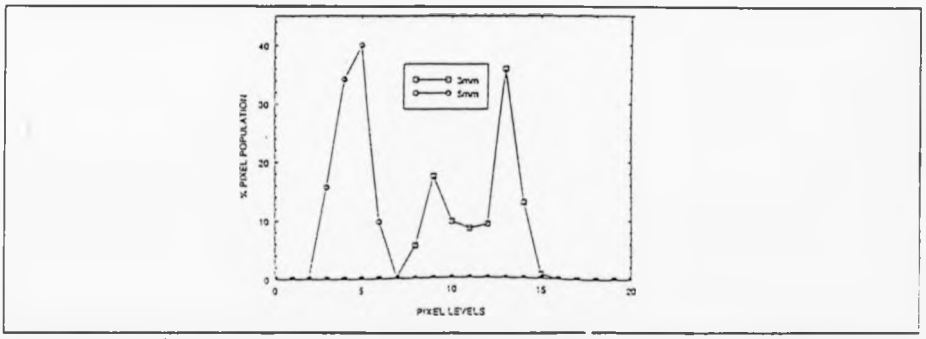

Figure 11.9: Comparison between the response of 3mm & 5mm 14.3J damaged W.Glass to C-scan. (Mean of 6 images).

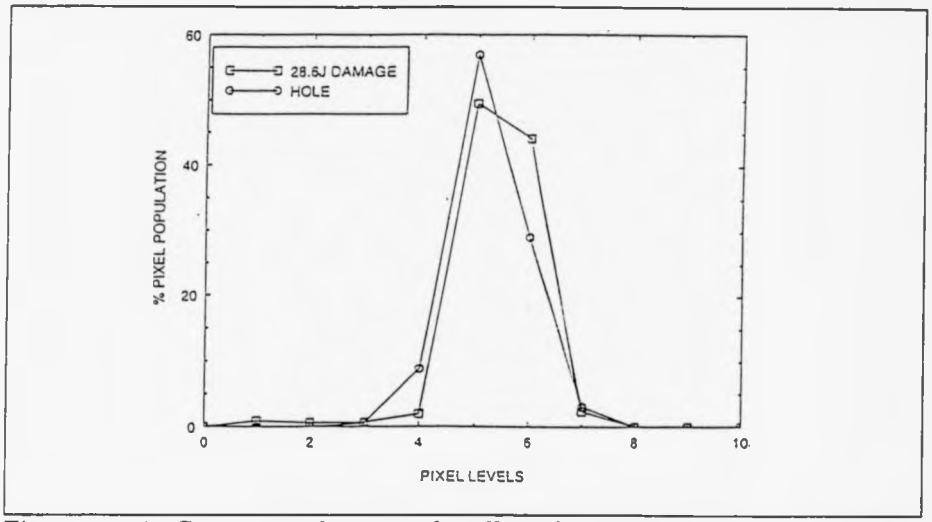

Figure 11.10: Comparison between the effect of a 28.6J impact and hole on the integrity of 5mm W.Glass component. (Mean of 6 images).

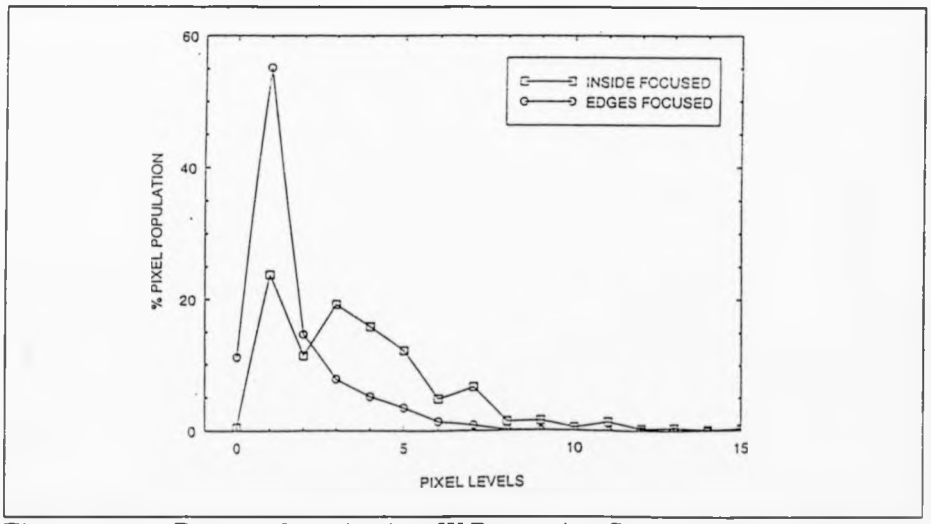

Figure 11.11: Damage detection in a W.Bone using C-scan. (Mean of 6 images).

(II) Basic Colour Mixing and Wave Search Through Technique (ORIGINAL CONTRIBUTION)

(A) Principles

The disabilities experienced by colour blind people show us the biological advantages of colour vision in detecting targets, in segregating the visual field and in identifying particular objects or states.

It is commonly suggested by various authors [213-218] that colour vision serves particularly to detect edges between equiluminant surfaces, surfaces of the same luminance but different chromaticity, but in fact, it is rare in the practical world for one surface to lie in front of another in such a way that both have the same reflectance, both lie at the same angle to the incident illumination and the nearer throws no shadow on the further. The luminosity can vary due to component surfaces lying at varying angles to the illuminant or having various reflectances.

One way in which colour assists our perception is the shared hue of different elements in a visual array. This may serve as a basis for perceptual segregation and so allow the identification of an image made from patches that vary in lightness. Segregation of the visual field into elements that belong together is an important preliminary to the actual recognition of objects.
Colour may also serve to do the following:

(a) It may help assigning an already segregated object to a given category.

(b) It may indicate what lies beneath a given surface.

In humans, the three classes of retinal cone exhibit overlapping spectral sensitivities, with peak sensitivities lying close to 420, 530 and 560 nm (Figure 11.12).

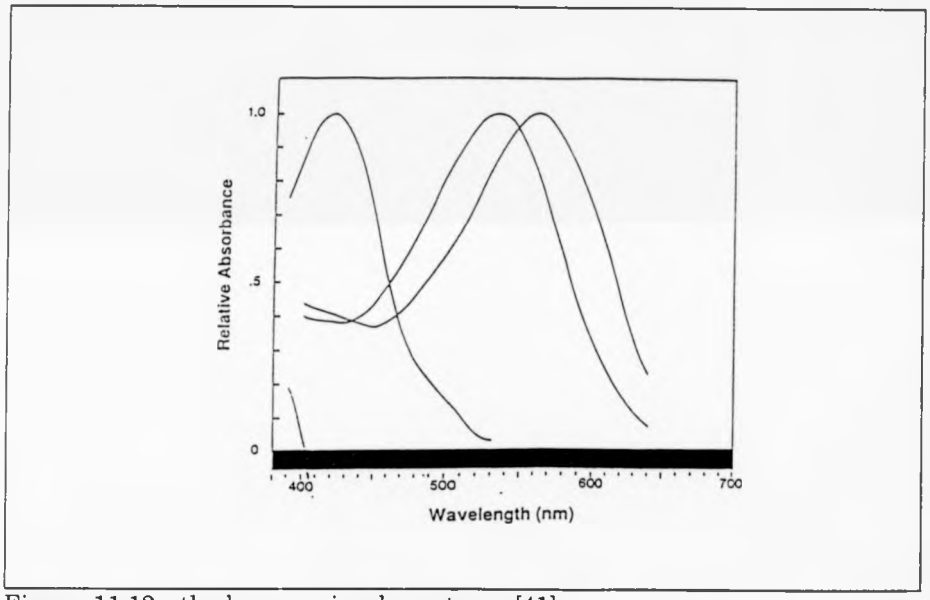

Figure 11.12: the human visual spectrum [41].

Notice the asymmetry of the spectral positions of the receptors, there is an interval of 100 nm between the short-wave and middle-wave receptors, but an interval of only 30 nm between the middle-wave and long-wave receptors.

The response of any individual receptor obeys the principle of univariance; its electrical response varies only with the rate at which photons are captured by

the outer segment, and all that changes with wavelength is the probability that any given photon will be absorbed. Thus, if the visual system is to learn about wavelength, independently of radiance, it must not only have receptors with different sensitivities but also the neural machinery to measure the relative rates of photon capture in different classes of receptors. Alternatively, we can always use wavelengths outside the scope of the human visual system to carry out damage detection and by intermixing of the original colours and their wavelength transform the captured image to fit within the human visual systems sensitivity range.

(B) The Colour Matching Functions.

Colour matching functions are simply plots of the relative amounts of three primary lights required to match monochromatic light. In other words, for any colour C_λ, colour matching functions plot the values at $R(\lambda)$, $G(\lambda)$ and $B(\lambda)$ that satisfy the expression:

$$C_\lambda = R(\lambda) + G(\lambda) + B(\lambda) \quad \text{(ALGEPRIC)} \qquad 11.(1)$$

Where:

$R(\lambda)$	:	Red (700 nm)	}
$G(\lambda)$	:	Green (546.1 nm)	} Tristimulus Values (Fig.11.13).
$B(\lambda)$	:	Blue (435.8 nm)	}

The standard light is monochromatic and so causes dramatically unequal rates

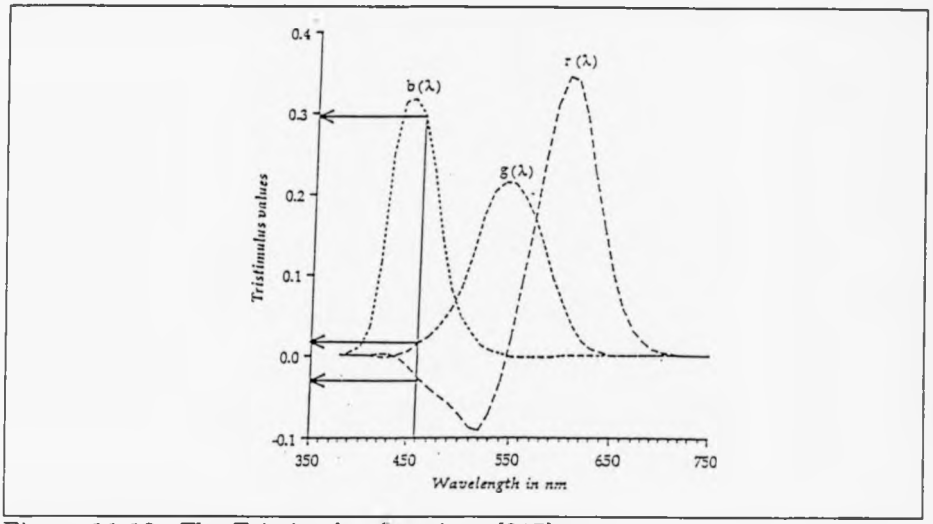

Figure 11.13: The Tristimulus functions [217].

of absorption in the three classes of cone. This can be appreciated by glancing at the cone spectral sensitivity (Figures 11.14 and 11.15). These unequal rates of absorption cannot be matched with the primary lights (except in the trivial case where the wavelength of the standard light is the same as one of the three primaries), and hence to achieve a match the standard light must first be desaturated by mixing in one of the primaries. Colour transformation is carried out through matching functions which can be used to derive tristimulus values for any spectral power distribution, and it is a fact that two colours with the same tristimulus values will match precisely. This is despite the fact that they may have very different spectral power distribution.

Our novel approach to defect detection using wave search through variation technique is illustrated in the following steps:

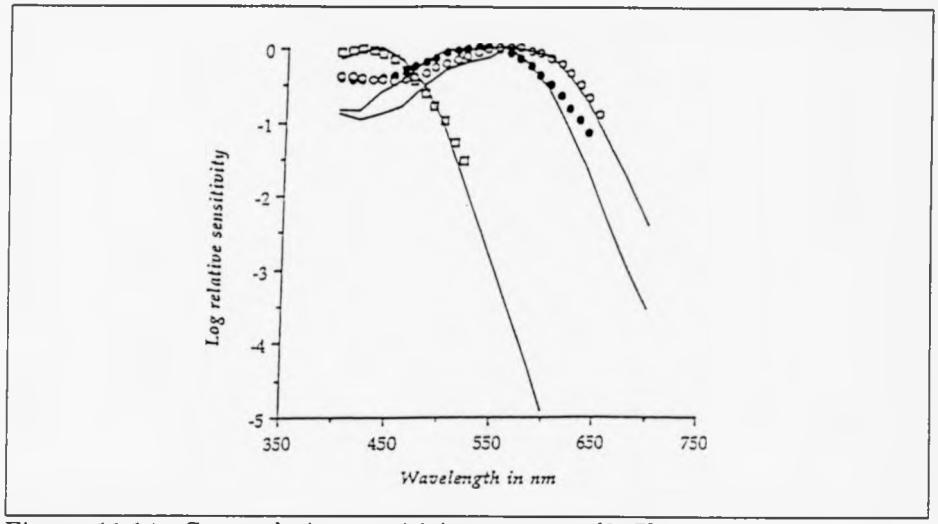

Figure 11.14: Cone relative sensitivity spectrum [217].

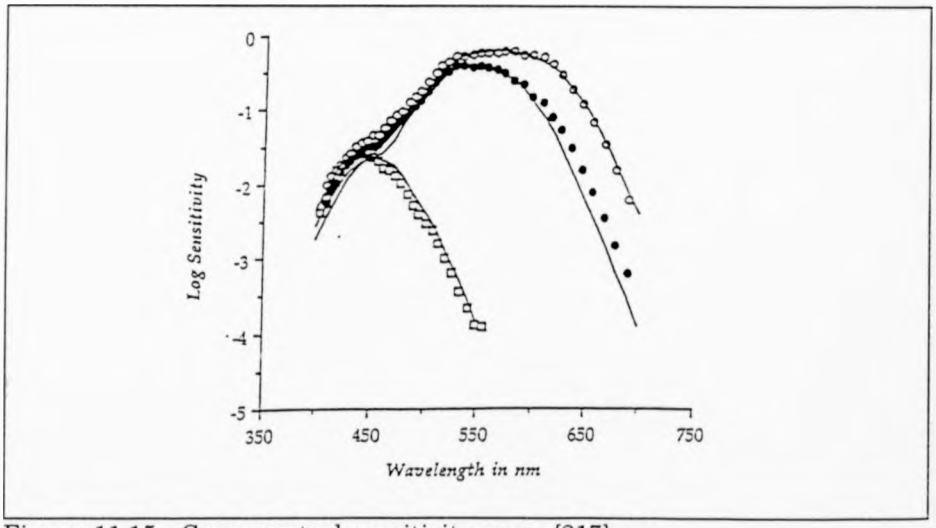

Figure 11.15: Cone spectral sensitivity curve [217].

(1) The captured image is allocated a map as shown in Figure 11.16.

(2) The mapping of the image takes place before format conversion as the only affected format will be stored in a separate file not affecting the

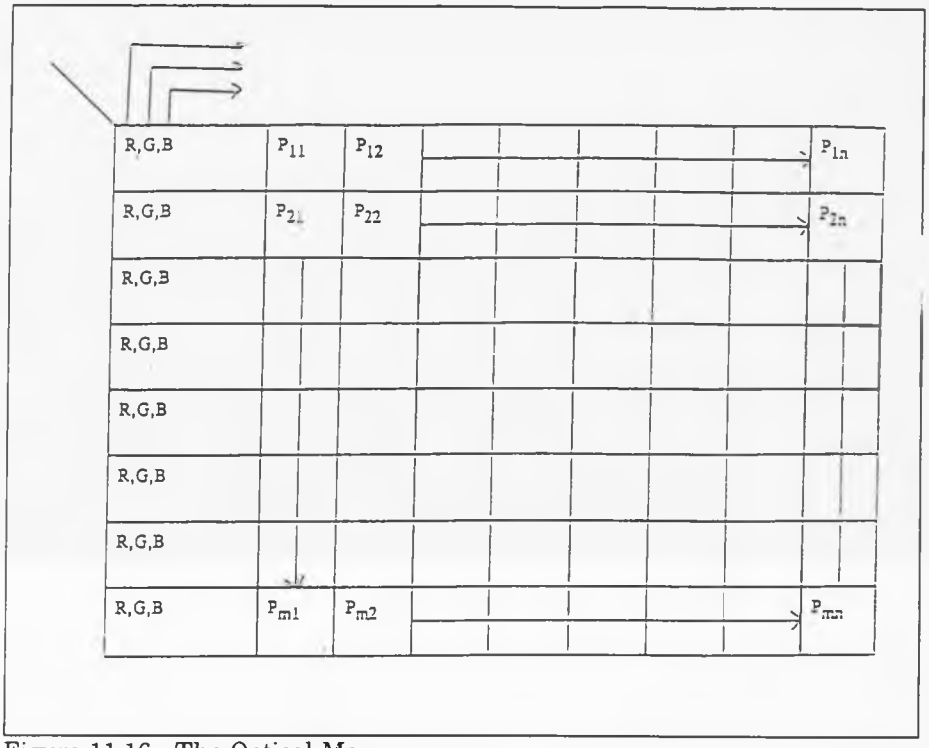

Figure 11.16: The Optical Map.

originally stored ones. This mapping and colour intermixing is based on a selection table shown in table 11.2.

The logic 0 in the table corresponds to keeping the colour value as it is fixed while the logic 1 corresponds to the one being varied at the time.

(3) When chosen the combination is used to produce separate images each of which has a separate data file that reflects the level of damage in a structure. This conversion and storage of detected damage is carried out through our image conversion software.

RED (R)	GREEN (G)	BLUE (B)
0	0	0
0	0	1
0	1	0
0	1	1
1	0	0
1	0	1
1	1	0
1	1	1

Table 11.2: Colour selection.

(4) Upon conversion of each searched through image, the resulting data files will hold the necessary data governing the state of the component and extent of damage. This is done in the form of tables such that the colour at logic one will sustain a constant new value throughout the new image file when varied resulting in the component being classified as healthy otherwise the component must have suffered a damage the extent of which is correlated to the change in the response of each single variation of the logic 1 colour data file structure.

Figures 10.6-10.8 show the obtained C-scan images for the 5mm woven glass components and the corresponding search through images carried out. Both the initial variation search through table and the subsequent ones serve to establish the extent of damage if it is seen in the original image and

highlight damages that could not be detected from the original scanned or captured image. This extent of damage is realised by establishing the number of defective layers per captured image and the reduction in the number of bits holding the original varied colour value per data file.

The images in Figures 10.6-10.8 are the source for the plots employed in Part (I) and analyzed through our novel sequential search through matrix-column classification which need only be applied to the original captured image without the need for cyclic colour variation. However, the information it provides is different in nature and application but easily correlated to the one provided by the technique described in this part.

Figures 11.17-11.19 illustrate the relationship between the original change in image composition (pixel amplitude) and the extent of damage (defective layers) for 5 mm components and the effect of impact energy level on the number of layers and defect diameter for 5 mm and 3 mm samples.

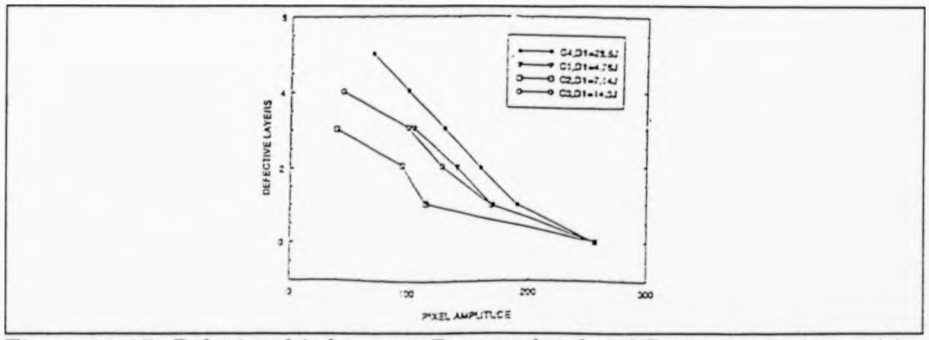

Figure 11.17: Relationship between Damage level and C-scan image intensities as a function of impact energy in 5mm W.Glass. (Mean of 6 images).

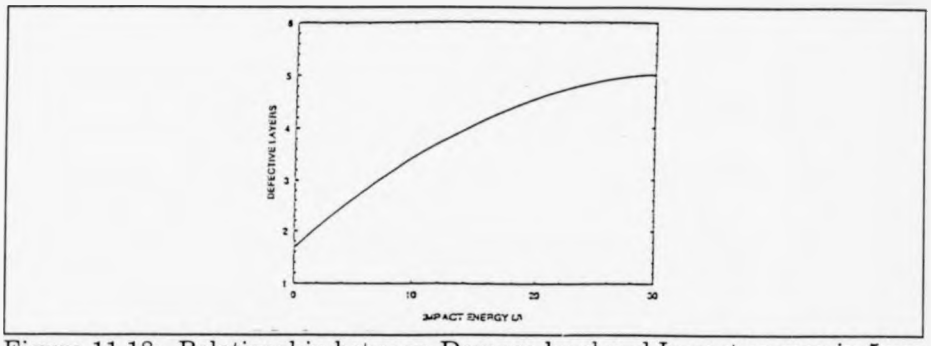

Figure 11.18: Relationship between Damage level and Impact energy in 5mm W.Glass using C-scan.

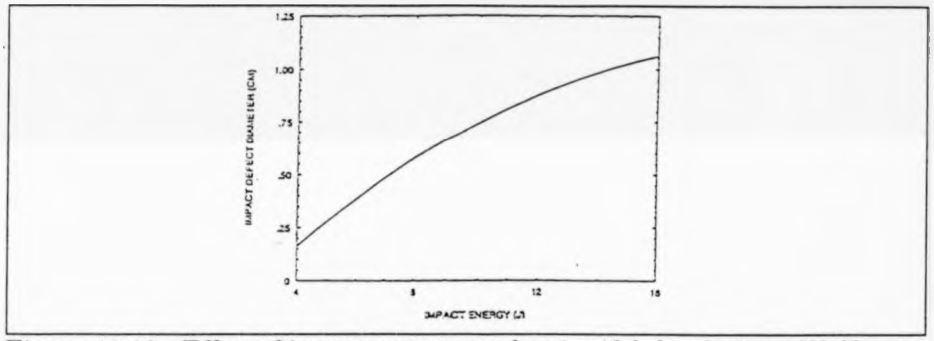

Figure 11.19: Effect of impact energy on the size if defect in 3mm W.Glass.

From the plots it is obvious that:

(1) The number of defective layers and hence extent of damage within a composite structure is proportional to the impact energy through a power law.

(2) The size of detected damage is proportional to the applied impact energy and follows similar power law.

The previous two main points are correlated in the sense that for the same impactor shape the larger the observed defect size the higher the damage extent both laterally and vertically. Hence we can hypothesize that:

$$\text{Defect diameter} \quad D = f(E_I) \qquad 11.(2)$$

and

$$\text{Number of Defects} \quad N = g(D) = g(f(E_I)) \qquad 11.(3)$$

From equations (2) and (3) and the analysis in Section 11.1 and part (I) of this section we can deduce that the 5mm specimen would have less defective layers compared to the 3mm ones for the same range of impact energies due to thickness effect.

Figures 10.9-10.10 show a 28.6J impact damaged 5mm sample with a hole drilled through it obtained through the wave search through algorithm with data files also included. Two plots are used to study the difference and effect on the specimen, namely, a direct plot of the path the transducer followed in C-scanning the component and change in data file pixel amplitude through wave variation to establish the level of damage caused.

From Figures 11.20-11.21 it is clear that both agree on the bigger damage and reduction in the component integrity due to a cut through the sample. The direct plot indicates a phase reversal which is due to change in medium, where the search through indicates layer effect due to more defective layers appearing as a result of impact with the effect of medium change neutralised, hence more accurate assessment.

Figure 10.11 illustrates C-scan images for the inner and outer parts of a wishbone which was analyzed in part (I) of this section using the matrix-column search through technique.

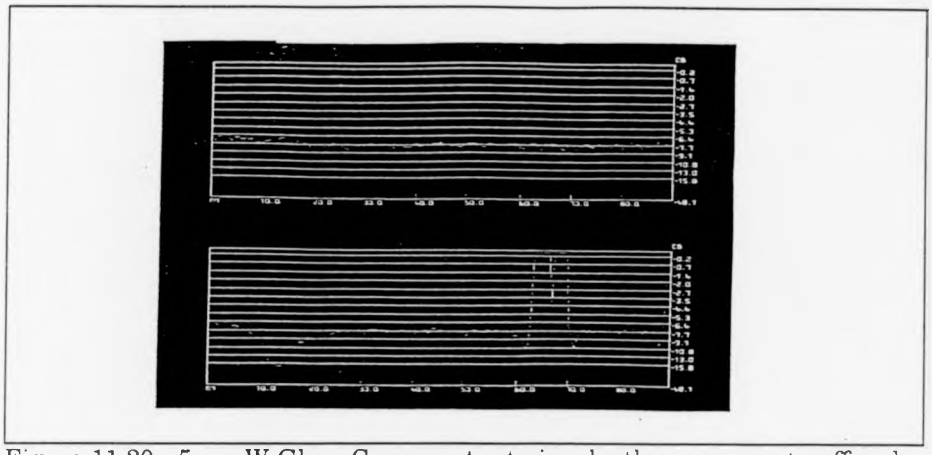

Figure 11.20: 5mm W.Glass C-scan output signals, the component suffered a 28.6J impact and a drilled hole.

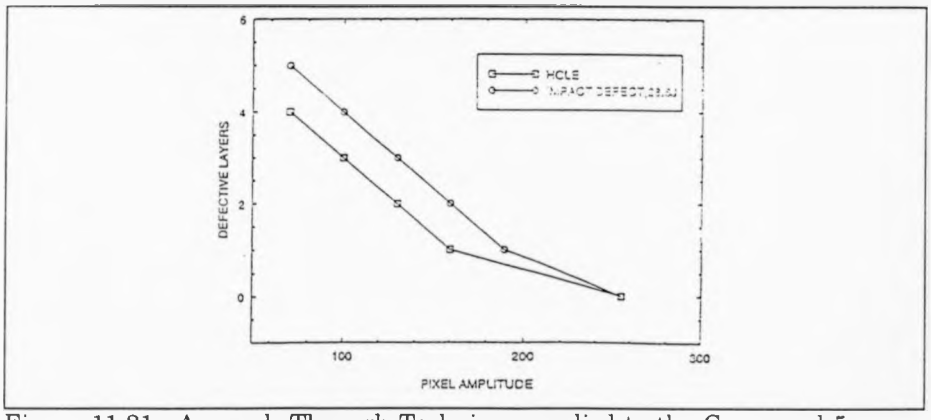

Figure 11.21: A search Through Technique applied to the C-scanned 5mm W.Glass with 28.6J impact damage and a hole. (Mean of 6 images).

(III) The Uniformity Factor Technique (ORIGINAL CONTRIBUTION).

Figures 11.22-11.25 show the effect of impact energy on the uniformity of the 3mm and 5mm woven glass samples. The uniformity factor algorithm is a

directional one that helps establish two main aspects of structural integrity:

(1) The boundary of the damage and size of defect.

(2) The phase properties of the induced damage as a function of matrix and fibre orientation through row, column comparison.

The mathematical base the algorithm adopts is explained in Chapter 8, Section 8.4, part A.

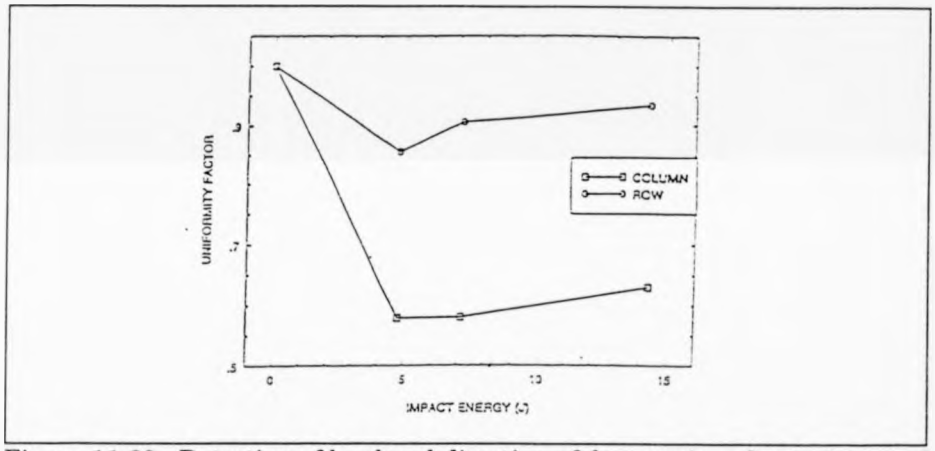

Figure 11.22: Detection of level and direction of damage in a C-scan image of 3mm W.Glass using the Uniformity Factor algorithm.(Mean of 6 images).

from the plots we immediately realize the marked effect impact has on the 3mm components compared to 5mm ones. This becomes clearer as we trace the response curve as a function of impact energy.

(A) Row Curves

As the impact energy is applied, the uniformity factor of both categories

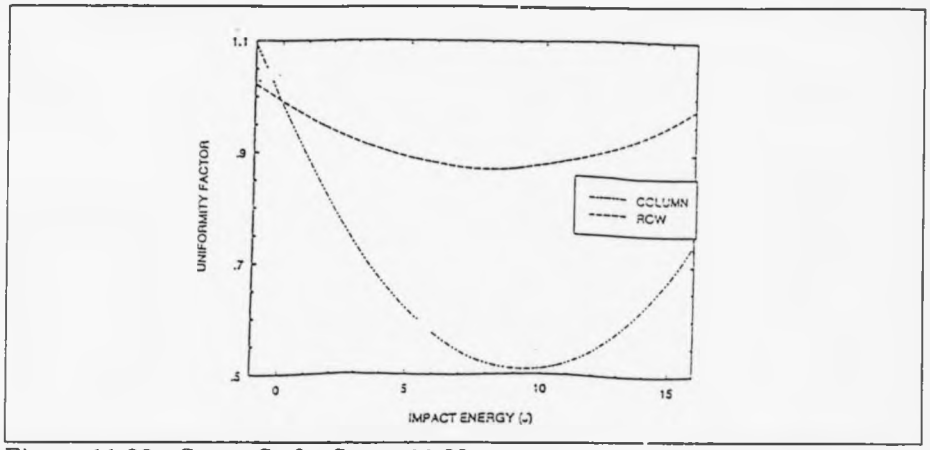

Figure 11.23: Curve fit for figure 11.22.

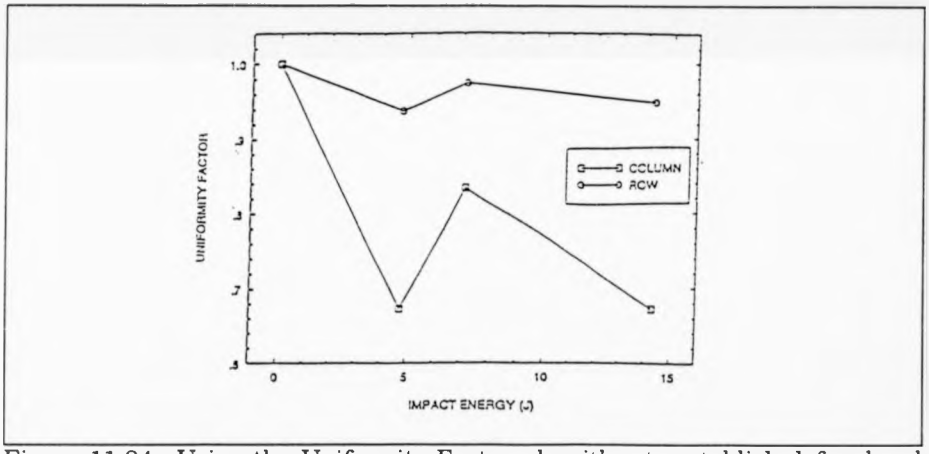

Figure 11.24: Using the Uniformity Factor algorithm to establish defect level and orientation in 5mm W.Glass through C-Scans. (Mean of 6 images).

decreases initially indicating a presence of damage. Increasing the impact energy causes both types to positively respond as the defect is scanned from within (we assume that an isolated defect is uniform).

Further increase in the impact energy has the effect of steadily increasing the uniformity factor reaction as the 3mm components enter the saddle

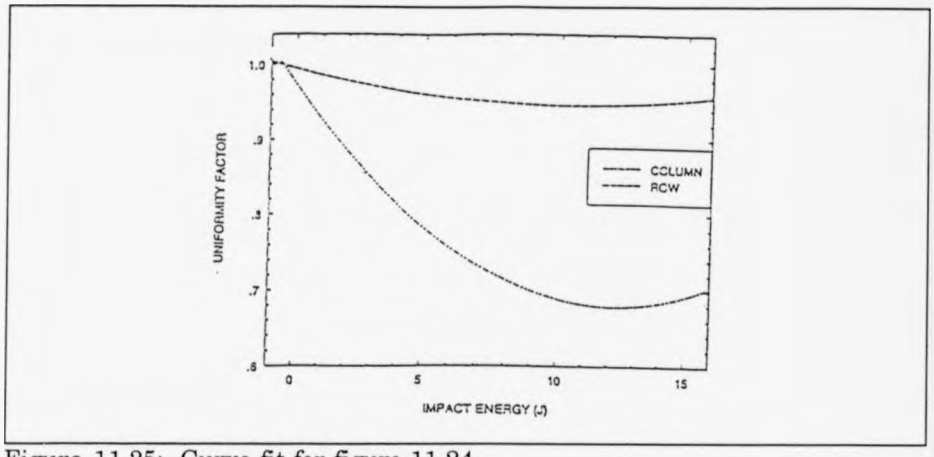

Figure 11.25: Curve fit for figure 11.24.

region of response with more lateral spread of damage while the 5mm samples enter their second cycle with the uniformity reduced corresponding to the introduction of another layer of contained, localized damage. (The thickness factor).

(B) Column Curves

The same effect is observed here with two additional important variations:

(1) The very large change in uniformity factor for the 5mm samples as they suffer localized damage (negative response).

(2) The smoother increase in the 3mm response as the components enter the saddle region.

Both (1) and (2) indicate that the main direction of damage propagation and spread is in the X-direction (as shown below) as smooth increase in the 3mm case indicates more intermediate energy levels being introduced (refer to

Chapter 4, Section 4.4 and Chapter 6, Section 6.2) while the large decrease in the 5mm case indicates that its capacity to withstand higher impact energies before reaching a saddle situation where the curves increase with uniformity.

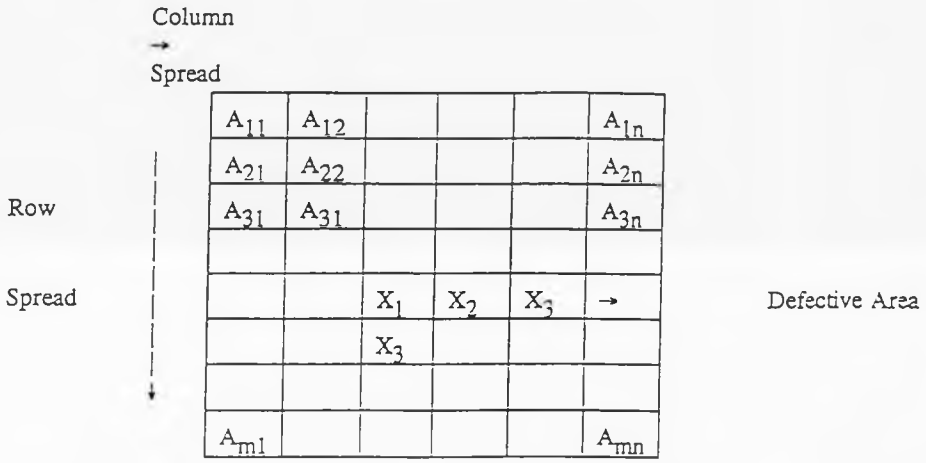

The previous ties very well with the previously used classification techniques with the advantage of providing the direction of defect propagation.

11.3 Visual Techniques.

(A) Low Temperature

(a) Woven Glass

Figures 10.12-10.17 show the overall sequential classification for a 3mm and 5mm samples using an electronic visual camera at room temperature. Three

different incident light levels at variable angles were employed in the testing process. From the plots and examining the response we realize the existence of damage due to the reduction in the classification value as a function of impact energy, but with no clear distinction between different impact energies.

This deduction required the use of our matrix column search through algorithm to interrogate each obtained image regarding effect of impact energy and thickness. Figures 11.26-11.28 illustrate the search through results.

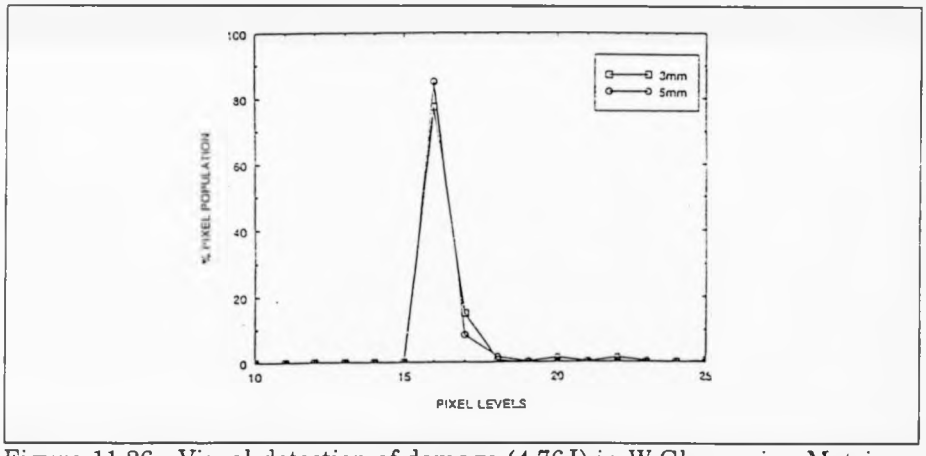

Figure 11.26: Visual detection of damage (4.76J) in W.Glass using Matrix-Column search through algorithm. (Mean of 6 images).

At 4.76J we recognize the effect of thickness as the 5mm suffers less damage, hence possess higher pixel population at the peak point. As the impact energy increased, the 3mm component starts to enter a saddle region and forms intermediate energy states with the 5mm component still holding to its overall integrity with the damage being localized. At 14.3J the situation is reversed as the 3mm contain higher percentage of pixel

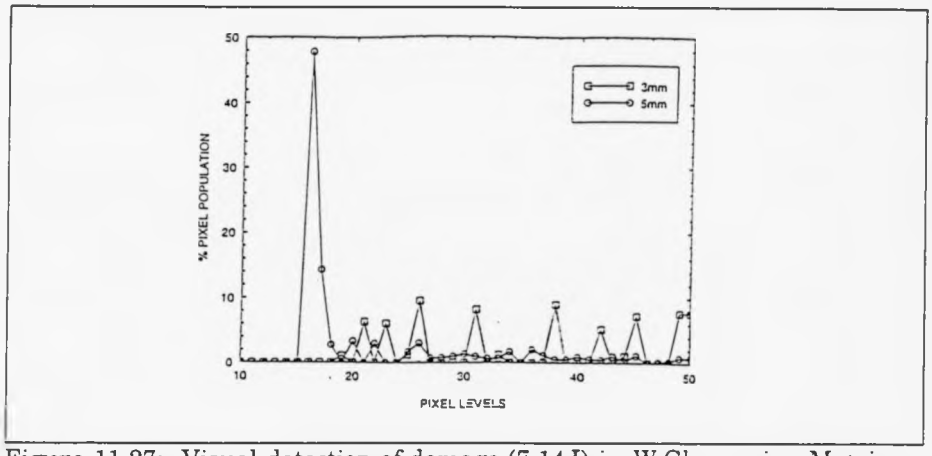

Figure 11.27: Visual detection of damage (7.14J) in W.Glass using Matrix-Column search through algorithm. (Mean of 6 images).

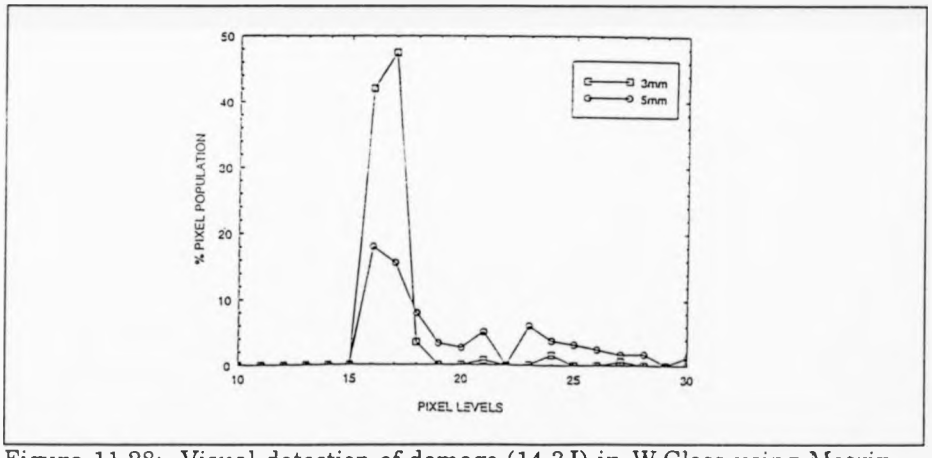

Figure 11.28: Visual detection of damage (14.3J) in W.Glass using Matrix-Column search through algorithm.(Mean of 6 images).

population corresponding to the saddle region being well established by this stage while the 5mm is just starting to enter its saddle area via intermediate states formation. This conforms extremely well with the tapping and C-scan results and provides another supporting evidence to the models established in Chapter 4 and Chapter 6.

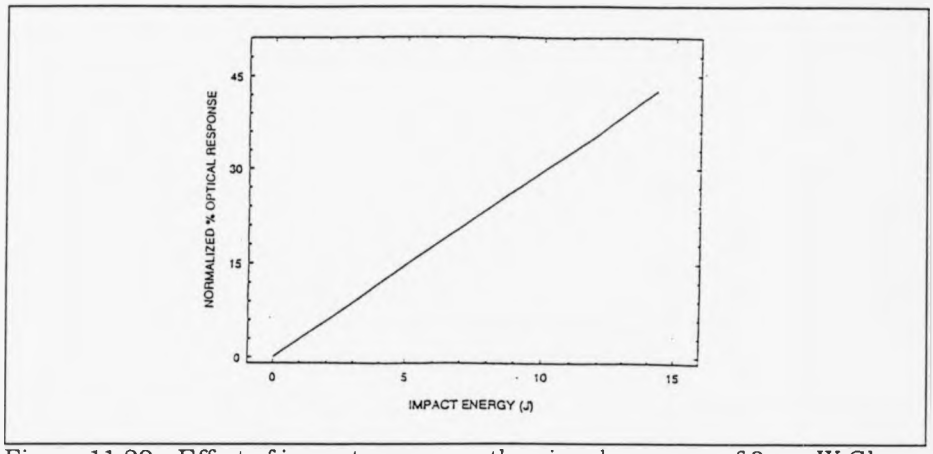

Figure 11.29: Effect of impact energy on the visual response of 3mm W.Glass.

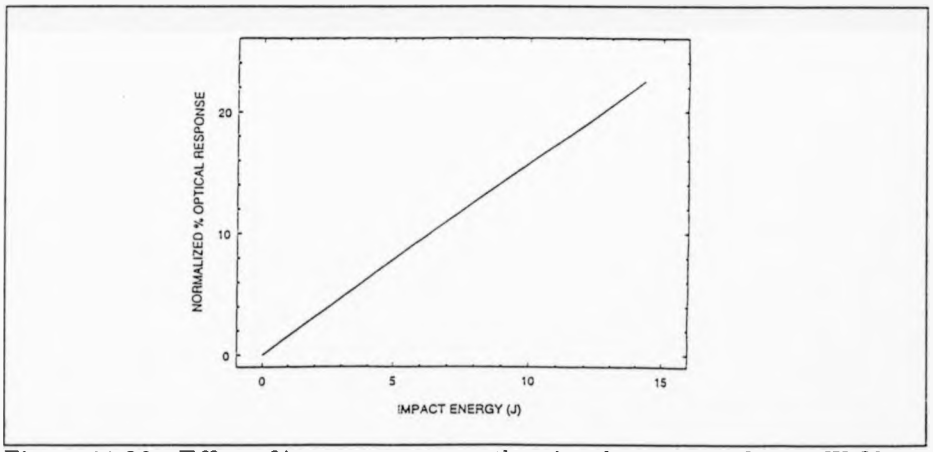

Figure 11.30: Effect of impact energy on the visual response of 5mm W.Glass.

The nature of response (shape function) of this composite material to various impact energies is illustrated in Figures 11.29-11.30. A clear direct and proportional(corresponding to the low level impact energy applied) response is observed which reflects the optical properties of such a composite under the applied conditions.

Figures 11.31-11.36 show the correlation between the visual and the C-scan tests using the sequential search through matrix-column classifier. As before at 4.76J the 3mm component is more affected by the impact hence producing closer responses. As the impact energy increased, the 3mm C-scan response approaches the visual one over pixel levels indicating the start of the saddle region and formation of the intermediate energy states where the response of the 5mm components show little sign of pixel levels transfer. As the impact energy is further increased the 3mm C-scan response moves away from the visual since the specimen now has a uniform spread of damage with the 5mm sample only suffers an amplitude reduction as it starts to enter the saddle region with intermediate levels about to be created and the damage up to this stage being localized.

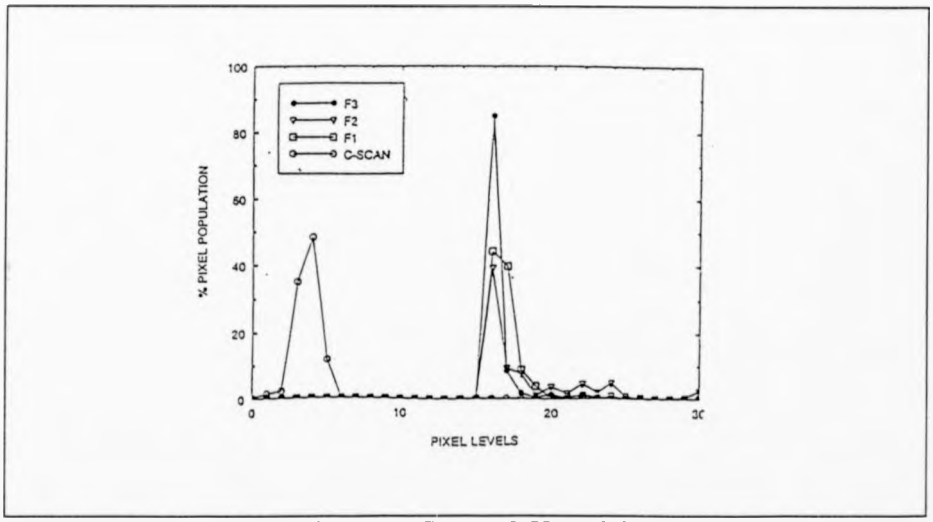

Figure 11.31: Correlation between C-scan & Visual detection of damage(4.76J) in 5mm W.Glass. (Mean of 6 images).

This concept of search through and correlation between different techniques

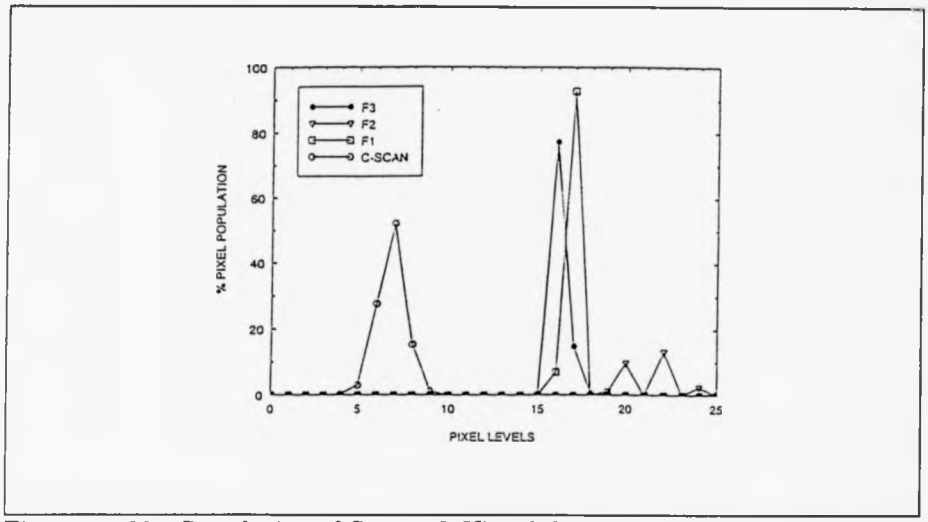

Figure 11.32: Correlation of C-scan & Visual detection of damage (4.76J) in 3mm W.Glass. (Mean of 6 images).

is a novel and useful one which is made possible by our matrix-column algorithm.

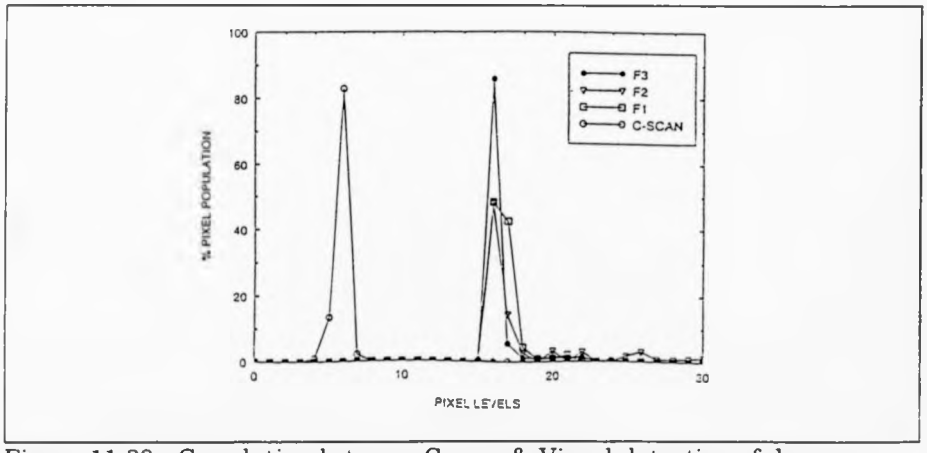

Figure 11.33: Correlation between C-scan & Visual detection of damage (7.14J)in 5mm W.Glass. (Mean of 6 images).

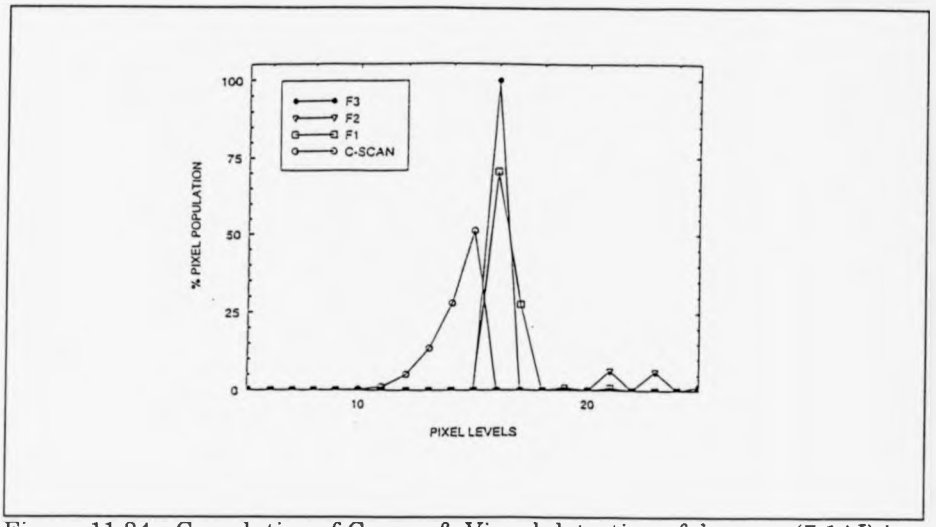

Figure 11.34: Correlation of C-scan & Visual detection of damage (7.14J) in 3mm W.Glass. (Mean of 6 images).

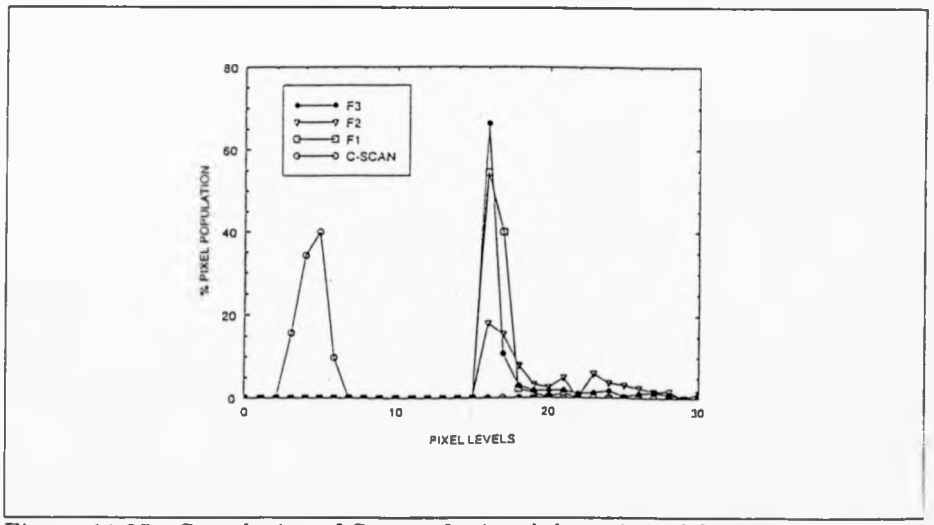

Figure 11.35: Correlation of C-scan & visual detection of damage (14.3J) in 5mm W.Glass. (Mean of 6 images).

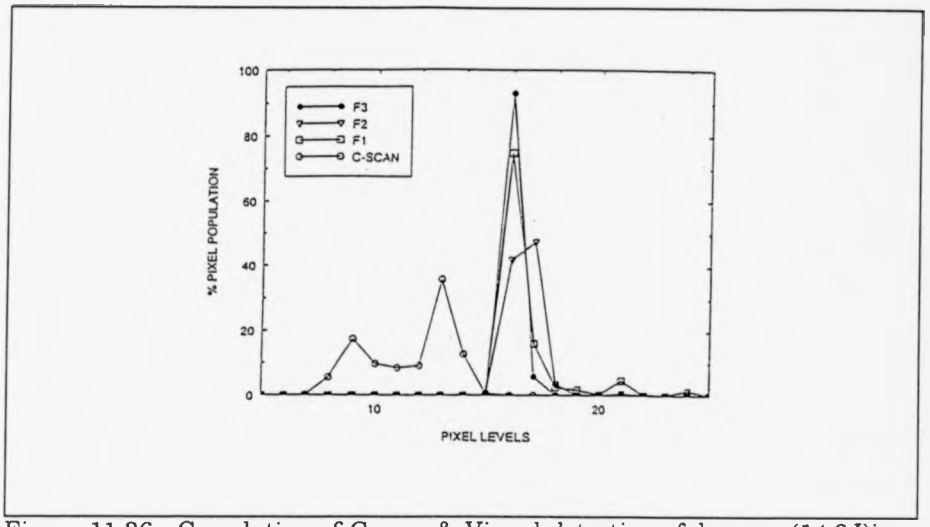

Figure 11.36: Correlation of C-scan & Visual detection of damage (14.3J)in 3mm W.Glass. (Mean of 6 images).

(b) RIM Composites

Images obtained for this type of composite (5mm and 2mm thickness) with various levels of impacts. These images were obtained using two types of our novel wave search through technique for defect detection:

(1) Outside-Image wave variation (O.I.W.V.): Variation of the applied light source externally with W.I.W.V. and W.I.D.C. used for classification.

(2) Inside-Image wave variation (I.I.W.V.): Variation of the captured image internally using developed software while keeping the applied external light source constant and employing with no need for W.I.W.V. and W.I.D.C. to be used for classification.

Further into this section we will employ another two search through

algorithms for (1), namely:

(1.1) Matrix-Column search through technique (Within-Image Wave Variation (W.I.W.V.)). This technique produces a finger print or a special pattern of the captured image and prepare the converted data file to be used as an input for Neural Networks.

(1.2) The uniformity factor technique (Within-Image Directional Classifier (W.I.D.C.)). This algorithm complement the W.I.W.V. one by producing a surface quality identification to be correlated to the captured image and level of damage using Neural Networks.

(1) The O.I.W.V. Search through algorithm:

Figures 10.18-10.22 show the impact damage images obtained using this concept. From the diagrams we realize the following main points:

(I) The existence of a defect can readily be revealed by cycling through different incident light sources applied at different angles.

(II) The deep and effective examination of components composition.

(III) The effect a change in any of the composite component properties have on the selection of the right light source for damage check.

Three different versions of the same component image are produced using this technique, namely; MB (normal light), MBL (florescent light), MBLR (mixture of MB and MBL).

The principle behind these images is related to the Energy Band Model developed earlier in Chapter 4, Section 4.4.

To have a clearer picture of the need to use more than one lighting source and its effect in interrogating a composite component a W.I.W.V. algorithm is used at two stages. Figures 10.23-10.28 illustrate the general response and first stage classification of the images in Figures 10.18-10.22.

The graphs represent the filtered change in response between the various light sources used over five sequences (S_1 - S_5). The wavelength was varied from L_1 to L_3 to establish an optical window setup function to trap and arrest the hidden impact damage defects and any surface irregularities.

The step function formed due to choice of light source and interaction with a reference sample as shown in figure 11.37.

The conditions associated with Figure 11.37 are:

$\%S_i = 100$ for $L_i = L_1$

$\%S_i = 50$ for $L_i = L_2$

$\%S_i = 100$ for $L_i = L_3$

From the classification map and the graphs we realize that for a non-defective components the change in sequential response is such that moving from L_1 to L_3 is a closed path, that is the classification of the optical response

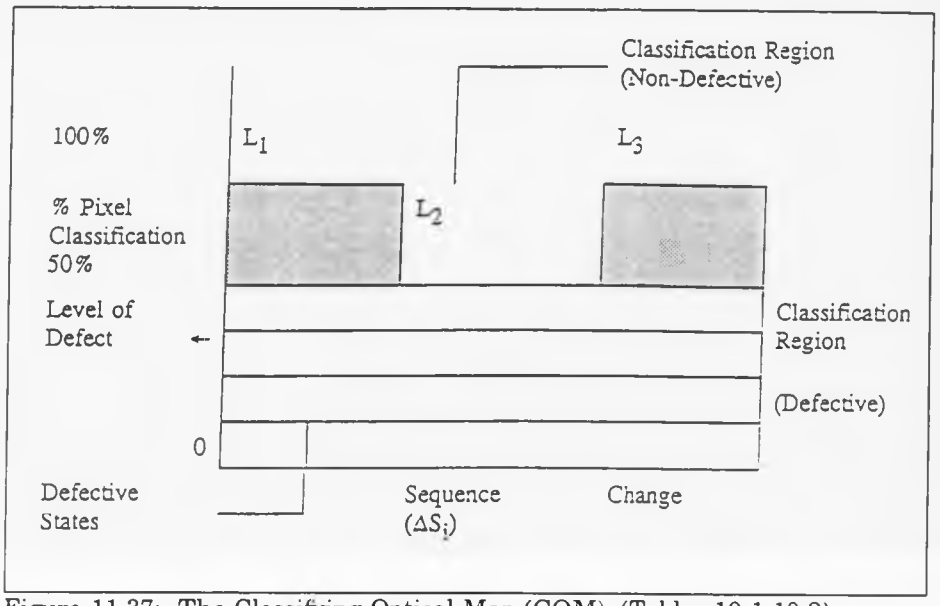

Figure 11.37: The Classifying Optical Map (COM). (Tables 10.1-10.2).

would be to pass half the first sequence pixels at L_2 with the summation of the other four sequences equal to 0.5 making the overall image of 1.0. Within certain boundaries, this applies to a non-defective component. For defective ones three changes in response are observed:

(1) A closed path is not realized as the damage in the component affects the response.

(2) The window function would pass less than half the pixels in the first sequence indicating the presence of damage.

(3) The window function would pass more than half of the pixels in the first sequence indicating the presence of both damage and reflective surface (white paint) covering the damage.

However, we can still employ a closed path function to classify the obtained response, preserving the overall characteristics.The thought of function is a CARDOID shaped function which has the general format of:

$$r = a (1 - \cos \theta) \qquad 11.(4)$$

To make this function work for us in closing the path of a damaged component yet preserve the level of classification needed an alternative parallel expression is used. This equivalent function would be:

$$R = \Delta S_i (L_i) [S_{th} - S_i (L_i)] \qquad 11.(5)$$

where:

i	:	1, 2, 3, ..., n-1
S_{th}	:	Threshold level sequence, $0 \leq S_{th} \leq 1$
n	:	number of sources needed
L_i	:	Optical source

Employing the above function in classification should produce a series of curves within each other as shown in Figure 11.38. The classification curve would operate in a manner to separate main groups of damaged components within each one a further classification of individual components.

Figures 10.29-10.32 illustrate the plots covering the complete sequence sets for the general sequential classification, second stage which indicates the way the rest of the sequence operates on the captured image. This should produce an identity graph that can be kept and produced when future tests are needed to verify any changes the component might have gone through.

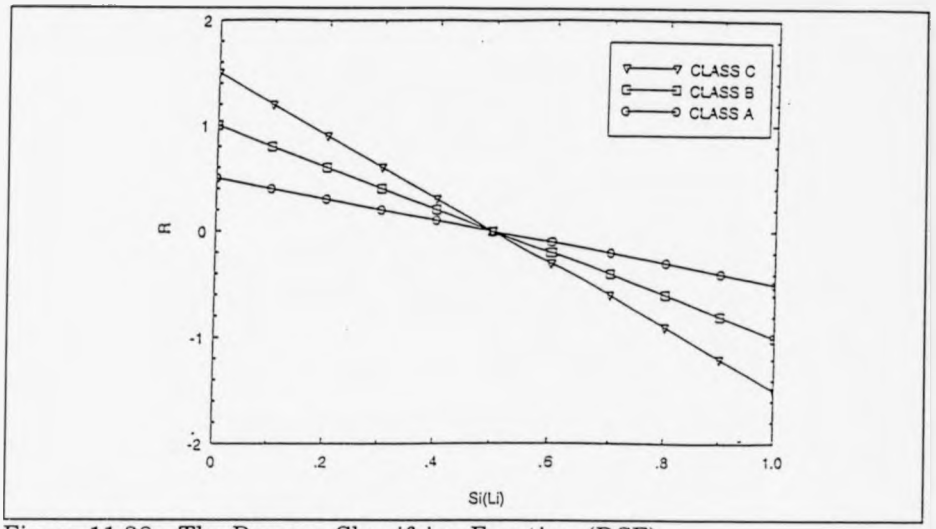

Figure 11.38: The Damage Classifying Function (DCF).

Figure 11.39 shows the overall sequential classification of a range of impact energies. We can easily notice the classification and separation properties of such an algorithm as both damaged groups are put at either side of the healthy component curve corresponding to two categories:

(1) Damaged components.

(2) Damaged and paint coated components (reflective coatings)

This effect of damage detection and components segregation is shown in Figure 11.40 as a function of impact energy. As the energy is increased the response drops slightly below 50% indicating a little or negligible effect up to an energy of 14.3J where it initiates a climb in the response meaning that start of the damage cycle. This cycle should continue to increase constantly to a maximum of (100% - ε%) where ε% is a variable and a function of

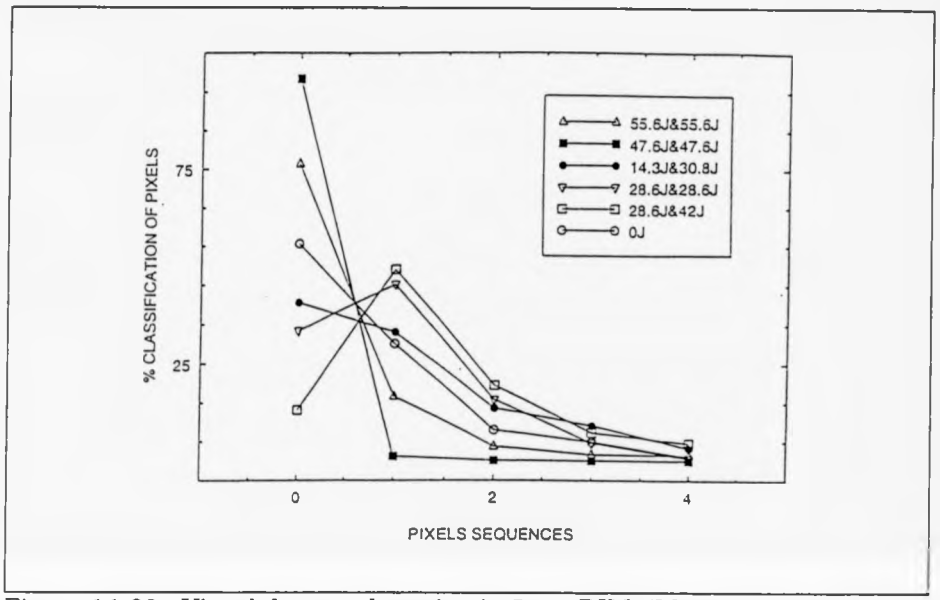

Figure 11.39: Visual damage detection in 5mm RIM. (Mean of 6 images).

impact energy with inverse proportionality. But instead it peaks at 42J then drops to a very low level at 47.6J as the sample is covered with reflective paint and rises slightly at 55.6J where the component which is also painted with reflective paint suffers a major crack that results in part of it removed, so the increase is proportional to the area of the sample with no paint covering it. The overall response agrees well with both low and high frequency analysis previously carried out and also with equation (11.5) for classification.

Difference between multi-layered, 5mm RIM components can also be established as seen in Figures 10.33-10.34, also plastic inclusions can be uncovered with this technique as shown in Figure 10.35.

Figures 10.36-10.38 illustrate the general sequential classification of 2mm

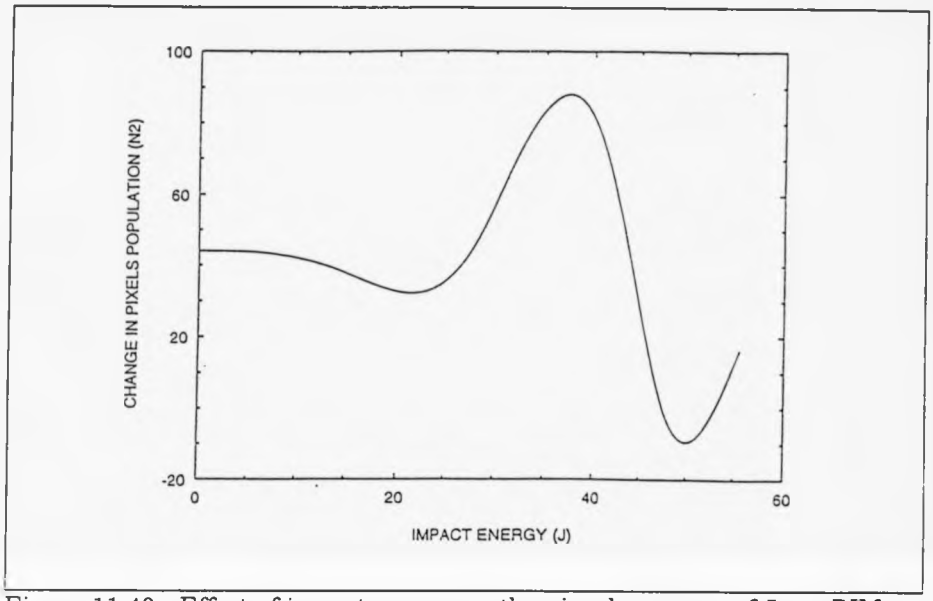

Figure 11.40: Effect of impact energy on the visual response of 5mm RIM.

RIM components and Figure 11.41 shows the response as a function of impact energy. It is clear that impact has more effect when applied to thinner RIM components. Up to 14.3J the curve agreed with all other findings using low and high frequency techniques but when increased further the response unexpectedly drops to a very low level.

This could be due to surface roughness of the component causing light scattering, hence reducing the ability to detect damage.

Figures 11.42-11.44 demonstrate a comparison between woven glass and RIM responses to impact energy using a detailed sequential classification (W.I.W.V.). From the graphs and for the same thickness of 5mm and the same impact energies, it is obvious that RIM components are affected to a larger extent by impact compared to woven glass.

This ties well with the findings using low frequency technique in terms of

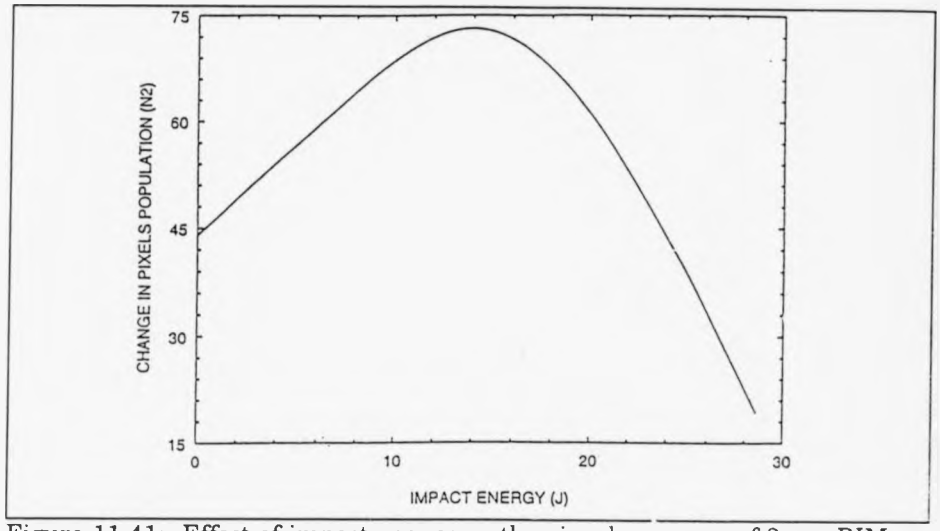

Figure 11.41: Effect of impact energy on the visual response of 2mm RIM.

the absence of saddle points in the RIM response and the faster decrease in its response compared to woven glass.

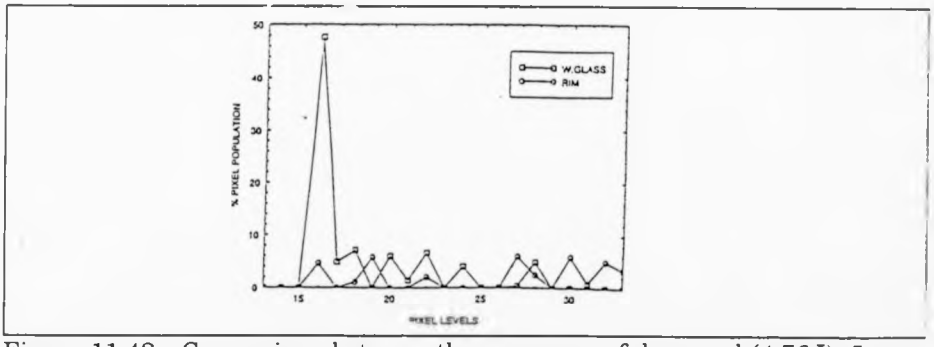

Figure 11.42: Comparison between the responses of damaged (4.76J), 5mm thick RIM & W.Glass. (Mean of 6 images).

Figures 11.45-11.46 illustrate the uniformity factor for 5mm RIM components. From the graphs we observe the initial reduction of component uniformity as an indication of the presence of damage followed by increase in its amplitude due to spread of damage (inside defect search through). As the impact energy is further increased another layer of damage is introduced

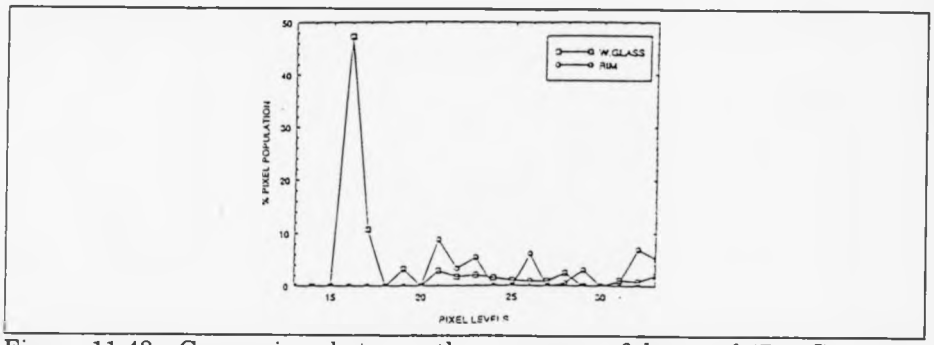

Figure 11.43: Comparison between the responses of damaged (7.14J), 5mm thick RIM & W.Glass. (Mean of 6 images).

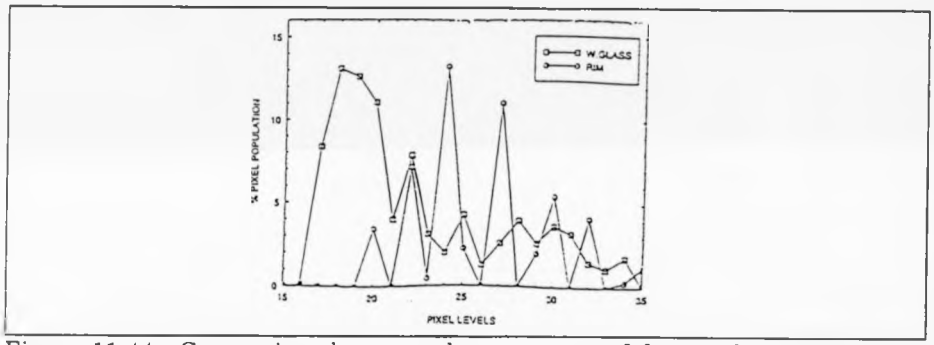

Figure 11.44: Comparison between the responses of damaged (14.3J), 5mm thick RIM & W.Glass. (Mean of 6 images).

resulting in reduction in the uniformity factor.

As it is a directional factor we realize that even though the uniformity factor can indicate the introduction of defective layers, the number of these layers introduced and their effect on the composite component integrity can better be studied using the other version of search through algorithm, the (I.I.W.V.) analysis and classification technique as discussed next.

Figures 10.39-10.45 show the images obtained for the previously discussed

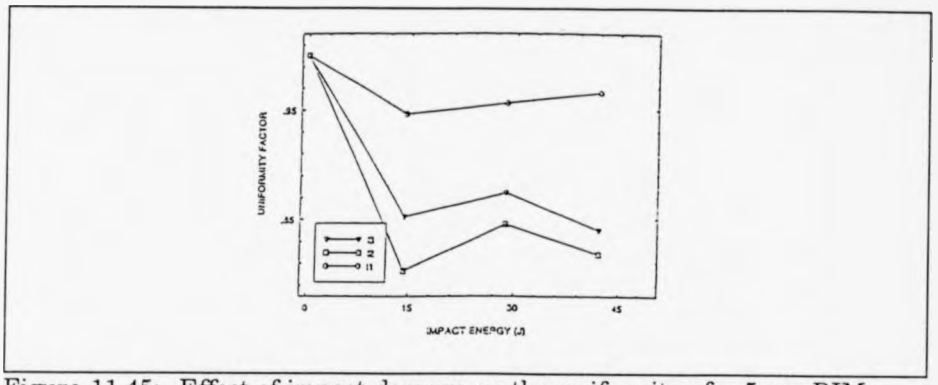

Figure 11.45: Effect of impact damage on the uniformity of a 5mm RIM component (ROW SPREAD), refer to figure 11.26.

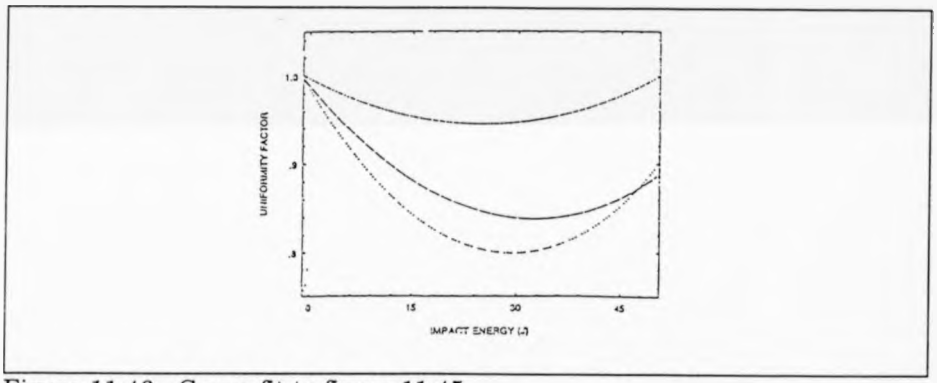

Figure 11.46: Curve fit to figure 11.45.

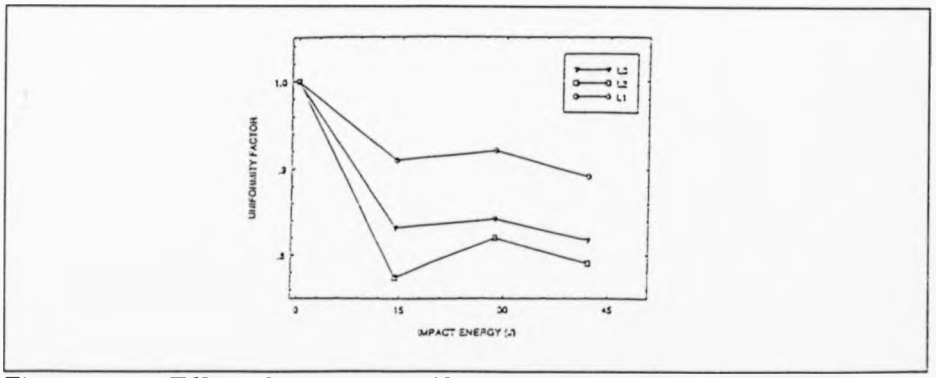

Figure 11.47: Effect of impact on uniformity of 5mm RIM (COLUMN).

5mm RIM components using Inside Image Wave Variation technique. From the produced images and the application of this novel algorithm we observe

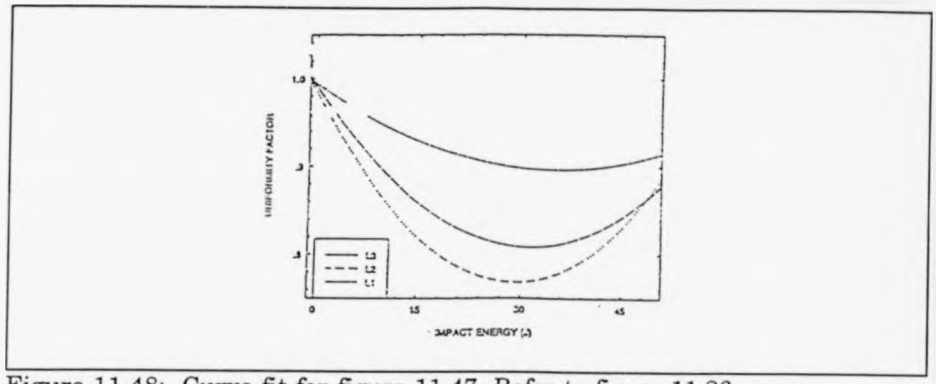

Figure 11.48: Curve fit for figure 11.47. Refer to figure 11.26.

the following:

(1) The ability to determine the extent of damage inflicted upon a component.

(2) The ability to establish the amplitude of energy applied to impact the specimen.

(3) Surface composition can be established.

(4) Correlation of damage detectability to the type of light source used.

(5) The effect of angle of impact on the resulting damage induced.

Figures 11.49-11.54 describe two main aspects of damage detection:

(A) Effect of impact energy on the number of defective layers introduced. hence, damage level and propagational characteristics.

(B) The confirmation and support of the analysis previously carried out using the O.I.W.V. technique that through the right choice of light sources and incident angles hidden defects can be uncovered with ability to classify their damaging effect through the number of layers counted.

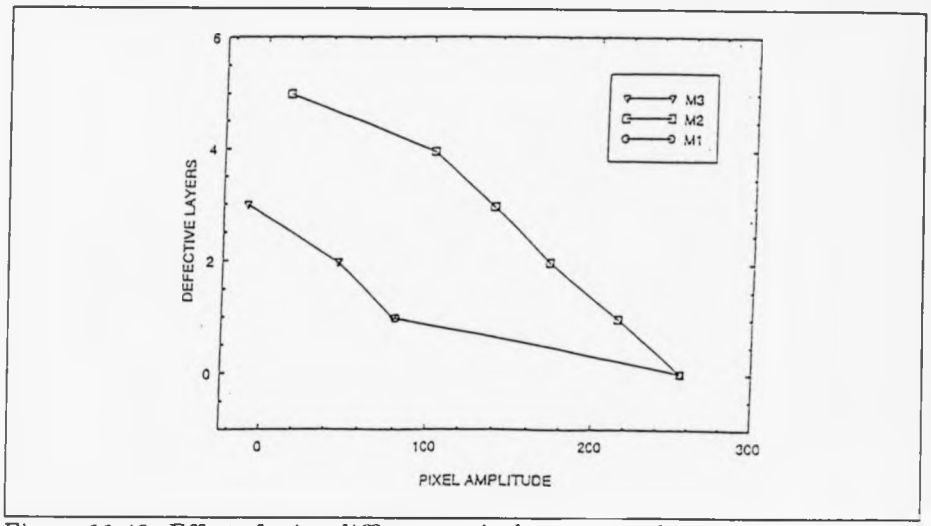

Figure 11.49: Effect of using different optical sources and impact energy (28.6J) on detection of damage level in 5mm RIM component. (Mean of 6 images)

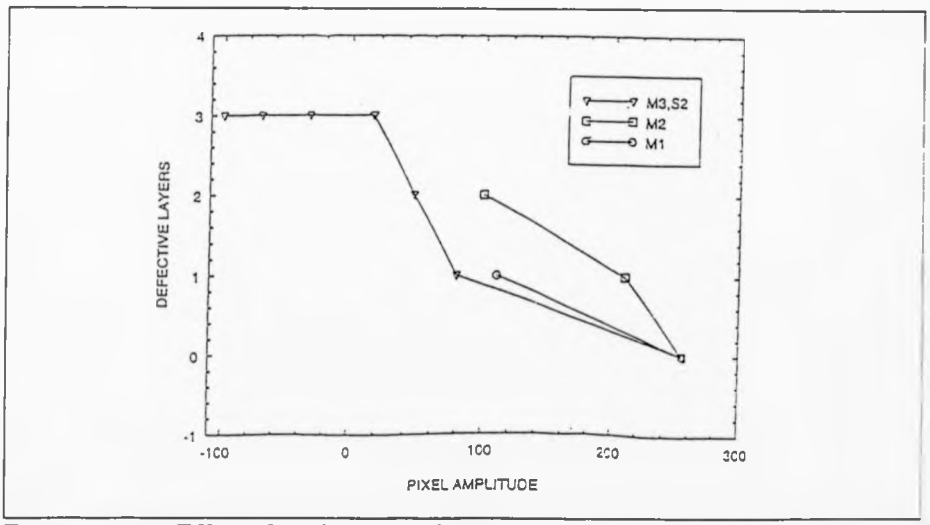

Figure 11.50: Effect of application of same impact energy (figure 11.49) at an angle on level of damage induced in 5mm RIM component using different optical sources. (Mean of 6 images).

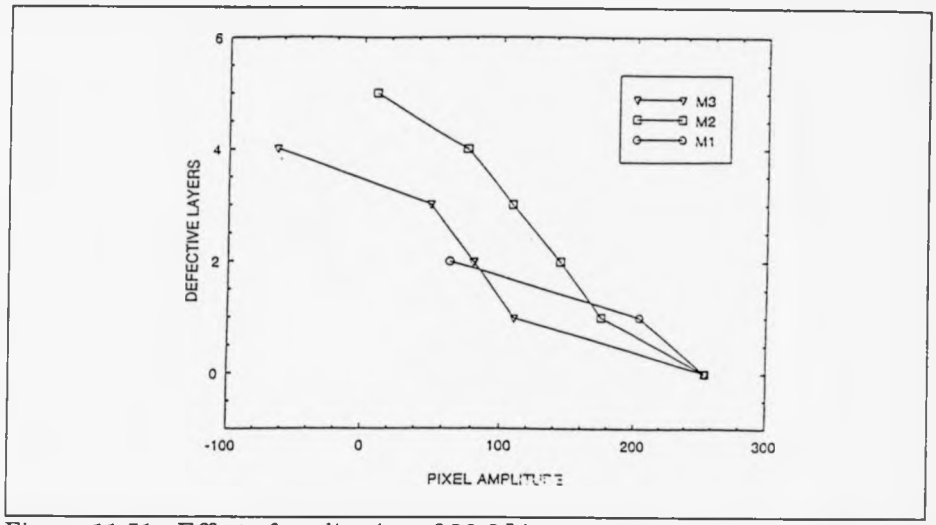

Figure 11.51: Effect of application of 30.8J impact energy and use of different optical sources on the detection of damage in 5mm RIM (refer to figure 11.50).

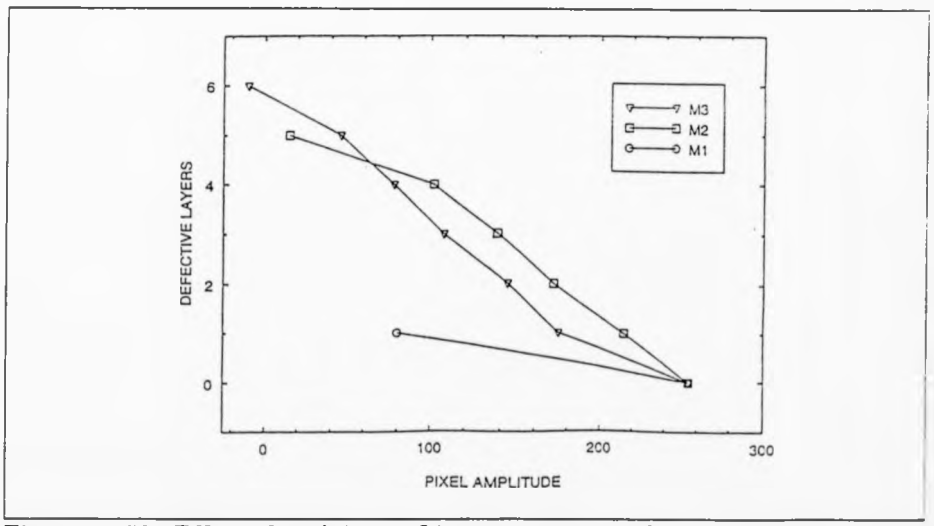

Figure 11.52: Effect of applying 42J impact energy and use of different optical sources on damage detection in 5mm RIM. (Mean of 6 images).

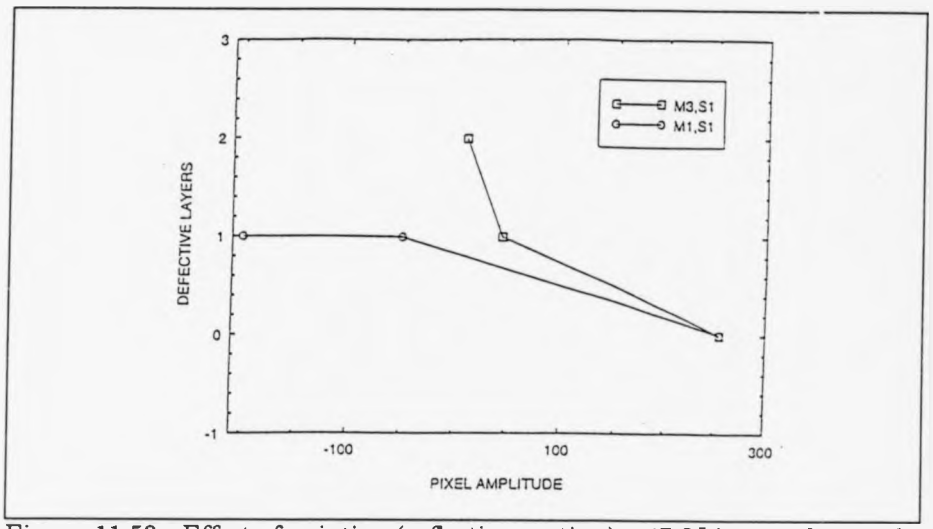

Figure 11.53: Effect of painting (reflective coating) a 47.6J impact damaged component on limiting the depth of detection in 5mm RIM (refer to figure 11.50).

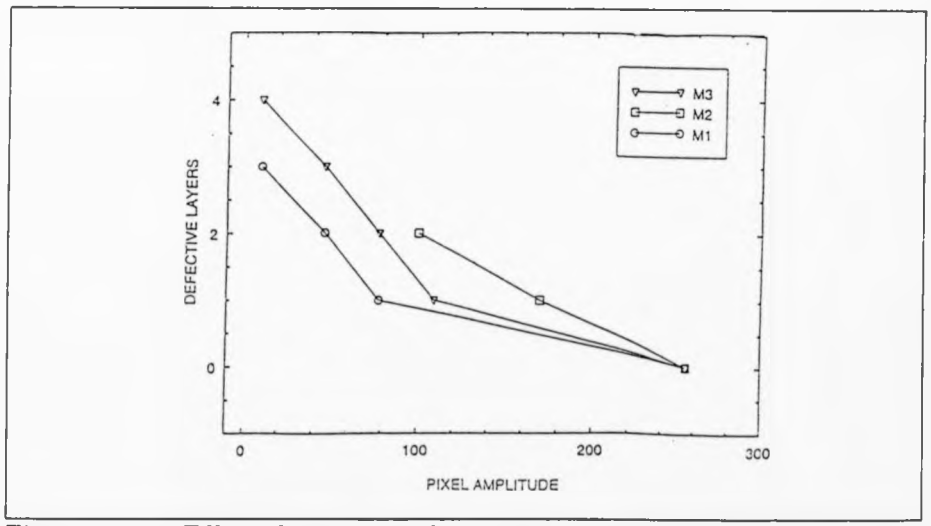

Figure 11.54: Effect of increasing the impact energy (55.6J) with part of the component surface extracted due to impact on depth of detection in 5mm reflective painted RIM. (Mean of 6 images).

Also the effect of applying the impact load at an estimated angle of 45 degrees is realized as changing the angle for the same impact energy results

in more damage has been introduced which is similar to a higher impact energy applied. This is achieved through counting of the number of defective layers as shown in Figures 11.49-11.50 where a 28.6J impact energy produced 3 defective layers, but when applied at an angle produced 5 defective layers similar to 30.8J impact energy effect.

The effect of reflective paint is also realized as impact energies (Figures 11.53-11.54) at much higher levels produce smaller numbers of defective layers compared to lower impact energies. However, with this technique we can still classify the component as either defective or non-defective. Also a change of the response in terms of the type of light source that reveals the existence of damage is realized when the component is painted.Figures 11.49-11.54 and figure 11.55 illustrate two main points.

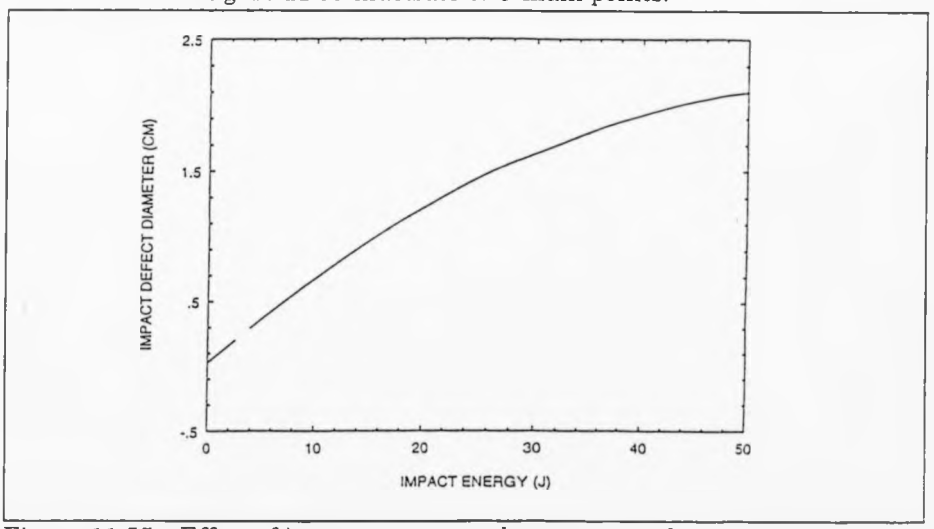

Figure 11.55: Effect of impact energy on damage spread.

(A) The number of defective layers is a function of the applied impact energy.

(B) The defect diameter is a function of the number of defective layers and applied energy.

The above agrees with the findings of equations (11).2 & (11).3.

(B) High Temperature

(1) Transmission Through High Temperature Visual Imaging.

(a) RIM

Figures 10.46-10.50 show images and plots regarding defect detection in 5mm samples through direct heating process (Thermal-visual imaging). From these we observe the following:

(1) The ability to establish the effect of various impact energies on the integrity of the tested specimen.

(2) The ability to distinguish between low temperature and high temperature detected defects for the same impact energy through the I.I.W.V. technique.

The effect of impact on such composites can easily be seen in the images obtained for different levels of impact with the spread of damage realized as dark areas in the red coloured image. Also the effect of impact load angle of contact with the specimen and its effect on the component integrity can be established as shown in Figure 10.46. Figure 11.56 illustrates the T-map for defect classifier which also correlate low temperature to high temperature classification with reference to different optical sources.The correlation takes the form of a rotating mathematical shape with the number of sides

proportional to the number of optical sources used (in our case a triangle as 3 sources (l_1,l_2,l_3) were used.).

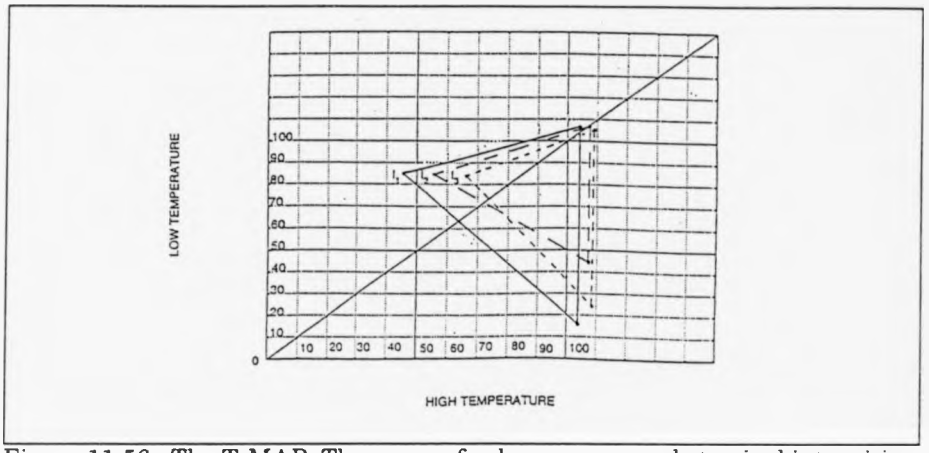

Figure 11.56: The T-MAP. The range of values corresponds to pixel intensities.

Figures 11.57-11.66 illustrate the application of the I.I.W.V. technique with the relevant defective layers classification plots.

Two important features of these images are:

(1) More defective layers are uncovered using this approach.

(2) The images can be used as timing diagrams to establish the true value of impact energy (including angles of load incidence, figure 11.61-11.63 & figure 11.66).

The heating elements used incorporated a far-field infrared part that obviously suffered less reflectance and scattering by the composite component surface compared to other forms of wave sources. One of the

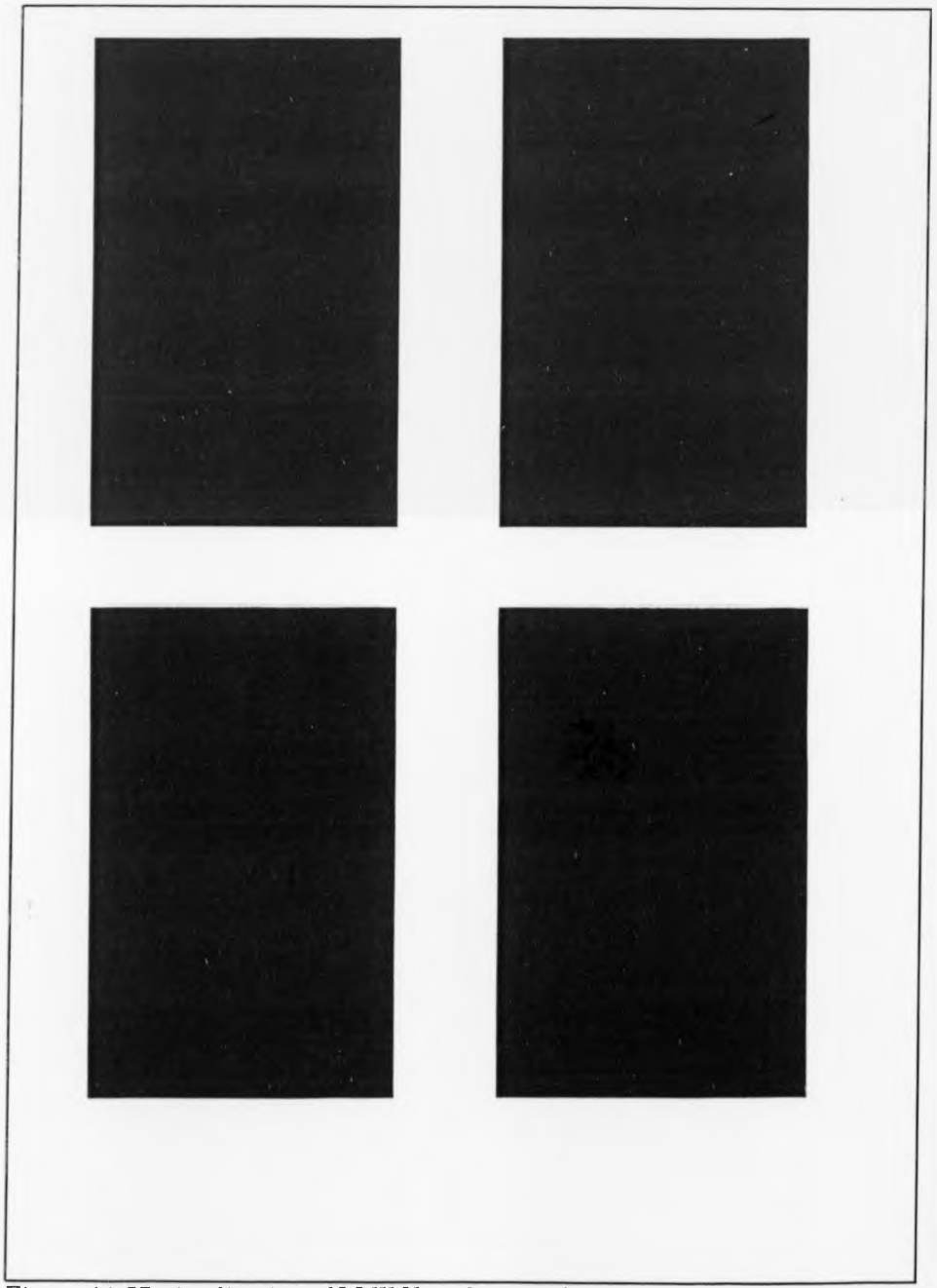

Figure 11.57: Application of I.I.W.V. to damage detection (28.6J & 42J) in 5mm RIM tested using high temperature source. (Cycles 1-4).

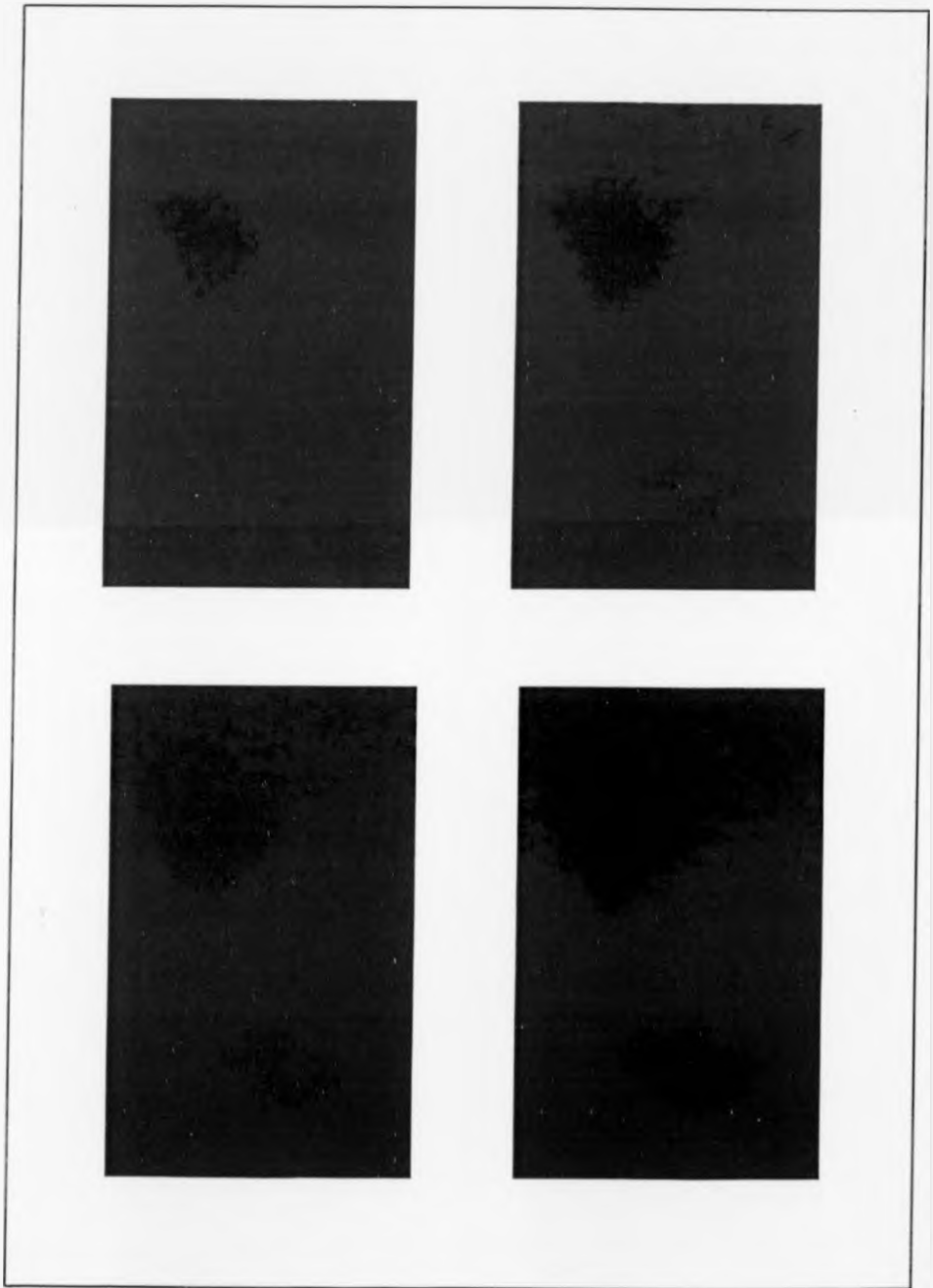

Figure 11.58: Application of I.I.W.V.to damage detection (28.6J & 42J) in 5mm RIM using high temperature source. (Cycles 5-8).

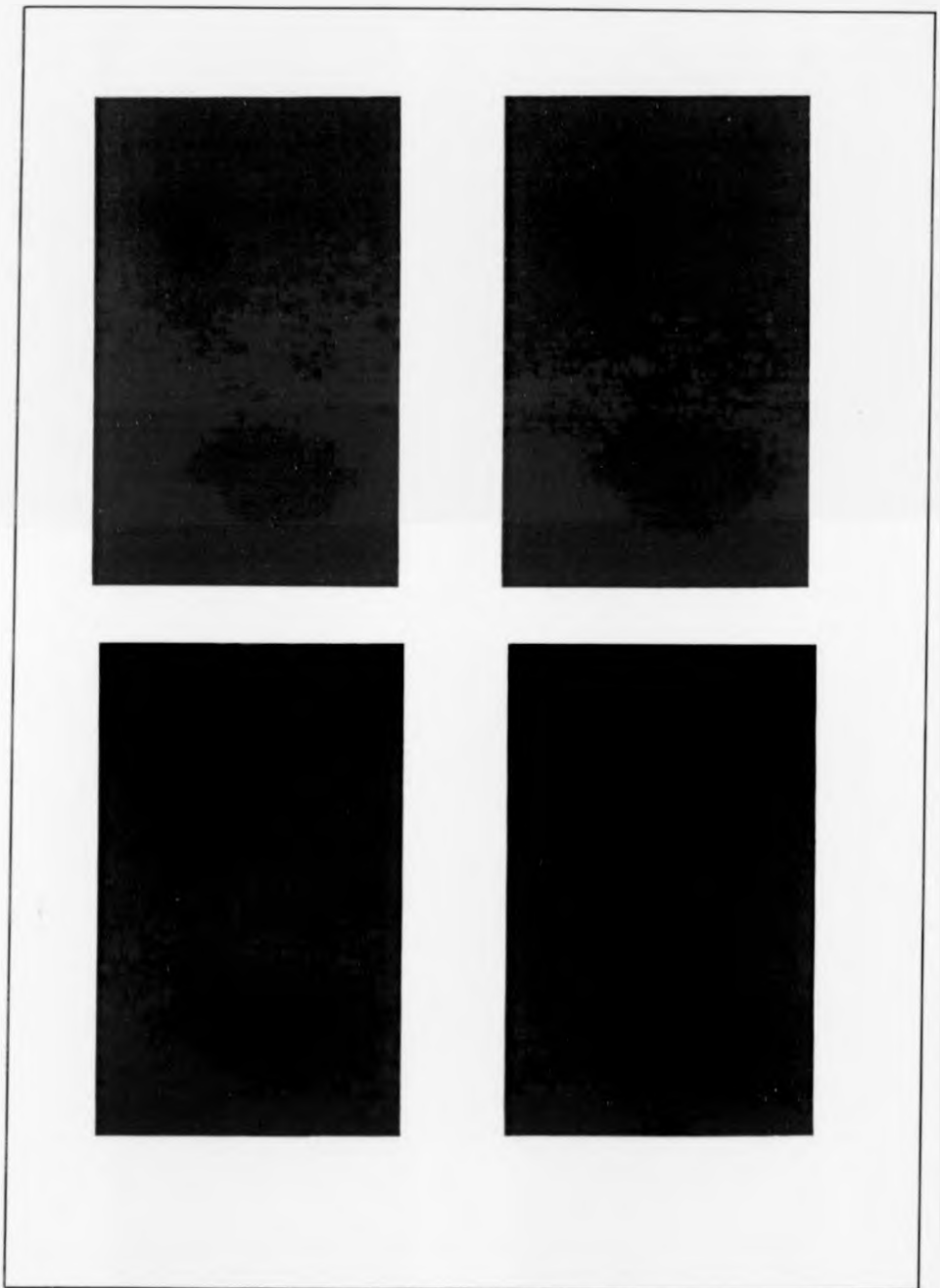

Figure 11.59: Application of I.I.W.V. to damage detection (28.6J & 42J) in 5mm RIM using high temperature source. (Cycles 9-12).

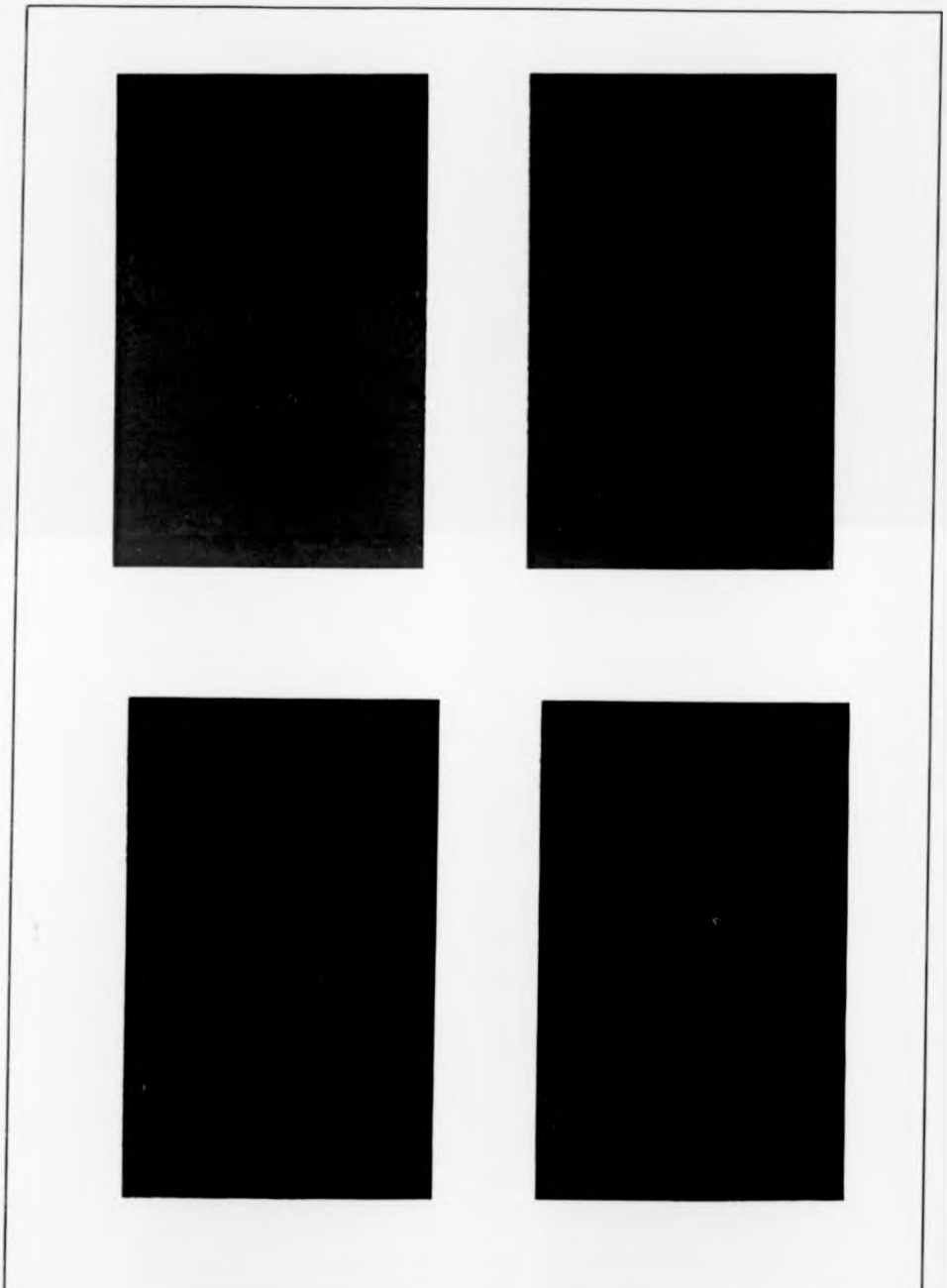

Figure 11.60: Application of I.I.W.V. to damage detection (28.6J & 42J) in 5mm RIM using high temperature source. (Cycles 13-16)

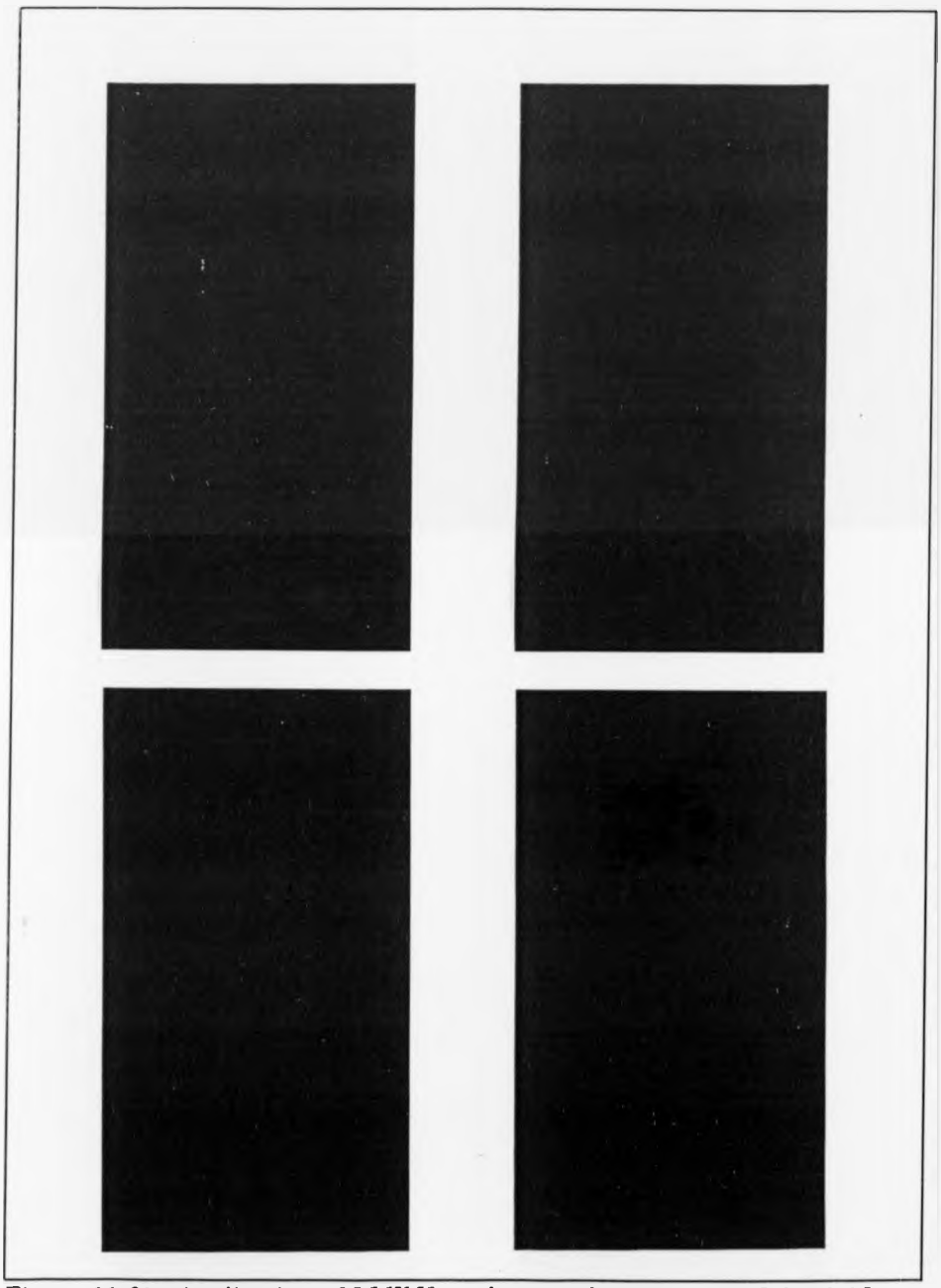

Figure 11.61: Application of I.I.W.V. to damage detection (28.6J & 28.6J applied at an angle to the normal) in 5mm RIM using high temperature source. (Cycles 1-4).

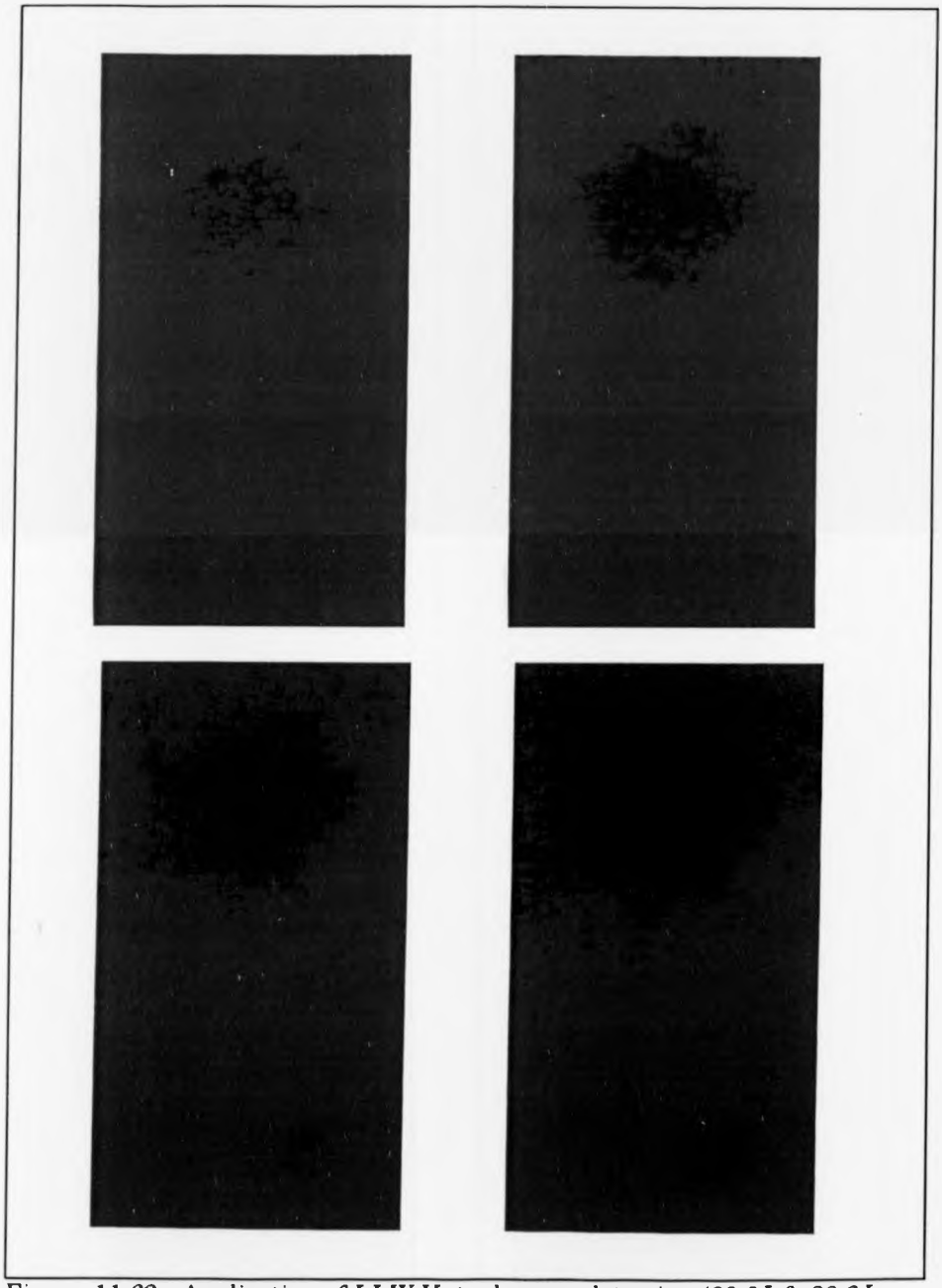

Figure 11.62: Application of I.I.W.V. to damage detection (28.6J & 28.6J applied at an angle to the normal) in 5mm RIM using high temperature source. (Cycles 5-8).

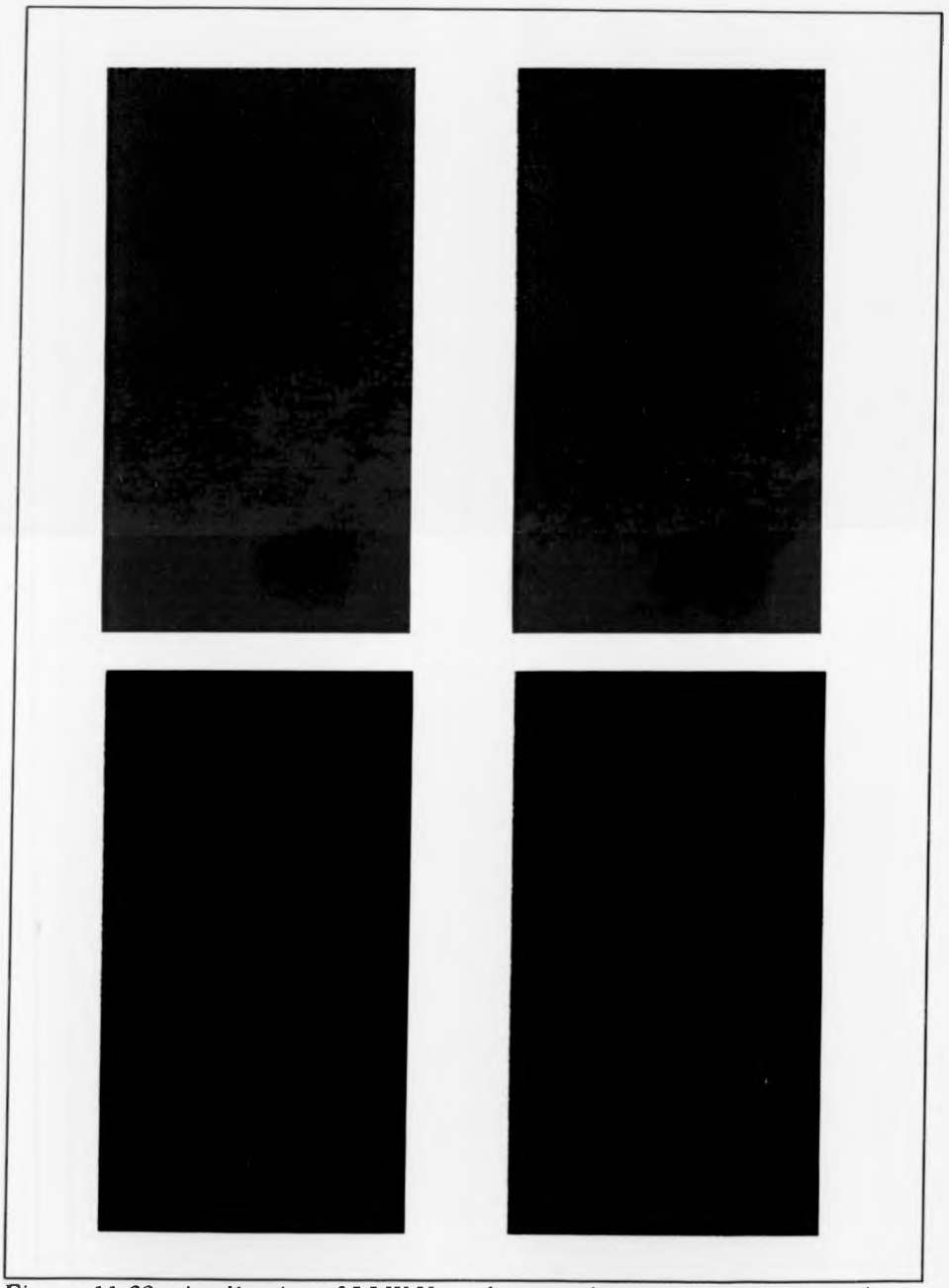

Figure 11.63: Application of I.I.W.V. to damage detection (28.6J & 28.6J applied at an angle to the normal) in 5mm RIM using high temperature source. (Cycles 9-12)

critical aspects of the I.I.W.V. technique is its ability to transform a single image to a time dependent set of images such that the appearance of damage as a function of impact is also a function of discrete time intervals which is also a function of impact energy that controls in correlation to specimen thickness, impactor dimensions and component properties the number of defective layers.

Based on the previous discussion, we can now confidently introduce what we can call the APPEARANCE FUNCTION Ap for I.I.W.V. images.This function which is time related is also a function of impact energy, hence:

$$Ap = f(t, E_I) \qquad 11.(6)$$

However, before we try to establish the nature of this function it is helpful to determine the relationship between the number of defective layers detected N and impact energy E_I.

From experimental results it is found that the number of defective layers is related to impact energy through the following expression:

$$N = E_I^k \qquad 11.(7)$$

where k is a real number and $0 \leq k \leq 0.75$ for both low and high temperature results. However, this overall range is smoothly divided between the two techniques such that:

$$N_l = E_I^{k_1} \qquad 0 \leq K_1 \leq 0.5$$

$$N_h = E_I^{k_2} \qquad 0.5 \leq K_2 \leq 0.75 \qquad 11.(8)$$

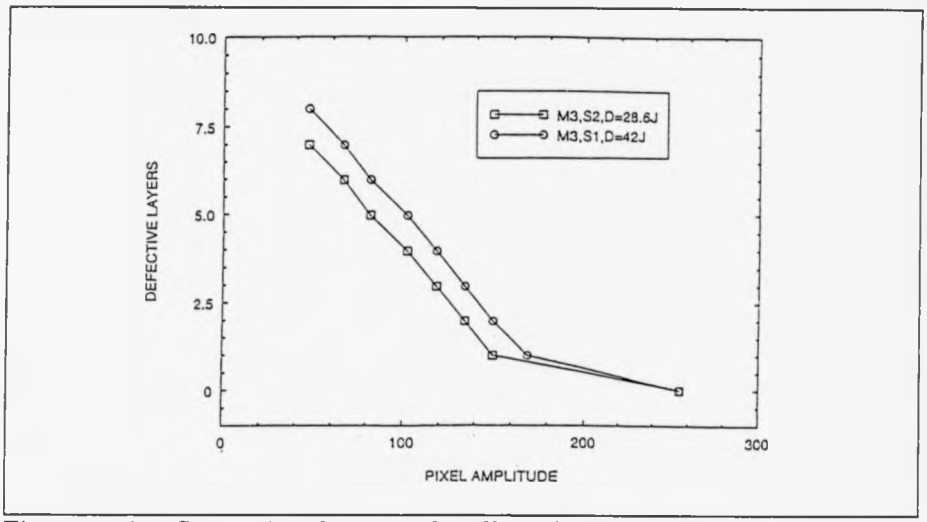

Figure 11.64: Comparison between the effect of 28.6J and 42J impact energies on the level of damage in 5mm RIM. (Refer to figures 11.57-11.60).

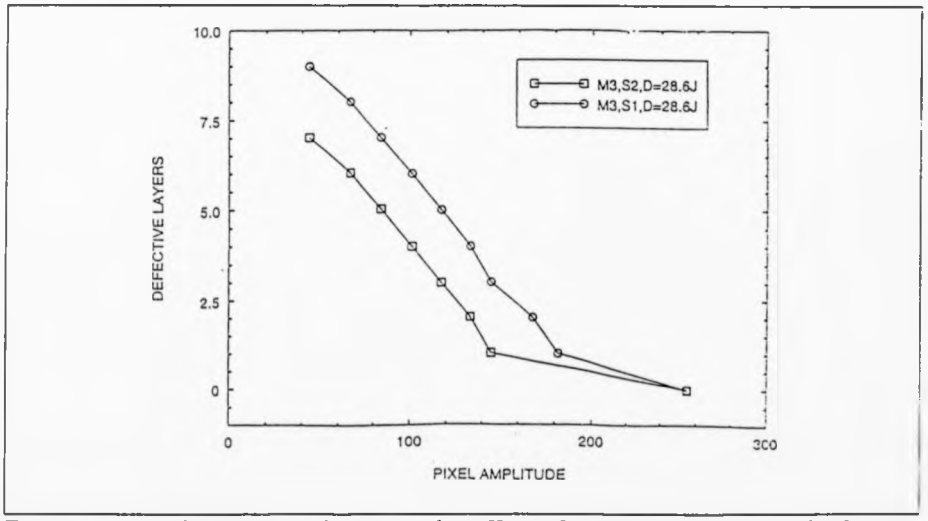

Figure 11.65: Comparison between the effect of 28.6J and 28.6J applied at an angle to the normal on the level of damage in 5mm RIM. (Refer to figures 11.61-11.63).

This smooth transition is consistent with the wavelength spectrum.

Also (8) can be written as:

$$N_\ell = \sum_{k_1=0}^{0.5} E_I^{k_1}$$
$$N_h = \sum_{k_2=0.5}^{0.75} E_I^{k_2} \qquad 11.(9)$$

From equations (9), (2) and (3) and experimental data we obtain:

$$\left.\begin{aligned} D_\ell &= \sum_{k=0}^{0.5} aE_I^k \\ D_h &= \sum_{k=0.5}^{0.75} aE_I^k \end{aligned}\right\} \quad 0 < a \le \frac{1}{N_\ell}, \frac{1}{N_h} \qquad 11.(10)$$

As the impacts were carried out at different levels of energy separately and at different points of the composite component a continuous describing function is not applicable or possible hence the discrete functions derived should be sufficient for the purpose of this research.

(2) High Temperature Pulse Video Infrared Imaging (PVT).

(a) RIM

Figures 10.51 and 11.66-11.67 illustrate thermally pulse heated 5mm RIM component and its time diagram. The images were manipulated through an I.I.W.V.

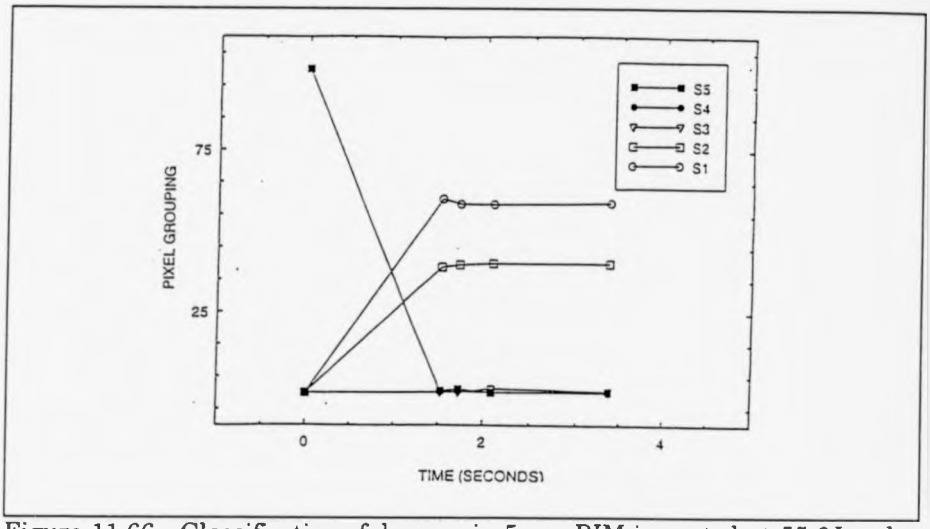

Figure 11.66: Classification of damage in 5mm RIM impacted at 55.6J and tested using High Temperature PVT. (Refer to figure 10.51).

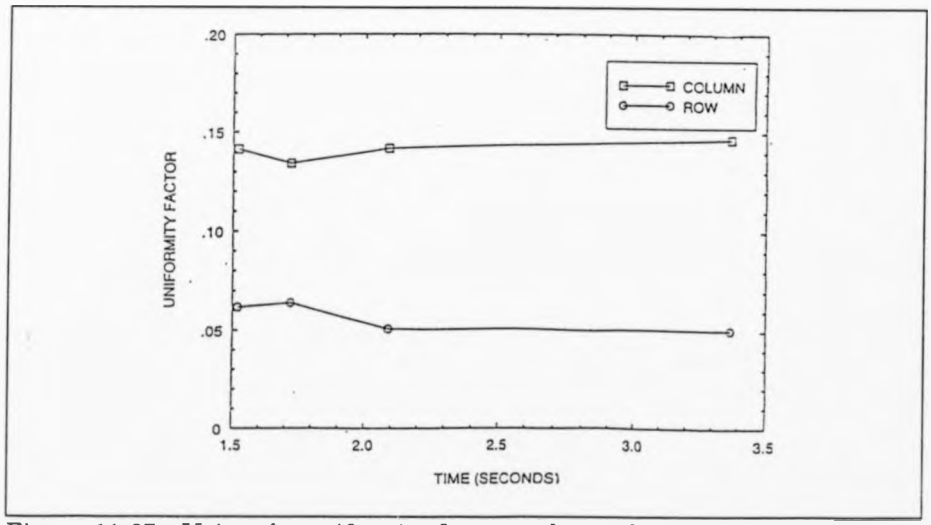

Figure 11.67: Using the uniformity factor to detect damage in 5mm RIM impacted at 55.6J by evaluating rate of energy propagation in a High Temperature PVT test.

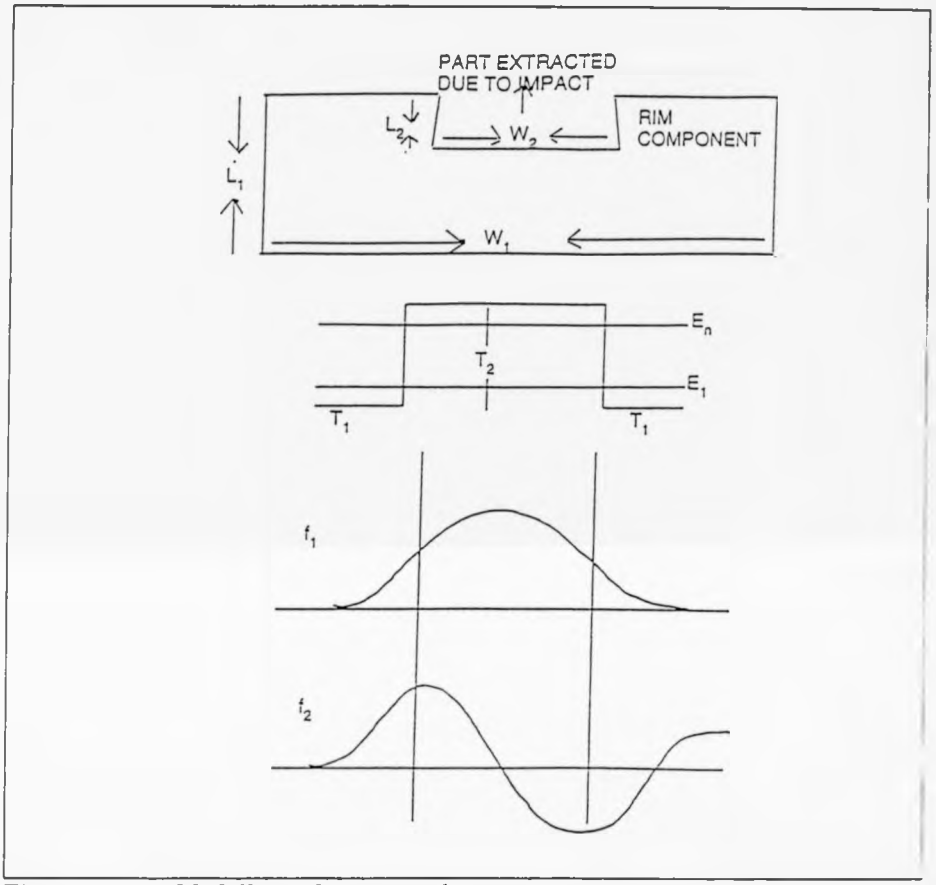

Figure 11.68: Modelling of energy pulse propagation in 5mm RIM impacted at 55.6J with part of the component removed.

Using our search through algorithms we were able to achieve the following:

(1) The ability to accumulatively freeze images.

(2) The ability to slice through time related images (Time-back-track).

(3) The ability to establish the extent of damage and component integrity through the rate of change in pixel population as a function of time.

(1) One of the very important aspects of this technique is the ability to visually see the whole sequence of heat wave propagating. This

consequently allows a speedy and accurate assessment of induced defects and how damaging it is to the component performance. Through experimental work RIM components proved to be very poor in holding differential heat. However, one set of components held the heat long enough with large but fast response compared to other composites.

The obtained response for the 55.6J component which was the only RIM sample to respond to high temperature pulses is due to a major crack and part extraction out of the component. This is seen in a classification context in Figure 11.67 with clear separation of the grouped pixel sequences S_1, S_2 from S_3, S_4, with S_5 acting as a source of classification. Refer to Chapter 8, section 8.4, part A.

(2) This is carried out through an I.I.W.V. technique which allows us to take one frozen image in time and space and then dissolve the image into its original components and produce a time related description of damage classification. This also has the advantage of data compression and memory saving.

(3) The extent of damage and the determination of a saddle point and number of cycles needed to achieve total damage is related to the rate of heat wave propagation through the component. In the case of RIM with part extracted at 55.6J it is found that due to thickness variation the heat pulse was detected with the difference in thickness acting as a potential well of finite depth and continuous energy levels within, as shown in Figure 11.68. These levels are made discrete by slicing through the accumulatively frozen images.

(b) Woven Glass.

Figures 10.51 and 11.69-11.70 illustrate thermoimaging time dependent diagrams with the classification plot for woven glass component.

From the plot it is clear that the 5mm sample presents a larger opposition to pulse dissipation at 28.6J compared to a similarly damaged RIM component. This is due to the following:

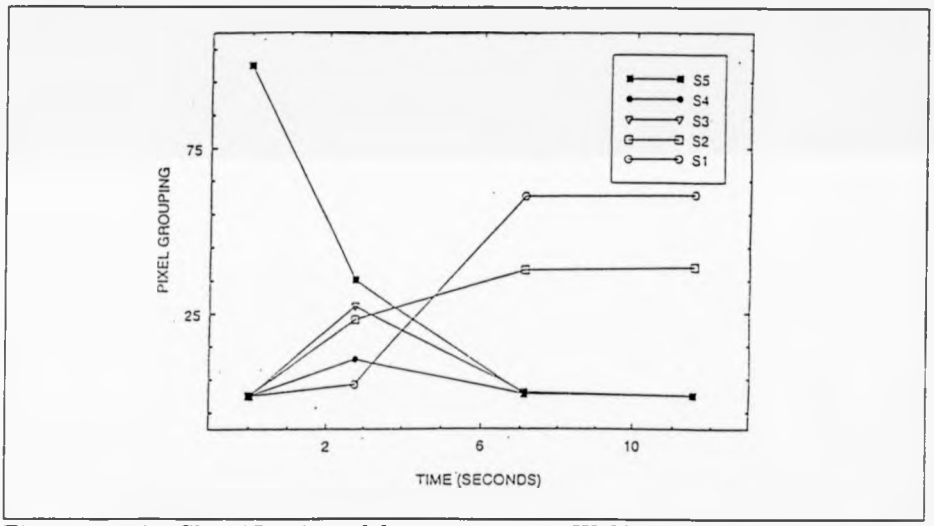

Figure 11.69: Classification of damage in 5mm W.Glass impacted at 28.6J using High Temperature PVT. (Refer to figure 10.51).

(1) The value of impact energy applied to the composite component.

(2) The nature of the material which allows it to have multiple slow cycles before critical damage is realized.

(3) The spread of damage throughout the component due to the existence of what we previously called saddle region.

(4) The more homogenous characteristics of such a composite which added

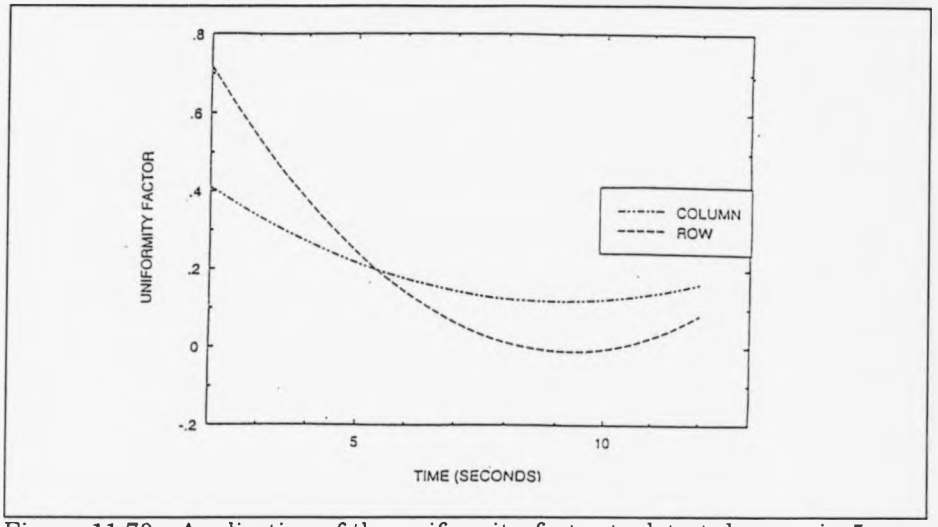

Figure 11.70: Application of the uniformity factor to detect damage in 5mm W.Glass impacted at 28.6J by evaluating the rate of energy pulse propagation in High Temperature PVT test.

to its stronger mechanical properties.

(c) GMT.

Figures 10.52 and 11.71-11.74 show images and pixels classification plots for GMT components. These were the most responsive to this type of test.

From the plots we notice the following:

(1) The correlation between the rate of dissipation of the heat wave to both level of impact and fibre orientation where perpendicular fibres showed a better characteristic than parallel ones.

(2) The conformation of cyclic response within the GMT structure to impact energies.

(3) The larger effect an impact has on GMT components compared to

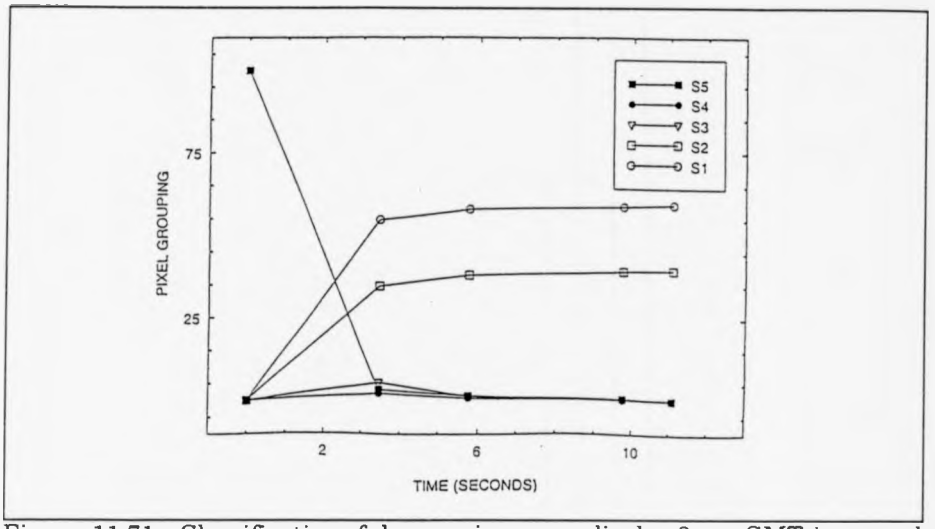

Figure 11.71: Classification of damage in perpendicular 3mm GMT impacted at 14.3J and tested using High Temperature PVT. (Refer to figure 10.52).

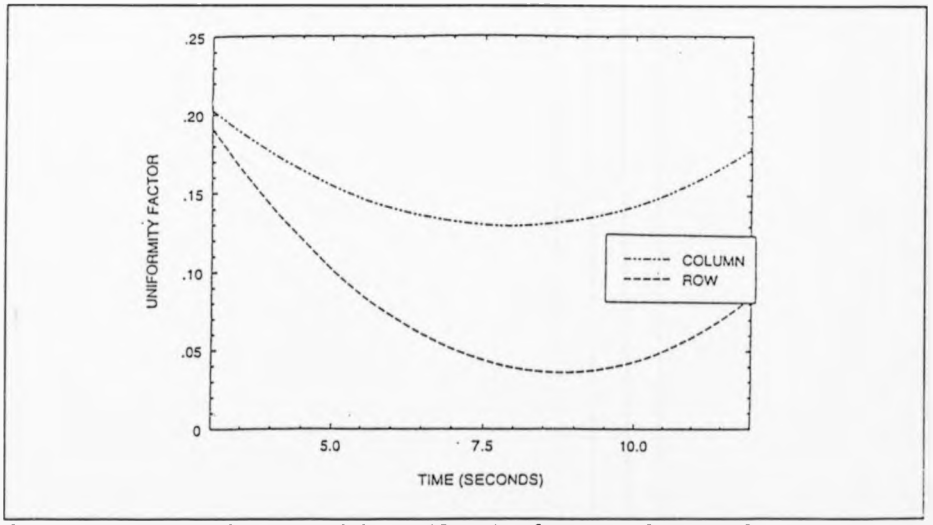

Figure 11.72: Application of the uniformity factor to damage detection in perpendicular 3mm GMT impacted at 14.3J using H.T.P.V.T. test. (Mean of 6 images).

woven glass ones.

Figures 10.53 and 11.75-11.76 illustrate thermoimaging results of a

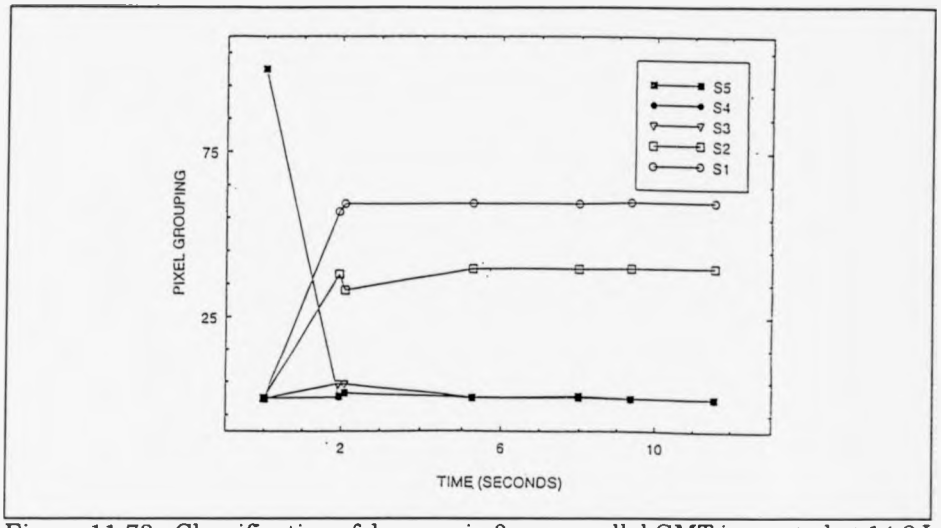

Figure 11.73: Classification of damage in 3mm parallel GMT impacted at 14.3J and tested using High Temperature PVT. (Refer to figure 10.52).

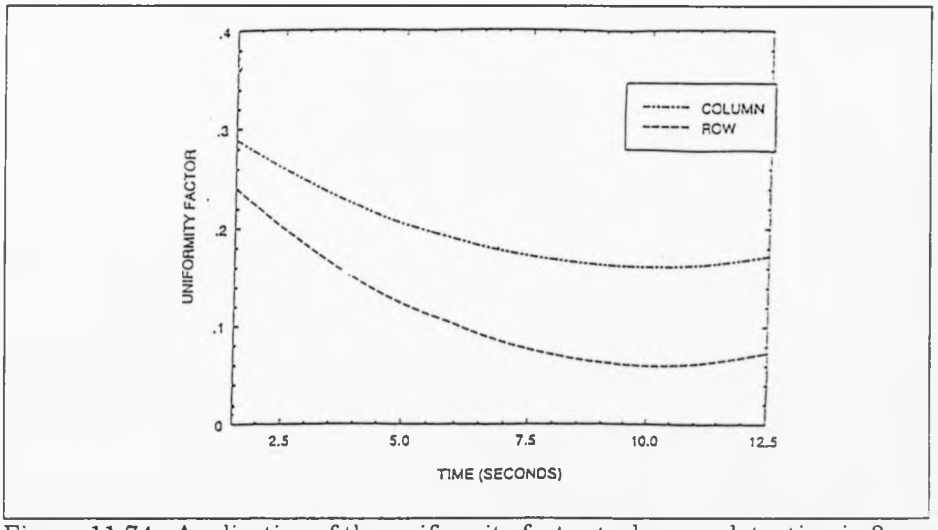

Figure 11.74: Application of the uniformity factor to damage detection in 3mm parallel GMT impacted at 14.3J using H.T.P.V.T. test. (Mean of 6 images)

wishbone. From the plots we realize that the damage in the component is more marked in the vertical direction.

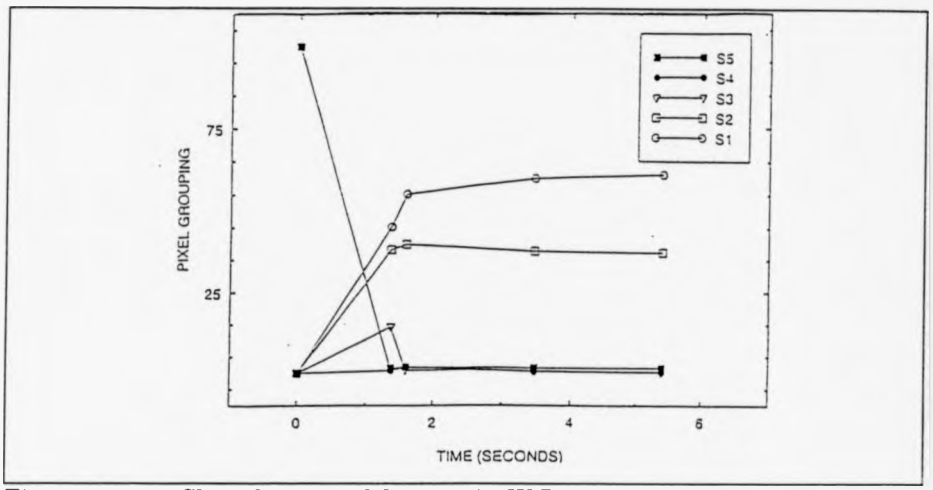

Figure 11.75: Classification of damage in W.Bone using High Temperature PVT. (Mean of 6 images).

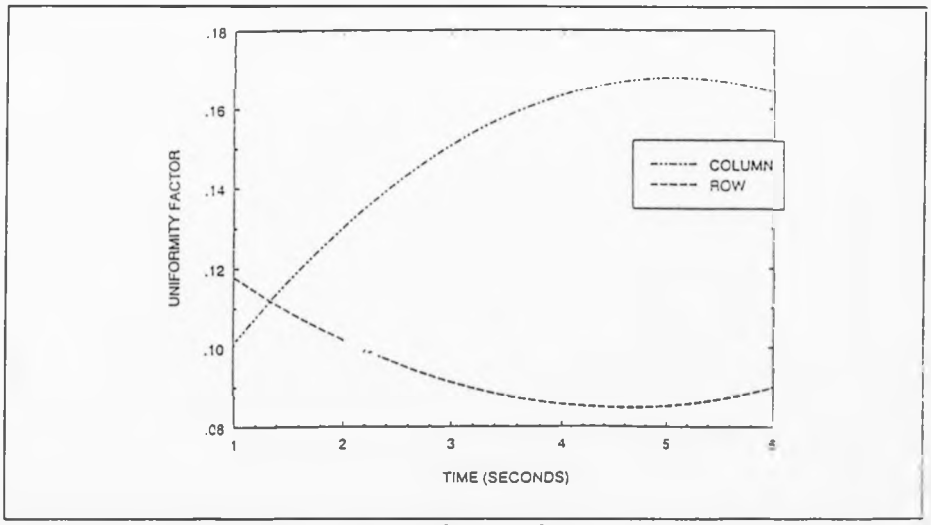

Figure 11.76: Application of the uniformity factor to damage detection in W.Bone using rate of energy pulse propagation in High Temperature PVT test. (Mean of 6 images).

From the previous discussion we can deduce the following regarding High Temperature PVT tests:

(1) The very high speed at which a heating pulse dissipates in a RIM component and Woven Glass reaches a steady state compared to GMT

even when painted with absorbing black paint.

(2) A further proof that woven glass is more resistive to impacts than GMT or RIM materials as it goes through slow varying cycles.

(3) Perpendicular GMT possess better mechanical properties compared to parallel GMT for the same impact energy levels. This is noticed in the steady change with time for the perpendicular and longer changing cycles compared to the short fast changing ones for the parallel components.

(4) The ideal uniformity response for time related applications when a defect is present is to initially decrease indicating the presence of defect then start to increase as the heat pulse dissipates, returning the captured image to a non-defective composition in appearance.

(3) Low Temperature Pulse Video Thermoimaging (LTPVT).

(ORIGINAL CONTRIBUTION).

Since the temperature differential between impact damaged regions and healthy ones within the same composite component (RIM, Woven Glass) is not detectable at high temperatures (fast pulses with high power in the KW range) according to this research findings and considering the obtained images from the other two techniques namely:

(i) Visual (low temperature) detection.

(ii) Visual (high temperature) detection.

we concluded that a suitable detection system should contain a low energy light source with a sensitive thermoimaging camera as a sensing receiver.

This theory which is also based on what we call the SATURATION or FLOODING effect was put to the test by using two low energy optical sources; one at 75 Watts and the other at 250 Watts. The cause behind the use of more than one source with different power is to allow for the energy pulse to propagate at controlled variable times hence allowing us to choose the optimum source for damage detection. It is noticed here that the highest source of energy used in this set of experiments is 8 times less in power compared to the ones used in the previous experiments involving thermoimaging tests by us and other researchers(refer to chapter 7,7.2).

The very same components used in the previous High Temperature PVT tests at AEA, Harwell were subjected to low temperature scanning at our laboratories with an AGEMA 870 thermoimaging camera employed as a detector. The impact damage which failed to uncover itself in most RIM and Woven Glass samples could not resist the temptation of our new technique and hence fully exposed itself.

The resulting images contained dark areas (cold spots) proportional in size to the applied impact energy and angle of load application when the heating pulse is applied at the first instance , then appearing as bright areas (hot spots) after a certain length of time dt, hence , operating as both heat resistance areas and heat storage points within a damaged structure, thus introducing a time delay factor of heat propagation. These findings agree with the general characteristics of equations 7.(3) and 7.(4) regarding heat flux and its propagation.

Figures 11.77-11.83 show some of the obtained images using this new concept.

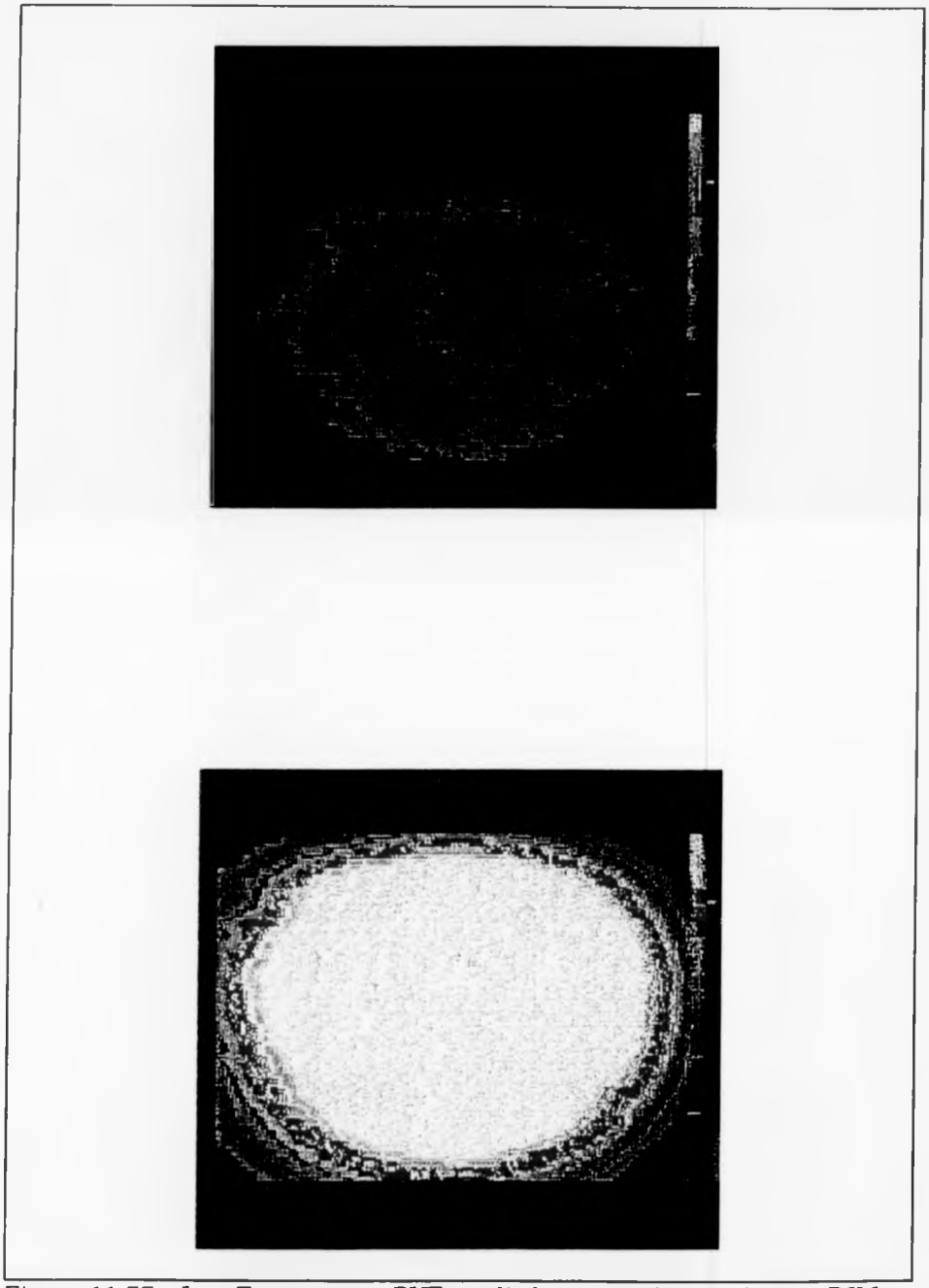

Figure 11.77: Low Temperature PVT applied to an undamaged 5mm RIM component with two different thermal ranges.

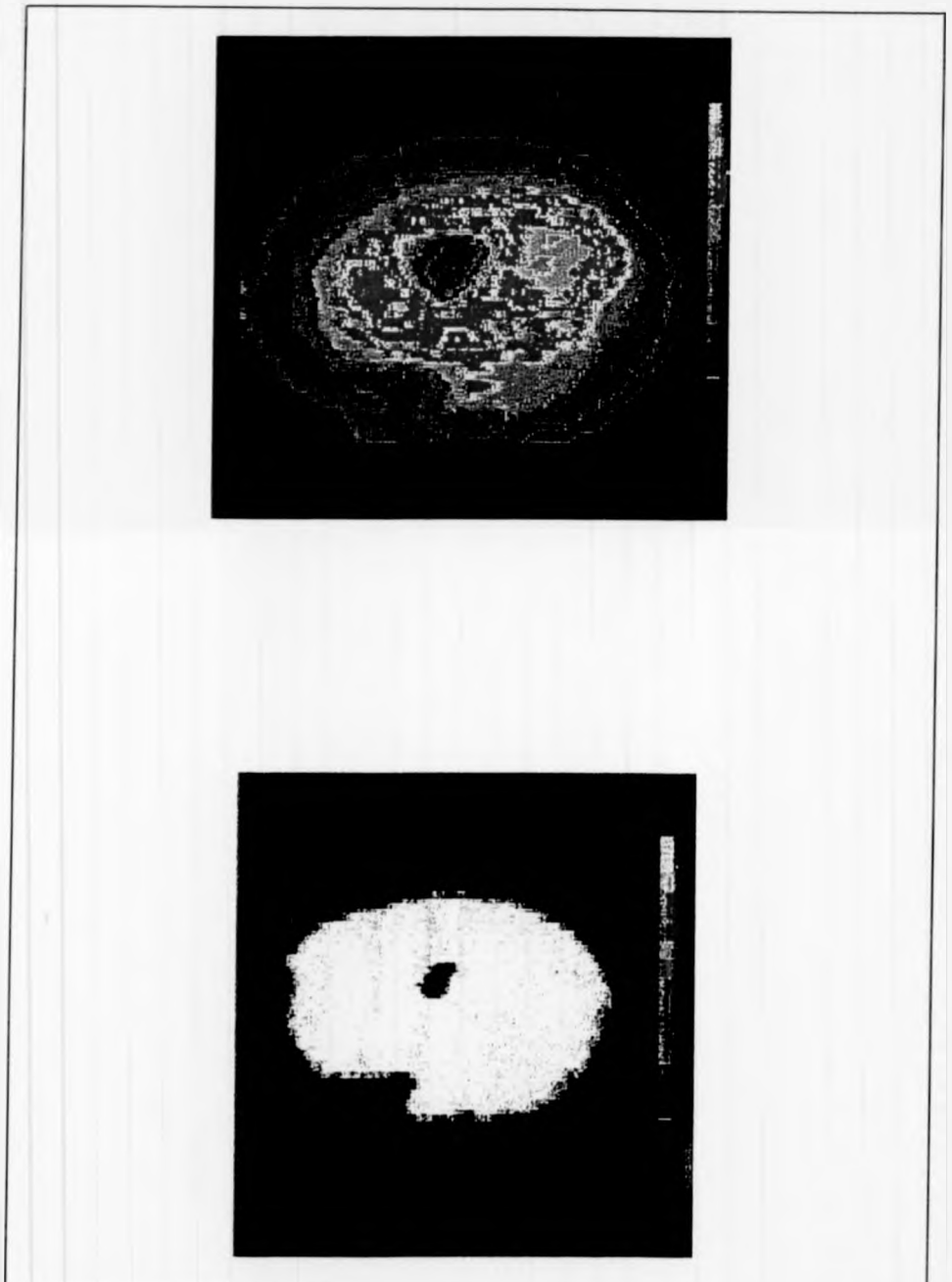

Figure 11.78: Low Temperature PVT applied to 5mm RIM impacted at 42J and tested at two thermal ranges after coating with absorbing paint.

Figure 11.79: Low Temperature PVT applied to 5mm RIM impacted at both 28.6J and 42J with the sample black painted. Notice the larger size of the cold spot in proportion to higher impact energy (42J).

7.4 Fast Classification and Parameters Prediction

(I) Decision Making

Tables 10.1 and 10.2 present an on line decision data obtained on the condition and extent of damage of tested woven glass and RIM components subjected to various levels of impact energies as discussed in the previous sections.

These truth tables are based on the non-destructive testing techniques applied with the smart classification and Neural Networks employed for analysis and interpretation. The tables also account for the proposed criteria in Chapter 8 (equations 18, 19 and Figure 8.14) and both the optical map classification (Figure 11.37) and equation 5 in the previous section.

From the image decision tables we realize that both woven glass and RIM materials have similar decision patterns with 1 = Non-defective and 0 = Defective. The decision making follows a modulated step function operating within specified boundaries such that the resulting truth tables are similar with the decision made on different materials accounting for material type and quality.Hence, for fast classification, the finger prints of the tested specimen is represented as a sequence of five variables (see Chapter 8, section 8.4) which is averaged out and a threshold is applied to obtain a Yes/No answer regarding the existence of damage within a material.

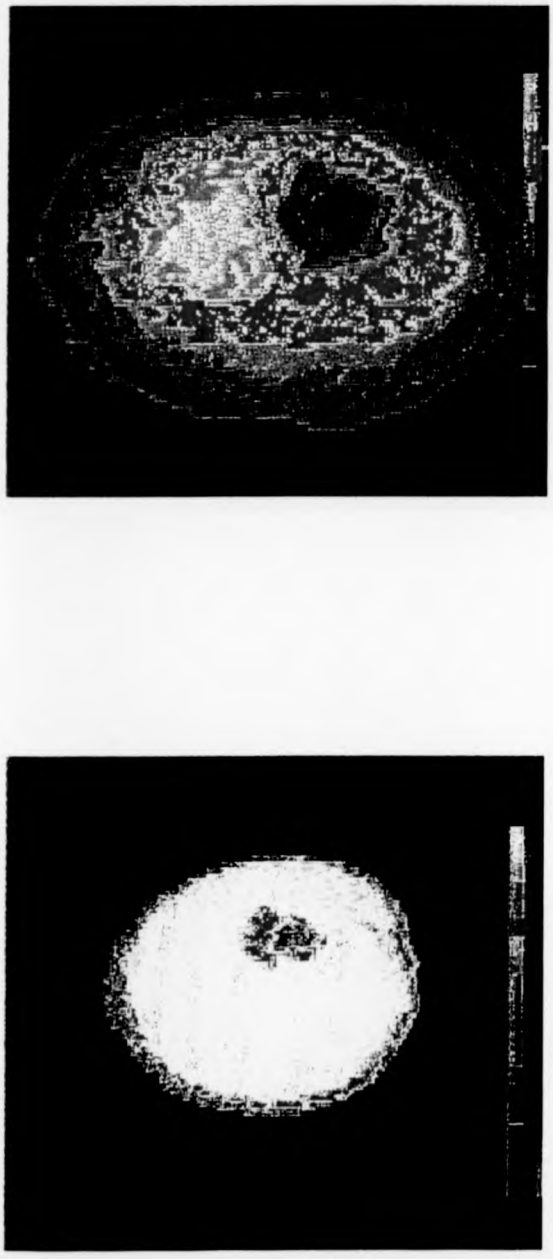

Figure 11.80: Low Temperature PVT applied to 5mm RIM impacted at 28.6J with the load applied at angle.Two thermal ranges.

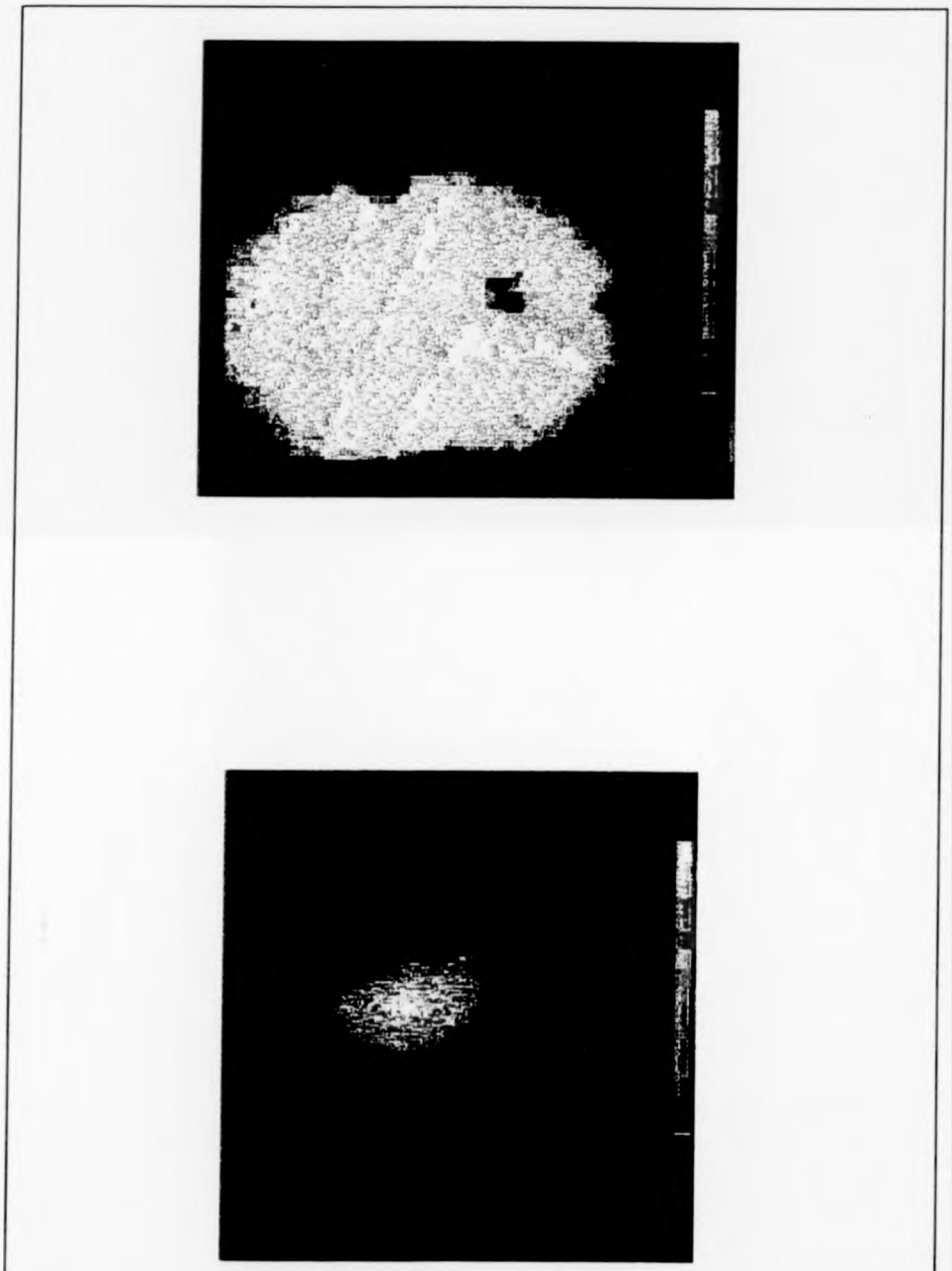

Figure 11.81: Low Temperature PVT applied to 5mm RIM impacted at 28.6J.

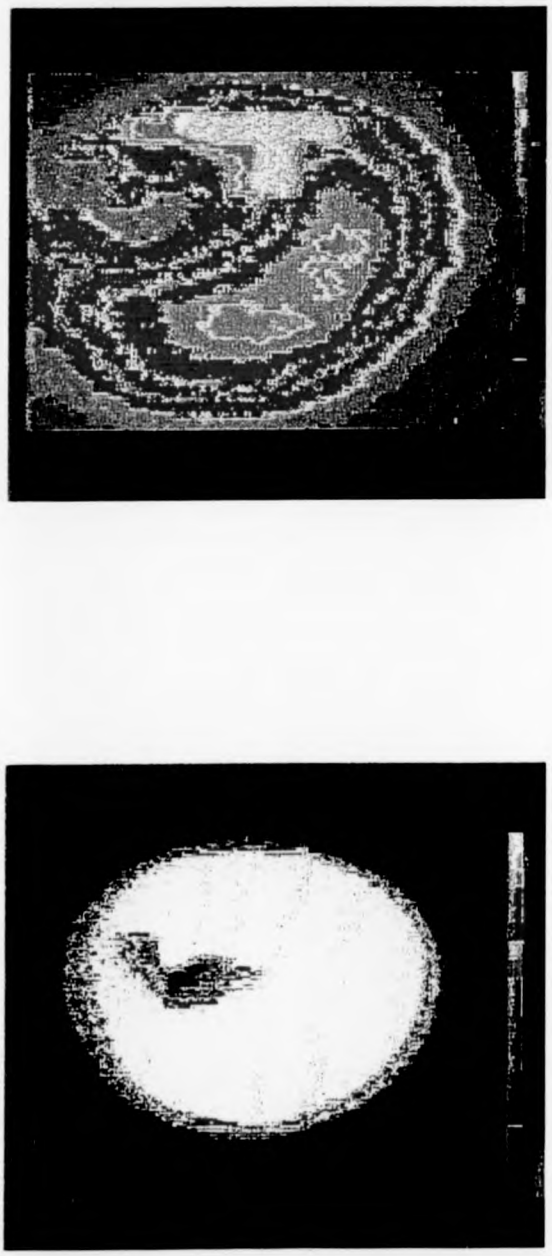

Figure 11.82: Low Temperature PVT applied to 5mm RIM impacted at 55.6J and painted with reflective paint.

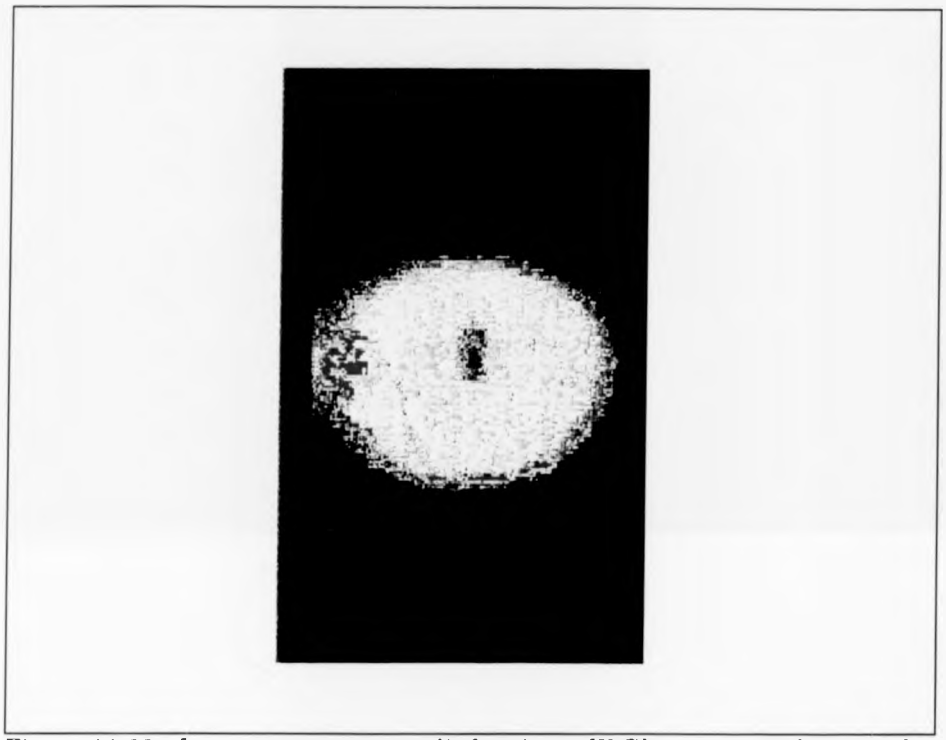

Figure 11.83: Low temperature applied to 5mm W.Glass impacted at 28.6J.

(II) Effect of Thickness on Material Response to Impacts

Figures 11.84-11.91 show the normalized response factor of RIM material components to various impact energies and sample thicknesses as predicted by the Neural Network software. From the plots we notice the following:

(1) The existence of saddle regions (dynamic equilibrium) within the response at thickness above 2mm.

(2) The evidence of cyclic behaviour with the length of cycles found to be a function of specimen thickness. The average correlating factor between cycles length and specimen thickness is found to be 2.6 for the first cycle followed by an increase of a factor of 4 for the remaining

cycles of response.

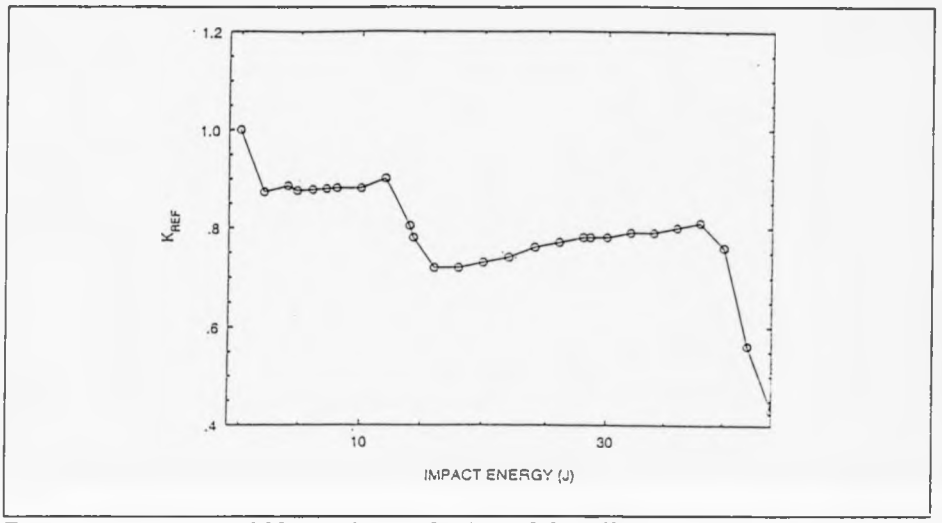

Figure 11.84: Neural Networks prediction of the effect of impact energy on the normalized response of 5mm RIM. (Complete cycle). (Mean of 30 points).

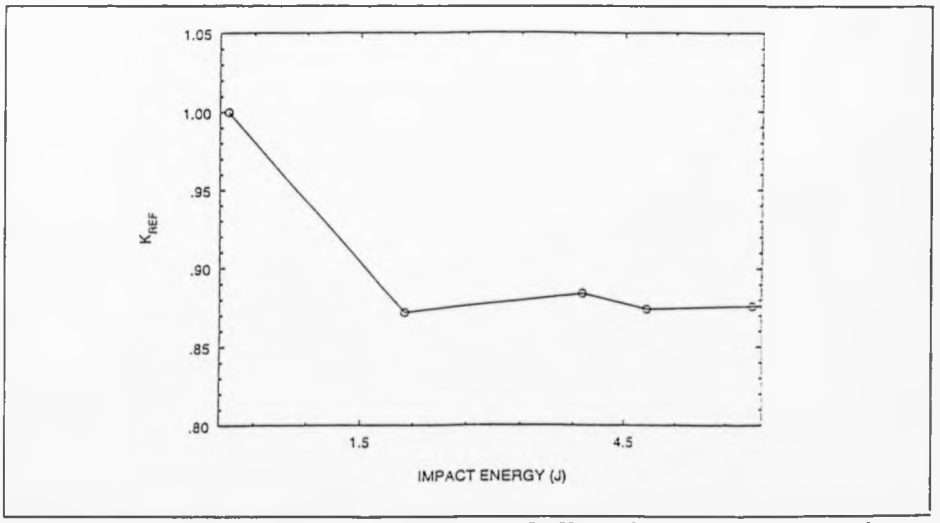

Figure 11.85: Neural Network prediction of effect of impact energy on the normalized response of 5mm RIM. (first cycle). (Mean of 30 points)

Figure 11.92 illustrates the power law behaviour of switching points between

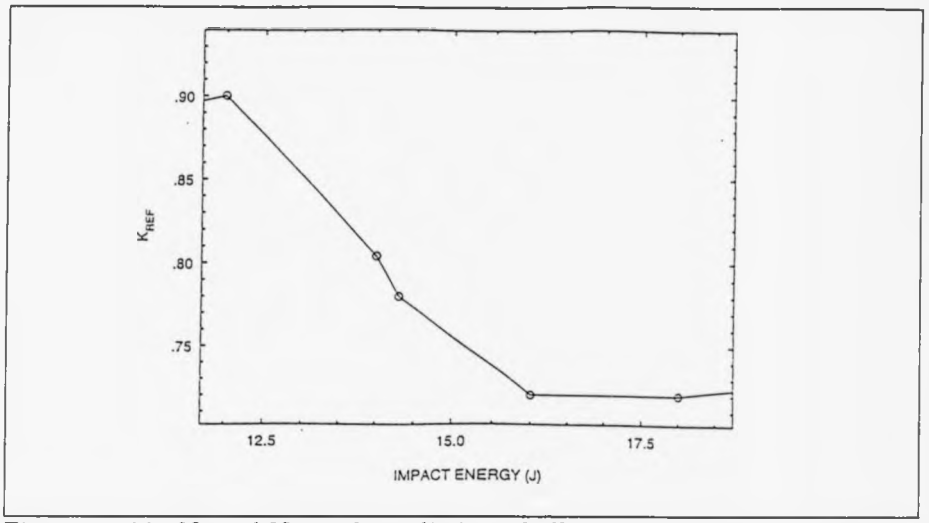

Figure 11.86: Neural Network prediction of effect of impact energy on the normalized response of 5mm RIM.(Second cycle). (Mean of 30 points).

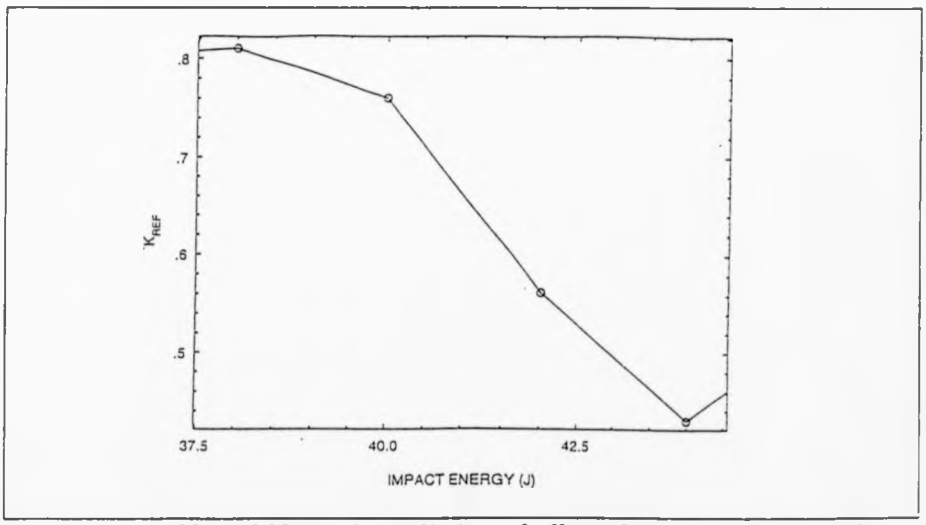

Figure 11.87: Neural Network prediction of effect of impact energy on the normalized response of 5mm RIM. (Third cycle). (Mean of 30 points).

response cycles as a function of sample thickness. As shown, the energy level needed for such switching is proportional to the thickness.

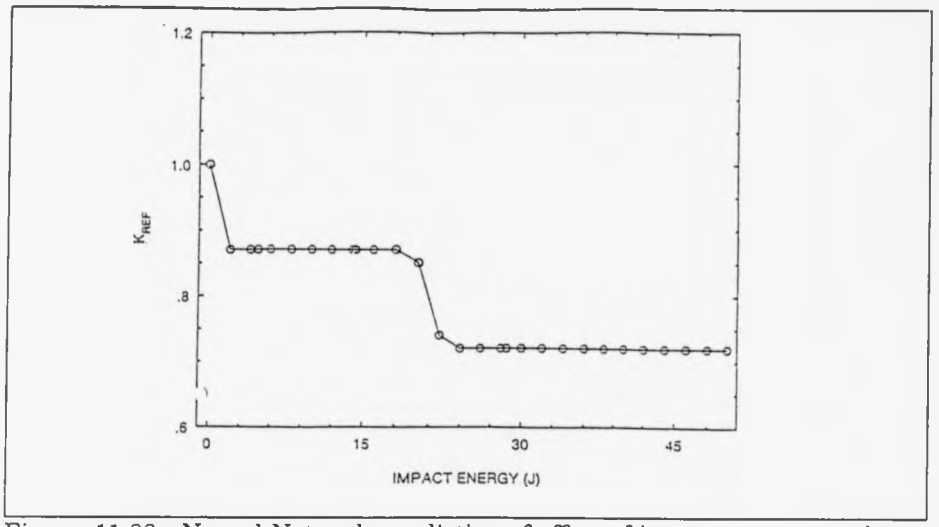

Figure 11.88: Neural Network prediction of effect of impact energy on the normalized response of 8mm RIM. (Complete cycle). (Mean of 30 points).

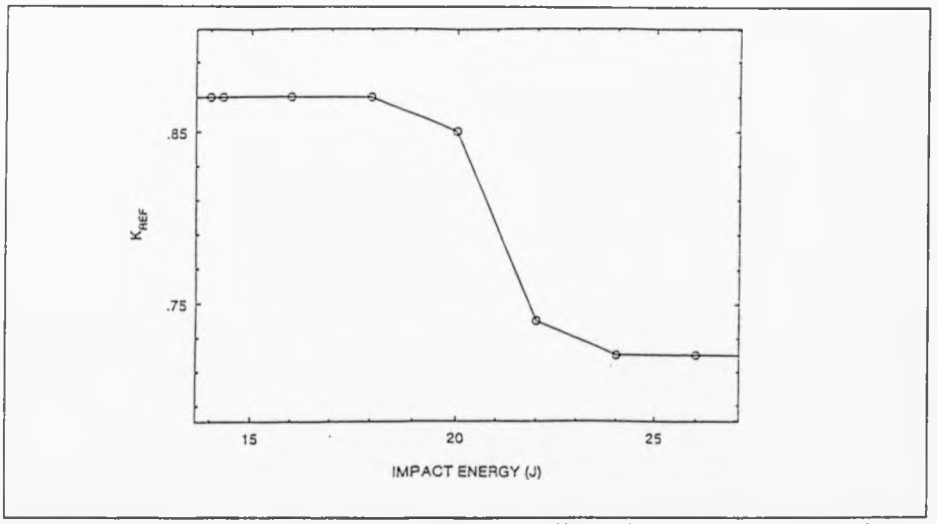

Figure 11.89: Neural Network prediction of effect of impact energy on the normalized response of 8mm RIM.(First cycle). (Mean of 30 points).

The number of switching points within a response spectrum is thought to be inversely related to sample thickness as the length of a cycle per spectrum

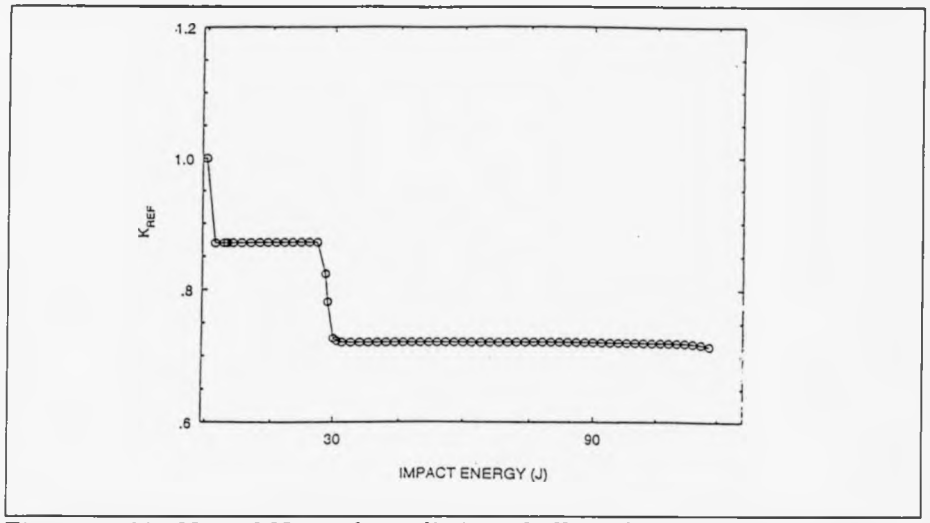

Figure 11.90: Neural Network prediction of effect of impact energy on the normalized response of 11mm RIM. (Complete cycle). (Mean of 30 points).

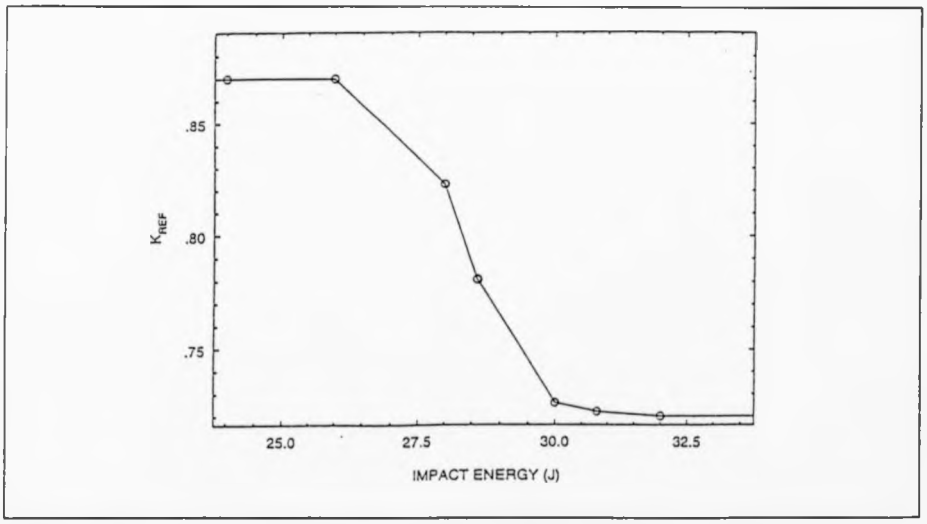

Figure 11.91: Neural Network of effect of effect of impact energy on the normalized response of 11mm RIM. (First cycle). (Mean of 30 points).

increases. Also from the plots we conclude that increasing impact energy

level has the effect of degrading the tested specimen mechanical and optical properties and reducing its integrity.

(III) Prediction and Correlation of Data

Table 10.3 contains predicted data for the three types of material tested. This prediction consists of two parts:

(1) Estimation of lost and distorted data.

(2) Estimation of existing parameters under different boundary conditions. The data in Table 10.3 is based on figures presented in Tables 10.4, 10.5 and 10.6.

The obtained results also correlate various sensing devices and their expected output response when applied to damaged composite structures. This is a very useful feature that the Neural Networks provide which eliminates the need to multi-sensor testing as necessary information regarding component integrity can be obtained through prediction. The established network can also distinguish between different tested materials through encoding. In our case the codes are:

1: Woven Glass

2: Random GMT

2.1: Perpendicular GMT

2.2: Parallel GMT

3: RIM

4: RIM with white coating

Using the above, a complex but easily trained network is formed which relates various material types, impact energies and thicknesses. This is very

hard to achieve normally when traditional analytical algorithms are employed.

(IV) Neural Networks and Aspects of Design

Having tested a large number of samples, designed and trained an appropriate network with optimum hidden layers and obtained data for the same material but with different shape, thickness, working conditions. Other loading parameters can be achieved through prediction. This enables an interface between a computer designed and tested structure (finite element analysis) and a production line. Hence a cheap and effective way to modify structural and other parameters even before the component is built and tested.

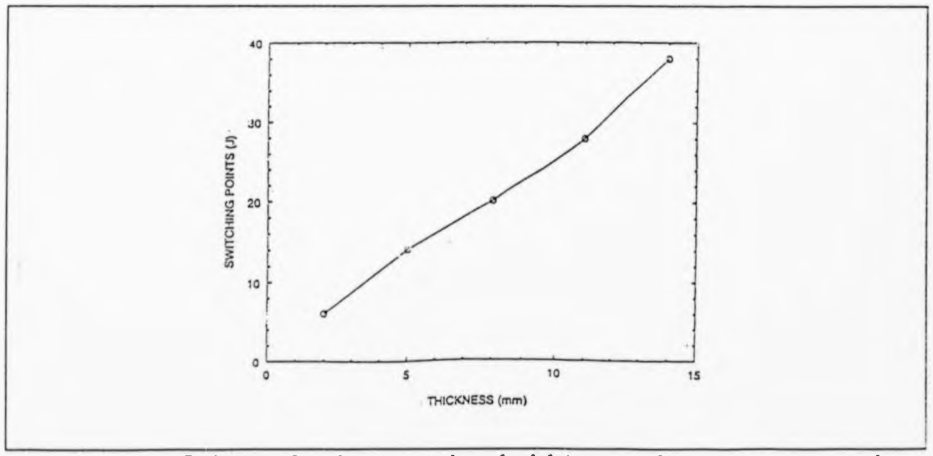

Figure 11.92: Relationship between threshold impact damage energy and component thickness. (Mean of 30 points).

CHAPTER 12

CONCLUSIONS

The objective of this research was to establish a promising NDT technique with appropriate analysis and interpreting algorithms to enable us to practically and economically interrogate composite structures about existing damage and to project the findings to cover component fitness and life cycle under different operating conditions before, during and after manufacturing process.

After implementing various techniques (low frequency, ultrasonics, visual imaging, thermography), modifying some (visual and thermoimaging) and developing our own (IR array system), it is concluded that the most promising technique is Low Temperature Thermoimaging (it eliminates the SATURATION effect) with wave variation facilities (it revels the extent of damage) and smart classification (for fast YES/NO decision) supported by neural networks as analytical and prediction algorithms. These algorithms can also be applied to other NDT techniques to improve their classification capacity.

With the ability of such algorithms to correlate various NDT techniques, the necessary parameters of any composite component can now be obtained without the need to use more than one NDT technique for testing as the rest can be predicted through associative methods performed by the Neural Networks. This is a very useful feature if used together with the hand held tapping device can provide a cheap, fast and accurate damage finder.

Also the following is concluded:

(1) A proportional power law relationship between the composite thickness and its threshold energy (energy above which a component begins to suffer measurable damage, equations 11.(7), 11.(8) and 11.(9)).

(2) Fibre orientation has a marked effect on the composite response to impacts such that a perpendicular GMT suffers less damage compared to parallel or random GMT and WOVEN GLASS proved to be the least affected by similar impact levels applied to both RIM and GMT.

(3) A relationship does exist between the amount of heat applied to a composite structure and the level of detectable impact damage.

(4) The amount of applied heat to a composite component that leads to damage detection is a function of the component thickness.

CHAPTER 13

IMPROVEMENTS, DEVELOPMENTS AND FUTURE WORK.

13.1 Introduction.

Three main areas of this research are already under further investigation. These are:

(1) The process of introducing impact defects.

(2) Analysis, interpretation and presentation of data.

(3) Practical and economical considerations regarding sensing devices; their size, speed of detection, reliability, versatility and adaptability.

In this chapter we will pay particular attention to (1) and (3) since we have already discussed in details data analysis and advanced interpretation techniques in Chapter 8.

13.2 The Impact Damage Process

Figures 9.1-9.2 in Chapter 9 illustrated the used system to carry out the task of composite damage at various energy levels. From the diagrams, it is clear that this impacting system suffers from lack of accuracy, consistency and reliability.Figure (13.1) shows a proposed system which could eliminate some of the drawbacks that the previous system suffers from.

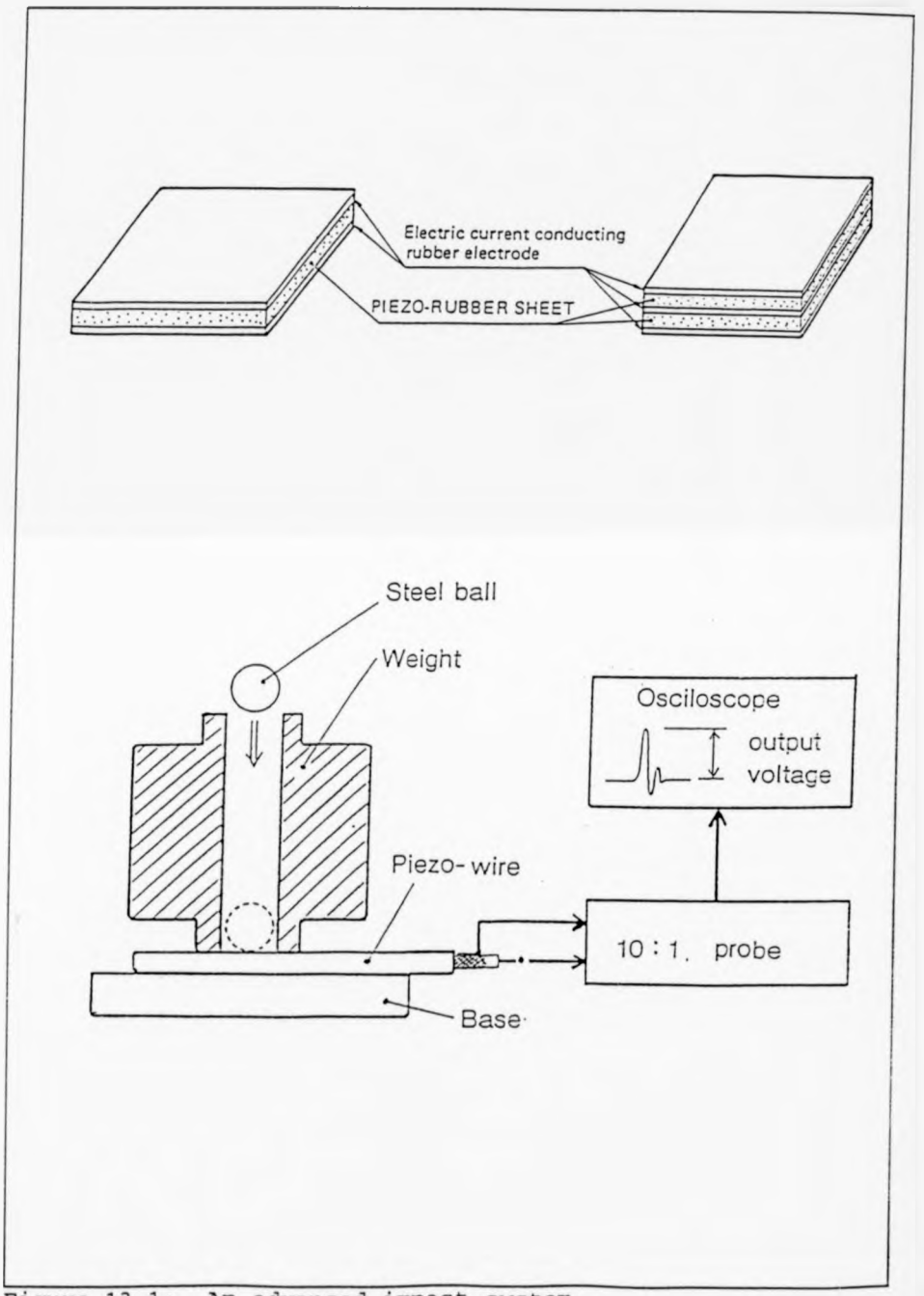

Figure 13.1: An advanced impact system.

The system adopts two types of sensors:

(1) Stress (friction) sensors

(2) Impact level sensor

A piezo-rubber sheet and cables can be used to implement the above functions hereby leading to the following:

(a) Establishing the lost energy during weight travel and up to the point of impact.

(b) Determining the exact impact energy level with correlation to height.

(c) Characterization of the manner an impact travels through a composite component in correlation to component structure and design.

(d) Determining the effect of boundary conditions on the level of damage induced in a component (e.g. clamping).

The above is achieved through different levels of complexity and expense. A simple portable system which interfaces to oscilloscope through amplification circuits can be utilised at a very small cost.

However, a more expensive computerized system, but within acceptable limits, can also be implemented through an analogue-to-digital conversion mechanism and software sampling system. Hence, a compromise can be achieved by using a hand-held data logger for data registration and storage for further analysis.

13.3 Practical and Economical Considerations.

Size and cost are important variables for a versatile, speedy examination and on-line detection of manufactured components. Two areas of NDT that were employed in this research are developed as follows:

(A) Low frequency tapping technique.

The used hand-held device presented in Chapter 6 suffered from the following:

(1) As it is a hand-held device, the measured data is greatly affected by the operator.

(2) The data format is such that another software is needed to obtain graphical representation of frequency and time response but not in real-time.

Figure 13.2 illustrates the new device that eliminates the above and provides the following:

(1) On-line colour dot display of defects through smooth scanning.

(2) Bird's eye view display by calculating the measuring data.

(3) The use of robotic arm to carry out the scanning.

(4) Colour tiling display by calculating the measuring data.

(5) The ability to interface the measured data to other data bases.

The colour display facility of images of defects ties very well with our image interpretation system discussed in Chapters 8 and 11 and conform to our

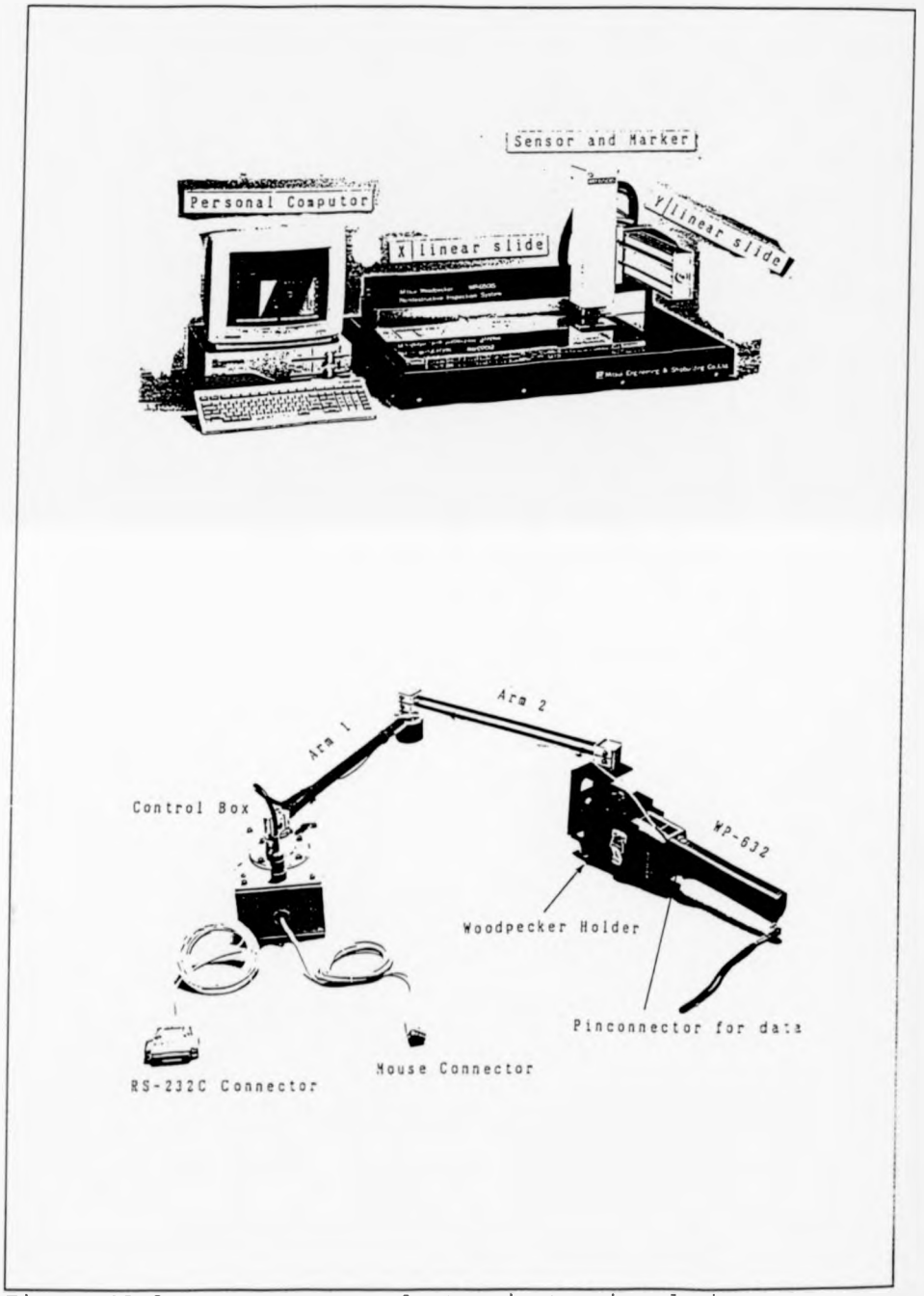

Figure 13.2: An accurate electronic tapping device.

proposal in Chapter 1 of unifying data presentation in the form of images. The use of artificial arm under computer control helps to enter and examine awkward places without risking the safety of the operator.

Figure 13.3 illustrates the type of images possibly obtained using the updated version.

(B) Visual and Infrared Optical Detection Techniques.

In Chapter 7 infrared and infrared thermoimaging concepts were discussed in detail. In this research both near-field and far-field IR techniques were used with video and thermal cameras as detection sensors producing images that can be manipulated by our search through techniques. In Chapter 11 we concluded that high temperature IR systems are not ideal to test RIM and woven glass composites with low energy impact damage. In addition the high cost of a thermoimaging camera and pulse heating system with its bulky size can be a disadvantage when awkward places are to be examined.

The previous prompted us to do two things:

(a) To develop and apply the concept of Low Temperature PVT as discussed in chapter 11.

(b) To develop a portable, cheap, detector array that is simple enough to use but accurate and can interface any form of optical detectors to a portable computer or data logger. It is also thought to be able to implement an

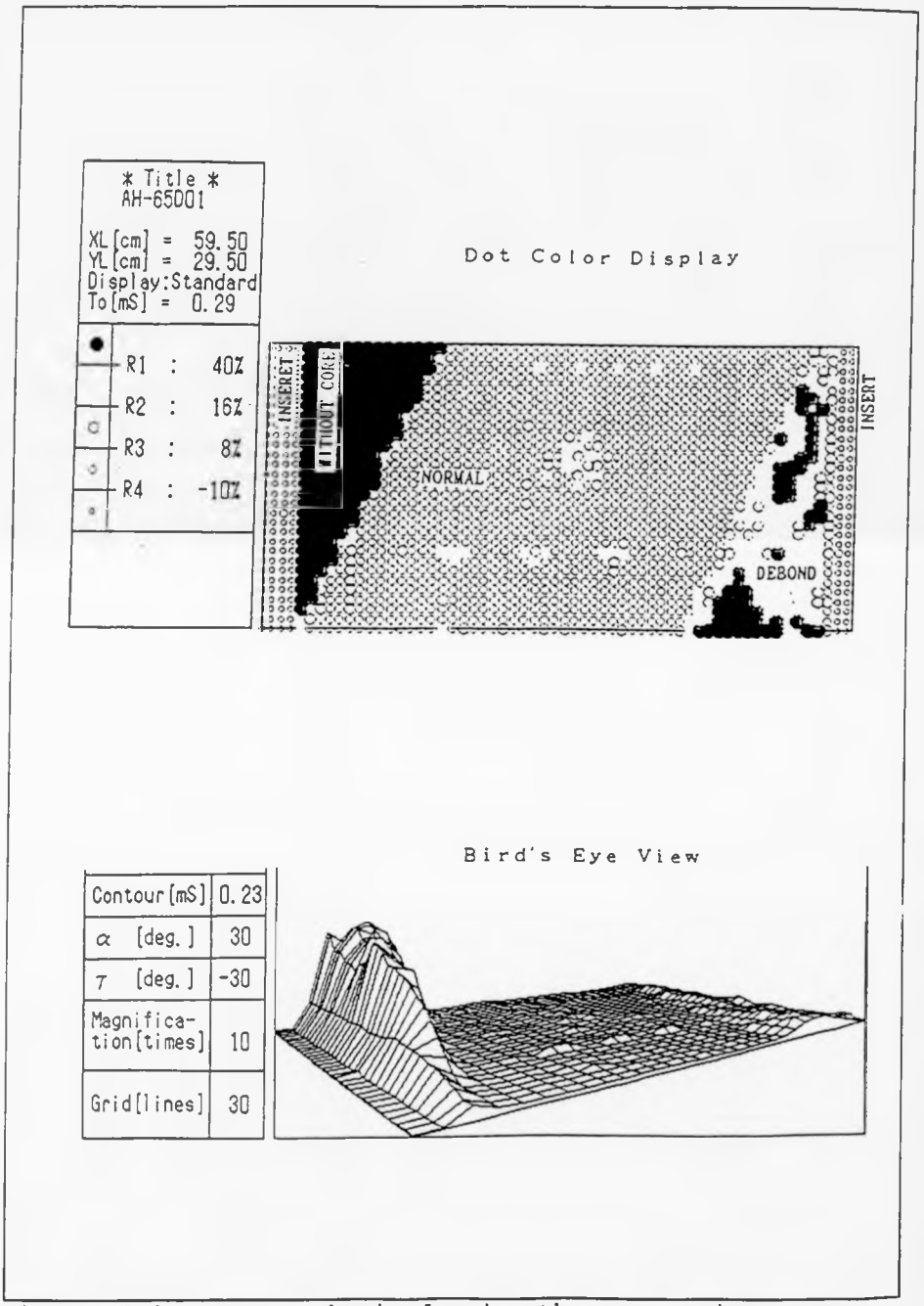

Figure 13.3: Images obtained using the new tapping system.

alternative concept in thermal imaging by simultaneously heating the component and applying the array system for IR transmission and detection, as a differential in temperature within the material will affect its response. Also, stress patterns can be established when the component is vibrated while IR array system is used to check its integrity. This system is at its first stage of development, a detailed report and discussion of its operation is available, (report No: MI.IR.1-1995-ATC).

CHAPTER 14

REFERENCES

1. Shen Bi-Xia and Huang Feng-Lai, "Carbon/Glass fibre hybrid and its epoxy composites", ICCM & ECCM, 1.231-1.239, Feb. 1988.

2. C.T.Sun and J.L.Chan,"A simple flow rule for characterizing nonlinear behaviour of fibre composites, Sixth International Conference on Composite Materials, ICCM & ECCM, 1.250-1.259, February 1989.

3. M.R.Piggott,"Toughness in composites: the need to consider the structural integrity", ICCM 2, 579-587, 1978.

4. B.Walter Rosen,"Design considerations for composite materials", ICCM2, 9-30, 1979.

5. Tsu-Wei Chou,"Microstructural design of fibre composites", Cambridge University Press, 1992.

6. Geoff Eckold,"Design and manufacture of composite structures", Woodhead Publishing Ltd., 1994.

7. Mel M. Schwartz, "Composite materials handbook", McGraw-Hill Inc., 1992.

8. Raynor M.Mayer, "Design with reinforced plastics", Design Council, 1993.

9. J.G.Morley, "High performance fibre composites", Academic Press, New York, 1987.

10. L.N.Phillips (Ed), "Design with advanced composite materials", Springer Verlag, London, 1989.

11. L.N.Phillips, "Potential commercial applications of advanced composite materials - 1985-2000", ICCM/2, 1648-1650, 1978.

12. G.R.Headifen and E.P.Fahrenthold, "Mechanical and electrical properties of glass and carbon fibre reinforced composites", American Society of Mechanical Engineers, Petroleum Division (Publication), PD, 32, 113-118, 1990.

13. C.H.Hsueh,"Interfacial debonding and fibre pull-out stresses of fibre-reinforced composites. No. II Non-constant interfacial bond strength", Materials Science and Engineering A: Structural Materials: Properties, Microstructure and Processing. A125, No.1, 67-73, May 1990.

14. A.E.Pearson, "Capabilities of compression test methods for evaluating unidirectional carbon fibre reinforced composites", International SAMPE Symposium and Exhibition, 36, 1, 1079-1093, 1991.

15. A.A.Baker, G.A.Hawkes and E.J.Lumley, "Fibre-composite reinforcement of cracked aircraft structures - thermal stress and thermal-fatigue studies", ICCM 2, 649-668, 1978.

16. M.R.Piggott, "Debonding and friction at fibre-polymer interface I: Criteria for failure and sliding", Comp. Sci. Tech., 30, 295-306, 1987.

17. J.Summerscales, "Manufacturing defects in fiber-reinforced plastic composites", Insight, 36, 936-942, 1994.

18. H.Sekine and S.Kamiya, "Fibre bridging effect on opening-mode crack extension resistance of unidirectional fibre-reinforced composites", Zairyo/Journal of the Society of Materials Science, Japan, 37, 416, 505-510, May 1988.

19. H.Sekine and S.Kamiya, Nippon Kikai Gakkai Ronbunshi,"Fibre bridging effect on in-plane shear mode crack extension resistance of unidirectional fibre-reinforced composites", A Hen/Transactions of the Japan Society of Mechanical Engineers, Part A, 55, 513, 1203-1208, May 1989.

20. C.H.Hsueh,"Interfacial debonding and fibre pull-out stresses of fibre-reinforced composites", Materials Science and Engineering A: Structural Materials: Properties, Microstructure and Processing, A123, 1, 1-11, January 1990.

21. N.S.Choi and K.Takahashi, "Stress fields on and beneath the surface of short-fibre reinforced composites and their failure mechanisms", Composites Science and Technology, 43, 3, 237-244, 1992.

22. Tsunco Hirai and Teruo Kimura, "Impact binding behaviour of fibre reinforced composite", ICCM 2, 1669-686, 1978.

23. D.W.Schmueser and L.E.Wickliffe, "Impact energy absorption of continuous fibre composite tubes", Journal of Engineering Materials & Technology, Transactions of the ASME, 109, 1, 72-77, 1987.

24. Y.Fujino, Nippon Kikai Gakkai Ronbunshu, "Simple formula for the dynamic stress intensity factor of an impacted freely-supported bend specimen", A Hen, Japan Journal Of Mechanical Engineering, 54, 501, 1101-1106, May 1988.

25. Z.L.Gu and C.T.Sun, "Prediction of impact damage region in SMC composites", Composite Structures, 7, 3, 179-190, 1987.

26. C.F.Buynak, T.J.Moran and S.Donaldson, "Characterization of impact damage in composites", SAMPE Journal, 24, 2, 35-39, March-April 1988.

27. P.O.Sjoblom, J.T.Hartness and T.M.Cordell, "On low-velocity impact testing of composite materials", Journal of Composite Materials, 22, 1, 30-52, January 1988.

28. W.J.Cantwell, "Influence of fibre stacking sequence on the high velocity impact response of CFRP", Journal of Materials Science Letters, 7, 7, 756-758, July 1988.

29. S.Langlie and W.Cheng, "High velocity impact penetration model for thick fibre-reinforced composites", American Society of Mechanical Engineers, Pressure Vessels and Piping Division, PVP, 147, 151-158, 1989.

30. C.Caratheodory, "Theory of functions of a complex variable", Chelsea Publishing Company, 1958.

31. Konard Knopp, "Theory of functions (Part One: Elements of the general theory of analytic functions)", Dover Publications, 1945.

32. A.Kyrala, "Applied functions of a complex variable", Wiley-Inter - Science. 1971.

33. Ian Stewart and David Tall, "Complex analysis", Cambridge University Press. 1988.

34. L.I.Volkovyskii, G.L.Lunts, I.G.Aramanovich, "A collection of problems on complex analysis", Pergamon Press, 1965.

35. L.V.Toralballa, Charles E, "Theory of functions", Merril Books Inc., 1963.

36. E.C.Titmarsh, "The theory of functions", Oxford University Press, 1950.

37. Zeev Nehari, "Conformal mapping", McGraw-Hill Book Company Inc., 1952.

38. K.J.Binns, "Numerical methods of conformal transformation", Proc. IEE, 118, 7, 909-910, July 1971.

39. P.J.Lawrence and S.K.Gupta, "Conformal transformation employing direct-search techniques of minimisation", Proc. IEE, 115, 3, 427-431, March 1968.

40. K.P.Srindhar and R.T.Davis, "A Schwarz-Christoffel method for generating two-dimensional flow grids", Journal of Fluids Engineering, Transactions of the ASME, 107, 330-337, September 1985.

41. Don E. Bray and Don McBride, "Nondestructive testing techniques", Wiley & Sons Inc., 1992.

42. J.Summerscales, "NDT of advanced composites - an overview of the possibilities", British Journal Of NDT, 32, 11, 568-577, 1990.

43. P.Halmshaw, "Nondestructive testing", Edward Arnold, 1991.

44. A.A.Khalil and A.N.Kagho, "Non-destructive testing of adhesively bonded joints using vibrational analysis", International Journal of Adhesion and Adhesives, 11, 2, 121-127, April 1991.

54. C.Norwood and L.Wood, "Use of vibration techniques in non destructive testing", Australian Vibration and Noise Measurement Prediction and Control National Conference Publication - Inst. of Engineers, Australia No.90, 9, 270-275, 1990.

46. P.Cawley, "The nondestructive testing of honeycomb structures by the coin-tap technique", and R.D.Adams, Sixth International Conference on Composite Materials, ICCM & ECCM, 1.415-1.423, February 1989.

47. P.Cawley and R.D.Adams,"Mechanics of the coin-tap method of non-destructive testing", Journal of Sound and Vibration, 122, 2, 299-316, April 1988.

48. R.S.Sharpe, "Research techniques in nondestructive testing, VIII", Academic Press, 1985.

49. P.Potet, P.Jeannin, C.Bathias, "Use of digital image processing in vibrothermographic detection of impact damage in composite materials", Materials Evaluation, 45, 4, 466-470, April 1987.

50. B.Clarke and R.Smith, " AN introduction to the ultrasonic inspection of composites", Imperial college, Jan. 1994.

51. Isao Kimparu, Mitsuo Takehana and Toshio Suzuki, "Analysis of thickness-direction ultrasonic wave propagation of fibre-glass reinforced plastic laminates".ICCM 2. pp 1105-1122, 1978.

52. R.S.Sharpe, "Research techniques in nondestructive testing", Published by Academic Press, 1973.

53. W.N.Reynolds and S.J.Wilkinson, "The analysis of fibre-reinforced porous composite materials by the measurement of ultrasonic wave velocities",Ultrasonics, 159-163, July 1977.

54. R.S.Sharpe, "Research techniques in nondestructive testing", Academic Press, 1977.

55. Warren J. McGonnagle, "Nondestructive testing", Gordon and Breach. 1982.

56. M.G.Silk, A.M.Stoneham and J.A.G.Temple, "The reliability of nondestructive inspection", Adam Hilger, 1987.

57. E.D.Blodgell, J.G.Miller and S.M.Freeman,"Correlation of ultrasonic polar backscatter with the Deply Technique for assessment of impact damage in composite laminates", Review of Progress in Quantitative Nondestructive Evaluation, 5B, 1227-1238, 1986.

58. G.R.Simula, E.C.Pakkala and R.J.Helsel,"Ultrasonic detection of cracked track pins on military vehicles", ASME Des. Eng. Div. Publ. DE. 9, 63-65, 1987.

59. R.J.Andrews, T.J.Moran and R.L.Crane, "Ultrasonic imaging of defects in fibre reinforced composites", Proceedings of the Symposium on Nondestructive Evaluation 15th. 209-218, 1985.

60. M.Arrington, "Acoustic emission - a review", Nondestructive Testing (Proc. 12th world Conference), 429-434, 1989.

61. Larry A. Duesing, "Acoustic emission testing of composite materials", Annual Reliability and Maintainability Symposium, 128-134, 1987.

63. Phillip T. Cole, "The emergence of acoustic emission in structural testing", Dunegan PAC Limited, Cambridge and Geoffrey S. Whalley, British Aerospace. UK., CME. 48-51, 1986.

64. R.D.Rawlings, "Acoustic and Acousto-Ultrasonics", Imperial College. Jan.1994.

65. Megamu Suzuki, Hiroshi Nakanishi, Masaharu Iwamoto, Eiichi Jinen, Zenichiro Mackawa, Akira Moria and Feng Sun,"A study on fracture mechanisms of CRFP by acoustic emission method", Sixth International Conference on Composite Materials. ICCM & ECCM, 1.385-1.394, February 1989.

66. C.K.H.Dharan, "Delamination fracture and acoustic emission in carbon. aramid and glass-epoxy composites", Sixth International Conference on Composite Materials. ICCM & ECCM, 1.405-1.414, February 1989.

67. Mohammed Charfaoui, James Roget, Alain Lemascon and Max Jeanville. "The study of acoustic emission from composites by means of multivariate data analysis". Sixth International Conference on Composite Materials, ICCM & ECCM. 1.424-1.432. February 1989.

68. D.Rouby, "Acoustic emission: A micro-investigation technique for interface mechanisms in fibre composites", Journal of Acoustic Emission, 9, 2, 117-121, 1990.

69. M.R.Karim and T.Kundu, "Acoustic material signature of fibre reinforced composites", American Society of Mechanical Engineers, Petroleum Division, 24, 131-134, 1988.

70. A.C.Wey, L.W.Kessler and H.L.M.dos Reis, "Nondestructively monitoring fatigue damage in fibre reinforced composites using acoustic microscopy", Ultrasonics Symposium Proceedings, 2, 953-956, 1990.

71. V.G.Badalyan, E.G.Bazulin and D.S.Tikhonov, "Non-destructive testing of cylindrical objects by methods of multifrequency acoustic holography", Defektoskopiya, 10, 29-36, October 1991.

72. J.M.Milne and W.N.Reynolds, "Applications of thermal pulses and infrared thermal images for observing sub-surface structures in materials and composites", SPIE 590 (Infrared Technology and Applications), 293-302, 1985.

73. Heevé Tretout, "Infrared thermography development for composite material evaluation", SPIE, 918 (Applications of Infrared Technology), 12-22, 1988.

74. James H. Williams, S.Hossein Mansouri and Samson G.Lee, "One-dimensional analysis of thermal nondestructive detection of delamination and inclusion flaws". British Journal of NDT, 113-118, May 1980.

75. V.Vavillov, "Infra-red nondestructive testing of bonded structures: Aspects of theory and practice", British Journal of NDT, 175-183, May 1980.

76. T.S.Duwani and A.Ranf, F.Lotti and S.Baronti, "Thermal imaging techniques for the nondestructive inspection of composite materials in real time", IEEE, 598-601, 1987.

77. J. Barney, H.Decker and J.Hodor, "New development in NDT infrared thermographic techniques help assess flaw delaminations in flight hardware", SPIE 510 (Infrared Technology X), 201-208, 1984.

78. "Transient thermal technique for infrared nondestructive testing of composite materials", Herve Tretout and Jean-Yves Marin, Avion Marcel, Dassault, France. Published in SPIE Vol.590 (Infrared Technology and Applications), pp 277-284, 1985

79. S.K.Lau and D.P.Almond, J.M.Milne,"A quantitative analysis of pulsed video thermography", NDT & E International, 24, 4, 195-202, 1991.

80. W.N.Reynolds, "Quality control of composite materials by thermography", Metals and Materials, 100-102, February 1985.

81. W.N.Reynolds and G.M.Wells, "Video-compatible thermography", British Journal of NDT, 40-44, January 1984.

82. J.M.Milne and W.R.Reynolds, "The nondestructive evaluation of composites and other materials by thermal pulse video thermography", SPIE 520 (Thermosense VII), 119-129, 1984.

83. Y.L.Hinton, R.J.Shuford and C.G.Pergantis, "Applications of real-time thermography for nondestructive testing of composites", SPIE 520 (Thermosense VII), 142-148, 1984.

84. M.Vikstrom, "Thermographic Non-destructive testing of sandwich constructions", The Royal Institute Of Technology, Sweden, 1-14, Report no.89-14, ISSN 0280-4646, 1989.

85. T.L.Williams, "Assessing the performance of complete thermal imaging systems", SPIE 590 (Infrared Technology and Applications), 172-178, 1985.

86. P.Stanley, "An appraisal of a new infra-red based stress analysis technique". . Published in SPIE 590 (Infrared Technology and Applications), 260-267, 1985.

87. Colin H. Jones, "Infrared imaging of vascular changes", Published in SPIE Vol.918 (Applications of Infrared Technology), 61-68, 1988.

88. Robert P. Madding, "Applications of infrared thermography in nondestructive evaluation", SPIE 814 (Photomechanics and Speckle Metrology), 413-420. 1987.

89. P.H.Smith, "Short- and long-wave solutions: Thermal imaging", Industrial Photography. 36, 5, A40-A44, May 1987.

90. T.S.Durrani, K.Boyle, F.Lotti and A.Rauf, "Computer aided thermal imaging techniques for the inspection of composite materials", IEE, London, 4. 1-4, 5, 1986.

91. T.S.Durrani, A.Rauf, K.Boyle, F.Lotti and S.Baronti. "Thermal imaging techniques for the nondestructive inspection of composite materials in real time".IEEE International Conference on Acoustics and Signal Processing, IEEE, New York USA, 598-601, 1987.

92. J.P.Holman, "Heat Transfer", McGRAW HILL, 1989.

93. J.Clark and M.Fitzgerlad,"Pinpoint temperature-related problems with thermal imaging", Power, 131, 1, 59-60, January 1987.

94. L.Warren and J.R.Paterson, "Use of thermal imaging for the development of materials to withstand extreme service conditions", IEEE Conference Publications. 289. 290-292. 1988.

95. M.J.Folkes and H.A.Potts, "Assessment of fibre orientation in composites using infra-red thermal imaging", Plastics and Rubber Processing and Applications. 10, 2, 79-84, 1988.

96. J.C.Murphy, J.W.Maclachlan and L.C.Aamodt, "Thermal imaging of barrier coatings on refractory substrates", Review of Progress in Quantitative Nondestructive Evaluation. 7A, 245-252, 1988.

97. J.Montoro, K.H.Lee and M.Anbar, "Study of regulation of skin temperature using dynamic digital thermal imaging", Proceedings of the Annual Conference on Engineering in Medicine and Biology, 11, 4, 1158-1159, 1989.

98. J.Y.Hutchingson, "Thermal imaging. Turning the heat on", Physicians and Computers, 6, 5, 36-39, September 1988.

99. K.A.Getty, R.O.Doney and M.S.McDonald, "Thermal imaging inspection of eroded/corroded piping", American Soc. of Mechanical Engineers, New York. USA, 157-161, 1989.

100. B.Wallin, "Advances in thermal imaging", Evaluation Engineering, 29, 5, 90-91. 93, May 1990.

101. V.M.Batenin, I.A.Vasil-eva, A.L.Golger, I.I.Klimovskii, A.A.Lash and D.N.Yundev, "Feasibility of measuring the absolute temperature distribution of the surface of ceramic samples by a luminescence-thermal imaging method", High Temperature, 27. 5. 779-782, March 1990.

102. D.Zheng, Hongwai Jishu"Thermal imaging system for submarine periscope". Infrared Technology, 14, 3, 12-14, June 1992.

103. J.H.Williams, S.H.Mansouri and S.S.Lee, "Thermal nondestructive testing of fibreglass laminates using liquid crystals", British Journal of NDT, 184-190, July 1980.

104. D.Hepp, Kunststoffe, "Pigmented and highly transparent impact resistance PVC for outdoor application" German Plastics, 77, 11, 28-30, 1177-1179, November 1987.

105. H.Mitsui, Y.Inoue, K.Kawahara and H.Yoshida, "Non-destructive insulation diagnosis by colour measurement", Cavanagh Associates, Leatherhead, England. 248-253, 1986.

106. P.S.Grant, W.T.Kim, B.P.Bewlay and B.Cantor, "Monitoring of deposit surface temperatures during spray-forming by infrared thermal imaging", Scripta Metallurgica, 23, 10, 1651-1656, 1989.

107. John Summerscales, "Nondestructive testing by Raman spectroscopy", Sixth International Conference on Composite Materials, ICCM & ECCM, 1.321-1.332. February 1989.

108. I.M.Robinson, R.J.Young and C.Galiotis and D.N.Batchelder, "Nondestructive evaluation of composite materials using a Raman optomechanical gauge", Sixth International Conference on Composite Materials, ICCM & ECCM, 1.333-1.340, February 1989.

109. B.Rief, G.Busse and P.Eyerer, "Nondestructive evaluation of carbon fibre reinforced plastics with optically generated thermal waves", Sixth International Conference on Composite Materials, ICCM & ECCM, 1.349-1.358, February 1989.

110. Wanfu and Xiong Binghen, "Measurement of deformation of loaded track by white light speckle method", Published in SPIE Vol.599 (Optics in Engineering Measurement), 124-128, 1985.

111. Jingtang Ke, Yaowa Ma and Caifu Zaho, "Measurement of residual stresses by modern optical methods (II)", SPIE Vol.597 (Optics in Engineering Measurement), 210-223, 1985.

112. Zhong Lin and Wen-Hong Chin, "A novel method for evaluating the resolution and the wavefront of plane diffraction grating with fft", SPIE Vol.599 (Optics in Engineering Measurement), 297-302, 1985.

113. R.J.Day, M.Zakikhari, R.J.Young and I.M.Robinson, "Measurement of deformation of high modulus fibres and composites using Raman microscopy", SPIE Vol.918 (Applications of Infrared Technology), 94-99, 1988.

114. R.Jones, "A review of optical techniques for the measurement of surface geometrics", SPIE 599 (Optics in Engineering Measurements), 309-316, 1985.

115. Tai-Huo Dong, Cheng-Kang Pao and Lin Dan, "The application of phase detection technique used in the ultra-precision surface flatness", SPIE 599 (Optics in Engineering Measurements), 317-324, 1985.

116. Kevin G. Harding, "Optical examination of highly curved structures", SPIE 814 (Photomechanics and Speckle Metrology), 406-412, 1987.

117. P.K.Kuo, R.L.Thomas and L.N.Favro, "Optical/thermal wave techniques for thin film metrology", SPIE Vol.814 (Photomechanics and Speckle Metrology), 428-432, 1987.

118. I.Grant and G.H.Smith, "Surface evaluation using non-destructive optical methods", The Welding Institute, Abington, England, 1, 171-180, 1986.

119. D.P.Almond, P.M.Patel and H.Reiter, "Nondestructive testing of plasma sprayed coatings using thermal wave interferometry", Welding Institute, Abington, England. 1, 163-169, 1986.

120. P.Moon and D.E.Spencer, "Field theory handbook", Springer-Verlag, 1971.

121. K.C.Cole, D.Noel and J.J.Hechler, "Applications of diffuse reflectance Fourier transform infrared spectroscopy to fibre-reinforced composites", Polymer Composites, 9, 6, 395-403, December 1988.

122. M.A. de Smet, "Holographic nondestructive testing for composite materials used in aerospace" SPIE, 599 (Optics in Engineering Measurements), 46-52, 1985.

123. John W. Newman, "Production and field inspection of advanced materials with holographic and speckle interferometry", SPIE 814 (Photomechanics and Speckle Metrology), 421-427, 1987.

124. Y.Y.Hung, "Shearography versus holography in nondestructive evaluation of tires and composites", SPIE 814 (Photomechanics and Speckle Metrology), 433-442, 1987.

125. S.L.Toh, F.S.Chau, H.M.Shang and C.J.Tay, "Flaw detection in composites using shearography" Sixth International Conference on Composite Materials, ICCM & ECCM. 1.341-1.348, February 1989.

126. S.Persson and E.Ostman, "Use of computed tomography in non-destructive testing of polymeric materials, aluminium and concrete: Part 2 - applications", Polymer Testing. 6, 6, 415-446, 1986.

127. L.Feinstein and R.J.Hruby, "Surface-crack detection by microwave methods",Proceedings of the Sixth Symposium on Nondestructive Evaluation of Aerospace and Weapons Systems Components and Materials, 92-106, April 1967.

128. A.D.Lucian and R.W.Gribbs, "The development of microwave NDT technology for the inspection of non-metallic materials and composites" Sixth Symposium on Nondestructive Evaluation of Aerospace and Weapons Systems Components and Materials, 199-232, April 1967.

129. A.J.Baden Fuller, "Microwaves", pergamon press, 1988.

130. D.K.Cheng, "Field And Wave Electromagnetics", Addison Wesley, 1989.

131. E.J.Gross, "Applied potential tomography; an introduction and applications for thermal imaging", American Society of Mechanical Engineers, Heat Transfer Division, 127, 19-23, 1990.

132. T.P.Ryan, M.J.Moskowitz and K.D.Paulsen,"The Dartmouth electrical impedance tomography system for thermal imaging", Proceedings of the Annual Conference on Engineering in Medicine and Biology, 13, 1, 321-322, 1991.

133. Philip C. Myers, "Basic principles and applications of microwave thermography", Department of Physics and Research Laboratory of Electronics, Massachusetts Institute of Technology, USA. 41-46, 1980.

134. A.Mamouni, B.Bocquet, J.C.Van e Velde and Y.Leroy, "Microwave thermal imaging by radiometry", Microwave Exhibitions & Publ. Ltd., Tunbridge Wells, England. 381-385, 1987.

135. N.H.Frost, "Microwave holography and coherent tomography", University of Pennsylvania, Philadelphia. 66-81, 1980.

136. Malcolm Slaney, Mani Azimi, "Microwave imaging with first order diffraction tomography", Schlumberger Palo Alto Research, Palo Alto, CA, USA; Department of Electrical Engineering, Michigan State University, USA; Avinash C. Kak, School of Electrical Engineering, Lawrence E. Larsen, Microwave Department, Walter Reed Army Institute of Research, Washington DC, USA. 184-212, 1980.

137. R.L.Smith, "The effect of scattering on contrast microfocus projection X-radiography", British Journal of NDT, 236-239, 1980.

138. N.N.Blinov, F.G.Gorelik and G.V.Kon'kova"Frequency response in X-ray image detectors", Biomedical Engineering (New York), 20, 3, 88-92, May-June 1986.

139. J.D.Memory, R.E.Fornes and R.D.Gilbert,"Radiation effects on graphite fibre reinforced composites", Journal of Reinforced Plastics and Composites, 7, 1. p 33-65, January 1988.

140. M.Hagiwara, A.Udagawa, S.Kawanishi, S.Egusa, H.Nakajima, M.Oshigiri and S.Shimamoto, "Effect of organic components on radiation stability of fibre reinforced composites", Swiss Inst. for Nuclear Research, Villigen, Switzerland. 688-691. 1985.

141. N.N.Blinov, F.G.Gorelik and G.V.Kon'kova, "Frequency response in X-ray image detectors", Biomedical Engineering (New York) (English translation of Meditsinskaya Tekhnika), 20, 3, 88-92, May-June 1988.

142. J.Harvey, C.Kozlowski and P.M.A.Sherwood, "X-ray photoelectron spectroscopic studies of carbon fibre surfaces part 6: Pilot plant surface treatment and epoxy resin composites", Journal of Materials Science, 22, 5, 1585-1596, May 1987.

143. Donald S. Frankel, Hunter Hancock, James Stark Draper, "A microcomputer neural net bench marked against standard classification techniques", IEEE First International Conference on Neural Networks, San Diego, California, IV651-IV658, 21-24 June 1987.

144. Lawrence Davis"Mapping classifier systems into neural networks", BBN Laboratories, BBN Systems and Technologies Corporation, 10 Moulton Street, Cambridge, MA 02238, 49-56, 16 January 1989.

145. William Y. Huang and William P. Lippmann, "Neural net and traditional classifiers", Neural Information Processing Systems, American Institute of Physics, New York, 1988. 387-396.

146. Pierre Baldi and Kurt Hornik, "Neural networks and principal component analysis: Learning from examples without local minima", Neural Networks Net 2, 53-58, 1989.

147. J.W.Gardner, E.L.Hines and H.C.Tandy, "Detection of vapours and odours from a multisensor array using pattern recognition techniques. Part 2: Artificial neural networks", Department of Engineering, University of Warwick, Coventry, CV4 7AL, UK, 1-11, December 1991.

148. Keinosuke Fukunaga and Warren L.G.Koontz, "A criterion and an algorithm for grouping data", IEEE Trans Comput, C-19, 917-923, 1970.

149. Bruce G. Batchelor, "Methods of pattern classification", Practical Approach to Pattern Classification, Plenum, London, 35-51, 1974.

150. Harry C. Andrews, "Introduction to mathematical techniques in pattern recognition", Wiley - Interscience, 1972.

151. Narendra Ahuja, Bruce J. Schachter "Pattern models", Wiley - Interscience. John Wiley and Sons, 1983.

152. Hung-Chun and Michael T. Manvy, "Iterative improvement of a nearest neighbour classification", Neural Networks, 4, 517-524, 1991.

153. C.H.Chen, "Pattern recognition and artificial intelligence", The Academic Press. 1976.

154. J.M.Mendel, "Adaptive learning and pattern recognition systems: Thermal applications". The Academic Press, 1970.

155. Peter W. Becker, "Recognition of patterns", Springer-Verlag, 1978.

156. Satosi Watanabe, "Frontiers of pattern recognition", Academic Press, 1972.

157. Julian W. Gardner, "Detection of vapours and odours from a multisensor array using pattern recognition, Part 1: Principal component and cluster analysis", Sensors and Actuators B, 4, 109-115, 1991.

158. Donald H. Foley and John W. Sammon, "An optimal set of discriminant vectors", IEEE Trans. Comput., C-24, 281-289, 1975.

159. Fabrizio A.M. Davide, Arnold d'Amico, "Pattern recognition from sensor arrays: theoretical considerations", Sensors and Actuators A, 32, 507-518, 1992.

160. Maureen Caudill and Charles Butler, "Naturally intelligent systems", MIT Press, 1991.

161. Robert Hecht-Nielson, "Neurocomputing", Addison-Wesley, 1991.

162. R.Beale and T.Jackson, "Neural computing, an introduction", IOP Limited, 1992.

163. Alison Carling, "Introducing neural networks", Sigma Press, 1993.

164. Igor Alexsander and Helen Morton, "An introduction to neural computing", Chapman and Hall, 1993.

165. S.G.Shirley, "Olfaction", International Review of Neurobiology, 1990. Original Draft.

166. J.J.Hopfield, "Neurons with graded response have collective computational properties like those of two-state neurons" Neurocomputing, 3088-3092, 1981.

167. Russell Leighton, "Geometric analysis of neural network capabilities", IEEE First International Conference on Neural Networks, III385-III392, 21-24 June 1987.

168. I.I.Mühlenbein and J.Kindermann, "The dynamics of evolution and learning - towards genetic neural networks", Connectionism in Perspective, 173-197, 1989.

169. Peter A. Jansson, "Neural networks: An overview", American Chemical Society. 357-362, 1991.

170. Yong Yao, Walter J. Freeman, Brian Burke and Qing Yang, "Pattern recognition by a distributed neural network: An industrial application", Neural Networks. 4. 103-121. 1991.

171. Stu Borman, "Neural networks applications in chemistry begin to appear",CZEN. 24-27. 24 April, 1990.

172. Doron Lancet, "The strong scent of success", Nature. 351, 275-276. May 1991.

173. alter J. Freeman, "Local information processing in Dendritic trees: subsets of spines of the mammalian olfactory bulb in Granule cells ",Brain Research, 1991.

174. Walter J. Freeman, Frank H. Eeckman "Asymmetric sigmoid non-linearity in the rat olfactory system", Published in Brain Research, 557, 13-21, 1991.

175. Walter J. Freeman, "A neural mechanism for generalization over equivalent stimuli in the olfactory system", SIAM-AMS Proceedings, 13, 25-38, 1981.

176. Walter J. Freeman, Yong Yao and Brian Burke, "Central pattern generating and recognizing in olfactory bulb: A correlation learning rule", Neural Networks, 1, 277-288, 1988.

177. J.J.Hopfield, "Olfactory computation and object perception",Proc. Natl. Acad. Sci., USA. 6462-6466, August 1991.

178. Z.Li, "A model of olfactory adaption and sensitivity enhancement in the olfactory bulb",Biol. Cybern., 62, 349-361, 1990.

179. Zhaoping Li and J.J.Hopfield, "Modelling the olfactory bulb - coupled nonlinear oscillators", Information Processing Systems I, 402-409, 1989.

180. Eric B. Baum, David Gaussler, "What size net gives valid generalization". Neural Computation, 81-90, January 1989.

181. Donald H. Foley, "Considerations of sample and feature size", IEEE Trans. Inform. Theory, IT-18, 618-626, September 1972.

182. Michael C. Mozer and Paul Smokensky, "Skeletonization: A technique for trimming the fat from a network via relevance assessment", Advances in Neural Information Processing Systems I, 107-115, 1989.

183. J.Sietsma and R.J.F.Dow, "Neural net pruning - why and how", IEEE International Conference on Neural Networks, I325-I333, 1992.

184. A.Ultsch and H.P.Siemon, "Kohenen's self-organising feature maps for exploratory data analysis", Kluwer Academic Publications for the International Neural Network Conference, 305-308, 9-13 July 1990.

185. Amir Dembo and Thomas Kailath, "Model-free distributed learning", IEEE Transactions in Neural Networks, 1, 1, 58-70, March 1990

186. Suzanna Becker and Geoffrey E. Hinton, "Self-organising neural network that discovers surfaces in random-dot stereograms", Nature, 355, 161-163, 9 January 1992.

187. Matthew A. Wilson and James Bower, "A computer simulation of olfactory cortex with functional implications for storage and retrieval of olfactory information", Computation and Neural System Program, American Institute of Physics, 115-127, 1988.

188. Frank H. Eckman, "The Sigmoid nonlinearity in prepyriform cortex", American Institute of Physics, New York, 242-247, 1988.

189. John McCollum, John Larson, Tim Otto, Frank Schottler, Richard Granger and Gary Lynch,"Short-latency single unit processing in olfactory cortex", Journal of Cognitive Neuroscience, 3, 3, 293-299, 1991.

190. Lewis B.Haberly and James M. Bower, "Olfactory cortex: model circuit for study of associative memory?", TINS, 12, 7, 258-264, 1989.

191. Lewis B.Haberly, "Neuronal circuitry in olfactory cortex: anatomy and functional implications", IRL Press Limited, Oxford, England, 219-238

192. Bill Baird, "Bifunction and category learning in network models of oscillating cortex", Physica D, 42, 365-384, 1990.

193. J.W.Gardner, E.L.Hines and M.Wilkinson, "Application of artificial neural networks to an electronic olfactory system", Meas. Science Technology, 1, 446-451, 1990.

194. John G. Taylor, "Neural modelling of vision and olfaction", Advanced Neural Computers, 313-322, 1990.

195. Joe Esenberg, Walter J. Freeman and Brian Burke, "Hardware architecture of a neural network model simulating pattern recognition by the olfactory bulb", Neural Networks, 2, 315-325, 1989.

196. Yong Yao and Walter J. Freeman, "Pattern recognition in olfactory systems: Modelling and simulation", Neural Networks, I-699 - I-704, 1990

197. Robert R.H.Anholt, "Molecular physiology of olfaction", American Physiological Society, C1043-C1054, 1989.

198. Theresa A. Harrison and John W. Scott, "Olfactory bulb responses to odour stimulation: Analysis of response pattern and intensity relationships", The American Physiological Society, 1571-1589, 1986.

199. Michael Meredith, "Patterned response to odour in mammalian of bulb: The influence of intensity", The American Physiological Society, 572-597, 1986.

200. Toshio Kisaka and Kiyoshi Hama, "Synaptic organization in the teleost olfactory bulb", Masson, Paris, 707-719, 1982-1983.

201. S.M.Ahn and Walter J. Freeman, "Steady-state and limit cycle of mass of neurons forming simple feedback loops (I): Lumped circuit model", Kybernetik 16, 87-91, 1974.

202. Leonid I. Perlovsky and Margaret M.McManus, "Maximum likelihood neural networks for sensor fusion and adaptive classification", Neural Networks, 4, 89-102, 1991.

203. W.Gopel and G.Gauglitz, "Biosensor systems based upon receptor functions", Chemie: G.Jung, Proceedings of International Workshop, 1-43, 1989.

204. F.H.Eechman and W.J.Freeman, "The Sigmoid nonlinearity in neural computation. An experimental approach", The American Institute of Physics, 135-139, 1986.

205. A.V.Gaponov-Grekhov and M.I.Rabinovich, "Nonstationary structures - chaos and order", Proceedings of the International Symposium on Synergetics at Schloss Elmau, Bavaria, 226-237, May 1983.

206. J.S.Nicolis,"The role of chaos in reliable information processing", Proceedings of the International Symposium on Synergetics and Shloss Elmau, Bavaria, 330-343, May 1983.

207. James R. Long, Vasilis G. Gregoriou and Paul J. Gamperline, "Spectroscopic calibration and quantification using artificial neural networks", Analytical Chemistry, 62, 17. 1791-1795, 1 September 1990.

208. D.S.Broomhead and David Lowe, "Radial basis functions, multi-variable functional interpolation and adaptive networks", Complex Systems 2, 321-355, 1988.

209. Laura Ignizio Burke, "Introduction to artificial neural systems for pattern recognition". Computers Ops. Res., 18, 2, 211-220, 1991.

210. John W. Clark, "Introduction to neural networks", Proceedings of the Workshop on Nonlinear Phenomena in Complex Systems, Mar del Plata, Argentina, 1-101, 1-14 November 1988.

211. Walter J.. Freeman, Joe Eisenberg and Brian Burke, "Hardware simulation of brain dynamics in learning the spock", IJCNN, III435-III442, 1989.

212. Jocelyn Sietsma and Robert J.F. Dow, "Creating artificial neural networks that generalize", Published in Neural Networks, 4, 67-79, 1991.

213. O.D. Faugers, "Fundamentals in computer vision (an advanced course)", Cambridge University Press, Cambridge, 1983, ISBN: 0521 25099 4.

214. Rafael C. Gonzalez and Paul Wintz, "Digital image processing, Addison Wesley Publishing Company Advanced Book Program/World Science Division, ISBN: 0-201-03044-6, ISBN: 0-201-03045-4 pbk, 1983.

215. "Computational Vision", Harry Wechsler, Computer Science Department, George Mason University, Virginia, USA. Published by The Academic Press Inc., 1990

216. Shi-Kuo Chang, "Principles of pictorial information systems design". Prentice Hall. 1989.

217. H. John Durrett, "Colour and the computer", The Academic Press, 1987.

218. J.R. Parker, "Practical computer vision", John Wiley and Sons, 1993.